Influence of film formers on magnetite properties under water-steam cycle conditions

The influence on acidic flow-accelerated corrosion and magnetite surface charge in conditions pertinent to condensate, feedwater and boiler systems

B. Bischoff Tulleken

MSc. Thesis

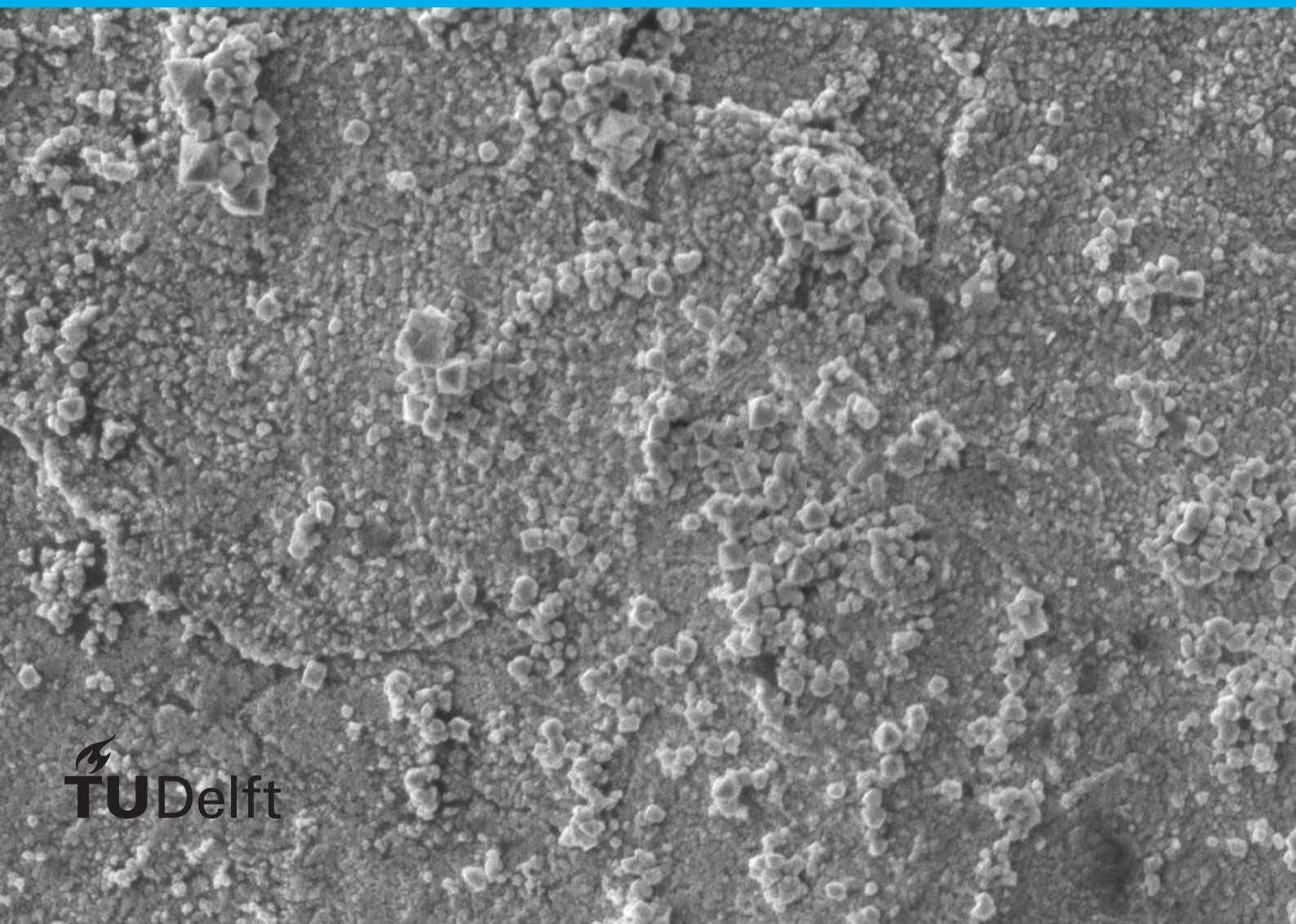

TU Delft

Influence of film formers on magnetite properties under water-steam cycle conditions

The influence on acidic flow-accelerated corrosion and magnetite surface charge in conditions pertinent to condensate, feedwater and boiler systems

by

B. Bischoff Tulleken

to obtain the degree of Master of Science
at the Delft University of Technology,
to be defended publicly on Tuesday July 6, 2021 at 16:00 PM.

Student number:	4351339	
Project duration:	April 12, 2020 – June 25, 2021	
Thesis committee:	Dr. ir. H. Spanjers,	TU Delft, chair
	Dr. ir. R. E. F. Lindeboom,	TU Delft
	Dr. S. M,. Vidojkovic,	TU Delft, University of Belgrade
	Dr. ir. D. H. Moed,	Evides Industry Water
	Prof. dr. ir. J. M. C. Mol,	TU Delft
	Prof. dr. A. R. D. Verliefde,	Ghent University

This thesis is confidential and cannot be made public until July 6, 2023.

TU Delft

Acknowledgements

Throughout this research I have had the honour and pleasure to work with, and receive support from, many wonderful people. This MSc. thesis would not have been possible without their contribution.

First and foremost, I would like to express my sincere appreciation to the chair of my committee, Dr ir. Henri Spanjers, for the support, discussions, and advise throughout the entire thesis, and for introducing me to the field of Industry Water. I would like to thank Dr. Sonja Vidojkovic for supplying me with this research topic and helping me get started with the experiments. Dr. ir. Ralph Lindeboom, thank you for all your advise, and for encouraging me to pursue the master track Environmental Engineering, for that I am very grateful. I am very grateful to Dr. ir. David Moed for our talks and all the support concerning the corrosion experiments. I am also grateful to Prof dr. Arne Verliefde for all the input and comments. Prof. dr. ir. Arjan, I am very grateful for your advise on the analytical methods and for the measurements at the Corrosion Technology and Electrochemistry group.

A big thanks to all the members of the Condensate Quality project. Especially, Peter Janssen, for his expertise on magnetite and flow-accelerated corrosion. Dr. Wolfgang Hater, Dr. Duygu Disci-Zayed and Julia Jasper for all the knowledge of, and advise on film forming amines. Special thanks to Karlien Dejeager and Yu Xue for helping me with the practical stuff concerning film formers. In addition, I would also like to acknowledge the Condensate Quality project, associated partners, DOW Benelux B.V., Ghent University, Evides Industriewater, Sitech Services, ISPT KWR Water Research Institute, Kurita Europe GmbH.

I am very thankful to all the lab technicians that performed the analyses or helped me perform analyses during this thesis, Ir. Durga Mainali, Ruud Hendrikx and Agnieszka Kooijman Banaszak. I would also like to acknowledge the lab technicians of the Water Management department WaterLab, Armand Middeldorp and Patricia van den Bos, as I could always count on you for help.

I would first like to acknowledge, Dr. Derek Lister and Dr. Barry Dooley, for our conversations and whose expertise was invaluable in formulating the corrosion experiments. Moreover, I want to express my gratitude to all the manufacturers and suppliers for helping and troubleshooting, Dr. Lietai Yang from Corr Instruments, Arie DeKeijzer and Thomas Montsch from Berghof Products + Instruments GmbH, Tjerk Kaastra Gibac Chemie B.V and Lucas Vroon.

Finally, my gratitude goes to my family for always supporting and believing in me. Heel erg bedankt! Cảm ơn! En Baie dankie! A warm thanks to my friends on which I can always count and who offered some well needed distraction from all the work. Lastly, much thanks to my girlfriend Nicky for all the love and support.

Ben Bischoff Tulleken
Rotterdam, June 2021

Summary

Corrosion and fouling are considered major factors affecting the performance of water-steam cycles (WSC). Magnetite is the most common corrosion product and subsequently the main source for fouling in the WSC. It forms as a (protective) layer on steel surfaces. Flow-accelerated corrosion (FAC), present in feed and condensate systems, is a well known corrosion mechanism, eroding and dissolving the magnetite layers. This leads to corrosion products entering the water, to be transported to the boiler. Fouling, by oxide colloids, is partly controlled by forces arising due to surface charging, with the point of zero charge (pzc) being an important value.

Film forming amines (FFA) are gaining acceptance as means to control FAC by forming a protective (hydrophobic) film on (metal) surfaces. However, its performance in low pH regions, such as the condensate system or regions affected by FFA breakdown, into organic acids, is unknown. In addition, despite FFA being a surfactant, its effect on the colloidal magnetite surface charge, and pzc are unknown. Therefore, this research aimed to determine the effect of FFAs on the formation of a protective magnetite layer and the protection it offers against acidic FAC, and to determine plus model the effect of FFAs on the surface charge of colloidal magnetite.

During immersion corrosion tests magnetite layers were formed on carbon steel (C1010) coupons, inside a high pressure high temperature autoclave under different treatments: untreated (blank), 2ppm Octadecylamine (ODA) and 2ppm Ammonia, 2ppm Oleyl Propylenediamine (OLDA) and 2ppm Ammonia, and only 2ppm Ammonia. The test duration was 48 hours, at a temperature of 230-250 °C. Re-immersion tests were performed to test the magnetite layer performance under acidic FAC, pH_{25C} of 6 using acetate 0.08ppm, PIVlab determined flow velocity of 0.6 m/s, at 150 °C for 48hours. After the corrosion tests, the layers were verified using X-Ray diffraction, contact angle measurements, digital microscopy, and EDS + SEM. The latter, together with standard weight loss measurements were used to determine the corrosion rate.

Potentiometric titrations were employed to measure the proton-induced surface charge of magnetite particles (10g/L) at an ionic strength of 0.01, and 0.1 mol/kg (KNO_3) in the presence or absence of ODA, or OLDA (2ppm) over a wide pH range (3 to 11), at 25, and 150 °C. This gave the magnetite surface charge density curves. The pzc was determined using the inflection point of titrations (pH_{infl}) and common intersection point (pH_{cip}) of the titrations. Commercial magnetite reagent grade 99% was chosen, as substitute for the widely used Puratronic magnetite powder, to perform the titrations. Particle size distribution was used to assess the ODA, and OLDA influence on colloid/particle size. A PHREEQC 2pKa surface complexation double layer model (SCM) was used to derive reaction constants from experimental and literature data fitting. Prior to the titrations ODA, and OLDA, adsorption experiments were performed at 25 °C, to assess the adsorption behaviour onto the magnetite particles, and to determine whether the unadsorbed amount of FFA could affect the surface charge calculation.

XRD confirmed the presence of magnetite layers on all coupons after the (re-)immersion tests. Contact angle measurements indicated the presence of a hydrophobic or smooth surface after the immersion tests, with 91.3 ±4.7, and 108.9 ±2.8 for ODA, and OLDA, respec-

tively. After the re-immersion tests this was 66.2 ±11.5, and 100.5 ±5.2 for ODA, and OLDA, respectively. The SEM measured magnetite layer decrease after the re-immersion tests was: 19.1%, 14.5%, 8.6%, and 23.3% for blank, ODA, OLDA, and ammonia treatment respectively. Weight loss determined corrosion rates taken over both immersion and re-immersion tests were: 0.070, 0.057, 0.060, and 0.073 mm/y for blank, ODA, OLDA, and ammonia treatment respectively. Weight loss (expressed as base material and oxide) measurements after the re-immersion was measured to be: 3.10 ±1.4, 0.05 ±0.05, 0.03 ±0.55, and 0.45 ±0.45 mg/coupon for blank, ODA, OLDA, and ammonia, respectively.

All magnetite surface charge density curves were unaffected by the presence of ODA, and OLDA, except for ODA at 0.1 mol/kg KNO_3 and 25 °C, which resulted in a raised/neutralised surface charge density curve in the alkaline pH region. The pH_{infl} value of the magnetite at 25 °C was 6.72 ±0.31, with ODA, and OLDA present the pH_{infl} values were 7.22 ±0.58, and 7.07 ±0.56, respectively. The pH_{infl} values of the magnetite at 150 °C was 4.94 ±0.05, with OLDA present this value was 5.19 ±0.21. The pH_{cip} value of the magnetite, at 25 °C, was 6.45, under ODA the pH_{cip} was 6.40, and OLDA 6.34 ±0.31. Particle size distribution measurements showed an increase of magnetite particle size after titrations performed with ODA, 59.64%, and OLDA, 66.94%.

A PHREEQC SCM was adequately fitted to the experimental magnetite surface charge density curves of the titrations performed at 25 °C. This gave the following reaction constants: pKa1 of 5.7, and pKa2 of 7.8. The reaction constants of the ODA, and OLDA to magnetite adsorption could not be obtained by fitting, as the potentiometric titrations, nor literature, yielded significant ODA, and OLDA impacted magnetite surface charge density data.

Under all treatments a protective magnetite layer was formed. Layers formed under ODA, and OLDA additions were smoother, thinner, and more uniform compared to layers formed under an ammonia only chemistry, and blank chemistry especially. Layers formed under the ODA, and OLDA chemistries were better resistant against acidic FAC and offered better protection, in terms of corrosion rate.

At the applied concentration ratio, and ionic strength of 0.01M, ODA, and OLDA did not affect the magnetite colloid surface charge over pH. However, both caused magnetite particles to agglomerate. At higher ionic strengths of 0.1M, ODA neutralised the magnetite surface charge in the alkaline region.

Due to the formation of a more protective magnetite layer under ODA, and OLDA, which was more resistant to acidic FAC it could be justified to implement FFA in addition to ammonia, despite its minor breakdown products. This would especially be beneficial for the condensate systems and complex boiler systems where another FAC mitigation method, namely oxygenated treatment cannot be implemented. Magnetite layers were formed during this study under zero flow conditions. More research should be performed on the formation of a (protective) magnetite layer under flow conditions with and without FFA, to assess its performance under 'operating' conditions.

Dosing of FFA is mainly based on surface coverage of metal, and pH control. Another factor should be considered, namely the effect of FFA as flocculant or dispersant. The argument given is that at low FFA concentrations and electrolyte strengths not enough FFA adsorbed onto the magnetite particles to affect its charge. However, it did seem to act as flocculant. Whereas at higher concentration ratio's (hydrophobic) stabilisation is expected together with a surface charge decrease (in the alkaline region) followed by a charge reversal. Quantitative research is needed to test this hypothesis.

Contents

Nomenclature

ACC	Air Cooled Condensers
AVT	All volatile treatment
AVT(O)	All volatile treatment oxidising
AVT(R)	All volatile treatment reducing
BET	Brunauer–Emmett–Teller
BTFs	Boiler Tube Failures
Cip	Common intersection point
COD	Chemical Oxygen Demand
DLVO	Deryaguin–Landau–Verwey–Overbeek
DMA	Dimethylamine
EDL	Electrical double layer
EDS	Energy Dispersive Spectroscopy
ETA	Ethanolamine
FAC	Flow Accelerated Corrosion
FFA	Film forming amine
Hfo	Hydrous ferric oxide
HPHT	High pressure high temperature
IEP	Isoelectric Point
IHP	Inner Helmotz plane
Infl	Point of inflection
M-O	Metal oxide interface
MOR	Morpholine
O-S	Oxide solution interface
ODA	Octadecylamine
OHP	Outer Helmotz plane
OLDA	Oleyl Propylenediamine
OT	Oxygenated treatment

PSD	Particle Size Distribution
PTFE	Polytetrafluoroethylene
pzc	Point of zero charge
Redox	Reduction and oxidation
RMSE	Root means squared error
SCM	Surface complexation model
SEM	Scanning Electron Microscopy
SHE	Standard Hydrogen Electrode
VCI	Volatile Corrosion Inhibitor
WSC	Water-steam cycle
XPS	X-ray Photoelectron Spectroscopy
XRD	X-ray diffraction
FSC	Fraction surface Sites Covered
HRSG	Heat Recovery Steam Generator

List of Figures

List of Tables

1 Introduction

1.1. Water-steam cycle for electricity and steam production

In many processes steam is applied e.g. to drive turbines for electricity production or used as heat source in industrial processes. The steam is generated within a boiler also known as a steam generator, and after its use it condenses, and is pumped back to the boiler as feedwater. This cycle is known as the water-steam cycle (WSC). Figure 1.1 gives a schematic representation of a simplified steam cycle. The operation of a WSC requires high energy/heat input and therefore optimal performance is essential. As of today the most important problems affecting the performance and economics of these systems are corrosion and fouling [29]. As corrosion leads to the loss of material, and fouling of the boiler causes, among others, a decrease of heat transfer.

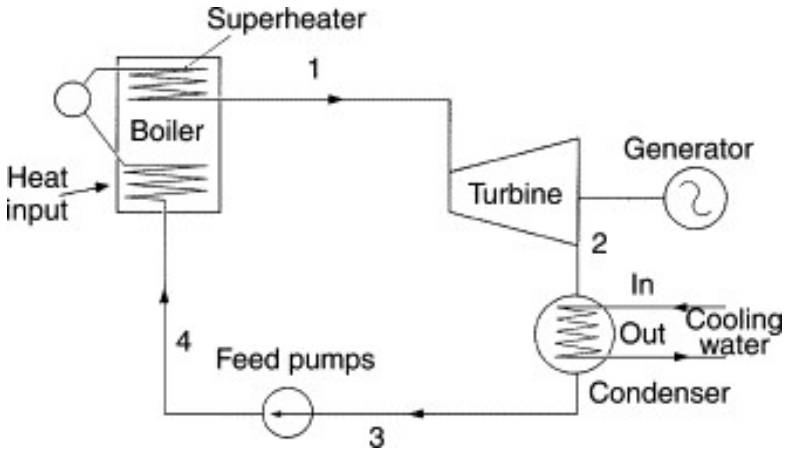

Figure 1.1: Schematic representation of the water-steam cycle [94].

1.2. Corrosion and fouling in the WSC

Corrosion is an (electrochemical) reaction that turns a steel into a more stable form e.g. dissolved iron or an iron oxide. Depending on the given environment the steel is in. Throughout the entire water-steam cycle corrosion of (carbon) steel occurs, resulting in the formation of corrosion products. Corrosion products that end up in the water, are eventually transported to the boiler where they can cause fouling by depositing on the boiler(tube) surface.

1.2.1. Corrosion and formation of magnetite

Magnetite, an iron-oxide, is the most common corrosion product formed in the WSC. A combination of high temperature, alkalinity, and low oxygen concentrations i.e. reducing or low electrochemical potential (Eh), results in magnetite being the most stable form of iron. This can be seen in a Pourbaix diagram, such as in Figure 1.2, where the Eh is plotted against pH, giving the stability regions of an iron aqueous system. Another iron oxide that is usually formed in environments with higher oxygen concentrations is hematite. At lower pH dissolved iron ions are the most stable form of iron. Both hematite and magnetite are passive forms of iron meaning these oxides can offer some protection against further corrosion of the base material. Magnetite is formed via a two step reaction, first the formation of ferrous iron followed by the so called Schikorr reaction. This reaction forms a layer in two directions, as a dense layer replacing the corroded steel, and a porous top layer. The dense layer offers the most protection whereas the top layer is prone to dissolution or being flushed away, eventually ending up in the boiler [7, 46, 115, 118].

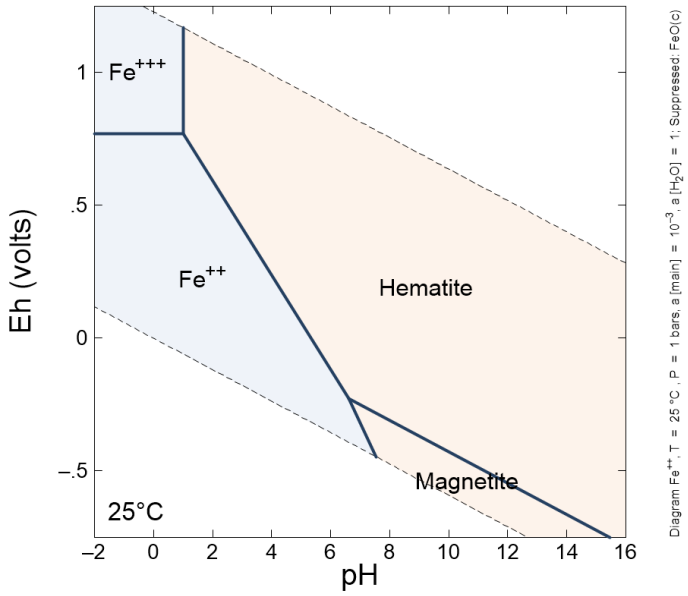

Figure 1.2: Pourbaix diagram for an iron water system at 25 °C, made with [103].

Flow-accelerated corrosion

In certain regions of the water-steam cycle, such as the feedwater system, low pressure boiler tubes or condensate system, a specific form of corrosion can be found called flow-accelerated corrosion (FAC) . Due to a combination of, among others, temperature (around 150 °C) and high flow velocities only half of the formed ferrous iron reacts to form magnetite, and the top porous magnetite layer is dissolved or flushed away. Both leading to more corrosion, and corrosion products entering the water [21, 46, 120].

First condensate corrosion

Another type of corrosion is called first condensate corrosion (FCC) that takes place in steel condensers e.g. air cooled condensers (ACC). Both FCC and FAC can be found in condensate systems [23, 46]. The first formed condensate is of very high purity and therefore prone to become acidic due to volatile impurities often reaching a pH of 4.5 or lower [46].

1.2.2. Magnetite deposition

Fouling is characterised by the accumulation of deposits, and is governed and affected by various conditions and parameters, such as flow effects, heat flux, concentrations, changes in solubility over temperature as well as by electrochemical factors [9, 29, 115]. The main deposit found is iron oxide, with magnetite being the foremost deposited [118]. This study focuses on the electrochemical phenomena governing deposition. Minerals, especially iron-oxides, such as magnetite, acquire a surface charge in an aqueous environment. The particles acquire a surface charge as a result of protonation and deprotonation reactions of the surface hydroxyl groups [102]. It is this charge that determines the particle stability of magnetite and the 'stick-ability' to surfaces. Two particles with a similar surface charge sign, e.g. both positive, repel each other, therefore avoiding agglomeration and settling. Moreover, a charged particle with a similar charge sign as a charged surface shows less tendency to 'stick' or foul that particular surface. Whereas particles with no charge, or net zero charge, are more prone to agglomeration [29, 102]. The pH at which the particle has no net charge is called the point of zero charge, or short pH_{pzc}.

1.3. Conventional chemical conditioning

A common treatment to mitigate corrosion, and therefore indirectly mitigate fouling by the reduction of corrosion products, is ensuring a stable environment for magnetite. Thus, an elevated alkaline pH, and low oxygen (Eh) concentration, this is achieved by dosing volatile alkalising amines, and oxygen scavengers. This treatment is called, all volatile treatment reducing AVT(R). Although, AVT(R) is not suitable to mitigate FAC. However, slightly oxidising (higher Eh) conditions, due to extra oxygen present in the water, together with dosing alkalising amines can 'stifle' the magnetite layer due to formation of hematite, reducing FAC. This treatment is called AVT(O), O standing for oxidising. Unfortunately this is only possible in all-ferrous systems and for the feedwater system and steam generator, not the condensate system [21, 22]. In addition, some plant operators are not willing to switch to AVT(O).

Fouling itself can be avoided by blowdown. This is the deliberate loss of boiler water to prevent highly concentrated boiler water. Other methods are based on dispersing polymers, or altering the surface charge, for instance by pH control, as the particle surface charge depends on pH, or with surfactants to alter/increase the surface charge [29, 32, 102].

1.4. Film forming amine based treatment

An alternative treatment method that is gaining acceptance in order to control corrosion, and therefore indirectly the oxide product transport to the boilers, is the application of film forming amines (FFA) . These surfactants are high molecular weight amines consisting of a long hydrophobic alkyl chain and a hydrophilic head. The hydrophilic part of the FFA attaches itself to a surface. If enough molecules do so the hydrophobic aliphatic 'tails' will form a non-wettable surface protecting the underlying steel [29, 81]. Two film formers that are widely used and studied are Octadecylamine (ODA) and Oleyl Propylenediamine (OLDA).

1.4.1. Effects FFA on corrosion

The corrosion inhibiting effect of FFA treatment has been studied in lab and field conditions. Results show a decrease in corrosion rates [4, 7, 15, 47, 73, 108]. Fewer studies have been performed assessing the impact of FFA on FAC [46, 120], both showing reduction of FAC rate under FFA treatment. Studies also focused on the formation of a protective FFA film [5, 41]. Whereas other studies also investigated the characteristics of the oxide layer formed under FFA. Theses studies determined, among others, the oxide layer thickness and roughness, showing decreased roughness and thickness of the layer together with an increased density

under the presence of film formers [46, 108, 109, 120].

1.4.2. Effects FFA on deposition

The effects of FFA on fouling due to magnetite deposition have been sparsely studied. Gasnier and Lister [32] studied the fouling inhibition of commercial FFA compared to polymeric dispersants at temperatures up to 100 °C, also reporting the effect of the FFA on the magnetite zeta potential at 25 °C. The zeta potential is often measured as means to (indirectly) study the surface charge of a colloid. It is the electrical potential, at the shear plane. The shear plane is the interface separating the fluid that travels with the particle from the bulk fluid. Little could be concluded on fouling, due to the agglomerating effect FFA has on magnetite. Whereas the zeta potential measurements indicated a reversal of potential, negative to positive in the alkaline region, in the presence of the FFA.

Similar studies have been performed on the effects of alkalising amines (morpholine (MOR), dimethylamine (DMA), ethanolamine (ETA) and ammonia), instead of FFA, on magnetite fouling [114], magnetite zeta potential [113] and surface charge [6]. These studies indicated an increased deposition rate, dependent on the nature and concentration of the amine [114]. A reason given, is the decreased surface charge due to the adsorption of cationic amines. With MOR, ETA and ammonia increasing the pH_{pzc} of magnetite from pH 6.7 to 7.2, 7.6 and 8.4 respectively [113]. However, Bénézeth et al. [6] did not detect any effect of MOR, DMA and ETA on the magnetite surface charge at 200 and 250 °C.

1.5. Problem statement

Prior research has shown FFAs to be a promising treatment to mitigate corrosion within the WSC. Especially in combination with an alkalising amine, to reduce FAC for systems unable to apply AVT(O) treatment. Despite this benefit plant operators require more knowledge into two possible disadvantages of FFA prior to its implementation. One of them is related to the thermal degradation, or hydrothermolysis, of FFA into volatile acidic products [18, 81]. The effect of these acids on corrosion should be determined. Only one study [46] assessed whether a magnetite layer, formed under FFA, still offers protection against FAC under acidic conditions. However, this research was performed at 300 °C, not representative to most feed and condensate systems. Lastly, studies focused on the effects of FFA on the formation of the protective magnetite layer are sparse, as studies mainly focus on the corrosion phenomena. Even though the nature of the surface oxide formed, affects further corrosion by FAC [25].

The second possible disadvantage is the risk of increased deposits in the boiler, i.e. fouling. It is known that certain surfactants can alter surface charges, leading to agglomeration and deposition. As FFA is a surfactant, its adsorption to magnetite, and effect on the surface charge of magnetite should therefore be determined. Although magnetite colloids have been widely studied using, among others, potentiometric titrations to obtain surface charge data at elevated temperatures and to determine the effects of certain impurities on the charge [61, 62, 64, 121, 123], the effects of FFA on the magnetite surface charge, especially at elevated temperatures more representative for boilers, have not been studied. Only one study performed at ambient temperature indicated a zeta potential reversal of magnetite particles in the presence of FFA [32].

Experimentally determining the surface charge has its challenges and limits. The commercial magnetite, called Puratronic (99.997% pure), widely used to study the magnetite surface charge [3, 6, 62, 117, 121, 123] has recently been taken out of production and a substitute should be found. An experimental limit would be the temperature. Surface complexation models have been fitted to experimental surface charge isotherms/curves in order to determine relevant reaction constants [49, 60, 62, 121]. Extrapolated reaction constants can pro-

vide models able to predict charges at higher temperatures, which is useful to simulate (high) boiler temperatures i.e. temperatures not achievable with certain setups.

Knowledge gaps
Summarised, little information is found in literature about:

- The effect of the FFA on the formation of a protective magnetite layer, in addition and opposed to conventional alkalising amine treatment.
- The resistance of the magnetite layer formed under FFA, in addition and opposed to conventional alkalising amine treatment, against acidic FAC pertinent to feed and condensate return systems.
- How other commercial magnetite powders relate to Puratronic in terms of surface charge and pH_{pzc}.
- The adsorption of FFA onto magnetite colloids and, the effect of FFA on the surface charge of colloidal magnetite over pH, especially at elevated temperatures.
- Surface complexation model describing the effect of FFA on magnetite and able to predict surface charges.

1.6. Objectives and research questions

This research focusses on the effects of FFA on magnetite layer properties related to flow-accelerated corrosion and effects of FFA on the magnetite particle surface charge. The main objective of this research is:

"To determine the effect of FFAs with respect to magnetite layer growth and its resistance against acidic FAC pertinent to feed and condensate water, and to determine plus model the effect of FFAs on the surface charge properties of colloidal magnetite at elevated temperatures"

This goal is reached, in such a way, that the results can help justify the implementation of film forming amines, in addition to ammonia, to control FAC. In spite of its limited breakdown into low molecular organics acids and possible negative effects related to fouling.

The following research questions were derived from the literature knowledge gap and the main objective:

1. What is the effect of ODA, and OLDA, in addition to ammonia opposed to: 1) only ammonia and 2) no chemical additive, on the formation of a (protective) magnetite layer?
2. What magnetite layer is best resistant to acidic FAC such as in locally low pH regions and condensate/condenser systems?
3. How do commercial magnetite of 95% purity and 99% purity compare with Puratronic in terms of surface charge over pH and pH_{pzc}?
4. What is the adsorption behaviour of ODA, and OLDA to magnetite particles?
5. What is the effect of ODA, and OLDA on the surface charge and pH_{pzc} of magnetite at 25 °C, and at an elevated temperature of 150 °C?
6. Can a surface complexation model adequately describe the experimental results and subsequently yield surface charge predictions at higher temperatures?

1.7. Research approach and report outline

To answer the research questions this thesis starts with the theoretical background. This background was used to formulate the experiments and surface complexation model. The theoretical background is provided in chapter 2. Next, three types of experiments were conducted. First: immersion and re-immersion corrosion tests, designed to answer questions 1 and 2. Second: an adsorption experiment, to answer question 4. Third: potentiometric titrations in order to answer question 3 and 5. Their methodologies are described in chapter 3. In addition chapter 3 also covers the surface complexation model, which sets out to answer question 6. Chapter 4 presents the results of the experiments together with the fitted model and model predictions. The results are discussed and compared with literature. Chapter 5 concludes on the results and provides answers to the research questions. Chapter 6 provides recommendations for future research.

2

Theoretical Background

This chapter starts with the theoretical background, from literature, regarding the water-steam cycle and its conditions. This is followed by a background on: corrosion in general, flow-accelerated corrosion in particular and common applied chemical conditioning. Corrosion measurements together with surface analysis are discussed too. These sections were helpful in order to define the immersion and re-immersion experiments. Moreover, this chapter covers the background of FFAs, fouling, the theory of particle surface charge, followed by background on potentiometric titrations and surface complexation models. These sections served to define the potentiometric titration experiments and the surface complexation model.

2.1. Water-steam cycle

In many processes, steam is applied as an efficient means of moving energy from point A, the steam generator or boiler to its intended use at point B e.g. electricity generation, heating or chemical reaction. During and after transferring the energy to: a chemical reaction, heating or driving a turbine, the steam condenses back to the liquid phase. Further cooling is required before returning to the boiler. The full cycle is called the water-steam cycle. The processes in which steam is applied vary from: industrial process heating, heating of buildings and electric power generation [29]. Further focus will lie on water-steam cycles producing high temperature and pressure steam for energy and industrial applications.

Figure 2.1 is a schematic overview of the water-steam cycle of an industrial boiler system, the figure also covers the main water flows within the system. Water is transported by the feedwater system to the boiler. The water passes a feedwater pump and preheater as means to increase efficiency before it enters the boiler where it is heated to form steam. The heat source can be provided by e.g. fossil fuel, nuclear reaction or waste heat from other processes. The produced steam is send to the 'users' to drive a high followed by a low pressure turbine, or it is used in industrial processes. When the steam delivers the heat at the point of use it condenses and returns to the lower energy level/state of a liquid. The aim is to collect as much condensate as possible to return to the steam generator. After turbines, surface condensers are used as an additional cooling resource after which steam is collected in a condensate receiver. In the case of steam use for process heating the condensate flash tank separates flash steam and condensate, the first can be used in low-pressure applications the latter is drained to and stored in a condensate receiver. From the condensate receiver the water is returned to the feedwater stream after passing a deaerator unit. The relatively pure steam leaving the boiler causes solids in the remaining water to increase in concentration. Boiler blowdown is the deliberate loss of boiler water to prevent highly concentrated water,

which in turn can cause fouling, scale and corrosion. To compensate for blowdown and any steam or condensate losses additional water called makeup water is added to the system as replacement. First this makeup water is treated to meet standard levels before it is mixed with the condensate return flow to form the boiler feedwater [29]. The next section discusses the phases, temperatures and pressures within the WSC via the Rankine cycle.

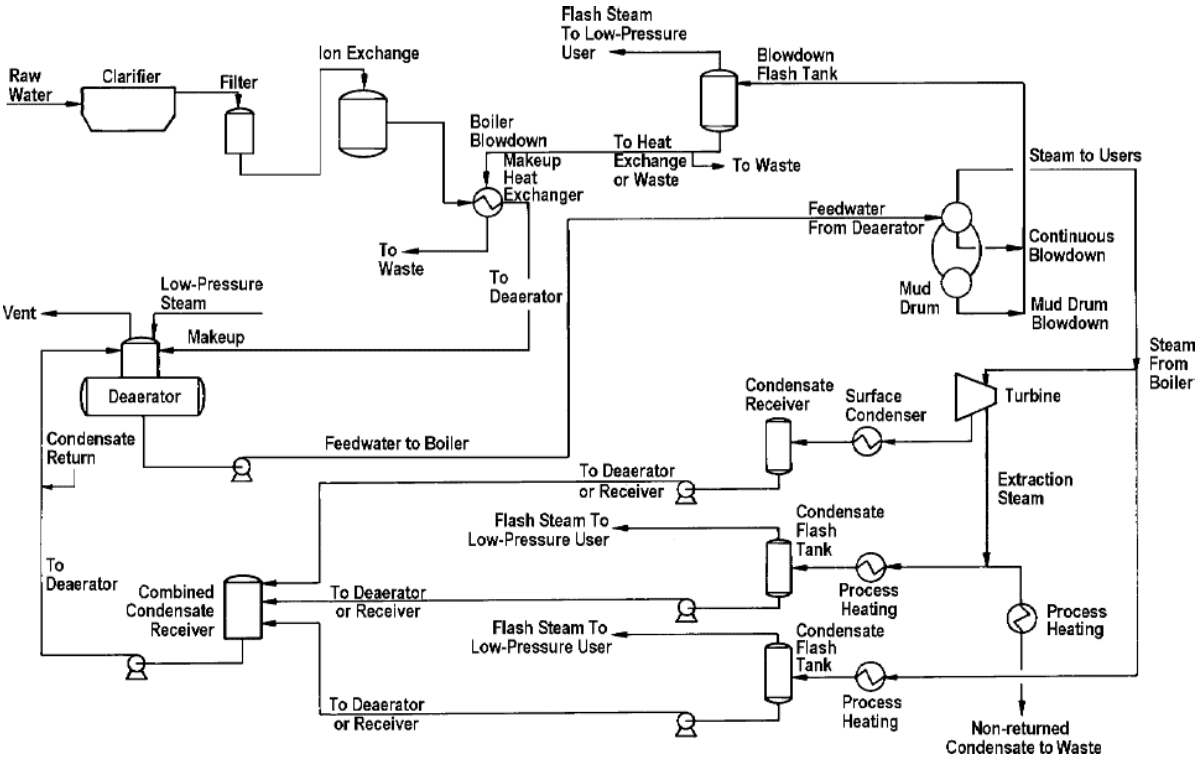

Figure 2.1: Schematic overview of a water-steam cycle as a typical industrial boiler system [29].

2.2. The Rankine cycle

The previous section discussed the general layout of an industrial boiler system. This section will discuss the possible temperatures, phases and pressures that the working fluid (water in this case) can undergo, described by the thermodynamic Rankine cycle, as it circulates through the components of the WSC. This (idealised thermodynamic) cycle describes the process by which a WSC extracts (mechanical) work, e.g. driving a turbine, from a working fluid, as it passes between the heat source and a heat sink [65]. This cycle is visualised in a temperature-entropy diagram, T-s diagram. For the WSC, a water-steam T-s diagram is used. The area of the Rankine cycle represents the amount of work exchanged by the system.

Figure 2.2 shows a schematic representation of a WSC, together with its (ideal) Rankine cycle, and a T-s diagram in metric units. The description of the process starts at point 5, the feedwater system, where the working fluid is still saturated liquid. From point 5 to 6 the liquid water experiences (isentropic) compression in the feedwater pump, and heating in the feedwater heater or economiser. Compressing the liquid prior to boiling results in a higher boiling temperature. A typical range of operating temperatures of low pressure economisers/preheaters and feedwater tubes is 40 to 50 °C [21].

The next process, step 6 to 1, is the transfer of heat to the working fluid at constant pressure. Where the fluid is heated in a steam generator followed by a super heater or more

specific for a heat recovery steam generator (HRSG): first in low, then intermediate, high pressure tubes, and lastly the superheater [86]. As the water is heated its entropy increases, at the boiling temperature the fluid is converted from saturated liquid to saturated vapour. Typical pressures for low pressure steam boilers do not exceed 1 bar and hot water boilers, that usually operate at temperatures of 82 to 121 °C, do not exceed pressures of 11 Bars [12]. Common boilers are natural-recirculating boilers, where water flows through the steam generator tubes as a result of heat differences and gravity. Operating pressures in natural recirculation boilers are generally limited to 175-200 bars. The reason is that at these pressures gravity flow is not possible anymore [29]. HRSG can generate steam at temperatures up to 650°C and pressures of 130 to 200 bars. In HRSG with multiple evaporators, conditions in the HRSG range from 535 °C and 170 bar for high pressure steam to 150-200 °C and 4 bar for low pressure steam [86].

Process 1 to 2 is known as the isentropic expansion of the steam as it passes the high pressure turbine. The working fluid becomes high quality steam and, at this new pressure, is reheated in the reheating boiler tubes to saturated vapour again. This is marked as process 2 to 3. In process 3 to 4 the working fluid undergoes isentropic expansion again, as it passes a low pressure turbine, from the saturated vapour pressure to the condenser pressure. At this (constant) condenser pressure, process 4 to 5, heat is transferred from the fluid via a heat exchanger. The working fluid leaves the condenser in its liquid state, lower entropy. Condensers can operate at pressures close to vacuum, such as ACCs do, to increase efficiency of the Rankine cycle. Common condensate system temperatures range from 20 to 80 C °[29].

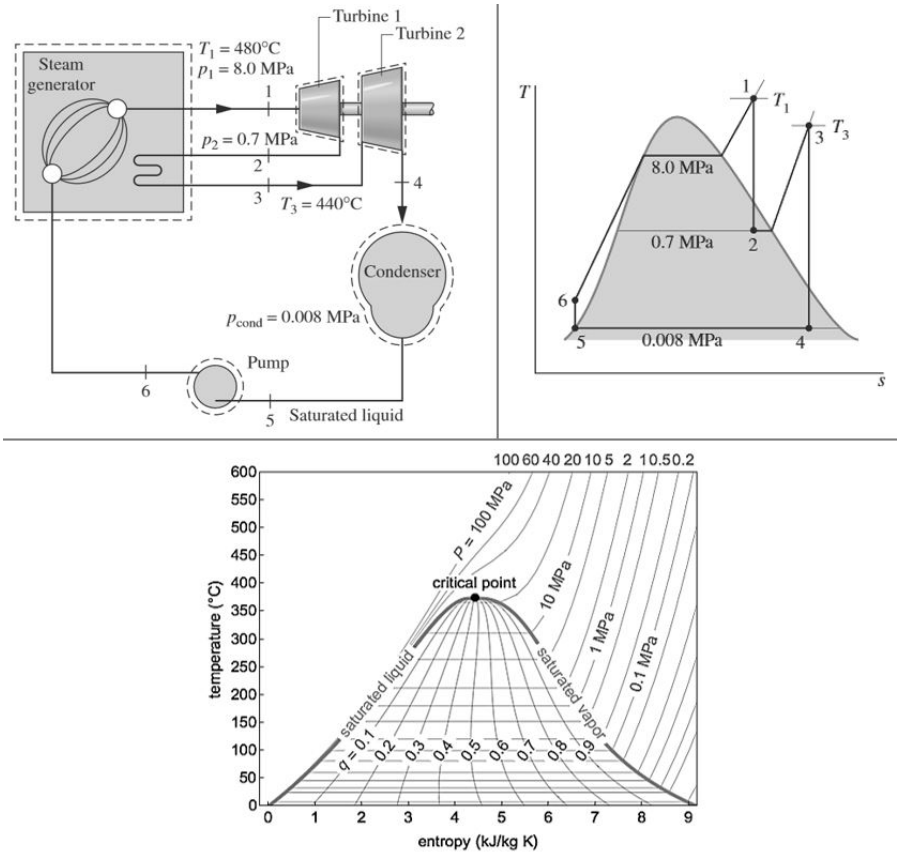

Figure 2.2: Top left: schematic representation of a thermal power plant, and top right: its Rakine cycle [65], below: a temperature-entropy diagram for water [48].

2.3. Corrosion in aqueous environments

From a thermodynamic point of view, corrosion is a reaction that turns a material into a more stable form. This form depends on the given environment the material is in. In many cases corrosion is synonymous with the degradation and destruction of a material as it alters critical properties such as strength [31, 63]. Shortly stated, corrosion implies the charge and mass transfer between the corroding material and its environment, in this respect the water of the WSC. This section will cover the theory behind the corrosion reactions, mechanisms and types of corrosion common in the WSC focusing on, among other things, iron-oxide(II,III) formation.

2.3.1. Thermodynamics of corrosion

Corrosion is an electrochemical process where an electrochemical reaction occurs on a metal surface turning the material to its natural oxide state [78]. This is represented by an oxidation reaction, see reaction 2.1.

The general oxidation reaction of metal generating an ion and electron:

$$\mathrm{M} \longrightarrow \mathrm{M}^{z+} + z\mathrm{e}^{-} \tag{2.1}$$

Simultaneously a reduction reaction needs to occur to accept the electron. For this an electrochemical corrosion cell has to be established in order for the electrochemical reaction to take place. This cell comprises of at least two electrical conductors (electrodes) called the cathode and anode, an ionic current path (electrolyte) and an electronic path, as is shown in Figure 2.3. Now the electrons created by the oxidation reaction at the anode can travel to the cathodic area where the reduction reaction can consume them. The water serves as the electrolyte. The cathodic reduction reaction in water under anaerobic conditions (when no oxygen is present) in neutral or alkaline pH, is characterised by the reduction of the water molecules itself, following reaction 2.2.

The cathodic reduction reaction of water forming hydrogen and hydroxide ions:

$$z\mathrm{H_2O} + z\mathrm{e}^{-} \longrightarrow \frac{z}{2}\mathrm{H_2} + z(\mathrm{OH})^{-} \tag{2.2}$$

The overall combined reduction and oxidation (Redox) reaction:

$$\mathrm{M} + z\mathrm{H_2O} \longrightarrow \mathrm{M}^{z+} + \frac{z}{2}\mathrm{H_2} + z(\mathrm{OH})^{-} \tag{2.3}$$

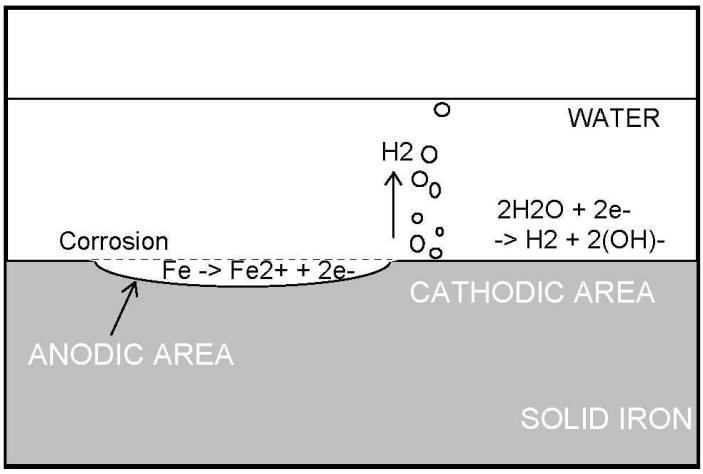

Figure 2.3: Schematic representation of the electrochemical corrosion of iron in an aqueous environment [85].

The force driving the electrochemical Redox reaction is the electrical-potential difference between the cathode and anode. This potential causes a current to flow between the anodic and cathodic areas. The metal ions produced in the initial oxidation half-reaction can be oxidised again by e.g. atmospheric oxygen to produce an insoluble metal-oxide, also known as rust in case of iron(III)-oxide, i.e. ferric oxide. What the corrosion product or thermodynamic stable phase of a specific material will be in a certain environment can be assessed via a Pourbaix diagram.

Pourbaix diagram

In general, the oxidation and reduction process related to corrosion can be deducted using a Pourbaix diagram, as shown in Figure 2.4. The diagram depicted plots the electric potential of a hypothetical metal as a function of pH of water at 25 °C together with the stability region of water, using two red dashed lines. Pourbaix diagrams plot the electrochemical stability for different Redox states of a specific element, normally as a function of pH. In fact, the Pourbaix diagram is essentially a phase diagram which maps regions based on potential and pH where various Redox species are stable. For metals the diagram includes regions marked as corrosive, where the metal oxidises, passive regions where metal exists as a stable oxide which forms on the metal surface, and immunity regions where both corrosion and passivisation is suppressed and the metal itself is the stable form [2, 63, 78]. The solid line in the diagram represents a combination of the potential and pH at which the two species on either side coexist in equal activities, at all other points, a single species is dominant i.e. stable.

Potential-pH (Pourbaix diagrams) and thermodynamic calculations are useful as a preliminary study to verify the expected stability domain of the magnetite oxide at various conditions of the water-steam cycle. Unfortunately, corrosion rates cannot be determined via Pourbaix diagrams. To map the stability regions between various Redox species one needs to plot the reactions acting as their boarders.

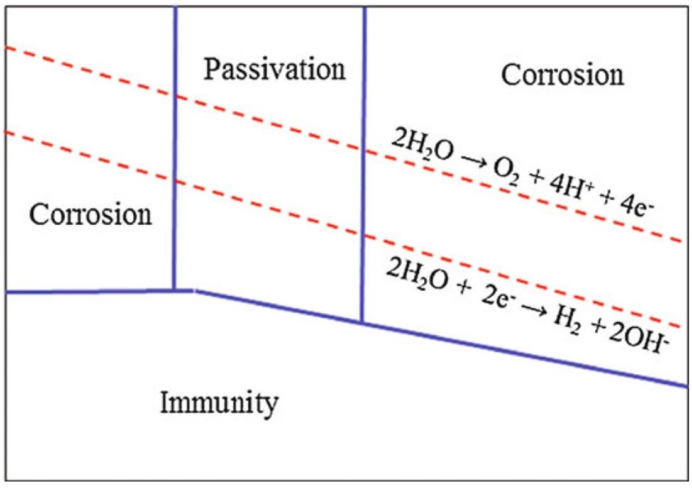

Figure 2.4: Schematic Pourbaix diagram depicting the regions of corrosion, passivisation and immunity for a hypothetical metal. Note: the y-axis normally represents the potential Eh and X-axis the pH [78].

The boarders, solid lines, of the diagram are represented by a reaction between two species on opposite sides of the line. In the case of reactions where electrons are involved, i.e. Redox reactions, the Nernst equation can be used to form the lines, Equation 2.5 .The Nernst equation is derived from the Gibbs free energy equation of a reaction, using the relation

of Gibbs free energy, and the voltage developed by a Redox reaction in an electrochemical cell [2].

Diagonal lines within the Pourbaix diagram are dependent on both E and pH, whereas horizontal lines separate species that are only affected by electrons (E) and vertical lines for species only affected by pH.

Redox reaction written in general form:

$$\mathrm{bB}_{red} + \mathrm{bC}_{ox} \longrightarrow \mathrm{dD}_{ox} + \mathrm{gG}_{red} \tag{2.4}$$

$$\Delta G_r = \Delta G_r^0 + RT \ln \frac{[D_{\mathrm{ox}}]^d \, [G_{\mathrm{red}}]^g}{[B_{\mathrm{red}}]^b \, [C_{\mathrm{ox}}]^c} \tag{2.5}$$

Here E_0 is the standard potential (Volt) where the substances are all at unit activity (1M, 1atm) at 25 degrees Celsius. R is the gas constant and T absolute temperature. The E_0 of the Redox half reactions are determined with a Standard Hydrogen Electrode (SHE) . The stability region of water is derived from the Nernst equation using the water Redox reactions, hydrogen evolution and oxygen reduction Equation 2.6 and Equation 2.7, and plotted as dotted lines on most Pourbaix diagrams. This is of specific interest to elements in aquatic environments.

$$2\,\mathrm{H}^+ + 2\,\mathrm{e}^- \longrightarrow \mathrm{H}_2 \qquad E_0 = 0.0V \quad SHE \tag{2.6}$$

$$\mathrm{O}_2 + 4\,\mathrm{H}^+ + 4\,\mathrm{e}^- \longrightarrow 2\,\mathrm{H}_2\mathrm{O} \qquad E_0 = +1.23V \quad SHE \tag{2.7}$$

A Pourbaix diagram of an aqueous environment containing iron at 1atm and 25 °C and 30 atm at 150 °C was made via the Geochemist Workbench Act2 software [103], see Figure 2.5. Focusing on the 25°C Pourbaix diagram, there are two stable oxides at the higher pH region, hematite and magnetite. Both these oxides will dissolve in the lower pH regions leaving iron ions, ferric or ferrous. A higher potential equals more oxidising conditions whereas a lower E corresponds to reducing conditions. The stable iron form is not present within this system as it only occurs in reducing conditions below the stability of water.

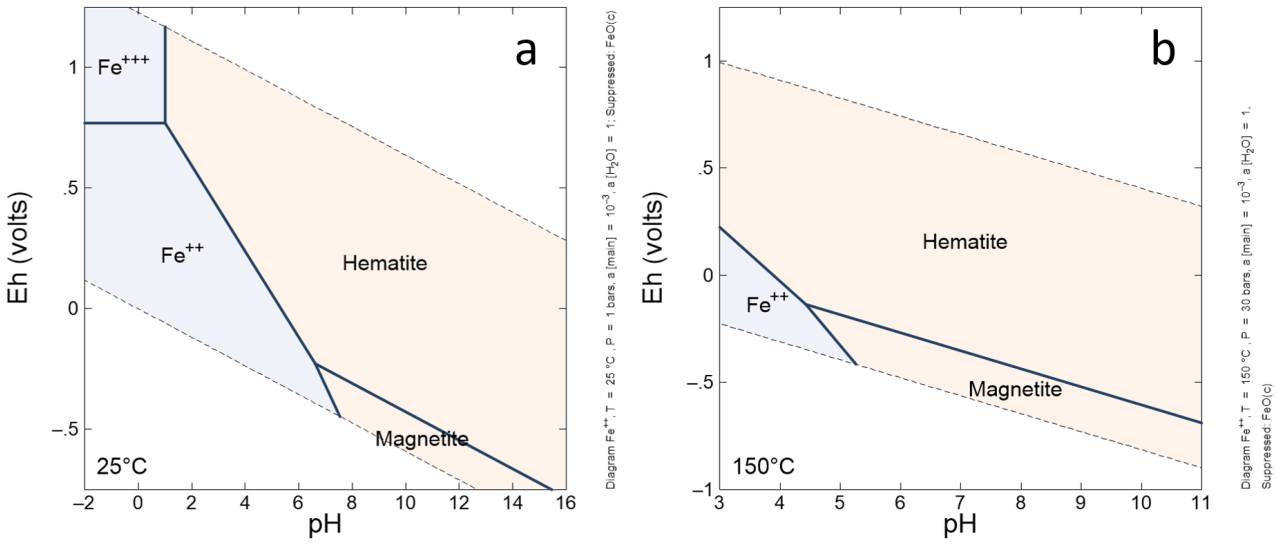

Figure 2.5: Pourbaix diagram of an iron water solution at a: 25°C and b: 150°C. Made with [103].

2.3.2. Formation and stability of Magnetite

Under the reducing (low Eh) and neutral or slightly alkaline pH conditions of aqueous systems such as encountered in the water-steam cycle. The total chemical reaction at the metal-oxide (M-O) or if no oxide is formed yet, metal-solution (M-S) interface, forming magnetite can be written as:

$$3\,Fe + 4\,H_2O \longrightarrow Fe_3O_4 + 4\,H_2 \tag{2.8}$$

The magnetite covers the underlying metal forming a protective layer. Formation of a magnetite layer at high temperatures above 180 °C is relatively fast, in 50 hours a layer can be complete [45]. Whereas below 150 °C formation is very slow [22]. At higher temperatures, above 240 °C, a denser layer is formed [89]. The total magnetite layer actually comprises out of two layers, an inner layer at the metal-oxide interface occupying the volume of corroded metal, and a less dense outer layer on top [83].

The formation of the two magnetite layers at relatively static or laminar flow conditions in the reducing conditions of the WSC can be described according to the following 4 reactions. The first two describe the oxidation of the metal at the M-O [57].

$$Fe \longrightarrow Fe^{2+} + 2\,e^- \tag{2.9}$$

$$2\,H_2O + 2\,e^- \longrightarrow 2\,H + 2\,OH^- \tag{2.10}$$

Under high temperature alkaline conditions the hydrogen atoms, from Equation 2.10, diffuse through the metal and form hydrogen molecules at the other side. Half of the ferrous ions generated at the metal-oxide interface directly forms as the inner more dense magnetite layer at same the M-O interface. Whereas the other half precipitates as the less dense magnetite at the oxide-solution (O-S) interface, both via the Schikorr reaction, see Equation 2.12:

$$Fe^{2+} + 2\,OH^- \longrightarrow Fe(OH)_2 \tag{2.11}$$

$$3\,Fe(OH)_2 \longrightarrow Fe_3O_4 + 2\,H_2O + H_2 \tag{2.12}$$

The formation of the ferrous hydroxide (Equation 2.11) is the rate limiting step to the overall Schikorr reaction, and slow below 200°C, therefore a reason for the slow magnetite formation at 150 °C [29]. Figure 2.6 is a schematic representation of the double magnetite layer growth. Hydrogen, and half of the $Fe(OH)_2$ formed in Equation 2.11 diffuse to the bulk, where the ferrous iron deposits as magnetite crystals. As mentioned before the inner-layer is a dense layer where the corroded steel used to be, whereas the porous top layer is composed of coarse magnetite crystals. The oxide layer, especially the fine grained layer protects against further reaction with water, slowing down the corrosion. However, not totally as it is still possible for species, especially hydrogen and water to reach the bare metal continuing the corrosion process. In other words the Schikorr reaction is an autonomous process that cannot be stopped [46]. At equilibrium the inner oxide layer measures about 10 microns compared to an outer layer of a couple of microns thick, the total not exceeding 20 microns [83, 22].

Magnetite dissolution

The magnetite dissolution is related to the solubility of magnetite, which is in turn a thermodynamical concept referring to the maximum equilibrium concentration of a solute that can be dissolved in a specific solvent under certain conditions [115]. These conditions can include pressure and temperature. A solubility constant describes the relationship between the dissolved and solid state of a certain compound at equilibrium, while a dissolution rate (reaction rate) constant K is used to describe the kinetics of the dissolution.

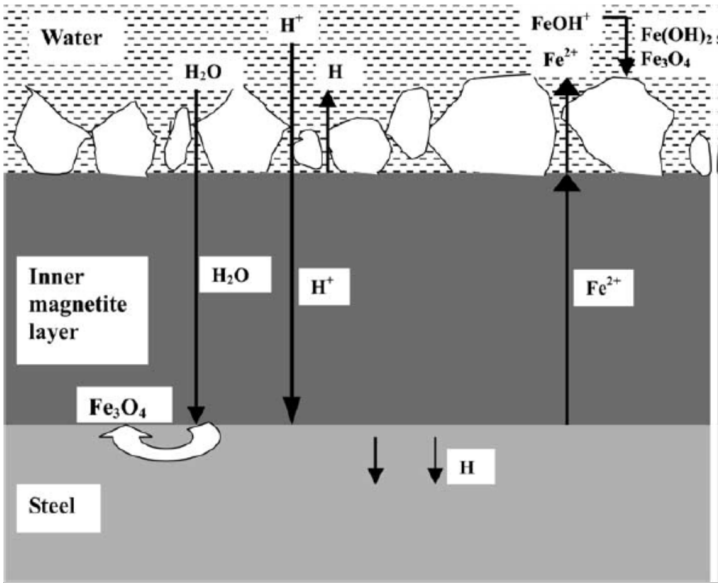

Figure 2.6: Schematic representation of the formation reactions of the double oxide layer, porous top layer above the dense layer [33].

The dissolution of magnetite is a reductive reaction where the iron of the magnetite is reduced by hydrogen therefore found under extreme reducing conditions (low Eh). During this reaction Fe(III) is converted to Fe(II). Experimentally measured solubilities at various pH and temperatures of magnetite show highest solubility at 120 to 150 °C, and overall increase at the lower end of the pH_{25C} region [100, 110]. The dissolution reaction and subsequent formation of ferrous of ferric species is described by:

$$\frac{1}{3}Fe_3O_4 + (2\text{-b})H^+ + \frac{1}{3}H_2 \longleftrightarrow Fe(OH)_b{}^{(2-b)} + (\frac{4}{3}-b)H_2O \tag{2.13}$$

$$\frac{1}{3}Fe_3O_4 + (3\text{-b})H^+ \longleftrightarrow Fe(OH)_b{}^{(3-b)} + \frac{1}{6}H_2 + (\frac{4}{3}-b)H_2O \tag{2.14}$$

The dissolution reactions of magnetite forming ferrous and ferric ions are marked by the left solid line and lower solid line of the magnetite stability region in the Pourbaix diagram. Appendix A provides Pourbaix diagrams of magnetite at temperatures of 230 and 250 °C, besides the Pourbaix diagrams given in Figure 2.5.

Having discussed the basic corrosion reactions, forming magnetite in water-steam cycle conditions and the stability of magnetite related to the reduction-oxidation potential and pH over various temperatures, the following sections will discuss two types of metallic corrosion.

2.3.3. Flow-accelerated corrosion

Many types of metallic corrosion occur in power plants and industrial boiler systems. From the various types of corrosion flow-accelerated corrosion (FAC) of carbon steel has been characterised as a severe issue for nuclear, fossil and industrial plants [16, 24]. Furthermore, FAC is one of the well known corrosion mechanisms that lead to iron oxide formation, a source for fouling. Another type being first condensate corrosion (FCC), mainly occurring in steam condensate systems [29, 46]. This section will discuss the FAC mechanism and parameters affecting the FAC. The following section, 2.3.4 shortly covers FCC.

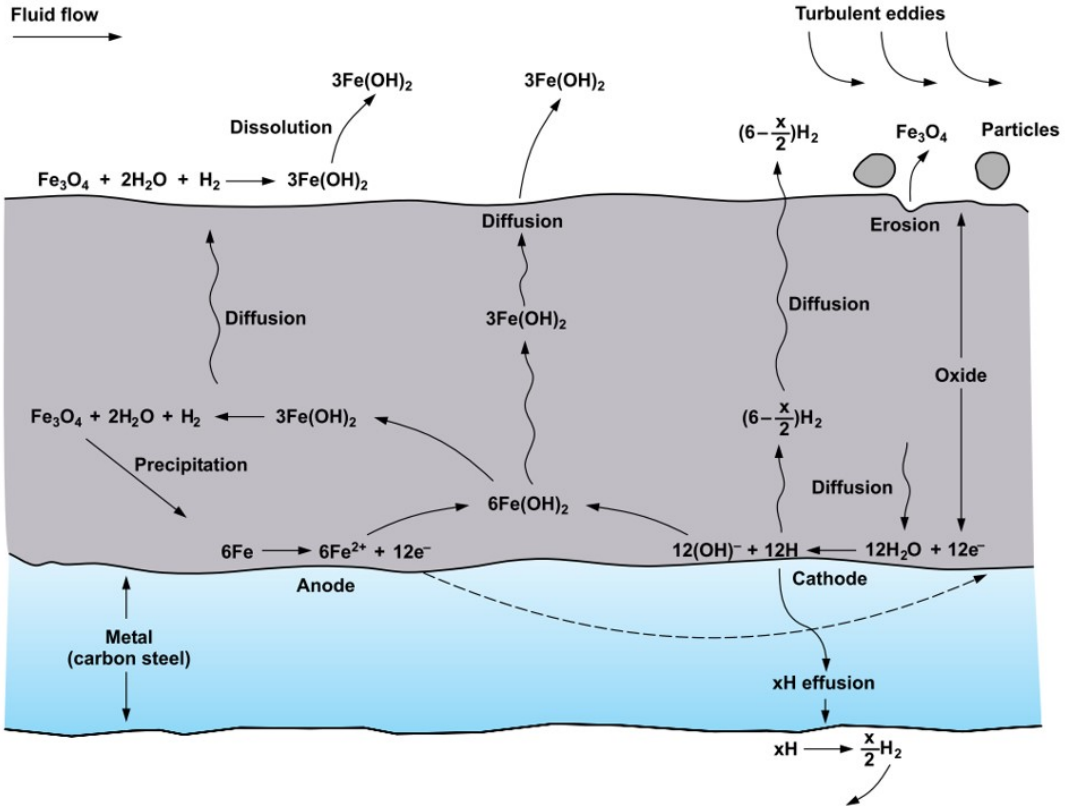

Figure 2.7: Schematic representation of the FAC mechanism, depicting the chemical reactions and transport processes at steady state corrosion [21].

Single- and two-phase FAC

FAC is a corrosion phenomenon that occurs under the conditions of flow, as the name suggests. Two types of FAC can be identified, single- and two-phase flow FAC. Single-phase flow, meaning only liquid (water in liquid form), and two-phase flow, standing for water in two phases, i.e. gas and liquid phase. Parts of the water-steam cycle prone to single-phase FAC are parts where only single phase water is present, such as feedwater systems and certain parts of the boiler tubes. Parts where water can be present in both forms, also called 'wet steam' parts, are heat recovery steam generators, condensers, ACC, and low-pressure turbines, are prone to two-phase FAC [21]. Note, at high steam qualities, resulting in pure/dry or superheated steam, no FAC occurs as some liquid water is needed to remove the oxide layer [24], and at lower steam qualities, the two-phase FAC resembles single-phase attack [21]. The remainder of this study will focus on single-phase FAC and the mechanisms of the FAC are described in the next paragraph.

Subsection 2.3.2 described the formation of magnetite in relative static conditions. Where the corrosion of steel, Schikorr reaction, results in the formation of a dense magnetite layer at the M-O interface and a porous layer on top at the O-S interface. At static flow conditions the solution is saturated in iron, allowing for the formation of the porous top layer. In contrast, flow-accelerated corrosion occurs in systems, in which the magnetite wants to dissolve, due to undersaturation of dissolved iron. This undersaturation is a result of the (turbulent) flow conditions removing the dissolved iron from the surface. Moreover, the undersaturation also prevents formation of the porous top layer by deposition of $Fe(OH)_2$ as magnetite crystals. This results in thinner magnetite layers and in return less protection [22]. At steady state FAC the amount of magnetite formed at the M-O equals the amount of magnetite that is dissolved (or

even physically eroded) at the O-S, resulting in a constant FAC rate [21]. The FAC mechanism with balanced reactions is depicted in Figure 2.7.

Factors influencing FAC

The following parameters, obtained from literature, directly or indirectly affect single-phase flow-accelerated corrosion.

- Temperature is related to the dissolution of magnetite. In turn this is related to FAC. The highest FAC rate is measured around 130 °C to 140 °C by Bignold et al. [10].
- The solubility of magnetite is related to temperature, and pH. A higher solubility leads to more dissolution. The highest solubility is determined to be around temperatures of 120 °C to 150 °C by Sturla [100] and Tremaine and LeBlanc [110]. In addition, both these authors also report higher solubilities at lower pH values.
- The flow speed (kg/h), a higher FAC rate over increasing flow is observed by Bignold et al. [10]. However, according to Dooley and Lister [21] turbulence must be considered as well.
- Turbulence influences the mass transport of dissolved iron. The local intensities of turbulence at the wall surface have significant effects on the FAC rate [71, 115].
- Oxygen concentration, as mentioned before, oxygen can form hematite and as result 'stifles' the magnetite layer. Lister et al. [56] relates oxygen concentration to FAC speed. At a pH_{25C} of 9.2, and temperature of 140 °C an oxygen concentration lower than 0.2 ppb results in significantly higher FAC rates.
- The material, or alloy affects the FAC. It is shown by Chexal et al. [16] that increased chromium contents result in decreased FAC rates. A Cr content below <0.2% leads to a high FAC risk, according to Betova et al. [8].
- A reducing environment effects the solubility of magnetite, i.e. presence of a reducing agent e.g. hydrogen, H_2 [115].

As seen above the process of FAC includes, among others, the initial reaction of iron, transport of $FeOH_2$ through the magnetite layer, and into the bulk liquid, and dissolution of magnetite. These processes include chemical kinetics, thermodynamics and fluid mechanics. Betova et al. [8] reports that the Sanchez-caldera model incorporates just a minimum number of variables/parameters necessary to describe the experimental FAC data. The Sanchez-caldera model of the FAC rate is given below [8]:

$$\frac{dm}{dt} = \frac{(\mathrm{C_{eq}} - \mathrm{C_0})\theta}{\frac{1}{\mathrm{K}} + (1-f)\left(\frac{1}{\mathrm{K_m}} + \frac{\delta}{\mathrm{D}}\right)} \tag{2.15}$$

Where dm/dt is the corrosion rate of the wall (mol $cm^{-2}s^{-1}$), C_{eq} is the equilibrium concentration of iron species (mol cm^{-3}), which in turn depends on: temperature, pH and hydrogen concentration. C_0 is the iron species concentration in the bulk flow. θ is the porosity of the layer (cm^{-3} H_2O/ cm^3), K_m is the mass transfer coefficient in cm s^{-1} (correlated to the transfer of ferrous ions to the bulk water). K is the reaction rate constant (of the reaction forming soluble ferrous iron at O-S and M-O), f is the fraction of oxidised metal directly converted to magnetite at the M-O, commonly f is equal to 0.5 (half of the oxidised metal), δ is the thickness of the magnetite layer and D the diffusion coefficient of the iron cations in water.

2.3.4. First condensate corrosion

FCC takes place at locations of first condensation of steam, such as in condensers like ACCs, and in reboilers [46]. Since condensate is formed form pure steam it is extremely pure, it generally has a pH of 6.5 to 7, and is aggressive to most metals. Due to its purity even small amounts of CO_2 or volatile acidic impurities can lower the pH, easily reaching pH 4.5 or lower. This can accelerate corrosion [29, 46]. A source of impurities is the thermal degradation of organic molecules in the boiler. This forms volatile low molecular weight organic acids, such as acetic acid, formic acid, and CO_2. The corrosion products of FCC are transported with the condensate water to the feedwater and end up in the boiler.

2.4. Chemical conditioning

As multiple factors cause and affect corrosion, there are almost equally as much intervention possibilities known to minimise corrosion, e.g. choice of material, alloy or hydrodynamic design. This section will deal with chemical conditioning as means to halt corrosion, first conventional water chemistry applied, subsection 2.4.1, and secondly treatment based on film formers, subsection 2.4.2.

2.4.1. Conventional water chemistry

First of all, the make-up water entering the WSC is demineralised or deionised water to avoid accumulation of impurities in stagnant areas such as the steam generator. This can lead to deposits and acidic conditions [29, 33]. The common treatment strategy to mitigate corrosion is ensuring a stable environment for magnetite, thus an elevated alkaline pH and low oxygen concentration (Eh). The elevated pH is achieved via a conditioning regime where volatile alkalising agents, such as morpholine, an amine, and ammonia, are dosed to the (feed)water. This cycle chemistry is called all volatile treatment (AVT). The volatility of the agents assure distribution over the whole WSC, thus neutralising/raising the pH of the condensate too [29]. Common feedwater pH levels range between pH_{25C} approx. 8.8 to approx. 9.8, depending upon the presence of copper alloys [21].

To ensure low oxygen concentrations (Eh) a reducing agent is dosed to the condensate or feedwater. A common reducing agent, or oxygen scavenger is hydrazine. When combined with an alkalising agent this cycle chemistry is known as AVT(R), the 'R' standing for Reducing, with oxygen concentrations generally below 10 ppb. Although AVT(R) is not suitable to mitigate FAC as it occurs under reducing conditions, under oxygen concentrations of typically less than 5 ppb. Fortunately, single-phase FAC can be mitigated by AVT(O), 'O' standing for oxidising [81]. This means that a reducing agent is not used and residual oxygen is present, as a result the Eh is slightly higher. The oxygen concentration in the range of 10-20 ppb allows hematite to form and 'stifle' the magnetite layer, halting further FAC [21]. A step further is to inject oxygen, this is called OT and stands for Oxygenated Treatment (OT). This is to provide more oxidising power. Concerning OT, the oxygen concentrations range from 30 to 50 ppb.

Unfortunately, AVT(O) and OT only work for all-ferrous systems, not on mixed-metallurgy systems e.g. containing copper alloys. Moreover it does not combat two-phase FAC. AVT(R) can offer protection to the copper alloys in the feedwater heaters and condenser. Whereas for two-phase units, such as deaerators, low pressure heaters and feedwater heaters, it is advised to replace thinned or failed tubing with a 1.25% or higher alloy [21]. Experience shows that FAC in condensers can be mitigated by increasing the pH value to above the common range of pH_{25C} 9.2 to 9.6 for all-ferrous systems. A condensate pH_{25C} of close to 9.8 is required to mitigate FAC.

2.4.2. Film forming amines

An alternative treatment method that is gaining acceptance in order to control corrosion, and therefore indirectly the oxide product transport to the boilers, are film forming substances. These film formers adsorb to the metal and/or oxides forming protective films. A more specific term being film forming amines (FFAs), should the molecules contain one or more amine groups. These film forming amines are high molecular weight amines consisting of a long hydrophobic alkyl chain and an hydrophilic head. The hydrophilic part of the FFA attaches itself to a surface. If enough molecules do so the hydrophobic aliphatic 'tails' will form a non-wettable surface [29].

Two film formers that are widely used and studied were chosen for further investigation in this study, named Octadecylamine (ODA) and Oleyl Propylenediamine (OLDA). Both are given below with their abbreviation and unique numerical identifier assigned by Chemical Abstracts Service (CAS).

- Octadecylamine (ODA) CAS-no.:124-30-1
- Oleyl Propylenediamine (OLDA) CAS-no.: 7173-62-8

The general formula of the FFA is R1-[NH-R2-]$_n$-NH_2, where n is an integer between 0 and 7, R1 is an unbranched alkyl chain containing 12 to 18 carbon atoms and R2 is a 1 to 4 carbon alkyl chain [7]. ODA, a monoamine FFA, having the simplest structure (n = 0, R1 = $C_{18}H_{37}$), thus a chemical formula of $C_{18}H_{39}N$ and molecular weight of 269.5 g/mol. OLDA has two functional amine groups, its structure is (n = 2, R1 = $C_{18}H_{35}$, R2 = C_3H_6) resulting in an overall chemical formula of $C_{21}H_{44}N_2$. OLDA has and molecular weight of 324.6 g/mol. The chemical structures are depicted in Figure 2.8. It is the lone electron pair in the nitrogen atoms of the amine groups that bind strongly to surfaces, a representation of monoamine film and diamine film is provided in Figure 2.9. These lone electron pairs are also able to adsorb hydrogen protons, making FFA a weak base.

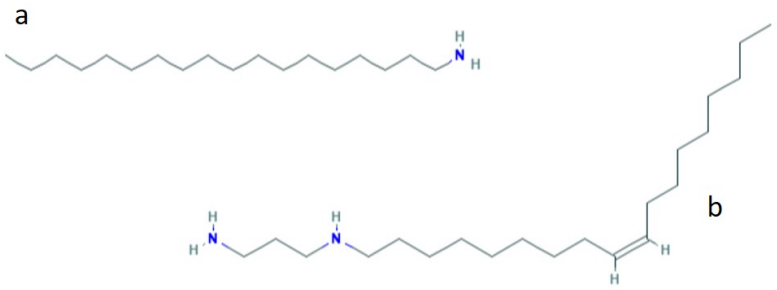

Figure 2.8: Chemical structure a, ODA and b, OLDA source:PubChem.

Terminology and categorisation

Some publications refer to FFA as fatty acids or polyamines. Polyamine is not totally incorrect but only applies to FFAs with a saturated carbon chain and more than three amino groups. The term 'fatty amine' originates from the fact that the FFA chemical group is derived from fatty acids [81]. The word surfactant is also used as means to refer to FFAs [7]. The definitions are given below:

- FFA: a film forming substance containing at least one or several amine groups and an aliphatic carbon chain, saturated or unsaturated.
- Polyamine: an organic compound having more than three amino groups.
- Surfactants: relatively small molecules that combines a hydrophillic (head) and a hydrophobic (tail) part in one molecule. Classification of surfactants is often based on their head group charge. Nonionic, anionic, and cationic for a none-charged, negatively charged and positively charged head respectively. A fourth class are the zwitterionics surfactants. This indicates a head group with two oppositely charged groups. When FFA is protonated it can be called a cationic surfactant, otherwise a nonionic surfactant.

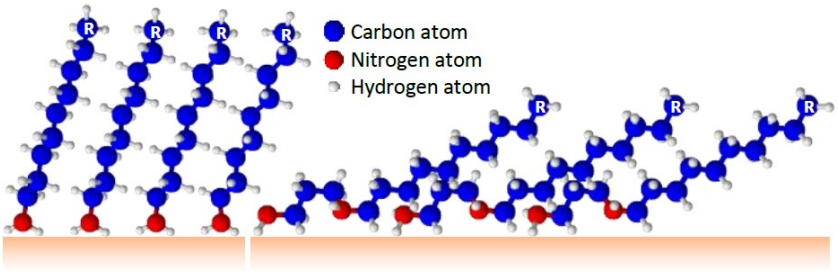

Figure 2.9: Schematic representation of FFA adsorption onto a surface, left monoamine and right diamine [44].

Thermostability of OLDA
One of the disadvantages of FFA is the thermal degradation and formation of low molecular weight organic acids [81]. De Meyer [18] investigated the thermostability of OLDA together with the possible formation of organic acids. It was found that the hydrothermolysis of OLDA at a temperature of 500 °C, a pressure of 120 bar, and oxygen concentrations below 20 ppb led to acetate and formate formation. Concentrations below 50 ppb for acetate, and below 20 pbb for formate were formed from the 5ppm OLDA starting concentrations.

Surface coverage
The amount of film forming amine to be dosed is related to the amount of surface area to be covered [81], De Meyer [18] calculated the theoretical surface coverage of the FFAs in m^2 using the following equation:

$$\text{Surface coverage of FFA} = \frac{m_{FFA}}{MW} \cdot N_A \cdot \text{projection area} \tag{2.16}$$

Where: m_{FFA} is the mass of dosed FFA, MW is the molecular weight of the FFA, N_A the constant of Avogadro. De Meyer [18] calculated the estimated projection area for OLDA to be between 62 and 127 Å². For both ODA and OLDA the average of these two values will be taken.

Henry adsorption constant
Jack et al. [44] studied the adsorption behaviour of FFA (OLDA/CHA mixture) onto steel and nickel alloy surfaces, and according to this study FFA adsorbs onto these surfaces with first-order kinetics. This adsorption was characterised with the Henry adsorption model, with the Henry adsorption constant as the characteristic parameter. This constant is equivalent to a/b in Equation 2.17. The model postulates that the coverage of the surface (g/m^2) at equilibrium

is proportional to the equilibrium concentration of the solution (g/m^3). Thus, a higher Henry adsorption constant indicates better adsorption.

$$\frac{a}{b} = \frac{V}{A_w}\left(\frac{C_b^0}{C_b^\infty} - 1\right) \tag{2.17}$$

Where: the Henry adsorption constant is equivalent to a/b, a being the deposition rate constant (m/s), and b is the release constant (1/s). V is the total volume of the system (the test solution)(m^3), and A_w is the total area of the wetted surface (m^2). C_b^0, and C_b^∞ are the initial, and equilibrium concentration of FFA in the solution, respectively.

2.5. Corrosion measurements

This section provides a background on the corrosion measurements based on the mass loss measurements, using both an immersion test and, a stirred lab setup for, a re-immersion test. Lastly, surface analysis techniques are discussed.

2.5.1. Mass loss measurements

The mass loss during an immersion test period can serve as a principle corrosion measurement assuming that localised or internal corrosion is not present. The mass loss is determined by weighing the specimen before the test and after the test when the cleaning procedure has removed all corrosion products from the specimen with a minimum removal of the base material [67, 69]. The methods of cleaning can be divided into three main categories: mechanical, chemical, and electrolytic. The average corrosion rate R can be calculated using Equation 2.18.

$$R = \frac{K \cdot W}{a \cdot T \cdot D} \tag{2.18}$$

where:

K = A coefficient to calculate the corrosion rate in the desired units
$= 8.76 \cdot 10^4$
W = Mass loss in g, to the nearest 0.1 mg
a = Surface area to nearest 0.01 (cm^2)
T = Time of exposure to test solution in hours to nearest 0.1h
D = Density (g/cm^3), density for carbon steel used: 7.85 (g/cm^3).

Corrosion rates can also be expressed in mils per year (mpy). When a corrosion rate expressed in mils per year is desired one should apply a coefficient K of $3.45 \cdot 10^6$.

2.5.2. Evaluating corrosion using a stirred lab setup

The re-immersion tests of this study are derived from and based on the following procedure by NACE et al. [68]. Currently used as a standard procedure for ”Evaluating and Qualifying Oil Field and Refinery Corrosion Inhibitors Using Rotating Cage”. See Figure 2.10 for a schematic diagram of a rotating cage setup. This type of setup and procedure has been employed in another study set out to investigate the galvanic effect of magnetite on corrosion under flowing conditions [96], and is used in this thesis to study the effect of FFA-formed magnetite layers on corrosion under flowing conditions (FAC).

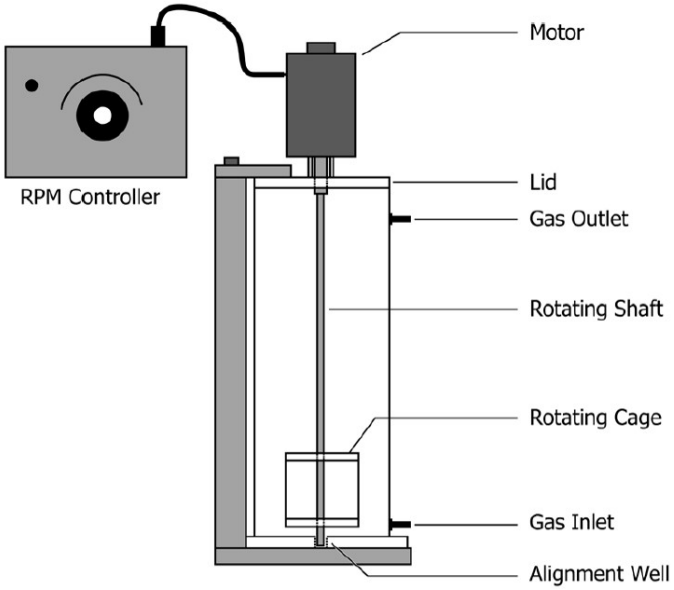

Figure 2.10: Schematic diagram of a rotating cage setup [68].

2.5.3. Surface analysis

This subsection provides short backgrounds on the various surface analysis methods used to study the oxide surface layer formed during, and present after the immersion and re-immersion tests. This to verify the mass loss measurements and to obtain more information on the corrosion behaviour.

XRD

A non destructive method in order to determine the crystallographic structure of a specimen, more precisely the top layer of a specimen, is X-ray diffraction (XRD). XRD peaks are produced by constructive interference of an X-Ray beam, scattered at specific angles depending on the crystalline structure of the sample. Consequently, the XRD peak pattern is an identifier of a periodic atomic arrangement of a given sample [53].

SEM

Scanning Electron Microscopy (SEM) is a common employed method, within corrosion studies, to study the surface morphology and cross sections of a sample, due to its ability to display the material with a resolution of only a few nanometers. Within the SEM microscope a source of electrons is produced at the top of a vacuum chamber, and are accelerated downwards passing through a combination of lenses to produce a beam of electrons. This beam of electrons scans the surface of a specimen. The interaction of the electrons with the atoms of the surface generates a characteristic back-scatter of released electrons. The SEM images are formed from this detected back-scatter and displayed on a monitor [92].

EDS

SEM devices are generally also equipped with an Energy Dispersive Spectroscopy system. This allows for the chemical analysis of the same features that are being observed on the SEM monitor [70]. Thus, while SEM is used to generate images of the surface, EDS can be applied to perform a chemical analysis of that particular surface. Similar for the generation of SEM images, a beam of electrons interacts with the surface of the specimen, generating a characteristic back-scatter of released electrons. This back-scatter can be used for the elemental analysis based on the energy that is transmitted by the electrons.

Contact angle

A drop of a liquid on a substrate, or surface, produces a contact angle θ. This is the angle that forms between planes tangent to the surface of the solid and the liquid at the wetting perimeter [102]. The wetting perimeter is also known as the three phase line, between the solid, liquid, and vapour. Figure 2.11 shows a profile of a liquid drop on a surface, the contact angle being referred to as 'θ'.

A simple way to quantify a phenomenon such as hydrophobicity of a surface is to measure the contact angle of a drop on that particular surface. This as hydrophobic surfaces are harder to wet. Wetting of a surface is a fundamental inter-facial phenomenon in which, for this case, the vapour phase is displaced by a liquid phase. A liquid drop on a solid can either spread out to form a thin film or it remains a drop. Four situations can be distinguished. The liquid drop does not make contact with the surface, the measured contact angle will be θ = 180 °. The drop produces a contact angle θ over 90 °, which indicates bad wetting, and a hydrophobic surface. Third situation, the drop produces an angle θ under 90 °, indicating partial wetting. Lastly the fourth situation, where the drop totally spreads out and no angle is measured, θ = 0 °[102].

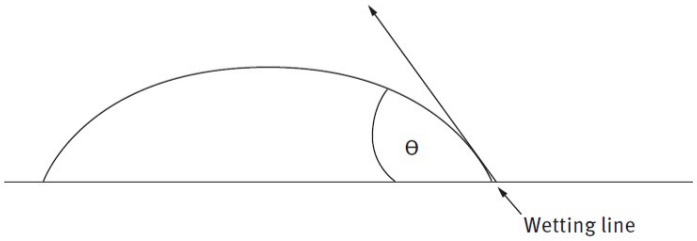

Figure 2.11: Profile of a liquid drop on a surface indicating the contact angle with θ. After [102].

The presence of a hydrophobic layer or lack of wettability of a surface has been used as a common and easy method to indicate the presence of an FFA layer on the surface [19, 73, 93, 120]. Weerakul et al. [120] used water droplets to show a hydrophobic surface along the length of a test probe. Whereas Odar [73] recommends contact angle measurements to verify the presence of FFA, and Smith et al. [93] used, among others, a non-specific hydrophobicity or droplet test to indicate the presence of OLDA.

However, a simple contact angle showing hydrophobicity can be an indicator of FFA being present, and can therefore be an indication of corrosion protection. It should be noted that non-hydrophobicity does not necessarily mean non-protection [81]. It could well be that an FFA layer is present but cannot be detected due to a rough surface with porous iron oxide. Furthermore, the contact angle is considered a qualitative method to detect FFA on a metal surface [81, 93].

2.6. Fouling of boiler systems

Fouling is characterised by the accumulation of deposits and is governed and affected by various conditions and parameters such as flow effects, heat flux, concentrations, changes in solubility over temperature as well as by electrochemical factors [9, 29, 115] Nowadays, with demineralisation of boiler feedwater, removing all hardness, the main deposit found is iron oxide, with magnetite being the foremost deposited [118], in extreme cases leading to boiler tube failures [29, 46]. Two fouling processes are given below:

- A chemical process, which is known as precipitation fouling. This involves crystallisation of dissolved metal from solution into one of its oxide forms at the wall or inside layers of pre-existing oxide layers.
- A physical process, which is known as particulate fouling. This depends on the adhesion of colloid particles to each other and subsequently to the surface.

This study will focus on particulate fouling i.e. colloidal fouling.

Particulate deposition

Kern [52] proposed a model where the net fouling rate of a surface is the difference between the deposition and removal rate of particles. The model is understood as a three step mechanism: deposition, removal and consolidation. The deposition itself comprises of two substeps, the transport stage and the attachment. The remainder of the study will focus on parameters controlling the attachment stage.

Particles may or may not adhere or stick to a surface, depending on forces that become significant as the particle is in the vicinity of the wall, or even another particle. According to Turner [112] and Turner et al. [114] the most important surface forces that come into play when particles get near a wall or other particle effecting attachment are:

- London-van der Waals forces between particles or particles and surfaces. These are always attractive.
- Electrostatic forces, these are a result form electric charges of the particles and surfaces, these forces can be attractive or repulsive and zero in absence of any net charge.

Turner et al. [114] has observed that the hematite particle deposition rate onto Inconel 600 tubes under flow boiling conditions were always higher compared to those for magnetite, and argues that the reason is most likely the sign of the surface charge of the oxide particles at the test pH. Magnetite had the same charge sign as the surface, whereas hematite and the surface were oppositely charged.

The remainder of this section will first discuss the fouling consequences, subsection 2.6.1 covers the theory on colloidal systems followed by subsection 2.6.2, which covers surface charge on minerals, followed by (polymer) fouling control, subsection 2.6.3. Lastly, subsection 2.6.4 describes the known interaction between FFA and magnetite colloids.

Fouling consequences

The deposition of corrosion products, among others magnetite, is a major cause of efficiency loss in power and industrial plants. This is associated with a decrease in heat transfer and increase of fluid flow resistance [22, 118]. Furthermore, the porous magnetite deposits form a crucial factor in boiler tube failures (BTFs) i.e. rupture of boiler tubes , as the deposits increase tube wall temperatures and also allow for a concentration built up of non-volatile dissolved impurities, up to corrosive levels [105]. Which in turn attacks the underlying (protective)

magnetite layer and steel, i.e. underdeposit corrosion. All the aforementioned can lead to a plant shutdown to (chemically) remove deposits or worse a shutdown as a result of material failure.

2.6.1. Colloidal systems

A colloid is a type of matter particle that is dispersed in water without being truly soluble. This dispersion is achieved by breaking down the material into particles slightly larger than ions and molecules and generally smaller than 10 microns. The principle behind this has to do with electric charge and scale. Almost all surfaces of matter (e.g. plastic, minerals, steel or glass) have a residue of electric charge. This charge can result in a high surface voltage. In the case of breaking down material and therefore reducing the particle and increasing the overall surface, the ratio of surface charge to mass increases exponentially. The resulting higher surface charge causes the colloidal particles to effectively repel each other and therefore maintaining the stable dispersion [29, 102].

Another force affecting the colloidal particle interaction is the van der Waals force, opposed to the electrostatic repulsion, this is an attractive force. The van der Waals force is weak and short-range. Together with the attractive force (electrostatic attraction) of an oppositely charged particle or surface the van der Waals force causes colloids to agglomerate and settle out of solution, or attach to surfaces. Hence colloidal stability depends on increasing or reinforcing the surface charge while preventing oppositely charged colloids or anything that causes neutralisation of the surface.

A well known theory of the stability of colloids is the Deryaguin–Landau–Verwey–Overbeek (DLVO) theory. This is the linear combination of the van der Waals attraction and electrostatic repulsive energy as a result from the double layer repulsion. The double layer is being formed by a cloud of counter ions around a charged particle [102]. This is discussed in the following paragraph.

Electrical double layer

The electrical double layer is the layer of adsorbed ions and a cloud counter ions around a charged particle. Three models have been proposed and are schematically depicted in Figure 2.12 a: the Helmholtz model, b: the Gouy–Chapman model, and c: the Stern model. The Stern model being the most accurate in describing colloidal phenomena [102]. The IHP refers to the closest distance of approach for specifically adsorbed ions and the OHP refers to the closest distance of approach for non-specifically adsorbed ions. The difference between the two adsorbed ions:

- Specifically adsorbed ions, have a non-electrostatic affinity to the surface and bind chemically. They reside at the distance of closest approach, inner Helmholtz plane or also known as inner Stern layer. The specifically adsorbed ions 'enrich' the surface but are not considered as part of it. Examples are cations on oxides or cationic and anionic surfactants on most surfaces. For instance, adsorption of cationic surfactant to a neutral surface can produce a positive charge on the surface. Important to notice is that a reversal of sign of the potential is possible when the number of specifically adsorbed (counter) ions exceeds the number of surface charges [102].

- Non-specifically adsorbed ions or physically adsorbed counter ions are adsorbed due to the electrostatic attractive force and are located at the outer Helmholtz plane, or also known as outer Stern layer. This plane is the closest approach for the hydrated counter ions. Non-specific ions are also referred to as indifferent ions, while counter ions experience an attractive force, co-ions experience a repulsive force [102].

The thickness of the double layer depends on the ionic strength of the solution [34, 102].

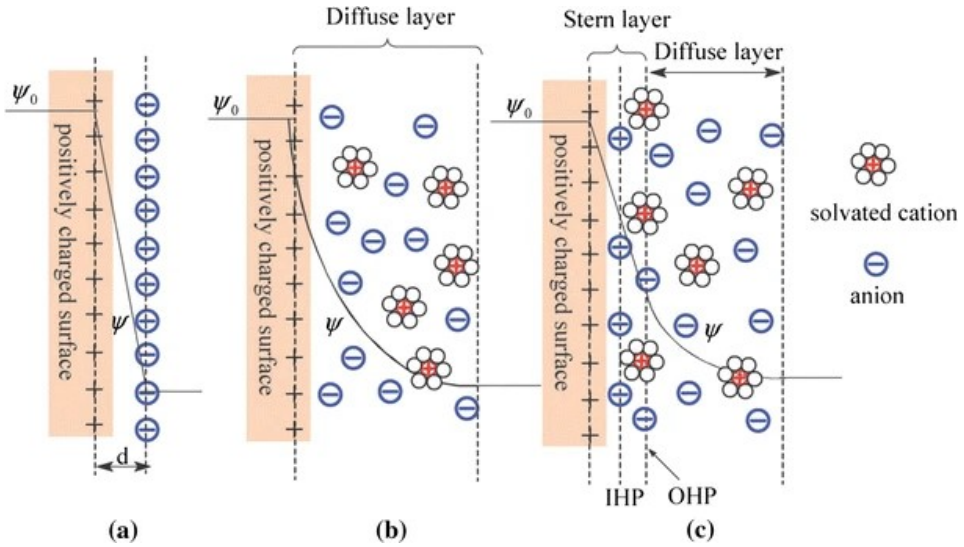

Figure 2.12: Schematic representation of double layer by the a, Helmotz model, b, Gouy-Chapman model and c, Stern model. The Stern model showing the inner and outer Helmholtz plane (IHP) and (OHP). d is the distance of the double layer described by model a. The surface potential at the particle surface and electrolyte denoted with ψ_0 and ψ, respectively [124].

Zeta potential

The zeta potential is often measured as means to, indirectly, study the surface charge of a colloid. It is the electrical potential, arising from the formation of the EDL, at the shear plane. The shear plane is the interface separating the fluid or charges that travel with the particle from the bulk fluid. The zeta potential is often determined via electrophoresis [102, 118]. The zeta potential is used as a parameter in the DLVO theory of colloidal dispersion stability to explain the overlap of the electrical double layers of two approaching particles, and the repulsive force it generates [36]. A higher the zeta potential results in more repulsion, and when the zeta potential approaches zero the likelihood of collision increases [29]. The point, or pH, at which the zeta potential is null is called the isoelectric point (IEP). .

2.6.2. Surface charge on a mineral

The previous sections discussed the stability of colloids in terms of the EDL and interaction between colloids via the DLVO theory. This section covers the background on how the surface charge on a mineral in contact with an aqueous solution arises.

The structural charge on minerals in contact with water is associated with terminal oxygen atoms at the surface of the mineral, which have unsatisfied valence that can react with the ions from the solution. These ions associate with the terminal oxygen surface sites. The major agent involved in these reactions is water which provide H^+ and OH^- ions after undergoing dissociation (self ionisation). It is assumed that the protons and hydroxyl groups reside at the surface of the mineral experiencing the surface potential of the mineral, however still free to exchange with the surrounding water [121]. The protons and hydroxides are therefore considered to be potential determining ions (p.d.i.). The simplest representation of these interactions is the one-pKa model, assuming one type of surface group to be present, M-OH, which is protonated and deprotonated depending on the pH.

$$\mathrm{M{-}OH}^{1/2-} + \mathrm{H}^{+} \longleftrightarrow \mathrm{M{-}OH_2}^{1/2+} \quad \mathrm{pK_H} \tag{2.19}$$

Where: M-OH$^{1/2-}$ is a deprotonated surface group, rendering it negative and M-OH$^{1/2+}$ is a protonated surface group, making it positively charged. pK_H is the negative logarithm of the acid dissociation constant K_H, or equilibrium constant of the reaction. This single site can, and is often re-formulated as a two-pKa model [59, 62, 101, 118]:

$$\mathrm{M{-}OH_2}^{2+} \longleftrightarrow \mathrm{M{-}OH} + \mathrm{H}^{+} \quad \mathrm{pK}_{a1} \tag{2.20}$$

$$\mathrm{M{-}OH} + \mathrm{H}^{+} \longleftrightarrow \mathrm{M{-}O}^{-} + \mathrm{H}^{+} \quad \mathrm{pK}_{a2} \tag{2.21}$$

Where: M-O$^-$ is a fully deprotonated surface group, rendering it negative and M-OH$_2^+$ is a fully protonated surface group, making it positively charged whereas M-OH is a neutral surface hydroxyl species. pK_{a1} is the negative logarithm of the acid dissociation constant K_{a1}, or equilibrium constant of the first reaction, Equation 2.20, similarly pK_{a2} for Equation 2.21. A schematic representation of an (iron-oxide) mineral surface containing hydroxyl surface species, protonated or deprotonated resulting in a net negative surface charge is depicted in Figure 2.13. The figure also depicts the representation of specifically and physically adsorbed ions, EDL and potential evolution over distance.

The surface charge formation reaction Equation 2.19 or Equation 2.20 and 2.21 are not only governed by a chemical part but also an electrostatic part due to the surface charge of the surface and therefore electrostatic potential. This can be formulated by the Gibbs free energy of surface charge formation. This reaction is:

$$\Delta G^{\emptyset} = \Delta G^{\emptyset}_{\mathrm{chem}} + \Delta G^{\emptyset}_{el} \tag{2.22}$$

Where: $\Delta G^{\emptyset}$ is the total Gibbs free energy of the reaction, $\Delta G^{\emptyset}_{\mathrm{chem}}$ is the chemical part of the reaction and $\Delta G^{\emptyset}_{el}$ the electrochemical part. The apparent ionisation constant or equilibrium constant being K_{app}:

$$\Delta G^{\emptyset} = RT \ln K_{\mathrm{app}} \tag{2.23}$$

Its chemical part is expressed with the intrinsic ionisation constant or equilibrium constant, K_{int}:

$$\Delta G^{\emptyset}_{\mathrm{chem}} = RT \ln K_{\mathrm{int}} \tag{2.24}$$

Where, for both Equation 2.23 and 2.24: R is the gas constant and T the absolute temperature. The electrostatic part is expressed by the potential difference of the surface.

$$\Delta G^{\emptyset}_{\mathrm{el}} = \Delta z F \Psi_0 \tag{2.25}$$

Where: Δz is the change in the charge of the surface group due to the reaction, F is the Faraday constant, and Ψ_0 is the surface charge of the particle.

Substituting Equation 2.23,2.24 and 2.25 into Equation 2.22, rewriting for K_{app} and taking for K_{int}: the concentration of reactants and products of the surface protonation reactions (Equation 2.20 and 2.21), one obtains the following surface protonation reactions, having K_{a1} and K_{a2} as apparent protonation constants:

$$K_{a1} = \frac{[\mathrm{M\text{-}OH}] \cdot a_{H^+}}{[\mathrm{M\text{-}OH_2^+}]} \cdot \exp\left(-F\psi_0/RT\right) \tag{2.26}$$

$$K_{a2} = \frac{[\text{M-O}^-] \cdot a_{H^+}}{[\text{M-OH}]} \cdot \exp\left(-F\psi_0/RT\right) \tag{2.27}$$

Where: [M-OH], [M-OH_2^+] and [M-O^-] are concentrations of the surface species and a_{H+} is the activity of the proton ions in the water. Note that Δz is negative, therefore has a minus value. The surface charge follows from the net positive and negative charges of the surface:

$$\sigma_0 = F \cdot \left(\left[\text{M-OH}_2^+\right] - [\text{M-O}^-]\right) \tag{2.28}$$

Where: σ_0 is the surface charge. The two pKa model also includes the adsorption of cations and anions from the solution onto the surface sites, according to the following equations:

$$\text{M}{-}\text{OH} + \text{H}^+ + \text{A}^- \longleftrightarrow \text{M}{-}\text{OH}_2{}^{2+} \cdots \text{A}^- \quad \text{pK}_\text{A} \tag{2.29}$$

$$\text{M}{-}\text{OH} + \text{C}^+ \longleftrightarrow \text{M}{-}\text{O}^- \cdots \text{C}^+ + \text{H}^+ \quad \text{pK}_\text{C} \tag{2.30}$$

Where: A^- is an anion and C^+ a cation. pK_A is the negative logarithm of the equilibrium constant for the anion binding reaction, K_A, similarly pK_C for the cation binding reaction. In a similar manner the equilibrium constants of the (counter) ion adsorption, including the potential part, is given with the following formulas.

$$K_A = \frac{\left[\text{M-OH}_2^+ \cdots \text{A}^-\right]}{[\text{M-OH}]a_{H^+}[\text{A}^-]} \cdot \exp\left(-F\psi_x/RT\right) \tag{2.31}$$

$$K_C = \frac{[\text{M-O}^- \cdots \text{C}^+]\, a_{H^+}}{[\text{M-OH}][\text{C}^+]} \cdot \exp\left(F\psi_x/RT\right) \tag{2.32}$$

Where: $\left[\text{M-OH}_2^+ \cdots \text{A}^-\right]$ and $[\text{M-O}^- \cdots \text{C}^+]$ are the concentrations of adsorbed anions and cations, respectively. Note, ψ is marked with an 'x' as the counter ions can either experience the surface potential or the potential of e.g. the Stern layer. For instance Wesolowski et al. [121] modelled specific cation and anion binding at the Stern layer, experiencing the potential of the Stern layer, and cation binding directly at the mineral surface (called ψ_M), these ions experience the potential ψ_0.

The surface charge of magnetite, or oxide minerals in general, depends on the pH. Higher pH values lead to more negatively charged surface sites, hence a negative potential in alkaline conditions, and the opposite holds for low pH regions. The particle surface charge switches between a negative and positive charge in or near the neutral pH region. This trend can be observed in Figure 2.14 where Vidojkovic et al. [117] measured the zeta potential of magnetite at 25°C.

Point of zero charge

Metal oxides experience a surface charge when in an aqueous solution. Generally being negative in alkaline solutions and positive in acidic solutions. This is based on the protonation and deprotonation of surface sites making them either positive or negative, these reactions are related to the pH. The point at which the surface sites and their associated bound proton or hydroxide groups are equally concentrated, hence establishing a zero net charge, is called the 'point of zero charge'. As mentioned the surface charging reaction depends on pH, thus another term for the 'point of zero charge' is the pH_{pzc}. The surface protonation constants given by Equation 2.20 and 2.21 and pH_{pzc} interrelate as follows:

$$\text{pK}_{a1} + \text{pK}_{a2} = 2\text{pH}_\text{pzc} \tag{2.33}$$

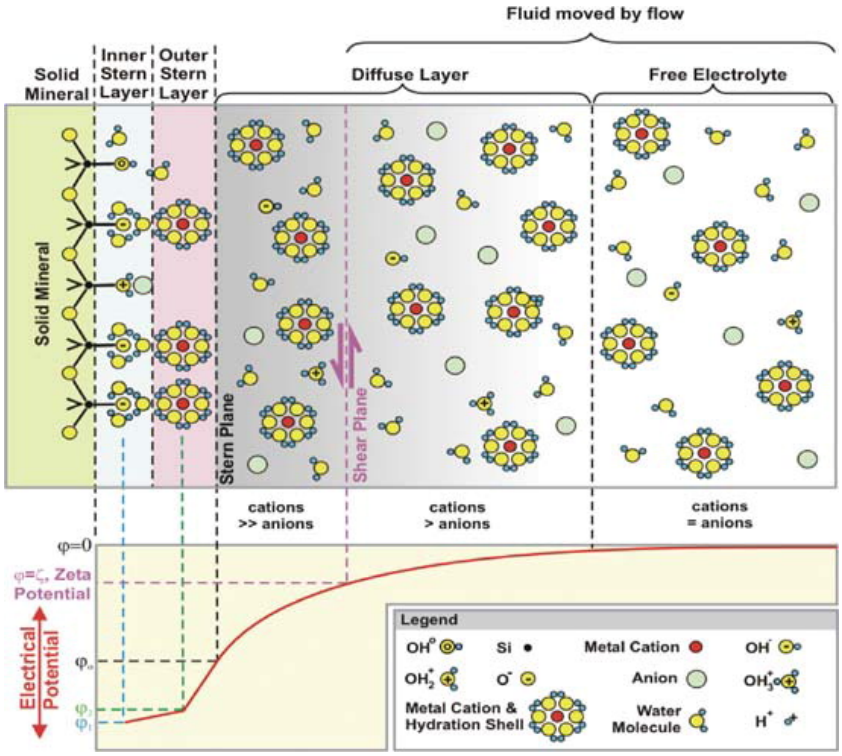

Figure 2.13: [Figure 1. A schematic representation of the surface charging with positive sites M-OH+2 and neutral M-OH and negatives sites M-O- and the resulting electrical double layer that exists at the interface between a (mineral) particle and water. Specifically adsorbed anions are depicted in green within the inner Stern layer and physically adsorbed hydrated cations in the outer Stern layer. The surface, inner Stern plane and outer Stern plane potential are given with, blue, green and black respectively (or from left to right within the figure. The zeta potential is the potential at the shear plane [34].

2.6.3. Fouling control using polymers

Polymers are used as last measure to control fouling [29]. Polymers have the ability to inhibit the agglomeration of iron-oxide particles and keep them dispersed. The definitions of polymers and certain types of polymers are listed below:

- Polymers are long, chain-like molecules consisting of many equal parts or monomers.
- Polymeric surfactants are polymers with surfactant properties.
- Polymers can be charged when they have ion exchange sites incorporated, then polymers are called polyelectrolytes. Positively charged are called cationic polyelectrolyte or cationic polymer and negatively charged are called anionic polyelectrolyte or anionic polymer. Cationic polyelectrolytes are either polyamines or quaternary amines.

2.6.4. FFA colloidal magnetite interaction

This subsection concerns the interaction between film formers and amines on the surface charge and related properties of colloidal particles, magnetite in particular. The most important hypotheses and conclusions of the literature review on the interaction between film formers, plus amines, and (colloidal) magnetite in terms of surface binding and the subsequent influence on charge, are listed below.

- FFA increases the zeta potential of magnetite over a large or even whole range of pH [32]. As a result the effect of the FFA on the IEP could not be determined.

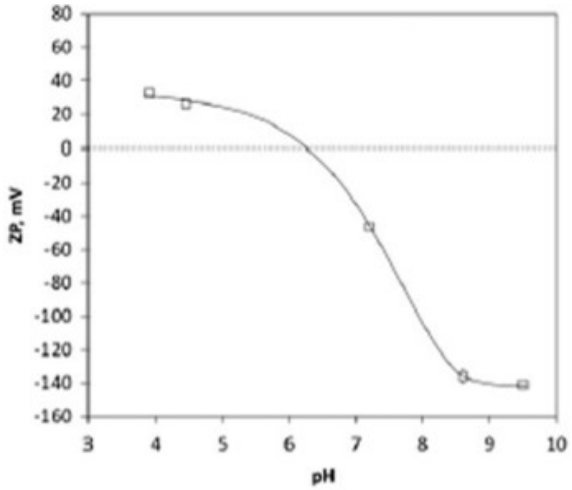

Figure 2.14: Zeta potential of magnetite over pH measured at 25°C [117].

- As FFA increases the zeta potential (to positive values) over a large pH range, it can provide an electrostatic repulsive force similar to polymeric dispersants [7].
- Since the FFA used in the study of Gasnier and Lister [32], commercial Cetamine, had a primary and secondary amine group, the authors propose that one of the amines was the anchor point of the molecule to the magnetite surface while the other amine group was protonated leading to a positively charged species.
- Unlike polymeric dispersants, which can increase the negative surface charge of an iron-oxide (in alkaline regions), the film forming amine shifts the surface charge completely to positive values, which could lead to unwanted effects [32]. Other conclusions were that at low concentration of FFA a reduction of magnetite deposition occurs, whereas at high concentrations a coagulation of the particles can be observed, illustrating the importance of avoiding overdosing of the FFA [81].
- Hajdú et al. [38] suggests in his study on the dispersion of magnetite nanoparticles that surfactants (note not FFA in particular) adsorb onto the magnetite surface via the surface hydroxyl sites (M-OH).
- Turner et al. [113] shows that the use of amines (ammonia, MOR and ETA) increase the IEP to higher pH values. The hypothesis is that the amines that were used are weak bases and incomplete dissociation of these amines enhances the adsorption of protonated amines on surfaces, therefore increasing the zeta potential. This means more positive in the acidic pH region and less negative in the alkaline region.
- Turner et al. [114] formulated that amines (note: FFA not investigated), which are weak bases, therefore present as a charged and neutral amine species are both likely to be adsorbed. Only the cationic species will reduce the negative surface charge of magnetite at high pH.
- Turner et al. [114] formulated a hypothesis concerning the size of the amine: ”a smaller amine molecule should correlate with greater adsorption and a higher particle deposition rate”.

2.7. Potentiometric titrations

Shortly, potentiometric titrations are a method for determining the proton induced surface charge at a colloid/water interface via measuring and relating the ”equilibrium” pH values of a colloidal dispersion over a titration with a strong base or acid to a similar titration without the colloid being present.

During a surface titration of a colloidal suspension the measured pH provides the H^+ proton concentration via the relation with the activity coefficient γ stated in Equation 2.34, and is compared to the H^+ proton concentrations determined via the measured pH of the titration of a 'i.e. blank' in absence of the solid. The expected pH of a solution in absence of the solid, the blank, can also be calculated from the known solution composition. The excess and missing H^+ in the solution can be explained by the dissociation of protonated surface groups, and adsorption onto the mineral surface (or alternatively, adsorption of OH^- onto the surface groups and neutralisation of H^+ by desorbed OH^-) [121]. The quantity of interest, the surface charge density, is subsequently determined by the amount of excess and missing H^+ in the test solution, usually expressed in micromoles, at each point during the titration divided by the total surface of the solid exposed to the test solution, multiplied by the negative value of the Faraday constant. Equation 2.35 gives this basic relationship.

$$pH = -log(\gamma[H^+]) \tag{2.34}$$

Where: γ is the activity coefficient of the solution calculated via the Davies approximation, valid for Ionic Strengths below 0.5M [99], and H^+ is the proton concentration of the solution in mol/L.

$$\sigma_0 = \left(\frac{"solutionexcess"\mu molsH^+}{m^2}\right)(-F) \tag{2.35}$$

Where: σ_0 is the surface charge density of the solid (C/m^2) as a result from the proton ad- and desorption, m^2 is the total surface of solids in solution and F is the Faraday constant. A negative sign is added in front of the Faraday constant as a ”solution excess” amount of protons means a negative surface charge while a negative ”solution excess” amount of protons i.e. ”missing protons” indicate adsorption of H^+ to the surface sites making the surface positively charged. When no other proton producing or consuming reactions occur in the solution the left-hand side of Equation 2.35 stands for the proton-induced surface charge density.

The following subsections provide three detailed methods to calculate the surface charge.

2.7.1. Calculating the surface charge

This section will cover three methods to calculate the surface charge. Named after the respective author: the ”volume-relationship” method [59], the ”Lützenkirchen” [59] method and the ”Szekeres and Tombácz” method [101]. Using the ”volume-relationship” method described by Lützenkirchen et al. [59] one calculates the surface charge at a specific pH value based on the difference in titrant volume between the colloidal titration and blank titration, Figure 2.15a. This method is described in the first upcoming subsection. Provided that the colloidal and blank titrations apply the same titrant addition volume per step, giving titration data points directly above each other, one can apply the ”Lützenkirchen” method to calculate the surface charge directly from the ΔpH, see Figure 2.15a. Lastly, the ”Szekeres and Tombácz” method is a substitute for when titration points are not directly above each other when plotted, due to difference in titrant volume addition during the experiments, Figure 2.15b. All methods should lead to the same or similar outcome, schematically depicted in Figure 2.15c.

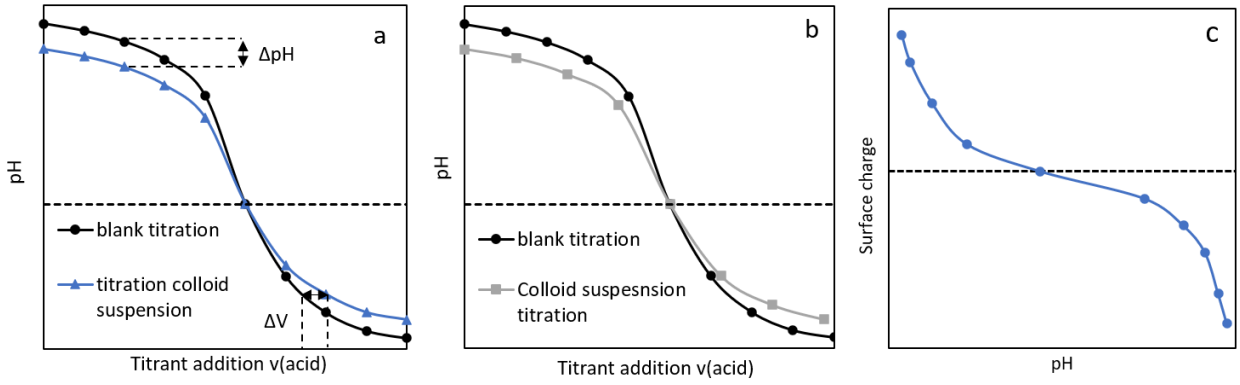

Figure 2.15: Representation of possible titration curves a and b. a: titration points align and experimental data can be used to calculate the surface charge figure-c via all methods. b: points do not align, calculation surface charge curve not possible via Lützenkirchen method.

Volume relationship

The volume relationship is based on the principle to add more or less titrant to achieve a similar pH for two different titrations. Knowing the acid or base concentration of the titrant one can calculate the excess or missing protons in solution. Looking at the ΔV in Figure 2.15 a, one sees that to achieve a similar pH more titrant, acid in this case, should be added during the colloidal titration, indicating missing' H^+ protons. An opposite relation holds above the dashed line. For a titration of a basic suspension with a strong acid the equation becomes:

$$\Gamma_{H^+} - \Gamma_{OH^-} = -\frac{c_{\text{acid}}\,(v_b - v_d)}{s \cdot \rho_i \cdot V} \tag{2.36}$$

For a titrations of an acidic suspension with a strong base the sign should be reversed:

$$\Gamma_{H^+} - \Gamma_{OH^-} = \frac{c_{\text{base}}\,(v_b - v_d)}{s \cdot \rho_i \cdot V} \tag{2.37}$$

Where: Γ represents the surface concentration of a certain species, units: moles per unit of surface area. $\Gamma_{H^+} - \Gamma_{OH^-}$ represents the net uptake of H^+ or release of OH^- ions per unit area, by the colloidal surface. This correlates to the excess and missing H^+ in the solution if dived by the amount of solid surface area present in the volume. c_{acid} and c_{base} are the concentrations of titrant. At the pH of interest the v_b and v_d are the volumes of titrant added in the blank titration and titration containing the dispersed colloids, respectively. s is the specific surface area of the solid. ρ_i is the mass concentration of the solids (mass of solid divided by V, the latter is the volume of the total titration liquid solution). The subsequent surface charge density is found by multiplying the excess or missing protons per unit area of solid with the Faraday constant.

$$\sigma_0 = F(\Gamma_{H^+} - \Gamma_{OH^-}) \tag{2.38}$$

Lützenkirchen method

Provided that both the blank and dispersed titration were executed with equal addition of titrant volume resulting in two plots with the titrations points above each other one can use the direct relation of ΔpH to calculate the surface charge. In this case Equation 2.36 and Equation 2.37 is rewritten by Lützenkirchen et al. [59] to:

$$\sigma_0 = \frac{-F}{s\gamma}\left(\left(c\,(\mathrm{H^+})_\mathrm{d} - c\,(\mathrm{H^+})_\mathrm{b}\right) - \left(c\,(\mathrm{OH^-})_\mathrm{d} - c\,(\mathrm{OH^-})_\mathrm{b}\right)\right) \tag{2.39}$$

Where: $c(H^+)_d$ and $c(H^+)_b$ are the proton concentrations in mol/L of the blank and colloidal titration, i.e. dispersion titration, respectively. Similarly, $c(OH^-)_d$ and $c(OH^-)_b$ are the concentrations of hydroxyl ions in mol/L of the blank and dispersion titration, respectively.

Szekeres and Tombácz method

For experimental titration results that do not align due to differences in titrant addition, as schematically depicted in Figure 2.15 b, one can use the method developed by Szekeres and Tombácz [101]. This method uses the blank titration(s) to construct proton concentration calibration plots. These plots contain the concentration of added base or acid on the x-axis and the y-axis is to plot the measured pH response, a linear trend should be observed, with the slopes called S_a and S_b for acid and basic titrations, respectively. The slopes give the relation of titrant addition to apparent pH and is comparable to the thermodynamic activity coefficient γ. With this method one calculates the net surface proton excess per unit area,- using the sum of the specific surface excess amounts of H^+ and OH^- (mol/g) denoted with: $\Delta n_{H+,OH-}$, divided with the specific surface area s.

$$(\Gamma_{\mathrm{H^+}} - \Gamma_{\mathrm{OH^-}}) = \frac{\Delta n_{H+,OH-}}{s} \tag{2.40}$$

$\Delta n_{H+,OH-}$ is calculated with Equation 2.41 at each titrant addition point from the difference between the actual proton concentrations ($C_{H+,OH-,0}$), calculated using Equation 2.42, and the measured hydrogen and hydroxyl ions, $C_{H+,OH-,e}$. The latter adjusted with the S_a and S_b factors according to Equation 2.43 to obtain the exact proton concentrations from the measured pH.

$$\Delta n^{\sigma}_{\mathrm{H^+,OH^-}} = \frac{V_{\mathrm{total}}\left(c_{\mathrm{H^+,OH^-},0} - c_{\mathrm{H^+,OH^-},e}\right)}{m_{\mathrm{oxide}}} \tag{2.41}$$

Where: V_{total} is the volume of the total solution including added titrant (L). m_{oxide} is the total mass of oxide within the solution (g).

$$c_{\mathrm{H^+,OH^-}} = \frac{c_{\mathrm{acid}} \cdot \sum_i v_{\mathrm{H^+},i} - c_{\mathrm{base}} \cdot \sum_i v_{\mathrm{OH^-},i}}{v_0 + \sum_i v_{\mathrm{H^+},i} + \sum_i v_{\mathrm{OH^-},i}} \tag{2.42}$$

Where: c_{acid} and c_{base} are the concentrations of acid and base titrant. $v_{H+,i}$ and $v_{OH-,i}$ are the volumes of the ith dosage of acid and base titrants lastly, v_0 is the volume of the initial test solution before titrant addition.

$$c_{\mathrm{H^+,OH^-},e} = \frac{10^{-\mathrm{pH}}}{S_\mathrm{a}} \quad \text{and} \quad c_{\mathrm{H^+,OH},e} = \frac{10^{-\mathrm{pOH}}}{S_\mathrm{b}} \tag{2.43}$$

Where: pH is the measured pH value at the titrant addition converted to pOH using pKw = 14 at 25 °C and pKw=11.64 at 150°C [119].

2.7.2. Determining the pH-pzc

Subsection 2.6.2 discussed the point of zero charge on a magnetite or other mineral oxide colloid and how it can arise. This study is in particular focused on obtaining the point of zero charge i.e. pH_{pzc}, as at this point the EDL collapses and hence, no repulsive forces are present between particles or a particle and a surface e.g. boiler tube wall. This subsection covers methods on how potentiometric experiments can determine the pH_{pzc} and how this point can be extracted from potentiometric data.

pH-znpc

The simplest method for determining the pH_{pzc} is to look at where the potentiometric titration and blank titration intersect. When the surface charge is calculated this would the point where the charge-line intersects the x-axis. In other words there are no excess or missing protons between the two titrations giving a σ_0 of zero, see Equation 2.35. This conditions is refered to as the pH_{znpc} or 'zero net proton condition' [97]. However, this method only holds in the ideal case where there are no impurities present in the solution (e.g. specific ions) or on the surfaces, and no additional account solid-solution interaction occur [121]. It is therefore advised to perform the potentiometric titration in an indifferent electrolyte such as KCl or KNO_3 to avoid specific adsorption of ions.

pH-cip

The point of zero charge can be found via potentiometric titrations. In case titrations, both blank and with the dispersion of interest, are performed at multiple ionic strengths. Often 3 different ionic strengths [101, 121] are used but 2 strengths is not uncommon [123]. When calculating the surfaces charges from these different titrations at various strengths and plotting them together the 'common intersection point' or pH_{cip} indicates the point of zero charge. This holds as the electrolyte concentration increases the σ_0 amplifies, becoming more negative in the alkaline region and more positive in the acidic region, due to better screening of the charge, this is depicted in Figure 2.16. At the point of zero charge there is no increase or amplification possible rendering it the point where all the isotherms/curves intersect [102]. Assuming that no specific ion adsorption takes place.

Szekeres and Tombácz [101] argue that two additional steps can be performed to ensure the identification of the point of zero charge using the pH_{cip} method. First to perform the titrations with different electrolytes in addition to different ionic strengths. Should the pH at the intersection be the same for both electrolytes one is sure the electrolyte does not influence the titration and pH_{cip} is pH_{pzc}. In all other cases, one of the electrolytes or both should be replaced, or the sample should be cleaned, as there might be adsorption of specific ions. The second step, to ensure an absolute pH_{cip} or as Szekeres and Tombácz [101] formulate 'CIP = PZC', one should verify if the common intersection point resides on the x-axis when the surface charge curves are plotted, see Figure 2.16b. If this is not the case a strong base or acid might be present and this should be eliminated. In case of Figure 2.16b too much base present causes the cip to be located above the x-axis. Often it is assumed that the pH of cip is the pH of the point of zero charge and the curves are simply shifted relative to the cip to obtain the absolute surface charge values [13, 116, 121], going from Figure 2.16a to b.

pH-infl

A third way to determine the point of zero charge is based on a derivative from a fitted, 3rd order, polynomial function. This method was applied in previous studies, Wesolowski et al. [122], and Zebardast et al. [123] fitted the polynomial function to their experimental surface charge isotherms/curves and subsequently differentiated them with respect to the pH. The maximum or minimum (depending on the nature of the curve's y-axis, being surface charge or excess proton concentration) of the obtained derivative curve indicated a point of inflection, named pH_{infl}.

This method is based on the nature of the surface charge over pH isotherm/curve shape, which follows an s-shape with the lowest tangent, supposedly, at the point of zero charge as surface charge switches signs.

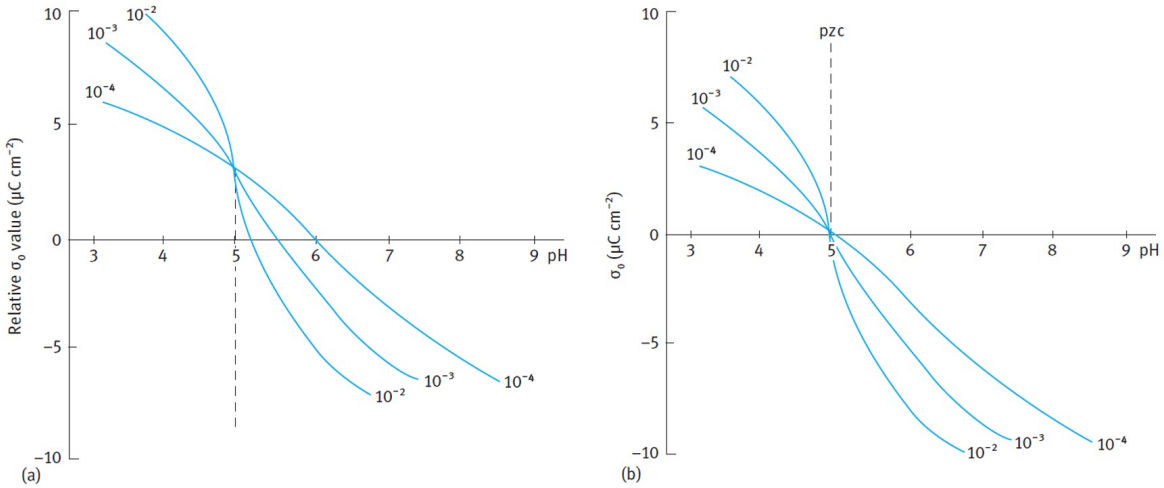

Figure 2.16: a: relative surface charge isotherms intersecting at the pHcip. b: absolute surface charge intersecting at cip is pzc [102].

2.7.3. Iron dissolution effects

The dissolution of magnetite, into ferrous iron and hematite, can affect the surface charge determination, as the dissolution reaction takes up hydrogen protons. This affects the pH measurement. As dissolution is more common in the lower pH region, the result is a lower solution excess of H^+ i.e. higher 'missing protons' from the solution. Mayant et al. [62] and Wesolowski et al. [121] both give the reactions to the magnetite dissolution, Equation 2.44 and 2.45. The first being the same reaction that dissolves the magnetite layer where b=0, see Equation 2.13. In both cases one ferrous iron as product needs two H^+ protons as reactant.

$$\frac{1}{3}Fe_3O_4 + 2\,H^+ + \frac{1}{3}H_2 \longleftrightarrow Fe^{2+} + \frac{4}{3}H_2O \tag{2.44}$$

$$Fe_3O_4 + 2\,H^+ \longleftrightarrow Fe_2O_3 + Fe^{2+} + H_2O \tag{2.45}$$

2.7.4. Determining the surface area via BET

To calculate the surface charge density of an oxide, its specific surface area is needed. The most common method to determine the specific surface area is the Brunauer–Emmet–Teller (BET) method with N_2 adsorption. In a BET analysis, the specific surface area of a specimen is derived from the volume of N_2 gas adsorbed onto the specimen. Portions of N_2 are added to a vacuumed cell containing the specimen, which in turn will be partly adsorbed, eventually reaching equilibrium with the gas phase per addition. In this way ad- and desorption points are recorded over the pressure increase. This allows to construct ad- and desorption isotherms. These isotherms in combination with the BET theory are used to derive the surface area [28, 75].

2.8. Surface complexation models

The theory and formulas governing surface complexation, e.g. the pKa1 and pKa2, have been discussed in subsection 2.6.2. This section focuses on surface complexation models (SCM), combined with the respective software, that can be used to fit a set of surface complexation equations onto the experimental data in order to obtain the equilibrium constants of the reactions. This can be helpful to test certain surface complexation reactions, in particular those linked to FFA and magnetite interactions, and secondly to obtain a trend of equilibrium constant change over temperature. These obtained trends can allow for extrapolation. Thus, making

predictions at higher temperatures possible, by modelling the surface charge using the set of complexation equations and extrapolated equilibrium constants. This section discusses four potential models that can be applied for fitting: PHREEQC, PHREEQC CD-MUSIC, Protofit and FITEQL.

- PHREEQC: a geochemical code containing a diffuse double layer surface-complexation model (DLM). In these surface complexation models the sorption is both dependent on chemical and electrostatic energy (ΔGtot = ΔGads + zFψ) [76, 77]. The model is depicted in Figure 2.17 as model (b) where a surface potential ψ_0 is slowly neutralised by an electrical double layer. In this model the specifically adsorbed ions are considered part of the surface and experience the surface potential. A triple layer model (TLM), Figure 2.17c, would be a more accurate representation as it has more planes for the ions to adsorb onto which can be used to represent the inner and outer Stern layer. The code allows for manual addition of reactions into a database along with modelling new conditions with extrapolated values of the equilibrium constants.
- PHREEQC CD-Music: Allows for multiple binding sites in addition to the standard surface complexation model [76]. This results in a better fit and prediction of the surface charge but also more constants that need to be found during the fitting exercise.
- Protofit: useful software to fit surface complexation models onto experimental data. SCM available include the constant capacitance model (CCM), and DLM. This software is used to derive the surface complexation constants from the fit. The Protofit software does the fitting automatically [111]. However, it is not a flexible method as it performs not allow the addition of newly formulated reactions. In addition, the software only gives equilibrium constants as output, and is not intended for predictive simulations.
- FITEQL: similar to Protofit, the FITEQL software provides an automatic way to numerically fit a SCM onto experimental data to obtain the fitting parameters, i.e. the equilibrium constants. The different models that can be chosen are CCM, DLM and the tripple layer model (TLM) [107].

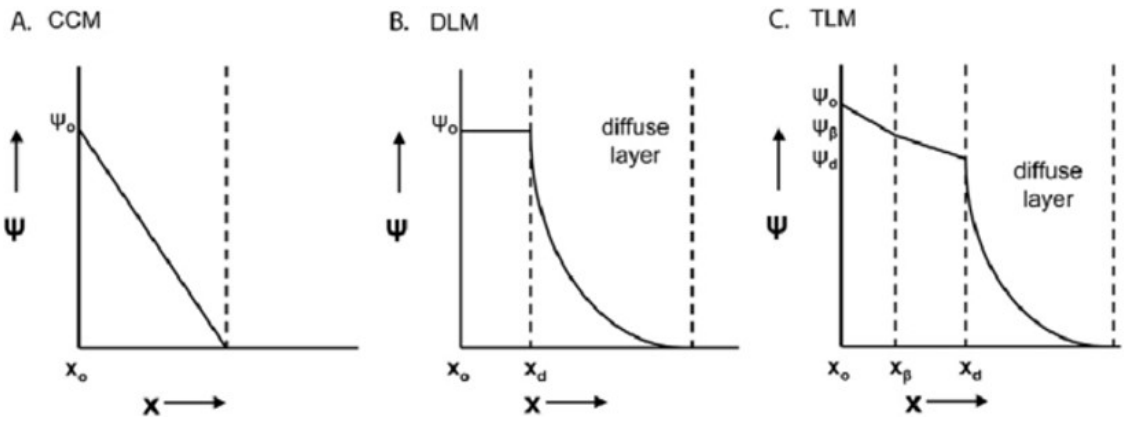

Figure 2.17: Schematic representation of the electric double layer in surface complexation models. a: constant capacitance, b: diffuse layer model, used by PHREEQC and c: triple layer model [35].

3

Material and Methods

To gain more knowledge into the effects of FFA on the formation of magnetite, and on the inhibition of acidic flow-accelerated corrosion, and its effects on colloidal magnetite surface charge both immersion corrosion experiments and potentiometric titrations were carried out in this study. This chapter will provide the materials and methods for both sets of experiments.

Immersion re-immersion corrosion tests

Laboratory immersion and re-immersion corrosion tests were carried out to gain knowledge on the influence of film former's in addition to ammonia on magnetite oxide layer formation and its protection against acidic FAC of carbon steel. This was done to provide answers to research questions 1 and 2.

The immersion tests were carried out to form a (protective) magnetite layer under different water chemistries. To test the influence of ODA and OLDA in addition to ammonia against an only ammonia chemistry on the formation of a (protective) magnetite layer, a blank chemistry was used as reference. Subsequent, re-immersion tests were carried out to test the protective properties of the formed magnetite layers in acidic FAC. After each corrosion test layers and coupons are examined and analysed to provide information on: chemical composition, hydrophobicity, surface morphology, layer-thickness, particulate oxide release and corrosion rate.

Section 3.1 deals with the preparation of coupons and the FFA used in this study, section 3.3 describes the test conditions of the immersion and re-immersion tests followed by sections discussing the setup used for the corrosion tests and the procedure of the experiments. Lastly, section 3.5 covers the coupon and oxide layer analysis.

Potentiometric titrations and surface complexation model

Potentiometric titrations were carried out to obtain knowledge on the influence of FFAs on the surface charge, and pH_{pzc} of colloidal magnetite at room and elevated temperature, to provide answers to questions 3 and 5. A surface complexation model was fitted to the experimental data to obtain reaction constant values. With the extrapolated reaction constant values predictions of surface charge at temperatures unreachable during the experiments were made.

Generally, two sets of potentiometric titrations have been performed: a blank (only electrolyte) and a magnetite colloid titration to determine the surface charge of colloidal magnetite. Using the same blank titration, together with a titration of a colloidal magnetite FFA solution one can determine the effect of FFA on the magnetite surface charge. In addition, adsorption experiments have been performed, at room temperature, to assess the absorbance of FFA to magnetite. Set out to provide an answer to research question 4.

The methods and materials for the adsorption experiments are discussed in section 3.6. Section 3.7 provides the general potentiometric experimental method and overview of the various performed titrations. Section 3.8 covers the magnetite and solution preparation. This is followed by two sections discussing the setups used and proton calibrations performed. Section 3.12 and 3.13 give the potentiometric titration procedures. Section 3.14 discusses the post titration analyses. Section 3.15 covers the model development and fitting methodology together with the predictive modelling strategy.

3.1. Coupon and film former preparation

This section deals with the preparation and storage of the coupons, and the FFAs: ODA and OLDA.

3.1.1. Coupon preparation and storage

Cold rolled commercial steel, carbon grade 1010, was used to make the steel coupons. The mild carbon steel coupons were cut in dimensions of approx. 75x10x1.6 mm, no holes nor stencils were present, and they were given a glass bead finish. Glass beaded finish typically results in a finely textured surface with a typical surface roughness of approx. 50 µIn RA on steel coupons. The surface roughness listed is for reference purposes only. The coupons were manufactured by FERALOY Corporation. Coupons were delivered and kept in VCI filled plastic packaging until the tests. The chemical composition is provided in Table 3.1.

Table 3.1: Chemical composition of the C1010 alloy (wt%)

C	Mn	P	S	Si	Cu	Ni
0.0820	0.4100	0.0120	0.0080	0.0160	0.0580	0.0190
Cr	Mo	Al	V	Ti	N	B
0.0490	0.0080	0.0390	0.0010	0.0020	0.0034	0.000

Prior to the immersion tests the coupons were removed from the plastic packaging, measured using a Vernier caliper to the nearest 0.01 mm, and weighed to the nearest 0.1 mg. Afterwards, they were cleaned with acetone, and dried in air. Coupons were carefully dried using tissues and shortly dried in air after being removed from solution. Between the immersion and re-immersion tests and after re-immersion tests, coupons were stored in vacuum sealed bottles with added nitrogen gas and stored in a silica filled vacuum closet at -0.04 MPa. This to prevent any oxidation of the magnetite layer.

3.1.2. ODA preparation

ODA (1-Octadecylamine C18H39N), 97% powder purchased from Alfa Aesar Lot# 10219115 and CAS: 124-30-1 was used in this study. As ODA is very insoluble in water and therefore harder to make a good dissolved ODA solution three methods have been applied to prepare an ODA solution, see Appendix B. In order to pick the best method spectrophotometry was used. From each ODA solution a sample was taken, and put in an ultrasonic bath for 1 hour at 40 °C, afterwards Bengal Rosa dye was added together with some acetic acid and placed in a UV-Vis spectrophotometer (Genesys 10S) [37]. The method corresponding to the solution giving the highest absorbance was chosen. Subsequently, a full absorbance calibration curve was made for the chosen solution. The Bengal Rosa method was used to choose a solution and to determine subsequent FFA concentrations, as this method is applied to monitor polyamine concentrations in boiler water. Higher absorbance means a better reaction between the FFA molecules (surface active amine) and the dye [55], lower adsorption might indicate michelle

formation [73], hence a bad solution. Moreover chemical oxygen demand (COD) measurements were performed to verify the adsorption measurements. The COD measurements were within ±10% of expected COD values (calculated based on amine concentration).

The chosen method to make the ODA solution comprised out of 2 steps. First an ODA emulsion was made by adding ODA powder and drops of 70 °C Milli-Q water into a bottle while manually stirring (by a stick/stirrer). This way an emulsion was made using 50mg ODA powder and 3ml Milli-Q water. Secondly, the emulsion was added to 1 liter of Milli-Q water heated to 70 °C while stirring, reaching a concentration of 50 ppm. The solution was kept at 70 °C while stirred for 2 hours, and poured into a pre-saturated flask. The flask was kept on top of a magnetic mixer and the solution was mixed for 24 hours. From this 50 ppm flask lower concentration solutions were made. Batches were kept for a max of 1 month and remained permanently stirred throughout this period. During this study two ODA (batch) solutions were prepared.

ODA concentration calibration curve

The optimum wave length to construct the ODA concentration calibration curve using the Bengal Rosa method was found to be at λ = 560nm, coinciding with the absorbance peak of an absorbance spectrum over a range of 150nm to 1000nm. This corresponds with literature [98]. 1cm cuvettes containing 3ml samples of accordingly diluted ODA solution were made using the 50ppm ODA stock solution. 120 µL of acid reagent and 120 µL of Bengal Rosa dye were added to the samples in that specific order. Samples were shaken and absorbance was measured using the spectrophotometer. Figure 3.1a provides the calibration curves of the two prepared ODA solutions. The figure also illustrates the need to put the ODA solution into the ultrasonic bath. Only small portions of the 50ppm stock solution were put into the ultrasonic bath using a small PTFE bottle. Ultrasonic bath treatment decreased from 1 hour to 15 minutes, as that was enough to fully increase the absorbance Appendix B Figure B.1

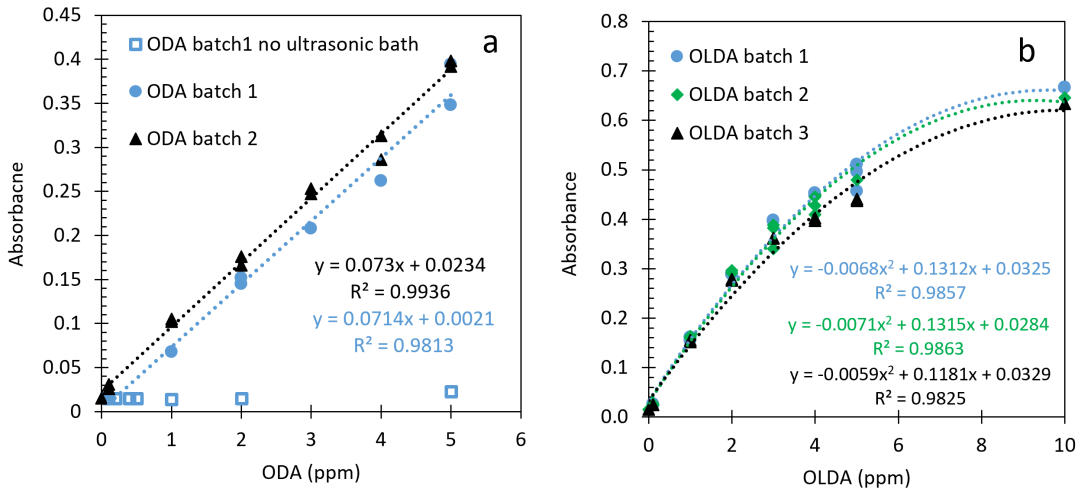

Figure 3.1: a: ODA and b: OLDA, absorbance-concentration plots constructed via the Bengal Rosa dye method.

3.1.3. OLDA preparation

A 1 w/w% OLDA ((Z)-N-9-octadecenyl-propaan-1,3-diamine) solution was supplied by Kurita under product name Cetamine G851 CAS: 7173-62-8. First a 500 ppm solution was made using Milli-Q water and the 1w/w% OLDA solution, after 15 minutes of stirring from the 500

ppm solution a 50 ppm solution was made which was immediately further diluted to 10 ppm. The 10 ppm solution was used to saturate a flask for 24 hours, while the 500 ppm was kept on the mixing plate. As the 50 ppm solution was directly consumed after the preparation, clean volumetric flasks were used. The following day the steps were repeated to obtain the desired 10 ppm OLDA solution in a pre-saturated flask. Again, COD measurements were performed to verify the concentrations. They were within ±10 % range of the calculated COD values. During this study three OLDA batch solutions were prepared. Batches were kept for a max of 3 weeks and remained permanently stirred throughout this period.

OLDA concentration calibration curve

The OLDA calibration curve was obtained in a similar fashion as the ODA calibration curve, see subsection 3.1.2. A wavelength of 560nm was used. However, the OLDA solution was not put in the ultrasonic bath prior to the calibration, as it did not show any signs of possible michelle formation. Figure 3.1b gives the calibration curves for the three prepared OLDA (batch) solutions.

3.2. Immersion corrosion experiments setup

Figure 3.2 shows the schematic of the setup for the immersion corrosion tests. The setup was used for the immersion corrosion test to form the magnetite layer and for the re-immersion FAC tests to test the layers. The setup consisted of a high temperature high pressure autoclave lined with PTFE (Berghof BR-500) containing the test solution, heater, temperature controller and thermo couple (Berghof BTC-3000), and nitrogen purging and pressurising gas. The custum made PTFE coupon holder was shaped in the form of a cylinder containing holes for the coupons to fit in.

For the magnetite layer formation immersion corrosion tests a high pressure pump (Gilson 305 Master pump) with pressure regulating manometric module was used to add the ammonia to the test solution after is has been sparged by nitrogen. This to avoid ammonia stripping. A balance was used to verify the ammonia addition.

For the FAC re-immersion test the overhead stirrer (Berghof BRM-1) was used to generate fluid flow conditions. See Appendix C for a photo of the setup.

3.3. Test environments

A total of four 48 hours immersion corrosion tests were performed, to test 4 solution chemestries on the formation of a magnetite layer on the C1010 coupons. Four coupons were used per immersion corrosion test, two of them were used for oxide analysis afterwards and two were used for the re-immersion corrosion test. Thus, a total of four 48 hours re-immersion tests were performed as well. The re-immersion tests simulated acidic corrosion. Table 3.2 provides an overview of the test solutions and conditions used. Runs 1 to 4 mark the different initial test solutions. X.1 stands for an immersion test and X.2 for a re-immersion test. Subsection 3.3.1 discusses how the chemical parameters of these solutions were derived and subsection 3.3.2 discusses how the hydrodynamic parameters were derived.

3.3.1. Test solutions verification

Despite multiple coupons being immersed at once during a immersion corrosion test, no duplicate runs were performed. Therefore one should guarantee the consistency of the test conditions and setup.

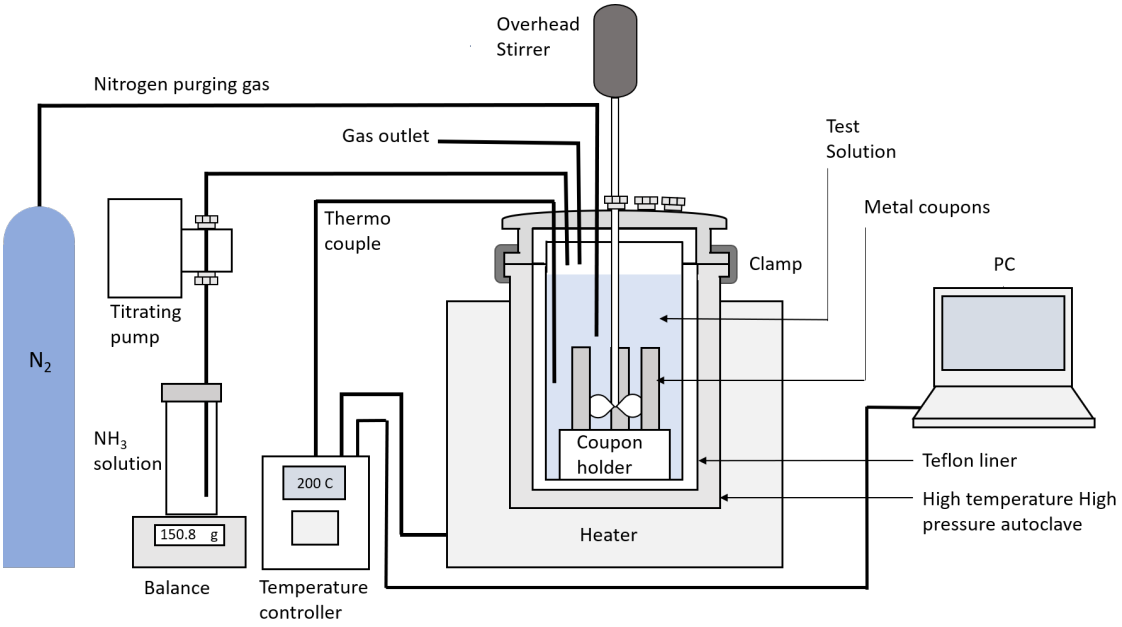

Figure 3.2: Schematic representation of the test setup for the immersion and re-immersion corrosion experiments.

Ammonia dosing verification
To verify an alkaline pH of 9 to 9.5 ammonia dosing tests were performed. 5.5ml of 0.025% of NH_4OH was dosed by the high pressure high precision pump into the autoclave. The autoclave contained a PTFE liner filled with 300ml Milli-Q water. The expected pH was calculated to be 9.5 but pH measurements of the Milli-Q water after the addition gave a pH of 9.12 ±0.02.

Acetic dosing verification
To ensure consistency of the acidic conditions during all re-immersion tests a sample of the test solution was taken to measure the pH after the dosing of acetic acid. Test samples for the re-immersion test solutions were prepared accordingly to allow for a sample to be extracted. The pH of the sample was measured at 25°C while being sparged with nitrogen.

Oxygen concentration
To ensure reducing conditions within the system two sparging tests were performed to determine the required sparging time and resulting dissolved oxygen concentration. Sparging the PTFE liner, containing 294.5ml Milli-Q water, using nitrogen for 1 hour and measuring the DO levels continuously (using a DO meter) a stable range between 36 and 39 ppb oxygen was reached. A similar sparging test for the ammonia solution was performed too. The reason: this solution was dosed separately into the autoclave after it has been sparged with nitrogen. The solution reached a stable DO content of approx. 15ppm after 1 hour.

3.3.2. Calculating hydrodynamic conditions
Ensuring flow-accelerated conditions during the re-immersion test, flow velocities were calculated and measured together with Reynolds number, and the shear stress on the coupons.

Fluid flow velocity
The first of two flow velocities depicted in Table 3.2 was calculated based on the spherical speed of the mixer using Equation 3.1.

$$U = 2 \cdot \pi r * n \tag{3.1}$$

Table 3.2: Overview test conditions immersion and re-immersion experiments. (a) determined via ammonia dosing test and (b) via pH measurement prior to experiment for both refer to subsection 3.3.1. (c) calculated with angular momentum of mixer (1st value) and using PIVlab (2nd value), (d) determined using PIVlab, for both see subsection 3.3.2. * Measured FFA content prior to the experiment.

Experiment		Chemistry condition Chemical (ppm)	pH25C (b)	Temp (Celsius)	rpm (-)	Velocity(c) (m/s)	Shear (d) stress (mPa)
Run 1	Run 1.1	Neutral	6.5	250 ±5	0	0	0
	Run 1.2	Acetic acid: 0.08	6.0	150 ±3	1000	1.9 0.5 - 0.7	178
Run 2	Run 2.1	NH3: 2.00 ODA: 2.11*	9.12±0.02 (a)	230 ±2	0	0	0
	Run 2.2	Acitic acid: 0.08	5.8	150 ±3	1000	1.9 0.5 - 0.7	178
Run 3	Run 3.1	NH3: 2.00 OLDA: 2.44*	9.12±0.02 (a)	230 ±2	0	0	0
	Run 3.2	Acitic acid: 0.08	6.1	150 ±3	1000	1.9 0.5 - 0.7	178
Run 4	Run 4.1	NH3: 2.00	9.12±0.02 (a)	230 ±2	0	0	0
	Run 4.2	Acetic acid: 0.08	6.2	150 ±3	1000	1.9 0.5 - 0.7	178

Where: U is the rotational speed (m/s). r is the radius of the mixing propeller (m) and n is the rotational speed (1/s). The second depicted flow velocity in Table 3.2 is determined via analysis of flow footage using PIVlab (Particle image velocity lab). This software was used to determine hydrodynamics in a similar (rotating cage) setup by Alvarado et al. [1]. A transparent liner was made. Coupons were placed into the autoclave and footage was shot using a 240.5 fps camera while the solution was mixed at 1000rpm. Provided with the frame rate and a reference scale the software can calculate flow patterns and corresponding speeds using the footage [104]. Flow speeds near the base of the coupons were chosen. See Figure 3.3, from left to right: the footage used, the flow velocity vectors, and the flow velocity gradient.

Reynolds number

For this setup the Reynolds number common for circular tubing was replaced with the mixing Reynolds number and calculated using Equation 3.2.

$$\mathrm{Re} = \frac{\mathrm{d} \cdot (\pi \cdot \mathrm{d} \cdot \mathrm{n})}{\nu} \propto \frac{\mathrm{d}^2 \cdot \mathrm{n}}{\nu} \tag{3.2}$$

Where: Re is the Reynolds (mixing) number (dimensionless), d is the impeller or mixing propeller radius (m), n the rotational speed (1/s) and ν the kinematic viscosity (m^2/s). Latter derived by dividing the dynamic viscosity (Ns/m^2) of water with the density of water (kg/m^3) both at at 150 °C. The Reynolds mixing number at 150 °C was calculated to be 109,000. Re as a parameter in industrial plants can often reach values of 100,000 or 1,000,000 (Derek H. Lister, University of New Brunswick Canada, personal mail correspondence, 18-12-2020).

Shear stress

Shear stress was derived using the relation of shear rate to shear stress with the dynamic viscosity, Equation 3.3. The simple shear rate (1/s) derived with PIVlab was used as input for

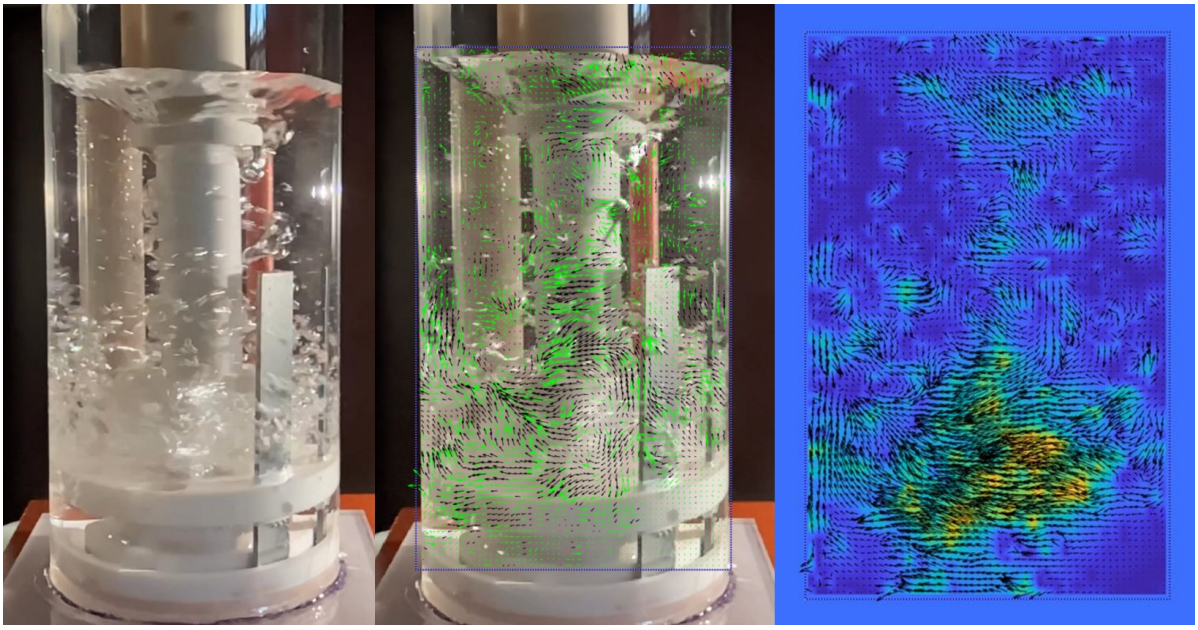

Figure 3.3: Left to right: PIVLab input footage, overlapped flow velocity vectors and flow velocity gradient.

the shear rate.

$$\tau = \mu \cdot \gamma \tag{3.3}$$

Where: τ is the shear stress (Pa), μ is the dynamic viscosity (Pa·s) and γ the shear rate (1/s). Given that a range of simple shear rate was obtained from PIVLab the calculated shear stress ranges from 0.5 to 0.7 mPa.

3.4. Procedure immersion corrosion experiments

Sections 3.1 to subsection 3.3.1 provided information on the solution and coupon preparation, immersion apparatus and the test conditions. This section will provide the step by step procedure of the immersion and re-immersion test. A re-immersion test was conducted a week after an immersion test to reduce storage time.

3.4.1. Layer formation immersion tests

The following will include the procedure for the corrosion immersion tests, during which magnetite layers were formed, denoted with run 1.1, 2.1, 3.1 and 4.1. Four metal coupons were prepared according to section 3.1 and placed within the PTFE coupon holder. The PTFE liner was filled with Milli-Q water and the appropriate FFA stock solution was added to achieve the required test solution chemistry (either 2ppm ODA, or 2ppm OLDA or no FFA addition), according to Table 3.2, volume 350 ml. A sample from the test solution was taken to verify pH and FFA concentration plus measure EC, volume sample 55.5 ml. The coupon holder containing the coupons was placed into the filled PTFE liner and the autoclave was closed sealed and sparged with nitrogen for 1 hour. After sparging a 5.5 ml 0.025% ammonia solution was added to the autoclave via the high temperature high pressure displacement pump. This was done for all immersion tests except for 1.1, the blank chemistry test. The 0.025% ammonia solution was made after injecting 0.25 ml of a 25% NH_4OH solution into a 250ml Milli-Q solution, after it was sparged for 1 hour with nitrogen.

The autoclave was pressurised to 20 bars using nitrogen and heated to 230 °C. Only the blank immersion test was heated to 250 °C, due to PTFE deformation risks other immersion test were performed at a lower temperature. The system was left for 48 hours after which the autoclave was cooled and depressurised. A sample from the test solution was taken to measure, FFA and iron concentration, pH and EC. Coupons were removed, dried, weighed (to the nearest 0.1 mg), photographed and stored according to section 3.1. Two out of four coupons were used for oxide and coupon analysis, section 3.5, while the remaining coupons were used for the re-immersion corrosion tests. The autoclave and PTFE parts were cleaned using 2-Propanol solution followed by Milli-Q water and dried with nitrogen to remove any FFA present in the system.

3.4.2. FAC re-immersion tests

The following will include the procedure for the corrosion re-immersion tests, used to test the magnetite layers formed during the immersion tests, denoted with 1.2, 2.2, 3.2, and 4.2. The two stored coupons from the respective preceding immersion experiment were placed within the PTFE coupon holder. The Teflon liner was filled with 350 ml Milli-Q water and 27 micro-litre of 0.1 v/v% of acetic acid was added (to achieve a pH_{25C} of 6) and placed into the autoclave. A sample of 50ml was taken to verify pH, detect any remaining FFA and measure EC. The coupon holder containing the coupons was placed into the filled PTFE liner and the autoclave was closed sealed and sparged with nitrogen for 1 hour.

The autoclave was pressurised to 20 bars using nitrogen and heated to 150 °C. The mixer was set to a speed of 1000rpm. The system was left for 48 hours after this the autoclave was cooled and depressurised. A sample from the test solution was taken to measure FFA, iron concentration, pH and EC. Coupons were removed, dried, weighed (to the nearest 0.1 mg), photographed and stored according to section 3.1. The metal coupons were both used for oxide and coupon analysis, refer to section 3.5.

3.5. Oxide layer analysis

As mentioned during the previous section 3.4 two out of four coupons from the immersion corrosion test and both the coupons from the re-immersion test were used for oxide and coupon analysis. Both coupons were photographed, see subsection 3.5.1. One coupon was used for XRD subsection 3.5.2, contact angle subsection 3.5.3, digital microscopy subsection 3.5.5, and mass loss measurements subsection 3.5.6. The remaining coupon was solely used for SEM subsection 3.5.4. An overview of the performed analyses after the corrosion tests combined with the information these methods can provide, and what it might indicate regarding corrosion and the oxide layer can be seen in Table 3.3.

Table 3.3: Overview oxide and coupon analysis performed after the immersion and re-immersion corrosion tests

Analysis	Information	What is might indicate	Performed
Photography	-Color -Shining of metal	-Type of oxide formed -Density of magnetite layer	Water-Lab Faculty of Civil Engineering
XRD	-Crystalline structure -Ratio of constituents	-Type of oxide formed -Percentage of oxide formed	3ME Factulty of Mechanical Engineering
Contact angle	-Hydrophobicity	-Presence of FFA	3ME Factulty of Mechanical Engineering
SEM + EDS	-Detailed surface imagery -Size magnetite crystals -Elements present -Thickness layer	-Growth and erosion of porous top layer -Type of layers present - Presence or absence of an oxide layer -Corrosion rate	DASML Faculty of Aerospace Engineering
Digital Microscopy	- oxide layer particle erosion	- Strenght of oxide layer	Water-Lab Faculty of Civil Engineering
Weight loss	-Change in weight of coupon -Weight of oxide layer	-Corrosion rate -Thickness layer	Water-Lab Faculty of Civil Engineering

3.5.1. Photography

Photographs were taken of both sides of the coupons after the immersion and re-immersion test. Coupons were first dried using a tissue and afterwards placed on top of a microscope slide. Pictures were taken with a white background.

3.5.2. X-Ray diffraction

Coupons were transported to the XRD laboratory facility using the vacuum bottles described in section 3.1. XRD measurements were taken at the day of issuing the sample. The instrument used: Bruker D8 Advance diffractometer Bragg-Brentano geometry with graphite monochromator and Vantec position sensitive detector. Measurement: Coupled θ -2θ scan 20° - 110°, step size 0.030° 2θ, counting time per step 2 s. Data evaluation was performed with the Bruker software Diffrac Suite.EVA version 5.2.

3.5.3. Contact angle measurements

Contact angle measurements were performed in order to indicate the presence of an ODA and OLDA layer on the coupons. Contact angles were measured with a tensiometer (Theta lite optical). This device was equipped with full OneAttension software for determination of the contact angle by the sessile/raising drop method with automatic base line detection. The device provided a continuous contact angle reading after the release of the 3.0 µL drop. Milli-Q water was used to produce the drops. For all measurements, the angle after 10 seconds of first contact was recorded. Contact angle measurements were taken at different parts of the coupon. The parts in question are depicted in Figure 3.4. Between measurements, drops were removed by softly wiping them with a tissue. This was to avoid corrosion.

In addition reference contact angles were measured, using fresh C1010 coupons and 4ppm ODA, and OLDA solutions. The C1010 coupons were removed from their packaging and rinsed with acetone plus dried in air prior to be immersed into either a 4ppm ODA or OLDA solution. Immersion was at room temperature for one hour. Afterwards these coupons were dried in air and nitrogen before measuring the contact angles.

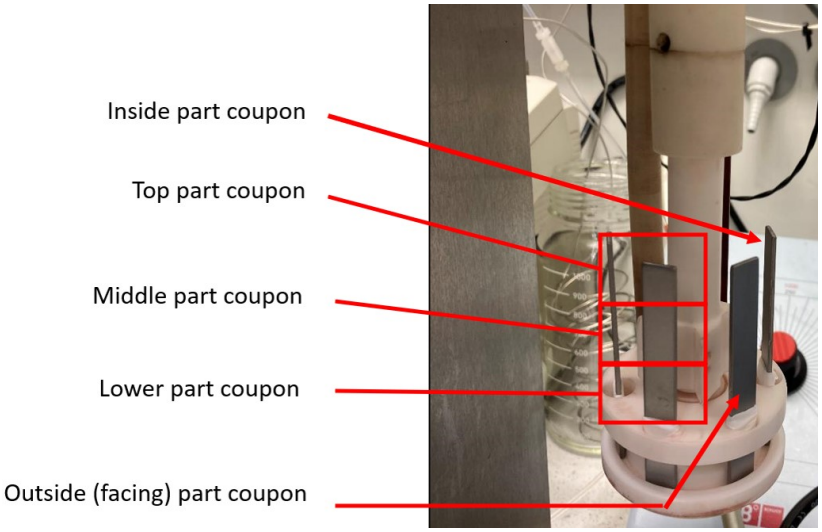

Figure 3.4: Different parts of the coupons distinguished for the contact angle measurement.

3.5.4. SEM

SEM surface and cross section images were taken after the immersion and re-immersion test to determine, surface layer thickness, and surface (layer) characteristics. Per test run one coupon was used for the SEM analysis. Coupons were stored according to section 3.1 until the SEM analysis. Coupons were transported to the SEM laboratory facility using the vacuum bottles described in section 3.1. At the facility the coupons were temporarily stored in a silica containing desiccator until the sample was prepared for SEM surface images and SEM cross-section images.

Surface imagery

SEM surface images were taken at the lower half of the coupon. In case of coupons from the re-immersion tests the images were taken at the inward facing side. See Figure 3.4 for the different identified coupon parts. The coupons were gold coated for extra conductivity, surface images were taken at a magnification of 1000, 2000, 5000 and 10,000 using a JEOL Electron Mircroscope LF7M06.

Cross-section imagery and EDS

Cross sections of the coupons were prepared for the cross-section SEM pictures. Coupons were embedded in Technovit 4071 prior to being cut. After cutting the samples were polished using sandpaper. Sandpaper was used from coarse to fine grained, FEPA: (Federation of European Producers of Abrasives) P180, P320, P1000, P2400 and P4000. Afterwards the sample was coated with gold to improve conduction. EDS was used to verify the presence of an oxide layer by looking at concentrated elemental oxygen. The thickness of the magnetite layer along the surface was determined using Image-J [90], by measuring the thickness of the magnetite layer on the SEM images. The thickness of the EDS determined elemental oxygen layer was measured via Image-J as well, as can be seen in Figure 3.5.

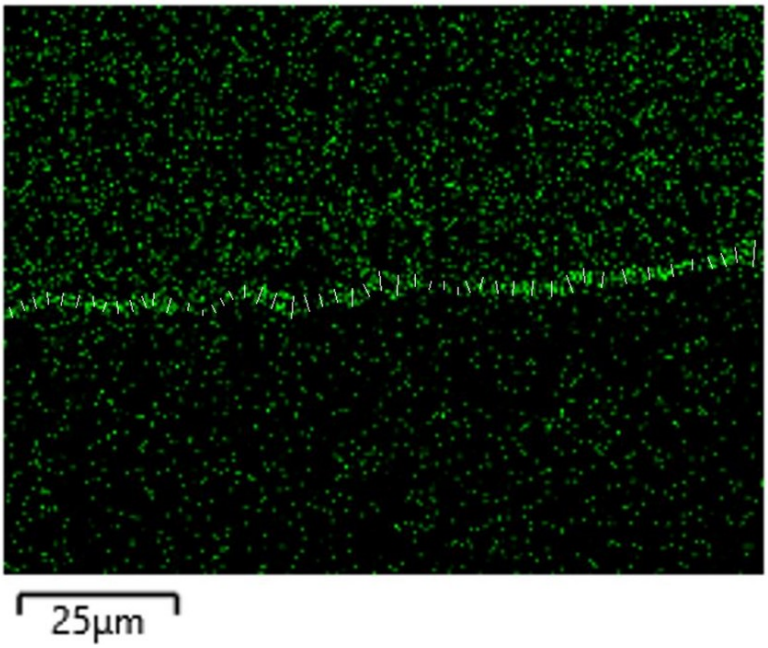

Figure 3.5: Determination of oxide thickness by Image-J measurement of the elemental oxygen layer. White lines drawn via image-J to determine the thickness of the layer.

Corrosion rate derived from oxide thickness

The oxide thickness was used as input to determine the corrosion rate, called: the 'oxide thickness derived corrosion rate', or 'SEM determined corrosion rate'. One standard way to determine the corrosion rate is to first obtain the weight loss of the specimen during the immersion test and calculate the corrosion rate according to Equation 2.18. This equation for corrosion rate was still used, only now the loss in weight was not directly measured after removal of the oxide layer (as was the case in subsection 3.5.6) but derived from the oxide volume. The weight loss was determined via the following equation:

$$W = (M_{clean-coupon} - M_{coupon+oxide}) + (A_{coupon} \cdot \frac{h_{oxide}}{10000} \cdot \rho_{oxide}) \tag{3.4}$$

Where: W is the mass loss of the coupon over the immersion test (mg), $M_{clean-coupon}$ is the mass of the clean coupon prior to immersion. $M_{coupon+oxide}$ is the mass of the coupon including the oxide after the immersion test. A_{coupon} is the surface of the coupon (cm^2), h_{oxide} is the thickness of the oxide layer (µm) and ρ_{oxide} is the density of magnetite (mg/cm^3), a density of 5170 mg/cm^3 was used.

3.5.5. Digital microscopy

The digital microscope was used to study the coupon/oxide surface at a magnification of 100, 200, and 400. For this a Keyence VHX Digital microscope with VH-Z100UR/W/T lens was used. The whole surface was examined for any signs of spalling erosion, especially near the edges of the coupon. A fresh coupon was also examined, serving as an optical reference.

3.5.6. Mass loss measurement

The mass of the coupons were measured before immersion. After immersion the visible oxide layer was chemically removed. This implied the removal of the oxide material from the surface of the coupon by dissolution in a chemical solution of 5% w/w HCl (hydrochloric acid) at an temperature of 50 degrees Celsius. A corrosion inhibitor, Lithsolvent 620, was added to the

chemical solution too, to minimise the removal of the sound metal.

Iron ion content samples were taken at intervals of 3 to 5 minutes during the chemical dissolution to verify the oxide dissolution process. Coupons were removed from the chemical solution once dissolved iron contents remained stable, indicating all oxide has dissolved. This method of chemical cleaning is applied to chemically rid boilers of magnetite layers [74] in which normally also HF 1% w/w is applied. After removing a coupon from the chemical cleaning bath it was flushed with ammonia water (pH 9-10) to temporally pacify the material to avoid flash rusting. When flushed the specimen was dried and weighed. The mass loss is given with the following equation.

$$W = (M_{clean-coupon}) - (M_{coupon-oxide-removed}) \tag{3.5}$$

Where: W is the mass loss of the coupon over the immersion test (mg), $M_{clean-coupon}$ is the mass of the clean coupon prior to immersion and $M_{coupon-oxide-removed}$ is the mass of the coupon after the oxide layer has been chemically removed.

Oxide layer thickness derived from mass loss

In the same manner as the 'SEM derived corrosion rate' was determined the mass loss measurement was used to obtain the oxide layer thickness called the 'oxide thickness via weight loss'. Prior to chemically removing the oxide, the coupon was weighed to the nearest 0.1mg. Combined with the weight of the coupon after the removal of the oxide layer the weight of this layer was determined by a simple subtraction to obtain $M_{oxide-layer}$. Assuming a constant oxide thickness, density of magnetite and knowing the surface of the coupon the thickness was derived. The following equation was used to derive the thickness of the oxide.

$$h_{oxide} \cdot 1 * 10^{-4} = \frac{M_{oxide-layer}}{\rho_{oxide} \cdot A_{coupon}} \tag{3.6}$$

Where: h_{oxide} is the thickness of the oxide layer (μm), $M_{oxide-layer}$ is the mass of the oxide (mg), A_{coupon} is the surface of the coupon (cm^2), and ρ_{oxide} is the density of magnetite (mg/cm^3) a density of 5170 mg/cm^3 was used.

3.6. Adsorption experiments

In order to determine the adsorption behaviour of FFA to magnetite, adsorption experiments were performed. The adsorption of ODA and OLDA onto suspensions of colloidal magnetite particles was determined by measuring the amount of FFA removed from the solution which was in contact with the oxide particles. section 3.1 provides more information on the film forming amines used and the preparation of the FFA stock solutions. The magnetite used was reagent grade Iron(II,III) oxide 99.99 %, purchased from of Sigma-Aldrich, referred to as Mag99, for more specifications see subsection 3.8.1. A measured amount of 1.0 gram of magnetite was added to solutions containing 0.01 ionic strength KNO_3 and a concentration of 2ppm FFA, the total volume of the solution being 100ml. pH was adjusted prior to FFA addition using 0.1N KOH. The solution was kept in glass bottles that allowed for sparging and subtraction of samples via rubber tubes, keeping the solution anoxic. The suspension was sparged with nitrogen for 15 minutes and kept on the shaker for 24 hours. During this time samples were taken at regular intervals, after a 5ml sample was taken the solution was again sparged with nitrogen for 15 minutes. FFA concentrations were measured using the Bengal Rosa method, refer to section 3.1. An overview of the performed adsorption experiments can be found in Table 3.4

Table 3.4: Overview of the performed FFA to magnetite adsorption experiments

pH_{25C}	FFA	Magnetite
7	ODA	Mag99
7	OLDA	Mag99
11	ODA	Mag99
11	OLDA	Mag99
11	-	Mag99

The adsorption experiments provided input for the potentiometric titrations of FFA containing solutions. First of all to determine adsorption equilibrium time prior to the titrations, and secondly to account for the effect of unadsorbed FFA.

3.7. Potentiometric titration runs

The start of this chapter stated that the potentiometric titrations were carried out to obtain knowledge on the influence of FFAs on surface charge. Section 2.7 provides background on the potentiometric titration method, how it determines the surface charge and how among others the pH_{pzc} can be obtained. Multiple titration runs were performed to:

- Determine the most suitable magnetite oxide powder for the titrations.
- Obtain the surface charge and pH_{pzc} of magnetite at room temperature and elevated temperature, serving as reference.
- Obtain the surface charge and pH_{pzc} of magnetite with FFA present at room temperature and elevated temperature.

The types and number of runs performed at 25 °C, and 150 °C are listed in Table 3.5. Appendix D provides a detailed overview of all individual runs performed.

3.8. Magnetite and solution preparation

This section discusses the studied magnetite powders, see subsection 3.8.1, together with the titration test solution preparation, see subsection 3.8.2.

Table 3.5: Overview of the potentiometric titrations performed

Oxide	FFA	Ionic Strenght (M)	Method	Titrant	Runs	Temp °C
Blank	-	0.01	Quick	acid	9, 35	25
		0.1	Quick		1,2,57	
		0.01	Standard	base	12, 23, 31,51	
				acid	13,	
M95	-	0.01	Quick	acid	18	
		0.1	Quick		3,4,5	
		0.01	Standard	base	16	
				acid	17	
Pur	-	0.01	Quick		44	
		0.01	Standard	base	14	
				acid	15	
M99	-	0.01	Quick	acid	36, 48, 59	
		0.1	Quick		38	
		0.01	Standard	base	22, 30	
				acid	24, 32	
	ODA	0.01	Quick	acid	43,46, 63	
		0.1	Quick		65,66	
		0.01	Standard	base	40	
				acid	41	
	OLDA	0.01	Quick	acid	49,60,61	
		0.1	Quick		55,56	
		0.01	Standard	base	50	
				acid	52	
Blank	-	0.01	Quick	acid	10,11,34	150
M99	-	0.01	Quick	acid	28,37	
	OLDA	0.01	Quick	acid	53,54	

3.8.1. Magnetite

Three types of magnetite have been used in this study. Magnetite (Iron (II, III) oxide: CAS 1317-61-9 Lot#: MKCD8301 which is a reagent-grade iron-oxide product purchased from Sigma-Aldrich, with provided purity of 95%, hereafter referred to as 'Mag95'. Puratronic Alfa Aesar (Iron (II, III) reagent-grade iron-oxide purity of 99.997% purchased from Alfa Aesar, hereafter referred to as 'Pur'. The third magnetite used is Iron(II,III) oxide 99.99 % reagent grade, Lot#:0000089716, CAS Number 1317-61-9, a product purchased from Sigma-Aldrich, hereafter called 'Mag99'. All magnetite powder was stored inside a silica containing vacuum closet at 0.04 MPa, packed in glass bottles closed with rubber stoppers and sealed by a crimper applied aluminium cap. The rubber stopper allowed for vacuuming the bottle and subsequent nitrogen addition, both via a syringe. When magnetite powder was needed a bottle was opened by breaking the aluminium seal, after extraction of the magnetite the bottles were sealed, vacuumed and stored again. XRD analysis was performed on the magnetite powders to confirm the manufacturers reported purity and impact of the way of storage, an overview of the compositions and w% is given in Table 3.6. See Appendix E for the XRD patterns plus measurement settings.

According to the XRD verification, both Mag99 and the Puratronic magnetite are equally pure, followed by Mag95. Moreover, Mag95 appears to have more other compounds compared to Mag99 and Pur which only show traces of hematite. The storage method of the

magnetite powder did not seem to have a detectable effect.

Table 3.6: XRD verification of purchased reagent grade magnetite powders, after arrival and 2-3 months of storage. XRD measurement performed by R. Hendrikx

Magnetite	After purchase arrival			After 2-3 months storage		
	Compound		Wt%	Compound		Wt%
M95	Magnetite	Fe3O4	98 ±1	Magnetite	Fe3O4	98 ±1
	Hematite	Fe2O4	2 ±1	Hematite	Fe2O4	2 ±1
	Akaganeite-Q	Fe+3O(OH)	<1	Goethite	FeO(OH)	<1
	Goethite	FeO(OH)	<1			
Pur	-	-	-	Magnetite	Fe3O4	99 ±1
				Hematite	Fe2O3	1 ±1
M99	Magnetite	Fe3O4	99 ±1	Magnetite	Fe3O4	99 ±1
	Hematite	Fe2O3	1 ±1	Iron	Fe	<1

Brunauer–Emmett–Teller (BET) analysis was performed to determine the specific surface area of the magnetite. The measurement was performed at and by, Delft Solids Solutions. All three commercial magnetite products were examined. Table 3.7 provides the measured surface area per gram of the purchased magnetite powders. These values served as input for the surface charge density calculations.

Table 3.7: The BET specific surface areas of the three purchased magnetite iron-oxides. BET performed by Delft Solid Solutions [28]

Sample	Sbet m2/g	Total analytical error m2/g
Mag95	7.16	0.33
Pur	3.77	0.1
Mag99	2.15	0.17

3.8.2. Solution preparation

All the solutions were prepared from Milli-Q water and from reagent grade chemicals. The electrolyte solution was prepared using potassium nitrate KNO_3, 99% (Alfa Aesar) Lot# 10215744 CAS: 7757-79-1. The acid used for titrations or to make a diluted titrant was nitric acid HNO_3, 0.1N Lot# 61800686 CAS: 7697-37-2. The base used for titrations or to make a diluted titrant was potassium hydroxide KOH, 0.1N Lot# 61801075 CAS: 1310-58-3. Solutions were sparged using nitrogen with a > 99.999 vol% purity with traces of O_2 5 vpm. The film forming amines, ODA and OLDA, used for this study are described in section 3.1, this section also covers the FFA stock solution preparation.

3.9. Room temperature pH titration apparatus

The low temperature potentiometric titrations, at 25°C were carried out in glass bottles within a heat controlled bath on top of a heater with magnetic stirring element (IKA C-MAG HS7) and temperature feedback sensor (IKA ETS-D5), thermo couple. Temperature of the heat bath was controlled and maintained at 25 ±1 °C. pH was measured via a standard portable pH reader and SenTix 940 probe. The inbuilt temperature sensor of the pH-probe was used to verify as well as store temperature data. Test solutions were magnetically stirred to mix the titrant and keep the magnetite suspended. A schematic overview of the setup is given in Figure 3.6. See Appendix C for a photo of the setup.

Potentiometric titrations were performed using 250ml bottles containing a test solution of 100ml. Exception to this are runs 1 to 7, and 9, which were performed in a 500ml sized bottle with the thermo couple directly emerged into the 350ml test solution, refer to Appendix D. The 250ml bottles caps contained septum through which the probe, nitrogen sparging needle were inserted to the test solution. Furthermore, the septum contained a gas outlet needle and a titrant insertion point. Titrant was added via a micropipette.

The 500 ml bottles were sealed off using parafilm to maintain an anoxic environment. The titrant was added via a side inlet which had to be opened up for the micropipette. Because of this titrant addition and use of parafilm instead of a septum, the dissolved oxygen concentrations during a titration run, run 4 were measured to verify anoxic conditions, see Appendix F. Dissolved oxygen concentrations during the run generally remained well below 0.1 mg/L which is below the anoxic oxygen concentration of 0.5 mg/L [66].

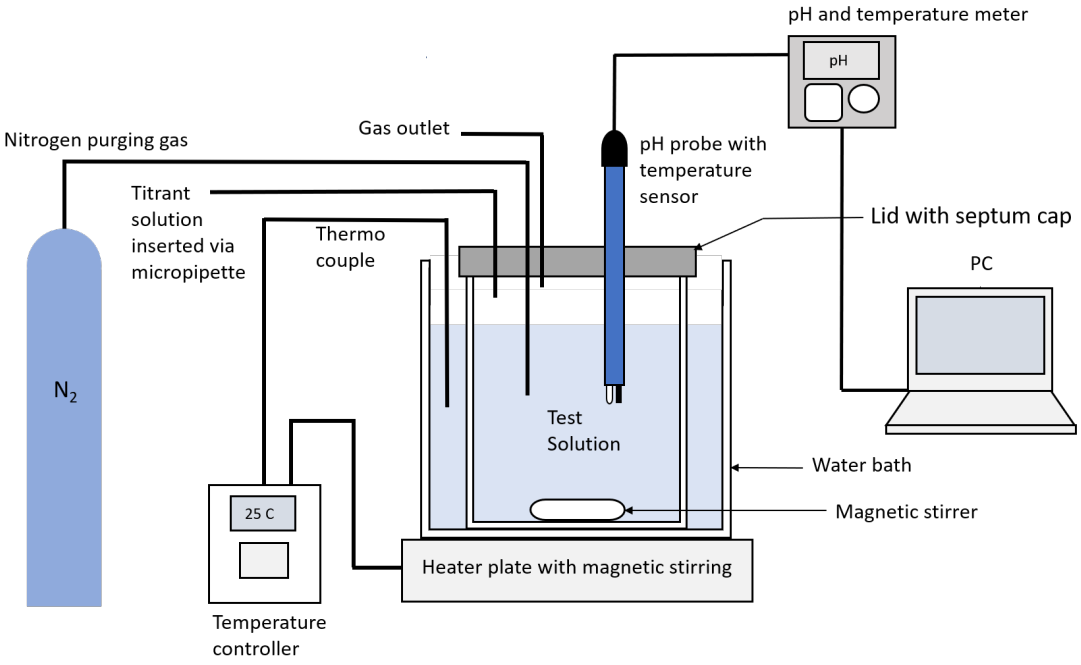

Figure 3.6: Schematic overview of the 250ml bottle setup for potentiometric titrations at 25 °C.

3.10. High temperature pH titration apparatus

All high temperature (150 °C) potentiometric experiments were carried out in a high pressure high temperature (HPHT) autoclave and with a PTFE liner. Figure 3.7 is a detailed schematic overview of the setup. Aliquots of titrant solution were pumped via a Gilson 305 Master pump into the autoclave (Berghof BR-500) containing the test solution. The pump has a manometric module to regulate pressure during pumping. pH measurements were performed by a high temperature and pressure resistant ZrO_2 based pH probe and a Ag/AgCl reference probe (Corr Insturments, LLC, USA), both connected to a dual-input analyser (Rosemount Emerson). The test solution was brought and maintained at the desired temperature by a temperature controller (Berghof BTC-3000), thermo couple and heater. An overhead stirrer (Berghof BRM-1) ensured conditions in which the magnetite particles did not settle. Prior to each experiment nitrogen gas (99.999 vol% purity) was used to purge the solution and to pre-pressurise the autoclave to 20 bars. The mV readings were send to a PC. A balance was used to verify the

titrant addition. Samples of the test solution were extracted directly after every titration via a liquid sampling point. See Appendix C for a photo of the setup.

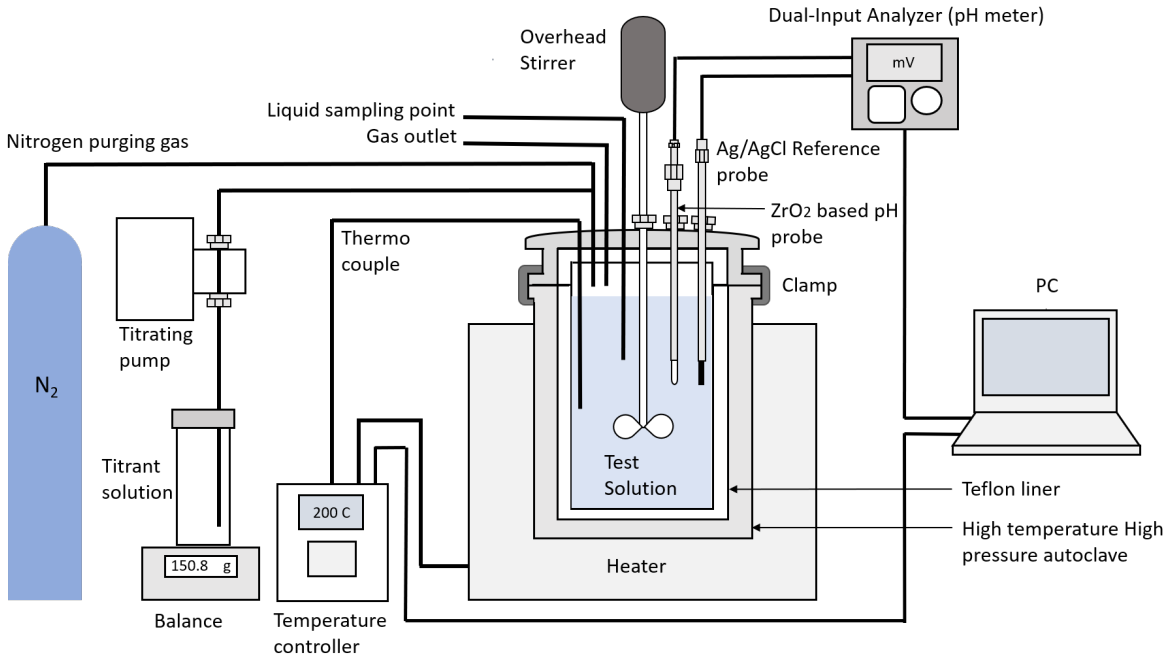

Figure 3.7: Schematic of the experimental apparatus for the high temperature potentiometric titrations.

3.10.1. High temperature pH and reference electrode calibration

This study used a high temperature high pressure resistant ZrO_2 based pH probe and a Ag/AgCl reference electrode which were coupled together via a dual input analyser. In order to correlate the measured potential to a pH value a calibration curve was performed. Prior to the start of the potentiometric titration runs a calibration using 4 stock solutions was performed. Besides the initial calibration, 3 re-calibrations have been performed to update the calibration, verify the probes and to detect any drift. The initial calibration (calibration 1) was performed at the operating temperature of 150 °C using the following high temperature pH-stock solutions: NaOH $1 * 10^{-3}$ mol/L, NaOH $1 * 10^{-4}$ mol/L, H_2SO_4 $5 * 10^{-4}$ mol/L and H_2SO_4 $5 * 10^{-5}$ mol/L. These stock solutions were also used by Zebardast et al. [123] to calibrate a similar probe and reference probe.The slope should show a Nernstian trend, and be close to the theoretical value given by Equation 3.7 with a less than ±15% error (Instruction Manual for high P&T pHRef Q0823, Corrinstruments, LLC, USA). This was not the case for calibration 1.1 and 1.2. An additional calibration (calibration 2) was performed using hydrochloric acid 0.01 mol/kg and disodium tetraborate 0.01 mol/kg as stock solutions, for having a strong buffering capacity (Lietai Yang, Corr Instruments, personal mail communication, 31-07-2020). Calibration 2 was used as the first pH calibration slope. All successive calibrations (3 and 4) were performed using hydrochloric acid and disodium tetraborate. The results of the calibrations are given in Table 3.8, for all titrations a Nernstian trend was observed. The corresponding pH_{150C} of the stock solutions, shown in Table 3.8, were provided by the manufacturer.

$$\text{slope mV per decade} = 1000 \cdot \frac{2.303 \cdot R \cdot T}{F} \tag{3.7}$$

Where: R is the universal gas constant, T the temperature (K), and F is Faraday's constant.

Table 3.8: Overview of the performed calibrations of the HTHP probe and reference probe

	H_2SO_4		NaOH		Theoretical slope (mV/pH)	Measured slope (mV/pH)	Regression coefficient
pH 150C	5*10-4 M 3.22	5*10-5 M 4.07	1*10-4 M 7.6	1*10-3M 8.59			
Calibration 1.1	587 mV	525 mV	252 mV	228 mV	83.80	69.94	0.990
Calibration 1.2	-	-	-	235 mV		69.01	0.986
	HCl		**Disodium tetraborate**		**Theoretical slope**	**Measured slope**	**Regression coefficient**
pH 150C	0.01 M 2.06		0.01 M 8.65		(mV/pH)	(mV/pH)	
Calibration 2	701 mV		205 mV		83.80	75.27	-
Calibration 3.1	697 mV		206 mV			74.51	-
Calibration 3.2	-		215 mV			72.84	-
Calibration 4	696 mV		215 mV			72.99	-

3.11. Proton concentration calibration plots

To calculate the surface charge using the Szekeres and Tombácz method, subsection 2.7.1, proton calibration plots were needed to determine the activity coefficients S_a and S_b used for these calculations. The plots were constructed by plotting the titration data of blank titrations, only electrolyte present. The concentration of added hydroxyl ions (base) negatively on the x-axis and concentration of added hydrogen ions (acid) positively on the x-axis while plotting the measured pH response on the y axis. Thus, having a clear separation between the acidic and basic sides of the titrations. The slopes of the plots correspond to S_a and S_b, for the acidic and basic part respectively.

An additional benefit of these calibrations was that the slope also provided information on the actual response of the pH electrode to the proton and hydroxyl concentrations added by titration. The proton calibrations plots, i.e. probe response, are depicted in Figure 3.8a, for blank titrations performed at 25 °C and Figure 3.8b for blank titrations performed at 150 °C. The derived fits with corresponding slope values are depicted in Table 3.9 and Table 3.10 for blank titrations performed at 25 and 150 respectively.

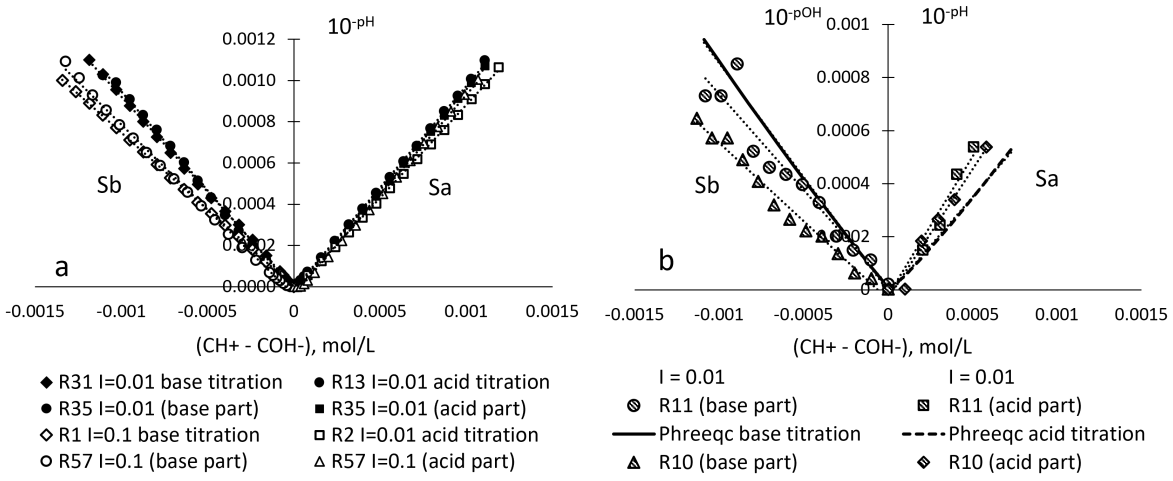

Figure 3.8: Proton concentration calibration plots from a: blank titrations at 25 °C and b: blank titrations at 150 °C, performed at 0.1M and 0.01M KNO_3 electrolyte concentrations.

Table 3.9: Overview of the linear fits to the 25 °C proton calibration data points, with regression coefficient, S_a and S_b values.

Temperature 25 degrees Celsius			
Run	**Linear fit**	**R2**	**Sb**
R31	y = -0.9226x - 2E-06	0.9996	0.9226
R35 (base part)	y = -0.96x -1E-05	0.9987	0.9600
R1	y = -0.7479x - 7E-07	0.9999	0.7479
R57 (base part)	y = -0.8269x -4E-05	0.9978	0.8269
Run	**Linear fit**	**R2**	**Sa**
R13	y = 0.9845x - 1E-05	0.9996	0.9845
R35 (acid part)	y = 0.9731x - 2E-05	0.9998	0.9731
R2	y = 0.9004x - 2E-05	0.9995	0.9004
R57 (acid part)	y = 0.9691x - 4e-05	0.9985	0.9691

Table 3.10: Overview of the linear fits to the 150 °C proton calibration data points, with regression coefficient, S_a and S_b values.

Temperature 150 degrees Celsius			
Run	**Linear fit**	**R2**	**Sb**
R11 (base part)	y = -0.7221 + 1E-05	0.9325	0.7221
R10 (base part)	y = -0.5891x - 4E-05	0.9833	0.5891
PHREEQC base	y = -0.8661x - 1E05	0.9995	0.8661
Run	**Linear fit**	**R2**	**Sa**
R11 (acid part)	y = 1.0467x - 2E-05	0.9681	1.0467
R10 (acid part)	y = 0.9735x - 3E-05	0.9735	0.9735
PHREEQC acid	y = 0.7384x -2E-05	0.9970	0.7384

3.12. Potentiometric titration at room temperature

Two types of experimental methods were applied, the 'standard' method and the 'quick' method. The main difference between the two methods was the starting pH value of the titration and therefore fact that for the batch method 2 runs were needed compared to 1 run for the quick method. The term 'quick' was borrowed from [62]. Firstly, these two methods are described based on the low temperature (25 °C) titrations in this section. Only the 'quick' method was applied for the high temperature (150 °C) titrations, which is explained in the following section, 3.13.

All the runs were conducted at ambient pressure inside a fume hood under constant nitrogen addition. The temperature of the test solution was kept constant at 25 ±1 °C. Test solutions contained 10g/L magnetite, if present 2ppm FFA, and the 100 ml electrolyte. Blank titrations comprised of electrolyte only. The electrolyte, Milli-Q with KNO_3, ionic strengths used were 0.1 and 0.01 equal to 0.1M and 0.01M KNO_3, respectively. Ionic strength definition used was obtained from Solomon [95]. Aliquot of acid (0.1N HNO_3) or base (0.1N KOH) were added to the solution, per step: 0.08 mmol per litre of test solution was added. The pH probe used was calibrated before each run using standard commercial pH stock solutions (pH 4.01, pH 7.00

and pH 10.01) and in a later stadium using 5 pH stock solutions (pH 1.68, 4.01, 6,87, 9.11 and 12.45).

Standard titration method

For the standard titration method the equilibrium time, time before addition of the titrant, was about 15 minutes for blank titrations and 30 min or until pH was stable (less than 0.01 change per minute) for runs with magnetite dispersed. All the titrations were started from a neutral pH, meaning no pre-addition of an acid or base to control the pH. Between each titrant addition step a max equilibrium time of 4 to 5 minutes was given or until the pH reading was stable.

Quick titration method

All the quick titrations started off at a pH_{25C} of 11.000 ±0.010. An alkaline starting pH was chosen, since other authors mentioned a higher solubility of magnetite in the acidic region [59, 123]. First the electrolyte was sparged using nitrogen, for a minimum of 15 minutes, before anything was added to the solution. A fixed amount of 1.12ml base (0.1N KOH) was added to the 100ml electrolyte to reach the desired pH of 11. Once the pH reading was stable the magnetite was added or acid (0.1N HNO_3) titrant addition directly, in case of a blank titration. The equilibrium time after addition of the magnetite into the test solution was 15 minutes or until the pH reading was stable within 0.01 pH per minute.

3.13. Potentiometric titration at high temperature

The runs were conducted at a pressure of 20 bars inside the HTHP autoclave. The temperature of the test solution was kept constant at 150 ±3 °C. The solution was not continuously sparged with nitrogen, only before the run. After the sparging period the autoclave was pressurised using the same nitrogen source. Test solutions contained 15g/L magnetite, when present 3 ppm FFA, and the electrolyte. Blank test solutions only contain the electrolyte. The electrolyte, KNO_3, solution ionic strengths used was 0.01 equal to 0.01M KNO_3. The test solution volume within the autoclave was 250ml. After reaching the desired temperature the solution was allowed to equilibrate for 2 hours. A precise amount of acid (0.02N HNO3) or base (0.02N KOH) was added step wise, per step 0.096 mmol per litre of test solution was added. Meaning a step size of 1.2ml for the 250 ml test solution. The same aliquots of titrant solutions were titrated into the blank solution. Generally four to five minutes of equilibrium time was taken before the next aliquot addition, or when the mV reading was stable (less than 1mV per minute). The concentration of acid and base titrants were lower to allow for addition of bigger aliquots, making the displacement pump more reliable. During the high temperature titration runs the acid titrant was continuously sparged with nitrogen.

For runs performed that started from pH_{25C} 11. The PTFE liner containing the electrolyte and FFA, when present, was first sparged for 30 minutes before the pH was adjusted to pH_{25C} 11. 2.7ml of KOH was used to adjust the pH. During pH adjustment the electrolyte was kept at 25 °C using a heat bath and heating plate. A low temperature pH probe, calibrated with standard pH stock solutions, was used to verify the pH adjustment. To ensure an anoxic environment during the adjustment of pH the Teflon liner was covered with parafilm, only allowing the pH meter, nitrogen and base (0.1 KOH) to enter the solution. For blank titrations the pH adjusted solution was placed directly inside the HTHP autoclave. For solutions containing magnetite, the respective amount was dosed to the pH adjusted solution and sparging continued for another 15 minutes before placing the PTFE liner into the autoclave. The top compartment of the autoclave was sparged for 30 min prior to pressurising.

3.14. Post titration analysis

After potentiometric runs containing magnetite samples were taken for the following measurements: dissolved iron content, subsection 3.14.1, particle size distribution (PSD) and particle size via digital microscopy, subsection 3.14.2. Samples were taken right after the run when the magnetite was still dispersed due to mixing, in case of the high temperature experiments samples were taken after the autoclave had cooled down and was depressurised. The samples for the dissolved iron concentration measurements were filtered using 0.45 µm filters. All samples from acid titrations were neutralised using KOH base, to prevent any further dissolution of magnetite.

3.14.1. Dissolved iron measurement

After each titration, containing dispersed magnetite, a sample was taken to measure dissolved iron. This to account for possible effects on the surface charge calculation due to proton consumption of dissolving magnetite (releasing Fe^{2+} in the process). As explained in subsection 2.7.3. Dissolved iron measurements were performed using a spectroquant (Merck Nova 60) with spectroquant iron test (limits: 0.010 - 5.00 mg/L Fe).

3.14.2. Magnetite colloid size measurement

Two methods have been used to determine the colloid size after the titrations, to see whether colloidal size remained constant and therefore the surface area. This was to ensure consistency of the surface charge calculations. Moreover, the particle size measurements were performed as means to determine the FFA effect on magnetite particle size.

Particle Size Distribution

Magnetite particle size was measured using the particle size distribution (Microtrac Bluewave), Milli-Q water was used as flow solution, and the standard operating procedure (SOP) was set to iron-oxide. The Microtrac Flex software was used to calculate/determine the particle sizes.

Digital Microscopy

Samples taken after the titrations were used to analyse the magnetite colloid size, using a digital microscope (Keyence VHX Digital microscope with VH-Z100UR/W/T lens) combined with monitor including particle size software (Keyence VHX-5000). The software was able to automatically distinguish between the particles and solution, based on contrast, and to separate agglomerated particles, see Figure 3.9. Lastly, mean diameters were determined and calculated by the software.

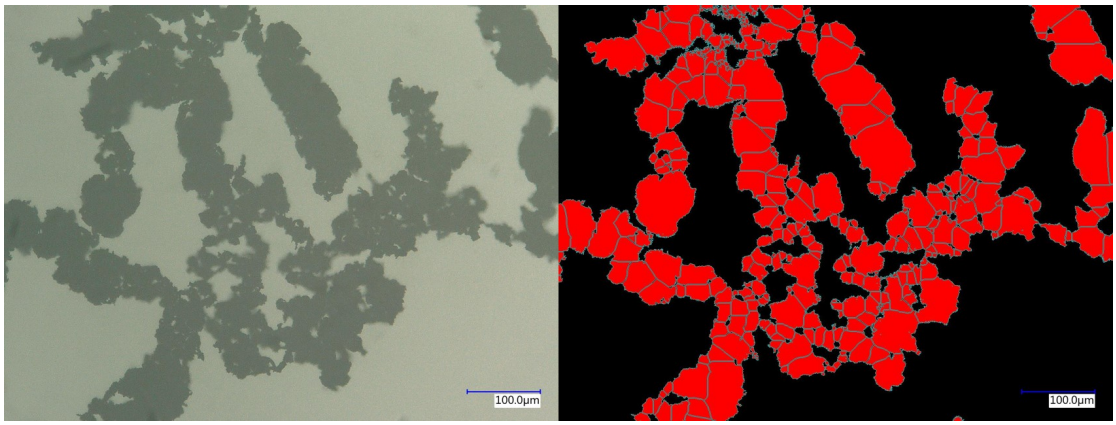

Figure 3.9: Keyence particle detection software, to enable particle size distribution determination. Left: magnetite particles as seen through microscope and right: particles detected by software.

3.15. PHREEQC surface complexation modelling

The geochemical code PHREEQC was applied in this study, first to fit a surface complexation model (SCM) onto the experimental potentiometric titration data, and afterwards using this model to predict the effect of FFA on the magnetite surface charge. For the surface complexation modelling PHREEQC (version 3.6.5) was used, and to validate the fit of the surface complexation model output to the experimental surface charge densities, Phyton (version 3.6.6.) was used. The default PHREEQC database (phreeqc.dat) was utilised. This database contains thermodynamic data, equilibrium constants (K or log_K), for aqueous species and minerals. The chemical equations used in the model, together with assumptions made prior to modelling are discussed in subsection 3.15.1. The modelling and fitting approach are discussed in subsection 3.15.2. The last two sections deal with additional equations applied within the model, see subsection 3.15.3 and subsection 3.15.4.

3.15.1. Model equations and assumptions

PHREEQC contains a surface complexation model based on the database of heavy metal ion complexation onto hydrous ferric oxide (Hfo) from Dzombak and Morel [26]. From this surface complexation model the standard protonation and deprotonation reactions of the surface hydroxyl species were used, describing the surface charge formation on the oxide. To which the reactions governing the acid base speciation of FFA, and adsorption of the FFA onto the metal oxide were added. This section presents the chemical equations used in the model, and assumptions made prior to the modelling. Lastly, this section will cover the PHREEQC keywords used. The assumptions made are listed below.

The assumptions made prior to modelling:

- New molecules were not added. The existing ammonia (Amm) molecule will serve as FFA molecule, for both ODA and OLDA. For modelling temperatures of 25 °C the pKa (log_K) value of this Amm was adjusted to match the one of ODA and OLDA. For the remaining temperatures the pKa values of ammonia were used, obtained from Bénézeth et al. [6].
- The hypothesis formulated by Gasnier and Lister [32] based on observations and literature [38, 114, 113] was used as input for the reaction governing the OLDA to magnetite interaction, and therefore was tested as plausible reaction. According to the formulated hypothesis OLDA binds to a surface site on the magnetite using the free electron pair of one amine group, while the other amine group is protonated. This research assumes the OLDA to bind onto a neutral (M-OH) active surface site. See, Equation 3.11.
- The hypothesis concerning ODA was different, as this FFA only has one amine group. It was assumed that this FFA only binds with the free electron pair of its amine group onto a neutral surface site of the magnetite. See, Equation 3.12.
- Assumption that ODA and OLDA do not only occupy the active surface group it adsorbs onto, but also multiple surrounding sites, see subsection 3.15.3.
- Dzombak and Morel [26] surface complexation database has weak and strong binding sties, for this model only the weak sites will be considered.

The chemical equations describing the protonation and deprotonation used in the SCM:

$$\mathrm{Hfo{-}wOH} + \mathrm{H^+} \longleftrightarrow \mathrm{Hfo{-}wOH_2{}^+} \qquad pKa1 \tag{3.8}$$

$$\mathrm{Hfo{-}wOH} \longleftrightarrow \mathrm{Hfo{-}wO^- + H^+} \qquad pKa2 \tag{3.9}$$

The chemical equations describing the the acid dissociation of the FFA, followed by the adsorption of OLDA, and ODA onto the active surface sites, respectively.

$$\mathrm{AmmH^+} \longleftrightarrow \mathrm{Amm + H^+} \qquad pKa \tag{3.10}$$

$$\mathrm{Hfo{-}wOH + AmmH^+} \longleftrightarrow \mathrm{Hfo{-}wOHAmmH^+} \qquad pKad(OLDA) \tag{3.11}$$

$$\mathrm{Hfo{-}wOH + Amm} \longleftrightarrow \mathrm{Hfo{-}wOHAmm} \qquad pKad(ODA) \tag{3.12}$$

An additional chemical equation was used (from the phreeqc.dat database) to describe the specific adsorption of calcium ions.

$$\mathrm{Hfo{-}wOH + {Ca_2}^+} \longleftrightarrow \mathrm{Hfo{-}wOCa^+ + H^+} \qquad pKa - calcium \tag{3.13}$$

The keywords used in the PHREEQC model to define the chemical reactions are: SOLUTION_SPECIES, for the chemical reactions in the water phase, and SURFACE MASTER_SPECIES, concerning the chemical reactions with the oxide surface. The test solution chemistry was defined with the SOLUTION keyword. The test solution was difined to simulate the electrolyte solution, and temperature of the potentiometric titrations. The addition of chemicals to the solution was done with REACTION. This to simulate the addition of acid or base during the potentiometric titrations. Lastly, to extract the results the keyword, SELECTED_OUTPUT was used. More information on these keywords can be found in Appelo and Postma [2]. The PHREEQC code used in the study can be found in Appendix G.

3.15.2. Modelling and fitting approach

The PHREEQC SCM consisted of chemical reactions which are defined by an equilibrium constant, i.e. pk or log_k. Within the modelling exercise these were determined by fitting the model onto experimental or literature data [32, 121, 123]. Therefore these constants were also referred to as 'fitting parameters'. The fitting exercise consisted of 3 steps. 1) Modelling the surface species of magnetite (mol/kg-solution) over pH using PHREEQC. 2) Importing the surface species from PHREEQC into Python, to calculate the surface charge density (C/m^2) of magnetite and compare this result to the experimental surface charge density using the root mean squared error (RMSE) . See, Appendix G for the Python code used. 3) Iteration step, repeated to improve the RMSE value (lower is better) by altering the log_k values of the chemical reactions. The iterative process was manual. The fitting parameters with related chemical reaction plus their order of fitting are given in Table 3.11. The parameters that remained fixed were the parameters that were controlled during the experiments. Namely, temperature (°C), amount of magnetite (g/L), SSA of magnetite (m^2/g), electrolyte strength (M) and total amine (FFA) in solution.

After obtaining the chemical reaction equilibrium constants, at various temperatures, via the fitting exercises, the PHREEQC SCM was used to predict the effect of OLDA on the surface charge density of magnetite. This prediction was made for a temperature value of 290 °C, which is above those of the performed experiments. This was done by using extrapolated equilibrium constants as input.

Table 3.11: Variable parameters, i.e. fitting parameters, that were used to fit the surface complexation model onto the experimental surface charge density curves. * indicates the range for the 25°C fitting exercise.

Order	Fitting parameter	Range	Reaction
1	Pka 1	3.8 - 5.5*	Hfo_wOH + H+ = Hfo_wOH2+
1	Pka 2	7.0 - 9.1*	Hfo_wOH = Hfo_wO- + H+
2	Active surface sites (/nm2)	10 - 30	Hfo_wOH
3	pkad FFA (ODA)	1 - 20	Hfo_wOH + Amm = Hfo_wOHAmm
4	pkad FFA (OLDA)	1 - 20	Hfo_wOH + AmmH+ = Hfo_wOHAmmH+
	Other parameters	**Range**	**Reaction**
	pKa FFA	-	AmmH+ = Amm + H+
	Specific cation adsoprtion	-	Hfo_wOH + Ca+2 = Hfo_wOCa+ + H+

3.15.3. Surface site coverage

The amount of available surface sites (/nm^2) was multiplied with the FSC factor, to account for the assumption that the adsorption of FFA occupies additional active surface sites besides the site it adsorbed onto. The FSC is calculated according to Equation 3.14.

$$FSC = \frac{(C_{FFA}/MW_{FFA}) \cdot N_A \cdot S}{N_{sites} \cdot (m_{oxide}/V_{total}) \cdot A \cdot (1.0 \cdot 10^{18})} \tag{3.14}$$

where:

FSC = Fraction of surface sites covered (-)
C_{FFA} = Concentration of FFA (g/L)
MW_{FFA} = Molecular mass of FFA (g/mol)
N_A = Constant of Avogadro ($6.022 \cdot 10^{23}$/mol)
S = Sites covered per FFA molecule (-)
N_{sites} = Surface sites density ($\frac{1}{nm^2}$)
m_{oxide} = Total mass of magnetite in solution (g)
V_{total} = Total volume of the test solution (L)
A = Specific surface area of magnetite (m^2/g)

The additional surface site coverage assumption was based on the hydrophobic interaction between hydrocarbon chains of a surfactant studied by Betova et al. [8]. This study concluded that both the hydrophobic tail and the polar head group determine the ability of a surfactant to adsorb onto iron oxides. Two hydrocarbon chains interacting or a hydrocarbon chain blocking/occupying surface sites could lead to additional site coverage. Additionally OLDA, having more amine groups and a slightly longer tail was assumed to cover more additional sites. Therefore the S value in Equation 3.14 for OLDA was 4 and ODA 2. Both S values linearly decrease, starting from 4 or 2, when below a concentration ratio of 300 (Magnetite (ppm)/FFA (ppm)) towards an S of 1 at a near zero concentration ratio. The latter, as it was assumed that with more FFA present more surface sites are solely occupied by FFA adsorption and no other interactions occur.

3.15.4. Relation surface charge density and surface potential

The surface charge (density) values were recalculated into surface potential values. This was done in order to related the SCM outcome to zeta potential data of Gasnier and Lister [32]. The relation between the surface charge density and surface potential was obtained from Chamousis and Osterloh [14], and expressed in Equation 3.15.

$$\phi_0 = \frac{2 \cdot k_B \cdot T}{e \cdot z} * sinh^{-1}\left(\frac{\sigma}{\sqrt{8 \cdot c \cdot \varepsilon_r \cdot \varepsilon_0 \cdot k_B \cdot T \cdot N_A}}\right) \quad (3.15)$$

where:

ϕ_0 = Surface electrostatic potential (V)
k_B = Boltzmann's constant ($1.38064852 \cdot 10^{-23} m^2 kg s^{-2} K^{-1}$)
T = Temperature (K)
e = Elementary electric charge ($1.602176634 \cdot 10^{-19} C$)
z = Charge of counter ions in solution (-)
σ = Surface charge density (C/m^2)
c = ion concentration (mol/m^3)
ε_r = Dielectric constant (-)
ε_0 = Vacuum permittivity ($8.854187 \cdot 10^{-12} F \cdot m^{-1}$)
N_A = Constant of Avogadro

4

Results and discussion

This chapter describes the results from the immersion and re-immersion tests, adsorption experiments and potentiometric titrations. The results are used to provide answers to the questions formulated in section 1.6. The results are discussed and compared to literature.

Results and discussion on the effect of FFA in addition to ammonia against only ammonia on the formation of a magnetite layer and the inhibition of acidic flow-accelerated corrosion are presented and discussed in section 4.1 to section 4.3. Results and discussion of the potentiometric titrations and effects of FFA on surface charge and size are presented in section 4.4 to section 4.9. The results and discussion of FFA adsorption onto magnetite colloids is presented in section 4.6. Section 4.10 of this chapter provides the results and discussion on the surface complexation model.

4.1. Effect of FFA on oxide layer thickness

This section describes the effect of the additives: ODA, OLDA both in addition to ammonia, against only ammonia and a blank reference chemistry in terms of the oxide layer thickness formed after the immersion experiments, and present after the subsequent re-immersion acidic FAC experiment. Layer thickness was determined via SEM, EDS, and weight loss.

4.1.1. Effect of FFA on oxide layer via SEM and EDS

The oxide layer thickness present on the coupons was determined via the Image-J software and SEM and EDS images according to subsection 3.5.4. These measurements were performed after the immersion and re-immersion tests. Figure 4.1 shows the SEM and EDS determined oxide layer thickness present on the coupon after the performed immersion and re-immersion (FAC) experiments under the tested additives.

Figure 4.1 clearly shows the oxide layer which was formed under untreated medium, the blank, formed the thickest oxide layer. The oxide layers formed under OLDA + NH_3, and NH_3 treatment had a similar SEM determined thickness. The layer formed under ODA + NH_3 additives appeared to be the thinnest. Both SEM and EDS show a similar pattern. However, the EDS measured thickness was a factor 2.78 higher compared to SEM measured thickness. A clear trend in the reduction of layer thickness after the re-immersion tests can be observed for the different test conditions by both SEM and EDS measured thicknesses: 19.1%, 14.5%, 8.6% and 23.3% for blank, ODA + NH_3, OLDA + NH_3, and NH_3 determined via SEM, and similarly determined via EDS: 47.3 %, 22.7%, 12.2%, and 34.9 %.

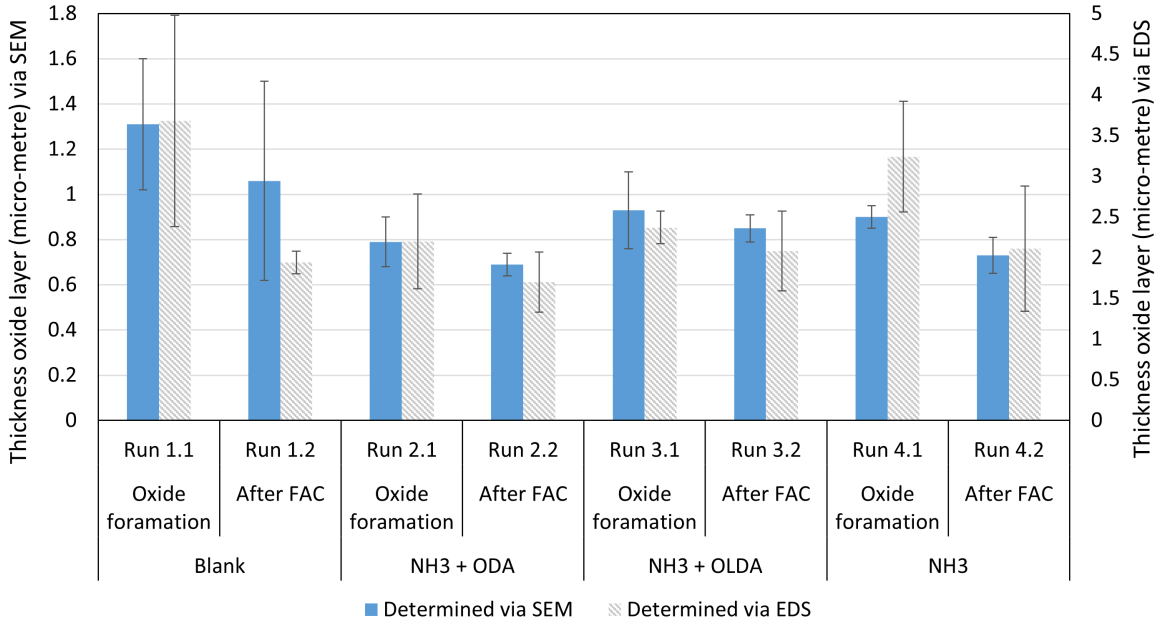

Figure 4.1: Oxide layer thickness via SEM and EDS after the immersion and re-immersion experiments. Standard deviation from the measurements at various locations of the cross-section. Concentrations of the additives ODA, OLDA and ammonia are all 2 ppm.

According to the SEM and EDS measurements, layers produced under FFA addition were reduced less under acidic FAC conditions, with OLDA performing better than ODA. Furthermore, it seems that FFA slowed the formation of an oxide layer. However, one thing should be noted, the layer formed during the blank immersion test was the only layer formed at 250 °C, instead of 230 °C. Although the Pourbaix diagram indicates a stable magnetite region for both 230 °C, and 250 °C at the set test conditions, the kinetics of the layer formation can deviate. This as the Schikorr reaction is more rapid at higher temperatures. Dubey and Kain [25] report bigger magnetite grains formed at higher temperatures under similar conditions. Thus it cannot directly be concluded whether the lower layer thickness is due to the presence of FFA or due to the temperature difference, despite literature supporting the notion [108].

Although both measuring methods indicated similar trends in terms of oxide layer reduction they clearly had a different scale. It is believed that the SEM values are more accurate for two reasons. One the EDS is a more coarse measuring method due to less data points. Second, as the embedding material cooled it shrunk and created a split along the surface, exposing the surface morphology. Whereas on the SEM the difference between layer-cross section and surface was clearly visible. The EDS might have detected the surface morphology as part of the cross-section. Lastly, a layer thickness in the range of 1 micro-meter is more common after 48h under the experimental conditions, Jäppinen et al. [47] reports a thickness of approx 1 micro-meter after 95h and 5wppm ODA addition.

4.1.2. Effect of FFA on oxide layer via SEM and Weight loss

The oxide layer thickness determined via Image-J software and SEM images, according to subsection 3.5.4, is presented and presented together with the oxide layer thickness determined via the Weight loss measurements. The method to determine the oxide thickness from Weight loss is explained in subsection 3.5.6. These measurements were performed after the immersion and re-immersion tests. Figure 4.2a: shows the SEM and b: Weight loss,

determined oxide layer thickness present on the coupon after the performed immersion and re-immersion experiments under the tested additives.

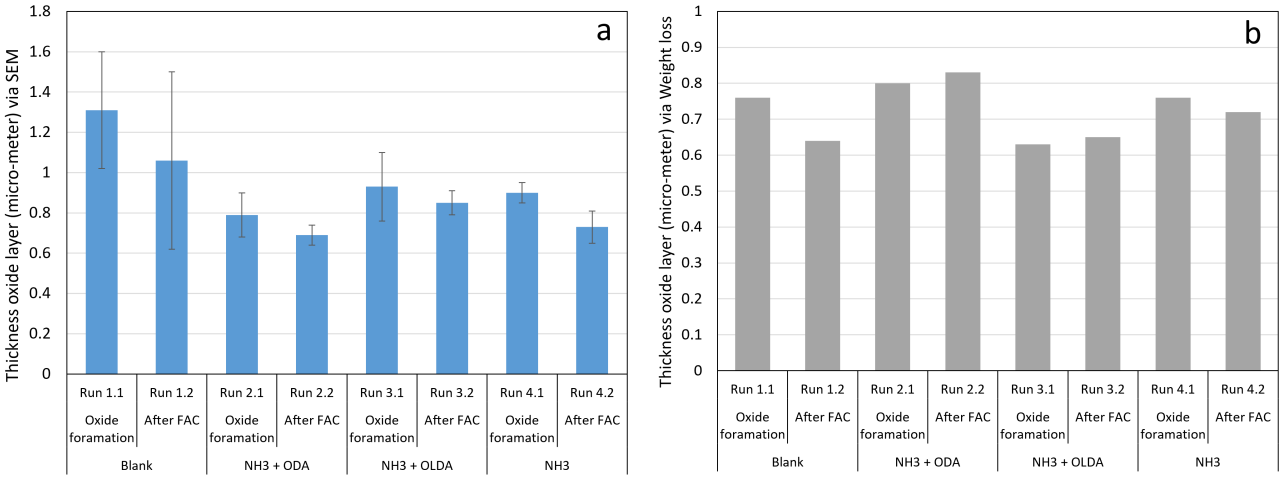

Figure 4.2: Oxide layer thickness via a: SEM and b: Weight loss, after the immersion and re-immersion experiments. concerning figure a: standard deviation from the measurements at various locations og the cross-section, figure b: no standard deviation as one coupon was used per weight loss measurement. Concentrations of the additives ODA, OLDA and ammonia are all 2 ppm.

Figure 4.2a and b, both show a similar trend on how the oxide layer thicknesses before and after the re-immersion tests relate to each other. Figure 4.2a shows the strongest reduction for the layers formed in the blank and NH_3 only conditions. The reduction in thickness given in percentages: 19.1%, 14.5%, 8.6% and 23.3% for blank, ODA + NH_3, OLDA + NH_3, and NH_3. Figure 4.2b shows the strongest reduction for the layers formed under blank, and NH_3 only conditions as well, and even an increase for the layers formed under FFA addition. The reduction (indicated with a minus sign) or increase in thickness, given in percentages: -15.8%, 3.75%, 3.2% and -2.7% for blank, ODA + NH_3, OLDA + NH_3 and NH_3.

From the weight loss determined oxide layer thickness it can be concluded that layers produced under FFA addition, against only ammonia or a blank chemistry, are reduced less or even increase under acidic FAC conditions. This was already concluded for the SEM derived oxide thickness subsection 4.1.1.

Still, two differences between Figure 4.2a and b need to be discussed. First, why the oxide layer formed under the blank chemistry was much thicker when determined via SEM, factor approx. 1.65. Second, why the layers thickness showed less reduction, or even an increase, after the acidic FAC conditions. Both can be explained in terms of the nature of the two measurements. To start, the SEM image was taken at the cross-section of the ”point of impact”, directly facing the mixer whereas the weight loss was determined over the whole coupon. PIVLab derived hydrodynamics showed the highest flow rates to be near the mixer, subsection 3.3.2, and SEM images of the surface taken at points other than the impact point showed less erosion of magnetite crystals after the re-immersion test. This indicates a higher probability for the layer to be reduced at the point of impact. Second, a fixed magnetite density of 5.0 g/cm^3 [47, 54] was assumed to calculate the oxide thickness from the weight loss data, whereas literature reports denser magnetite layers after the addition of FFA [40, 41, 46]. Meaning that oxide layer formed under a blank chemistry could indeed be less dense compared to the other layers, and therefore the density used to calculate the layer thickness from

the weight loss data was not representative. A density of 2.9 g/cm^3 would have yielded a similar thickness for the oxide layer formed under a blank chemistry, run 1.1. Indicating that this layer might be approx. 40% less dense.

Recommendations for future studies would be to use a cage setup where the coupons are moved relative to the liquid, providing more uniform flow conditions along the entire coupon. Another option would be to cover other parts of the coupon which are less exposed to the hydrodynamic conditions. These measures can reduce differences between the SEM and Weight loss determined thickness.

4.1.3. Effect FFA on oxide layer formation via SEM

The corresponding SEM cross sections images from which the 'SEM derived surface thicknesses' were determined are depicted in Figure 4.3. These SEM images were taken after the immersion experiments testing a: the blank (non-treated) chemistry, b: ODA and NH_3 chemistry, c: OLDA and NH_3 chemistry and d: NH_3 chemistry. Images taken after the re-immersion experiments can be found in Appendix H.

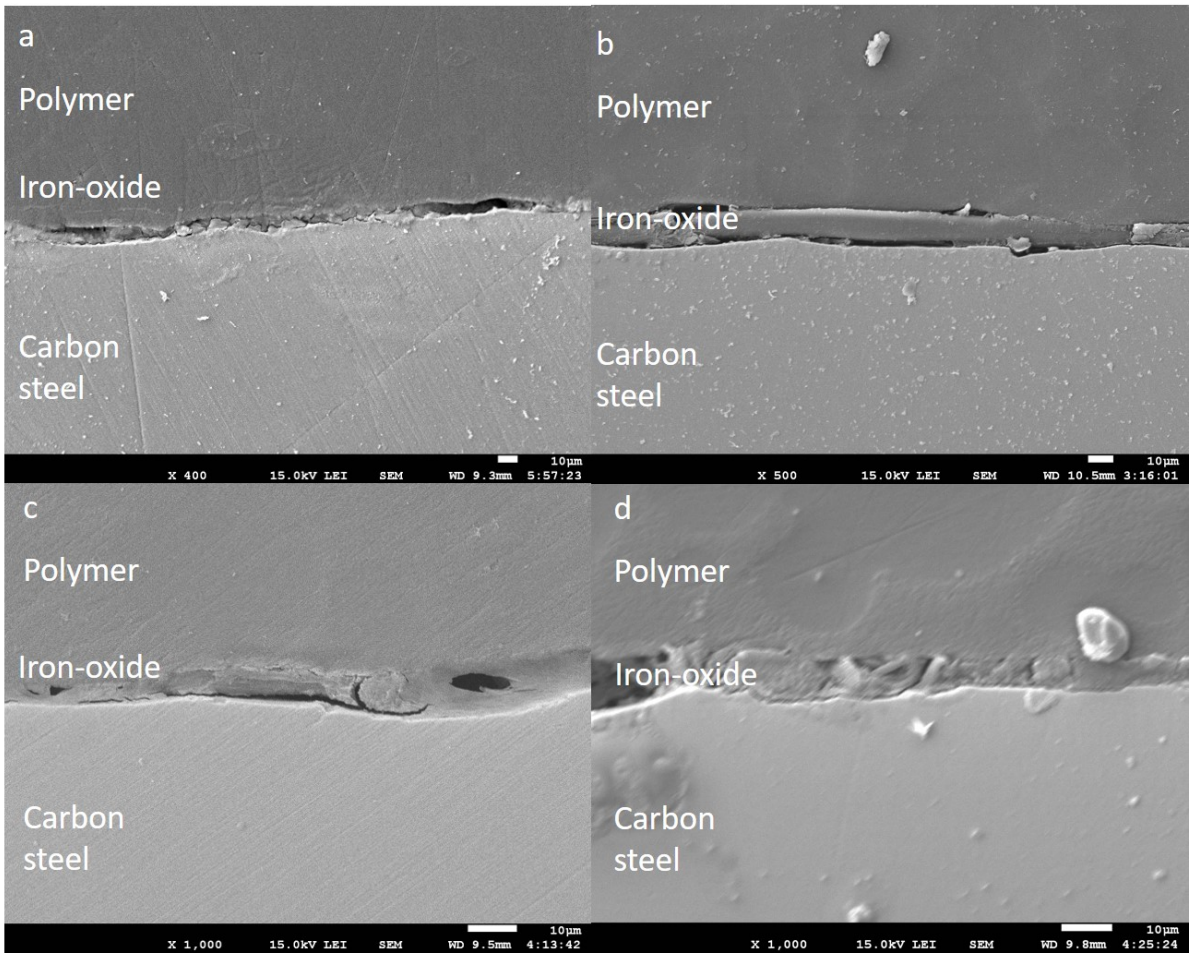

Figure 4.3: SEM cross section images taken after the immersion test with a: a blank chemistry b:ODA and ammonia additives c: OLDA and ammonia additives and d:ammonia additive, depicting the iron-oxide layer (middle, white), carbon steel (below) and polymer embedding material (above, dark grey). Photos taken by Durga Mainali. Note: be aware of the image scale. Concentrations of the additives ODA, OLDA and ammonia are all 2 ppm.

Figure 4.3 shows the effect of the different treatment methods on the homogeneity and 'smoothness' of oxide surface layer. In all cases of an immersion test with a water additive

present a smooth and thin layer was seen. Smoother layers were observed for runs with an FFA present. This is in accordance to what is published in literature [40, 41, 108, 109]. The layer formed under OLDA addition was the smoothest and most uniform.

The smaller standard deviations of the layers formed under FFA compared with the layer formed under the blank condition is an additional indicator of the layers being more homogeneous. See Figure 4.2a. Run 1.1 had a standard deviation of 0.29 µm, and 2.1, and 3.1 of 0.11, and 0.17 µm, respectively. This is also reported by [108]. However, the standard deviation of the layer formed with only ammonia present, run 4.1, was 0.05 µm. Whereas Janssen and Savelkoul [46] report a more 'compact and shiny', and finer layer formed under FFA treatment compared with one formed under ammonia. However, their runs took 4-6 weeks. Probably resulting in a more clear difference between the additives in favour of the FFA. Longer immersion runs could be conducted to verify this.

4.2. Effect of FFA on corrosion rate

The corrosion rate calculated via the SEM determined layer thickness according to subsection 3.5.4, is presented in this section, and compared with the corrosion rate determined via the weight loss measurement. This measurement is explained in subsection 2.5.1. These measurements and subsequent calculations were performed after the immersion and re-immersion tests. Figure 4.4a: shows the corrosion rate via the SEM measured oxide thickness and Figure 4.4b: the corrosion rate determined via weight loss. Corrosion rates were determined over the immersion test run, given as X.1, and over both immersion and re-immersion test runs combined, given as X.2. Referred to as the overall corrosion rate.

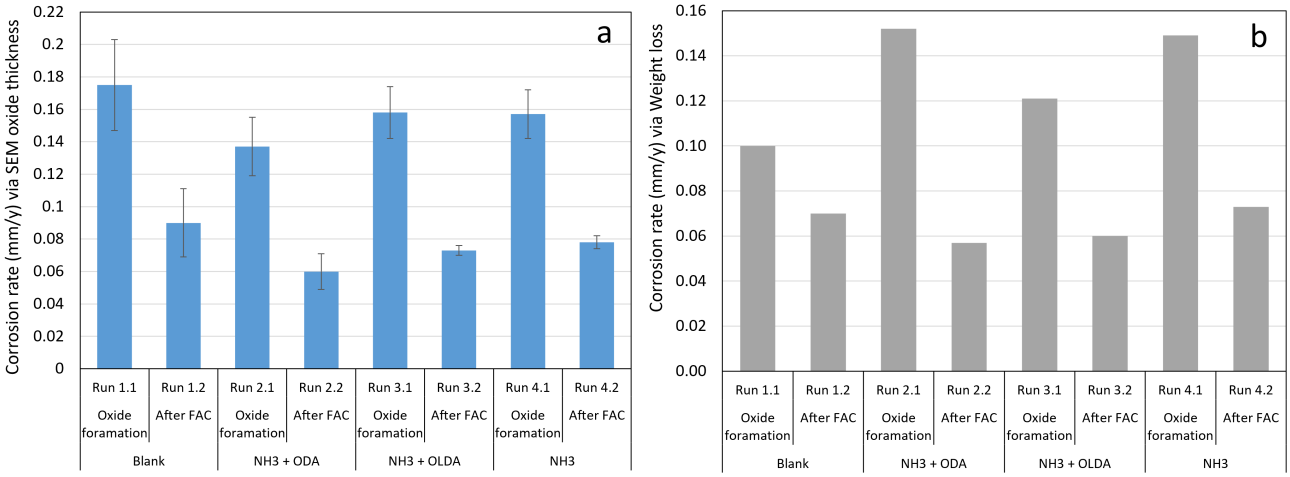

Figure 4.4: Corrosion rates determined after the immersion tests, and overall corrosion rates determined after the re-immersion tests via a: SEM images and b: Weight loss measurements. Concentrations of the additives ODA, OLDA and ammonia are all 2 ppm.

Both Figure 4.4a and b show a similar trend in how the overall corrosion rates were half of the corrosion rates determined after the immersion test. Layers formed under ODA, and OLDA show the strongest reduction in corrosion rate and had the lowest overall corrosion rates measured after the re-immersion run. Lower corrosion rates under FFA (ODA, and OLDA) addition is also supported by literature [7, 47, 120]. Using Equation 4.1 the efficiency of the corrosion inhibition was calculated, based on the weight loss determined corrosion rates. The

inhibition values were 18.6 for ODA in addition to NH_3, 14.3 for OLDA in addition to NH_3, and no inhibition under the NH_3 only chemistry.

$$IE = \frac{cr_0 - cr}{cr_0} \tag{4.1}$$

Where: cr_0 is the corrosion rate in absence of the chemical additive, blank, and cr is the corrosion rate in presence of the chemical additive and the same test solution.

Both ODA, and OLDA, in addition to ammonia, form magnetite layers that offer a better resistance against acidic FAC, in terms of corrosion rate, compared with layers formed under an ammonia only or a blank chemistry.

Still a difference between Figure 4.4a and b needs to be discussed. Namely, the higher corrosion rates determined via SEM, especially for run 1.1. This could be explained by the nature of the calculation. SEM determined corrosion rate is dependent on a chosen magnetite density, see subsection 3.5.4. In case of a too high density an overestimation in corrosion rate can be made. Especially concerning run 1.1., where the magnetite layer density might be well below the chosen 5.0 g/cm^3. Not having to assume densities makes the weight loss method a more direct way to calculate the corrosion rate.

A weight loss determined corrosion rate of approx. 0.12 mm/y during immersion test followed by an overall corrosion rate measuring just half, approx. 0.06 mm/y of the value can be explained by the Schikorr reaction. This is an autonomous process that cannot be stopped, even when ODA, and OLDA are present. But when a magnetite layer is formed it offers protection against any further corrosion of the metal, hence a corrosion rate of half of the original. This was not the case for the blank chemistry. Having a lower corrosion rate during the first run, 0.10 mm/y and a relative high one after the re-immersion test, 0.07 mm/y. The low rate can be a result of the higher temperature of 250 °C applied during the test, apposed to 230 °C. This could have resulted in a faster Schikorr reaction leading to a quicker magnetite layer formation, halting further corrosion. Followed by a higher overall corrosion rate after the re-immersion test. As the layer was presumably less protective. Additional research using an electrical resistance probe in order to measure the corrosion rate over time [120] could be useful to verify this assumption. Or longer immersion test times should be applied, of at least 200 hours. After which the flow-accelerated corrosion speed becomes linear dependent on time [45]. This leaves out any effects the initial layer formation has on the corrosion rate.

The FAC rates during this study were significantly lower than what is reported by literature, despite the acidic environment. Weerakul et al. [120] reports rates ranging from 2.84 to 8.69 mm/y for a blank chemistry at 140 °C. The higher rates can be a result of higher fluid velocities and shear stress, 13.06 m/s and 388Pa, compared with 0.5 - 1.9 m/s and 178 mPa of this study, see Appendix I. Another factor could be the chromium content, as Lister and Uchida [58] report on the linear dependence of FAC rate on chromium content. Weerakul et al. [120] uses 0.001 wt% whereas this study used steel with a 0.0580 wt%. However, it is believed that forming the magnetite layer, at no flow conditions and a temperature above 220 °C, prior to the FAC re-immersion test was the real reason of the low corrosion rates. As Poulson et al. [84] reports FAC rates of 1.2 mm/y in similar conditions to this study, 0.06Cr and an Re of 1.04 x 10^5 (Re of 1.09 x 10^5 for this study) at a temperature of 115 °C. A follow up research, could be to form the magnetite layer, with FFA present, under flow conditions at a lower temperature. Afterwards this layer can be tested under acidic FAC.

Lastly, the better resistance against acidic FAC of magnetite layers formed under the presence of ODA and OLDA in addition to ammonia could be attributed the layer being denser. This

denser layer compensates for the fact that it was thinner compared with a layer formed under the blank chemistry. Janssen and Savelkoul [46] report FFA treatment to form more shiny and compact layers compared with a layer formed under ammonia treatment, 'indicating that the formed magnetite is composed of finer crystals'. Poulson et al. [84] relates a thinner magnetite layer to increased FAC velocities. However, when one takes Equation 2.15, and assumes all parameters to be constant except oxide porosity and oxide thickness, then decreasing porosity results in a decreased corrosion rate while the opposite holds for oxide thickness. Following this equation, the decreased oxide thickness was presumably compensated by a decrease in porosity resulting in the decreased FAC rate.

4.2.1. Effect of FFA on combined coupon and oxide mass loss

The difference in weight per coupon after an immersion or re-immersion test is given in Figure 4.5. This difference was determined by weighing the coupon prior and after immersion without cleaning the oxide layer. Hence this 'weight difference' includes both differences due to metal and/or oxide mass change.

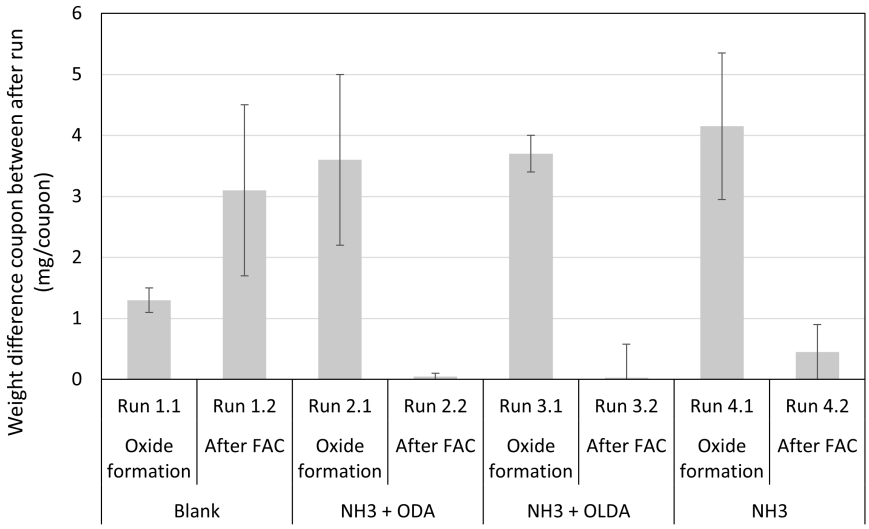

Figure 4.5: Weight difference, the positive values indicate weight loss, of coupons. Determined by measuring weight before and after the immersion test, without removing the oxide layer. Concentrations of the additives ODA, OLDA and ammonia are all 2 ppm.

Figure 4.5 shows that for layers formed with FFA there was little to no loss in weight, or material loss, during the re-immersion tests. It can be concluded that the magnetite layers formed with ODA, and OLDA present in addition to ammonia offer a better protection during acidic FAC.

The results presented in Figure 4.5 support the conclusion that magnetite layers formed under ODA, and OLDA were better resistant to acidic FAC. See subsection 4.1.1. As results show less mass loss due to either dissolution, erosion or corrosion of the underlying steel. Furthermore, the results seem to support the notion made in subsection 4.1.1. Stating that the magnetite layer formed under the blank chemistry was formed faster and thicker as it was formed at 250 °C. A reason given is the Schikorr reaction being quicker at higher temperatures, and therefore more corrosion product was redeposited (faster) as the secondary magnetite layer. This could have lead to a lower mass loss during the immersion test, run 1.1.

4.3. Oxide layer analysis

This section describes the effect of the additives: ODA, OLDA both in addition to ammonia, against ammonia, and a blank reference via the oxide layer surface formed after the immersion experiments, and oxide layer surface after the re-immersion acidic FAC experiment.

4.3.1. XRD results

X-Ray diffraction analyses were performed on the lower part of the coupon. In case of the re-immersion experiments the location of XRD analysis was at the coupon side facing the mixer. See Figure 3.4 for the distinguished coupon parts. After runs 3.1 and 3.2 the top part of the coupon was also examined by XRD. All XRD results indicated the presence of Iron, Fe and, Magnetite, Fe+2Fe2+3O4. No other compounds were detected. See Appendix J for an overview of the performed XRD analyses and results. Evidently the ODA and OLDA did not suppress the oxide layer formation.

4.3.2. Contact angle analysis

Contact angle measurements were performed to indicate the presence of an ODA, and OLDA layer on the coupons according to subsection 3.5.3. The results are presented in Figure 4.6 and Figure 4.8. Representative drops can be seen in Figure 4.7. These results should be interpreted with caution, as an FFA layer can be present but can not be detected due to a rough surface, or porous iron oxide [81, 93].

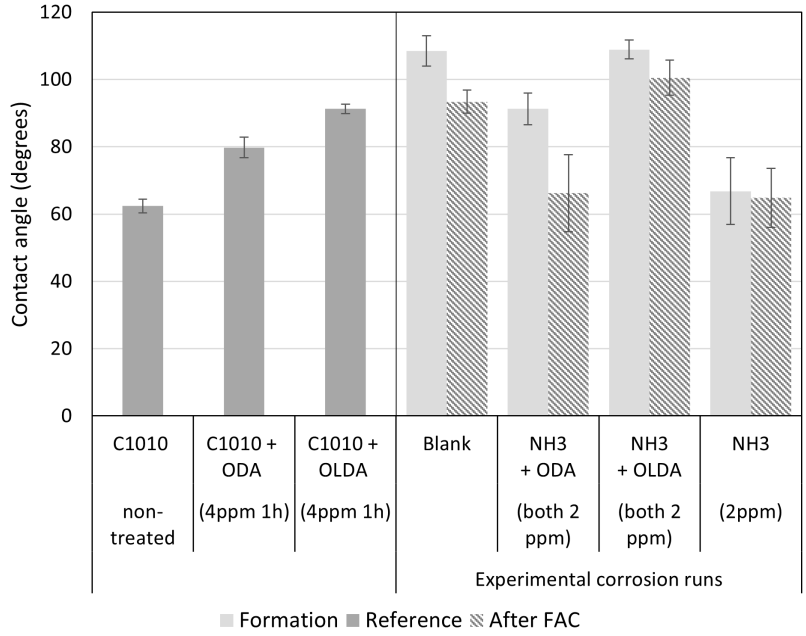

Figure 4.6: Contact angle measurements of the coupons after the immersion (formation) and re-immersion (After FAC) tests on the right side, and on the left side reference contact angle measurements. On coupons immersed in 4ppm ODA or OLDA solution at room temperature.

Figure 4.6 shows that the layers formed under an FFA chemistry have higher contact angles compared with the layer formed under an ammonia only treatment. Furthermore, the values of the contact angles seem to follow the same trend as the reference contact angles. OLDA resulted in a more hydrophobic layer on fresh reference coupons compared with ODA, and both do compared with the non-treated coupon. This is in accordance with literature [5, 33]. Considering this one could say that OLDA formed magnetite layers that were either

smoother and/or contained a more hydrophobic FFA layer compared with ODA or ammonia only formed layers. Lastly, OLDA formed magnetite layers remain either smoother and/or lose less FFA under acidic FAC compared to ODA formed magnetite layers.

The higher contact angles measured after the blank chemistry immersion test, and re-immersion test, could be attributed to OLDA contamination. As a concentration of 0.03 ppm FFA was measured after the blank immersion test. This is suspected to be OLDA, because prior to the blank immersion test, the autoclave including PTFE liner were used for a potentiometric titration using magnetite powder and 3 ppm OLDA. In addition the higher temperature applied during the blank chemistry immersion test, 250 °C compared with 230 °C, could have resulted in a better FFA adsorption. De Seranno et al. [19] reports higher coating temperatures to result in more hydrophobic surfaces. Lastly, the higher contact angles of the coupon treated in blank chemistry could also be explained by the surface being smoother. Only, this does not align with the observations presented in subsection 4.1.3. Which reports the magnetite layer formed under blank chemistry to be less smooth compared to layers formed under ODA, and OLDA chemistries.

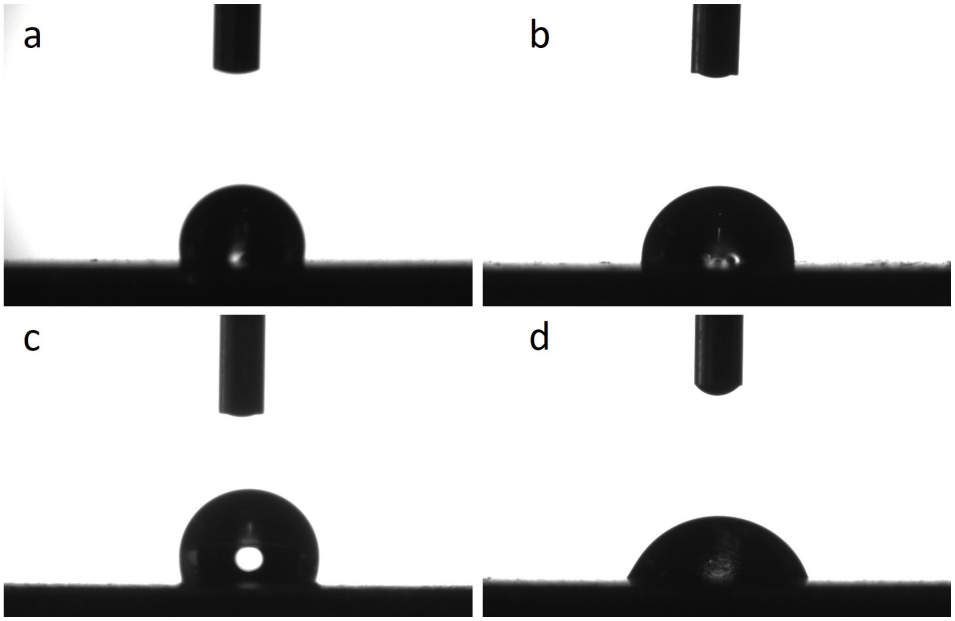

Figure 4.7: Sessile drop images taken after the immersion tests. The immersion tests (48h at 230-250 °C) performed under a: blank-, b: ODA and ammonia-, c: OLDA and ammonia-, and d: only ammonia chemistry. All additives were present at a concentration of 2ppm.

Figure 4.8 shows the contact angle measurements performed on six identified parts of the coupon. Measurements were performed after the immersion, and re-immersion experiments, and on the reference coupons. The six identified parts were the side facing the mixer (inside), not facing the mixer (outside) and these were subdivided into three sections, lower, middle, and top. Figure 3.4 shows these different parts.

A significant difference between the contact angles measured at the inside and outside of ODA, and OLDA coupons after the re-immersion tests can be seen in Figure 4.8. For the ODA + NH_3 treated coupons the contact angles at the inside were on average 8.0 degrees lower compared with the outside. For OLDA + NH_3 treated coupons this difference was 11.1 degrees. This is possibly a sign of more extreme hydrodynamic conditions at the surface facing the mixer. Definite conclusions on whether this could be assigned to the surface becoming

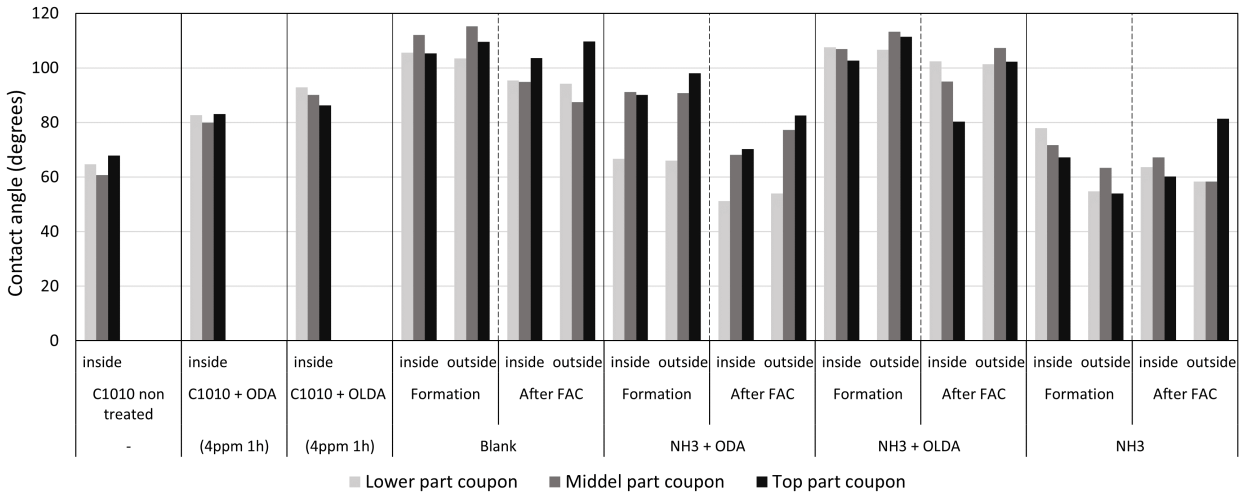

Figure 4.8: Contact angle measurements of various locations on the coupon surface. On the right side, after immersion (Formation) and re-immersion (After FAC) tests. On the left side the contact angles of the reference coupons.

more porous and/or rougher, or the ODA, and OLDA film being removed cannot be made based on this data.

Additional methods in order to semi or fully quantify the presence of an FFA layer after the immersion, and re-immersion tests could be the Kurita 'whipe test', and XPS (X-ray Photoelectron Spectroscopy). These could be applied to differentiate whether contact angle measurements are a sign for more porous layers or decreased FFA films. This can providing an answer to the ODA, and OLDA film resistance towards flow conditions, and if the FFA film still contributes together with the magnetite layer in resisting FAC. The Kurita 'whipe test' would be a semi quantitative method where the FFA present is transferred into a solution. Afterwards the Bengal rose dye method can be applied to determine the FFA concentration [93]. The XPS analysis, already applied to study the FFA film on a surface by Ochoa et al. [72], can detect the amine nitrogen on material surfaces. This method is considered to be fully quantitative.

4.3.3. Surface morphology

This section presents and discusses the SEM and digital microscope images of the oxide surface.

Digital microscope

Figure 4.9 shows signs of oxide spalling from the coupon surface. The image was taken after the re-immersion acidic FAC test, and shows the oxide layer formed under OLDA and ammonia chemistry. The lighter colour indicates the bare metal underneath the oxide layer as this colour/brightness corresponds with a fresh C1010 coupon surface. No signs of magnetite spalling was observed after the immersion tests, and after the re-immersion test of the layer formed under ODA and ammonia treatment. This indicates that the magnetite layer formed under the ODA ammonia chemistry offered better protection against the hydrodynamic forces responsible for spalling. Digital microscope images of the layers formed under a blank-, ODA and ammonia, and ammonia only chemistry taken after the re-immersion tests can be found in Appendix K.

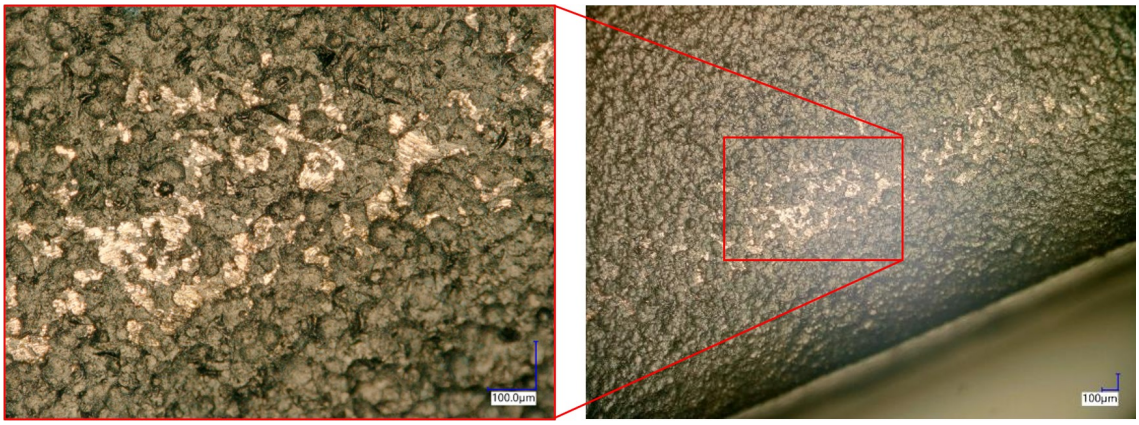

Figure 4.9: Digital microscope images, zoom 100 and zoom 400, of the coupon oxide surface after the acidic FAC re-immersion test. This might point to spalling. The magnetite layer seen on the figure was formed under OLDA and ammonia chemistry.

SEM Surface images

Figure 4.10, on page 75, presents the representative SEM surface images taken of the oxide surface after the immersion and re-immersion tests. Images were taken according to the procedure explained in subsection 3.5.4.

Figure 4.10 a,c,e and g, shows the oxide surface after the immersion test. Under the blank, ODA and ammonia, and ammonia only solutions/chemistries a fully grown secondary layer can be seen. Composed of visible magnetite crystals, showing cubic, octahedral faces, with sharp corners and edges. The layer formed under the blank conditions had the biggest crystals, and the layer formed under ammonia had smaller not fully grown crystals. Concerning the secondary magnetite layer formed under the OLDA and ammonia chemistry, except for some areas, (see Figure 4.10e) no uniform growth of magnetite crystals was identified. Smaller magnetite crystals formed under FFA present is in accordance to what is stated in literature [41, 46, 108]. However it is also reported that magnetite layers formed under a polyamine treatment are more compact compared to layers formed under ammonia treatment, indicating finer magnetite crystals [46]. This could not be seen in the SEM images. Possibly more time should be given for the crystals to fully grow, to get a more clear difference between the treatment methods, as discussed in subsection 4.1.3.

The SEM images of Figure 4.10 do support the notion that under higher temperatures magnetite crystals grow faster, as discussed in subsection 4.1.1. The argument given is that the layer formed under a blank chemistry was the only test performed at 250 °C. Moreover the SEM surface images do also support the notion that the blank formed layer was less smooth compared to the layers formed under the other chemistries, discussed in subsection 4.1.3.

Figure 4.10 b,d,f and h, shows the oxide surface after the acidic FAC re-immersion test. The SEM surface image-b shows far smaller, sharper/pointier, to no magnetite crystals. Indicating heavy dissolution and erosion during the re-immersion test, of the magnetite layer formed under a blank chemistry. This dissolution and erosion effect was also observed for the other layers. The layer formed under ODA and ammonia chemistry showed the least signs of erosion, as magnetite crystals were generally similar in size, and not sharper/pointier. SEM surface image-h shows better grown crystals as compared with image-g, however not uniformly covering the surface. From the SEM surface images it follows that the secondary magnetite layer, i.e. crystals, formed under the ODA and ammonia treatment was best resistant to the

acidic FAC conditions of the re-immersion test.

In addition, the SEM images of Figure 4.10 do support the conclusions made in subsection 4.1.2 and subsection 4.2.1. Namely, the magnetite layers formed under a blank and ammonia chemistry are less strong and more prone to acidic FAC than magnetite layers formed under ODA and ammonia, and OLDA and ammonia treatment.

Lastly, two points deserve further discussion. The first point concerns the FAC pattern. Kain [50] mentions one should see scallops as a typical FAC pattern. However, this pattern was not observed in both the SEM, and digital microscope images. It can be that more time was needed during the test in order to observe such a pattern. Although, Weerakul et al. [120] reports not observing any obvious scallop patterns after FAC tests of 30, 50, and 70 days, but mentions seeing that the corroded surface was 'ragged and porous'. Similar to what was observed in Figure 4.10 b.

The second point concerns the growth of the secondary magnetite layer, or magnetite crystals, under OLDA and ammonia treatment. Under this treatment no uniform secondary magnetite layer was formed. Despite enough ODA, and OLDA adsorbed to cover the coupon with 170, and 174 layers, respectively (calculated using Equation 2.16). It could be possible that the OLDA film covered the coupon better than the ODA film, leading to crystals only growing at micro-structural irregularities. To verify this in future research one should accurately identify these locations and observe them again, using SEM, after cleaning the oxide. Another option to explain the irregular magnetite crystals found on the surface could be magnetite colloid deposition. Although, it is more likely to have grown on the surface after comparing the SEM images to Gasnier and Lister [32]. Which shows a SEM image of deposited magnetite colloids, looking more floc like, dispersed, and is loosely attached to the surface.

4.3.4. EDS

EDS analysis was performed on the cross section according to subsection 3.5.4. Results were used to verify the presence of an oxide layer on the SEM images. This was done by overlapping the EDS results and SEM image, to see whether the elemental oxygen was concentrated at the identified oxide layer region. Secondly, EDS results were also used to determine the oxide layer thickness, also according to subsection 3.5.4.

The EDS results confirmed the presence of the oxide layer on the SEM cross-section images. More elemental oxygen was concentrated on what was seen as the 'light-grey' region, or layer, in the SEM images. See Appendix L for a representative EDS image overlapped on top of a SEM image.

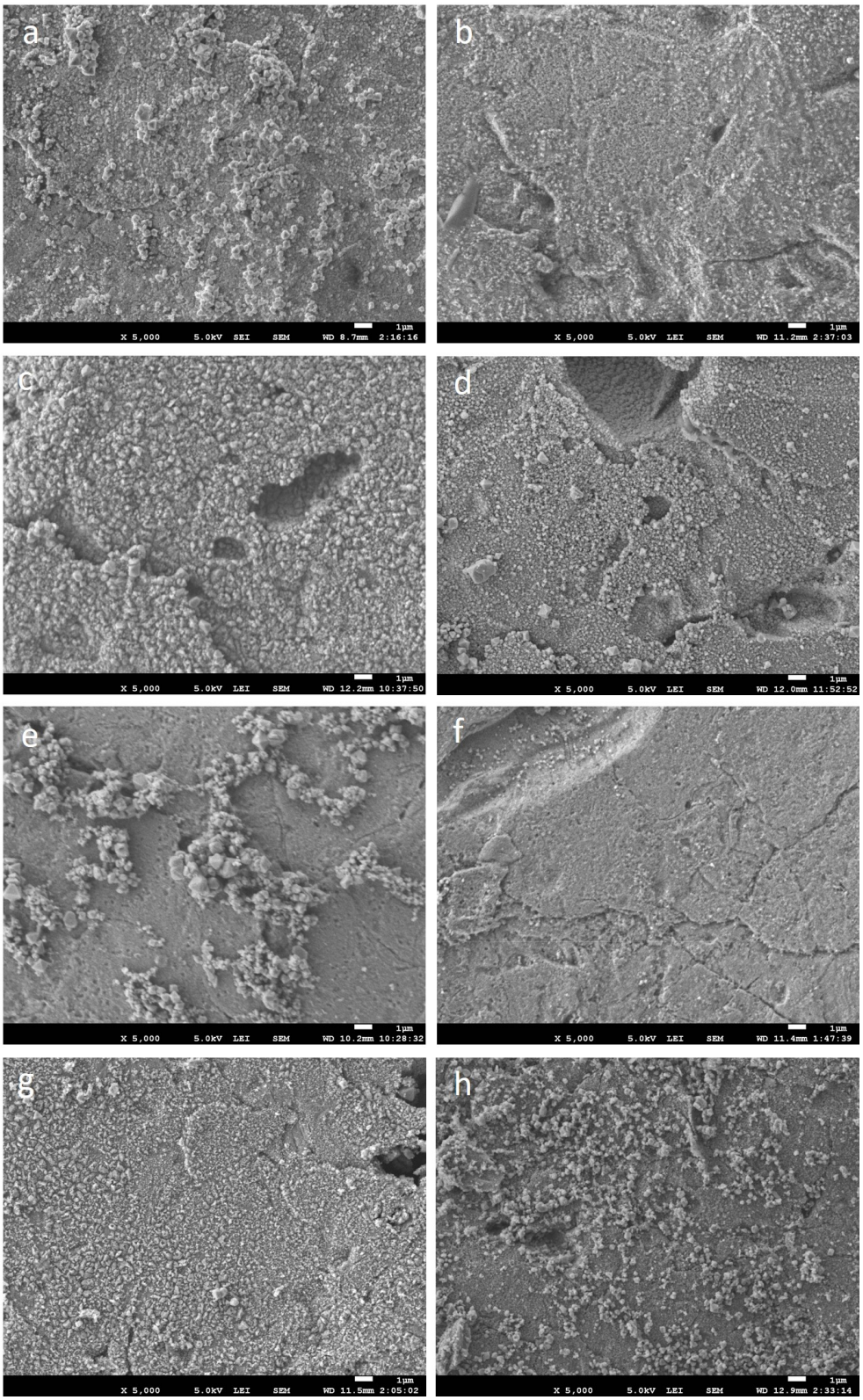

Figure 4.10: Surface morphologies of carbon steel samples after exposure to immersion tests a: 46.3h blank solution, c: 48.0h ODA and ammonia solution, e: 47.2h OLDA and ammonia solution and d: 47.8h ammonia solution. All concentrations at 2ppm. The surface morphologies of b, d, f and h are the respective re-immersion test under acidic pH_{25c} FAC conditions for 46.3, 48.0, 48.0 and 47.9 hours respectively, combining a and b, c and d, e and f, g and h as immersion and subsequent re-immersion tests. Magnifications 5000x. Pictures by Durga Mainali.

4.4. Potentiometric titrations of commercial magnetite suspensions

This section presents the results of the magnetite titrations, performed at 25 °C, on the commercial magnetite powders, 95% (Mag95), 99.99% (Mag99) and 99.997% reagent grade (Puratronic, short: Pur). Titrations were performed according to the procedure explained in section 3.12. The results of the titrations, the surface charge density curves, can provide an answer to the question of how the commercial magnetite Mag95, and Mag99 compare to Puratronic in terms of surface charge and pH_{pzc}.

The surface charge density curves of the three commercial magnetite powders are given in Figure 4.11a, 3rd order polynomial fits were made on the selected curves and are presented in Figure 4.11b.

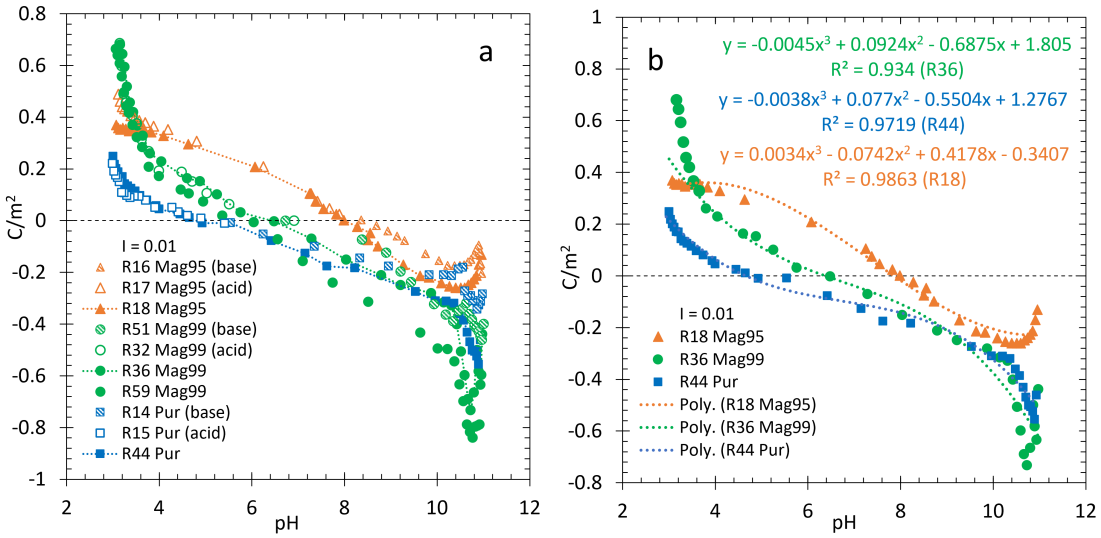

Figure 4.11: a: surface charge density curves of the different commercial magnetite powders, Mag95, Mag95 and Pur performed with both the quick method, and standard method (last, denoted with: base and acid). Titrations were performed in a KNO_3 background electrolyte of ionic strength 0.01 at a temperature of 25 °C. b: polynomial fit to the surface charge density curves and respective equations.

In general, the surface charge density curves for dispersed Mag99 and Puratronic were rather similar within the experimental scatter, especially in the pH region above pH 6. In addition, looking at the equations of the polynomial fits, both the Mag99 and Puratronic curves followed the same trend. Namely $-a \cdot x^3 + b \cdot x^2 - c \cdot x + d$. Whereas the surface charge density curve only slightly fits the Puratronic surface charge density curve within the experimental scatter above a pH of 9. Furthermore, its polynomial fit followed a different trend of $a \cdot x^3 - b \cdot x^2 + c \cdot x - d$. This resulted in a z-shaped curve for Mag95, opposed to the s-shaped curves for Mag99 and Puratronic. The net point of zero charge (pH_{npzc}), point of intersection (pH_{cip}), and point of inflection (pH_{infl}) are presented in Table 4.1. These points were determined according to subsection 2.7.2. Subsection 4.4.1 discusses these results.

Table 4.1: The net point of zero charge (pH_{npzc}), point of intersection (pH_{cip}) and point of inflection (pH_{infl}) of Mag95, Mag99 and Puratronic.

	pHnpzc	pHcip	pHinfl
Mag95	8.21 ±0.20	8.19	7.41 ±0.10
Mag99	6.25 ±0.30	6.45	6.72 ±0.31
Pur	4.89 ±0.15	N/A	6.88 ±0.12

From the results (Figure 4.11 and Table 4.1) it follows that magnetite 99.99% reagent grade was the most similar to Puratronic magnetite in terms of surface charge density and point of zero charge. In fact, magnetite 95% reagent grade did not compare well concerning these aspects. Therefore is not considered a suitable replacement for Puratronic magnetite.

The fit of Mag99 and Puratronic probably would have been better, concerning the region below pH 6, given less magnetite dissolved during the Mag99 titrations. As discussed in subsection 2.7.3 and section 4.5, the dissolution of magnetite can influence the surface charge calculation. More dissolution results in a higher, more positive, surface charge. Measurements of dissolved iron, Fe^{2+}, indicated more dissolved iron was found after the Mag99 titrations compared to the Puratronic titrations, on average 3.69 mg/L, and 0.29 mg/L, respectively.

The standard titration method resulted in less negative surface charge curves in the alkaline region, this could be seen for all the commercial magnetite powders. Mayant et al. [62] also reports a similar difference between the two applied methods, a 'slow batch titration method' and a 'rapid continuous titration'. See Figure 4.12. The 'slow batch titration method' also executed using two suspensions, for an acid and base titration, just as the present study. Whereas the 'rapid continuous titration' also applies just one titration to obtain a surface charge curve. The nature of the titration starting point could have played a role. This could allow the magnetite colloids to acquire more extreme surface charges at a higher starting pH.

One last point that needs to be discussed is the deviation of Mag95 compared to the other two commercial magnetite powders. This could be assigned to too much impurities, such as hematite. Table 3.6 already indicated a significant amount of hematite to be present within the powder. Moreover the pH_{cip} and pH_{npzc} of Mag95 are more in accordance to experimental pH_{pzc} values of hematite found in literature. Fokkink et al. [30] reports a pH_{pzc} of 8.7 for hematite, and Pivovarov [80] and Karasyova et al. [51] report values of pH_{pzc} 8.25 and pH_{pzc} 8.6, respectively. Lastly, a brown solution colour was observed after Mag95 titrations, see Appendix M, possibly indicating hematite.

Figure 4.12 presents the surface charge density curves of Mag99 and Puratronic in comparison to literature. In general, both curves obtained in this research are rather similar within the experimental scatter to the literature data [62, 121]. The agreement of the Mag99 and Puratronic experimental data of this study with literature, indicates their suitability for further study of: the FFA effect on the magnetite surface charge.

A small deviation between the experimental surface charge densities curves reported by literature [62, 121] and this study can be explained in terms of iron-dissolution and ionic strength of the background electrolyte. Mayant et al. [62] accounts for the iron dissolution effects for the calculation of the surface charge density curve. Whereas Wesolowski et al. [121] does not. This explains why his magnetite surface charge density in the acidic region (below pH 6) is relatively high. In addition, Wesolowski et al. [121] also performs his titration in an electrolyte of 0.03 ionic strength, resulting in higher surface charges in both the alkaline and acidic region.

4.4.1. Point of zero charge of magnetite at 25 degrees Celsius

The point of zero charge for Mag99 was determined via two methods, the common intersection point-, and inflection point method, according to subsection 2.7.2. The results, and how they relate to each other are presented in Figure 4.13a and b.

A pH_{pzc} could be determined via both methods. The pH_{cip} was found at the 0-line, and close to the pH_{npzc}. This indicated an absence of specific ion adsorption and a free strong acid or base being present. Except for Run62 where probably a free acid was present, as later performed titrations were possibly exposed to accumulated impurities. Similarly, Szekeres and Tombácz [101] report free acid to cause surface charge curves to translate downwards. The

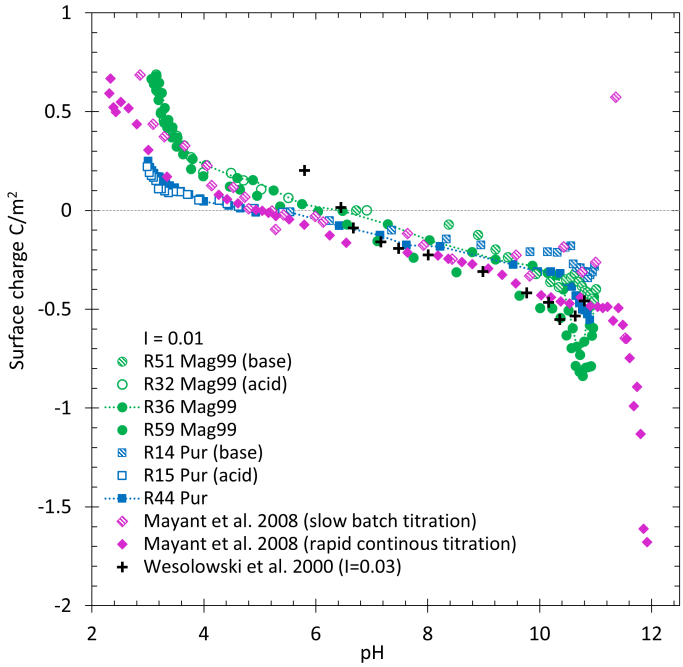

Figure 4.12: Commercial magnetite Mag99 and Puratronic surface charge density curves compared to literature Mayant et al. [62] and Wesolowski et al. [121].

pH_{cip} and pH_{infl} were in close proximity of each other with the pH_{infl} at a higher pH, this is also reported by literature [121, 123]. The values can be found in Table 4.1. The results show that pH_{cip}, and pH_{infl} were good estimations of each other, and the pH_{npzc}, therefore a good representation of the pH_{pzc} for the Mag99 used in this study.

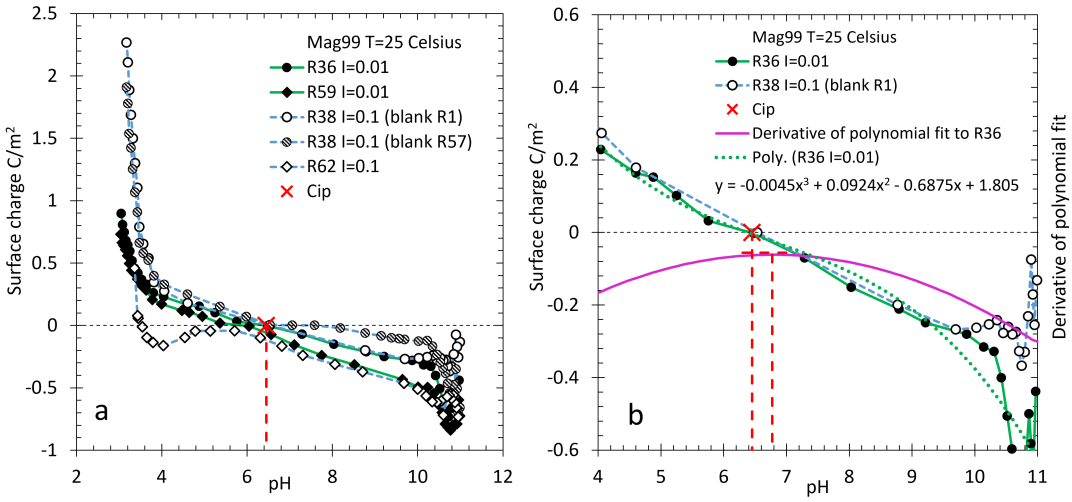

Figure 4.13: Determination of pHpzc via a: common point of intersection method and b: infliction point method.

4.5. Magnetite dissolution

Iron analyses were performed to account for proton, H^+, consumption via the dissolution of magnetite during the potentiometric titrations, as this affects the surface charge calculations. For every two mols of protons consumed one mol of Fe^{2+} is released, see subsection 2.7.3. Dissolved ferrous iron, Fe^+, concentrations were determined according to subsection 3.14.1. The results of the dissolved ferrous iron, Fe^+, measurements combined with the last recorded pH values of the titrations are plotted, together with similar data from literature [62, 121] in Figure 4.14.

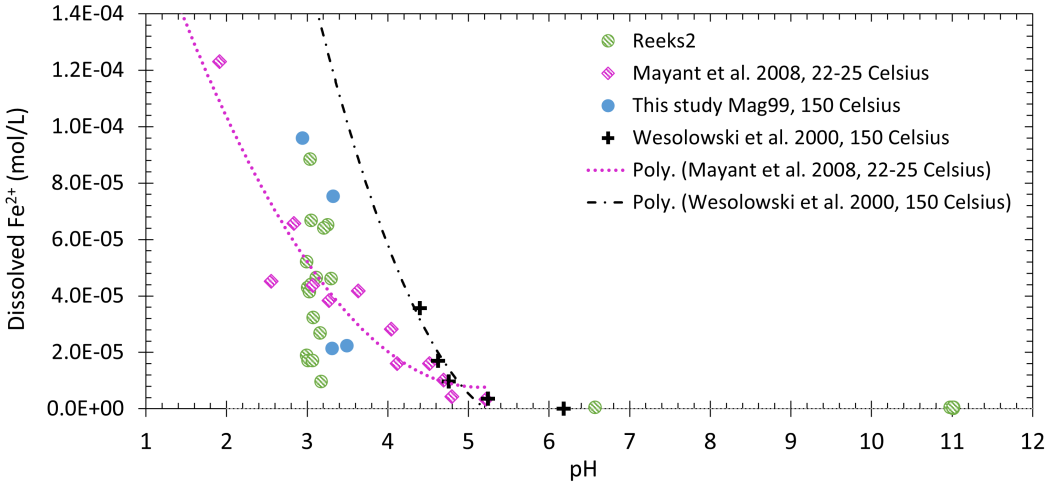

Figure 4.14: Dissolved Fe2+ measured after the potentiometric titrations in order to determine the proton consumption influence on the surface charge density, compared to literature values Mayant et al. [62] and Wesolowski et al. [121].

Considering the dissolved ferrous iron measured after the titrations performed at 25 °C, no significant dissolution was measured in the alkaline pH range of 6.5 to pH 11. Generally, the dissolved iron scatter measured after the 25 °C titrations aligns with the measured dissolved Fe^{2+} trend of Mayant et al. [62]. Indicating that below a pH of 4 the iron dissolution becomes significant concerning its impact on the surface charge. This value is also reported by Wesolowski et al. [121], as above pH 4, no to little influence of magnetite dissolution is seen on the shape of the his surface charge curve.

However, Mayant et al. [62] has 57m^2 of magnetite per litre test solution, whereas this study just had 21.5 m^2 per litre. This means that a similar measured dissolved ferrous iron concentration results in a bigger influence on the surface charge density calculation, for this study. Therefore it was not only sufficient to measure the dissolved iron content as a proxy. Hence, this effect was directly related to the surface charge density. The average iron dissolution at pH3 was $4.38 \cdot 10^{-5}$ $\pm 2.10 \cdot 10^{-5}$ mol/L. By using the surface area of magnetite per litre, 21.5 m^2/L one can calculate the effect on the 'excess amount of H^+ protons' per square meter followed by the effect on surface charge density (C/m^2) when Faraday's constant is used. This is an effect of 0.39 C/m^2, which is significant considering the experimental spread of 0.2 C/m^2. Whereas this effect, judging from Mayant et al. [62] trend, would be 0.17 C/m^2 at pH 4, which is within the experimental spread. Hence, only the portions of the titrations curves at pH's above pH 4 were considered to reflect the surface charge density of the magnetite. This is also done by Wesolowski et al. [121] as the proton consumption is a kinetically-controlled process which the study is 'not able to correct for'. Consequently, this study applied all the polynomial fits (for pH_{infl} calculation) up until pH4, excluding the lower pH region.

The dissolved ferrous iron measured after the high temperature titrations of 150 °C, all remained under the measured values of Wesolowski et al. [121]. Wesolowski et al. [121] reports no significant effect of the magnetite dissolution on the surface charge density curve at 150 °C up until pH 5. A similar outcome can be assumed for this study. The reason: Wesolowski et al. [121] has a similar magnetite surface area of 34.6 m^2 per litre solution compared to this study, 32.3 m^2 per litre.

It can be concluded that the dissolution of magnetite had no significant impact on the surface charge density curves of 25 °C, and of 150 °C, up until pH 4, and pH 5, respectively. All parts of the curves below these values were not considered to reflect the magnetite surface charge.

4.6. Film former adsorption to magnetite colloids

The adsorption behaviour of ODA, and OLDA to magnetite colloids at pH 7, and pH 11, at 25 °C was investigated according to, section 3.6. This was, among others, to verify the amount of FFA adsorbed over time at the starting pH values of the potentiometric titrations. This served as input for the equilibrium time, plus determination of the background effect of free FFA, a weak base, on the surface charge density calculation. The ODA and OLDA concentration left in solution over time are plotted in Figure 4.15 and Figure 4.16.

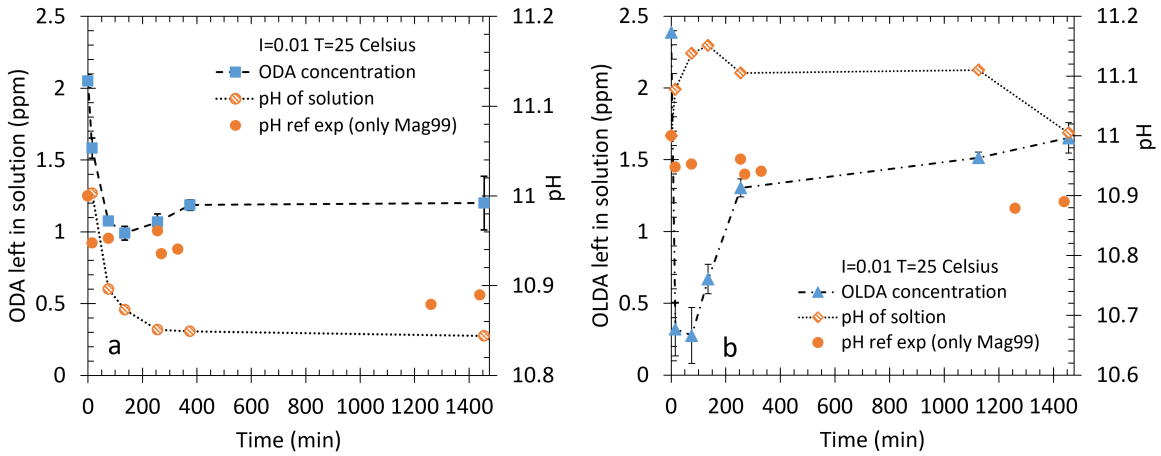

Figure 4.15: a: ODA and b:OLDA left in a 10g/L dispersed magnetite solution over time. The solution starting at pH 11, pH also recorded over time.

Figure 4.15a and b shows a similar trend for ODA, and OLDA adsorption: a quick adsorption in the first 15 to 75 minutes, followed by a desorption, to finally reach an equilibrium after 400 minutes. For OLDA this trend is more extreme. Figure 4.16a and b also shows a similar trend for ODA and OLDA adsorption: a quick adsorption within 15 minutes, almost reaching the equilibrium value. This value was reached after approx. 330 to 360 minutes.

Assuming 1st order kinetics. The Henry adsorption constants (calculated by Equation 2.17) for the adsorption of ODA and OLDA onto magnetite, at pH7, were 0.1395, and 0.2016 L/m^2, respectively. For the adsorption of ODA and OLDA, at pH11, this constant was, 0.0329, and 0.0332 L/m^2, respectively. These are very low compared to the reported constant, 45 L/m^2, of OLDA adsorption onto stainless steel at pH 8.5-8.8 at 25 °C [39]. Furthermore, the low Henry adsorption constants could be ascribed to the relatively low temperature, as literature reports better adsorption of FFA onto surfaces at higher temperatures [17, 20, 40, 44].

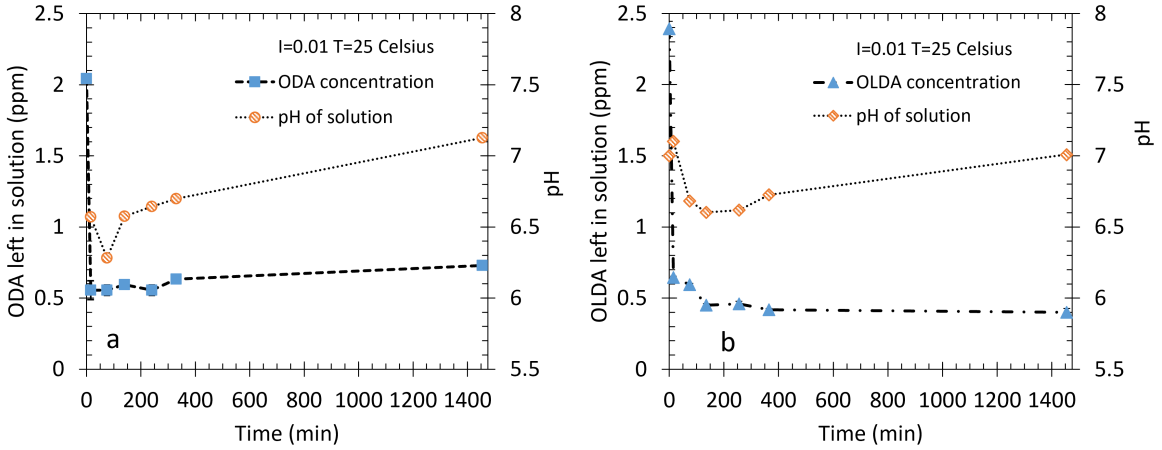

Figure 4.16: a: ODA and b:OLDA left in a 10g/L dispersed magnetite solution over time. The solution starting at neutral pH, pH also recorded over time.

To summarise, the adsorption of ODA and OLDA onto magnetite particles was better at pH7 than pH11, overall the adsorption was quite poor compared to adsorption onto metal surfaces. Regarding the potentiometric titrations of magnetite and FFA suspensions: in both neutral, and alkaline pH (pH 11), 15 to 30 minutes was enough to reach the max FFA adsorption value. Not to confuse with the equilibrium value, as at pH11 the FFA desorbed again. Lastly, the unadsorbed FFA (ODA or OLDA), being a weak base, was calculated to not significantly effect the surface charge density. PHREEQC was used to determine the effect of 0.5 ppm free OLDA on the 'excess and missing protons' per unit area on a 10g/L magnetite solution (total surface area of 21.5 m^2/L), and subsequently to C/m^2. This would lead to a surface charge density increase of 0.06 to 0.05 C/m^2 in the region pH3 to pH9 and less than 0.05 C/m^2 after pH9. These values were less than the experimental spread of 0.2 C/m^2.

It should be noted that the adsorption of ODA and OLDA onto magnetite at pH 11, followed an uncommon pattern, of adsorption and desorption before it had reached equilibrium. A reason for this could be assigned to the way FFAs adsorb. According to the hypothesis of Turner, Hadju and Gasnier [32, 38, 113, 114], OLDA binds to a surface site on the magnetite via the free electron pair of an amine group. In addition, Potapova et al. [82], reports on the effect of calcium and sodium silicate on the adsorption effect of an anionic surfactant onto magnetite, in the alkaline region. Calcium ions increase the zeta potential of magnetite, less negative, resulting in more anionic surfactant adsorption. Whereas sodium silicate decreases the zeta potential, more negative, resulting in less anionic surfactant adsorption. Considering this, it could be that the FFA quickly adsorbed onto the magnetite before it was deprotonated, and therefore not fully negative yet. As the magnetite slowly became more negative due to deprotonation of the surface groups, also indicated by the decrease of the solution pH, the free electron pairs of the amine groups were repelled by the negative surface. Hence, this led to the desorption of the FFA. This hypothesis is partly supported by the finding of Cuoq et al. [17]. It states that better OLDA adsorption depends on a higher temperature gradient which causes the Seebeck effect, resulting in electrons moving to the colder region of the material. Less electrons at the hotter side in turn results in more FFA adsorption. To test the hypothesis one can add the FFA after the magnetite is halfway-, and after it has reached full negativity. In order to see whether this adsorption and desorption effect is half to what was observed, to non observable. This hypothesis could also account for the reason to why more ODA, and

OLDA were adsorbed onto magnetite at pH 7 compared to pH 11. As at pH 7 the magnetite colloid is not or almost not negatively charged.

The dissociation of FFA into cationic and anionic species, and binding of the cationic species to magnetite could be an additional explanation to why more ODA, and OLDA adsorbed at pH7. More cationic species are present at a lower pH, due to the nature of the dissociation of the FFA, being a weak base. More cationic species means more adsorption. This could be tested by performing similar adsorption experiments onto an uncharged surface at multiple pH intervals.

4.7. Effect ODA on surface charge magnetite colloids

This section presents and discusses the effect of ODA on the magnetite colloid surface charge density curve at 25 °C. Potentiometric titrations performed on a blank solution, magnetite dispersion, and magnetite ODA dispersion were performed in electrolyte strengths of 0.1 and 0.01M, according to section 3.12, to obtain these results. Standard titrations performed are denoted with, acid or base, for the respective titrations with a strong acid or base. Figure 4.17a and b, show the results of the ODA effect on the magnetite surface charge density curves at an ionic strength of 0.01, and 0.1M, respectively.

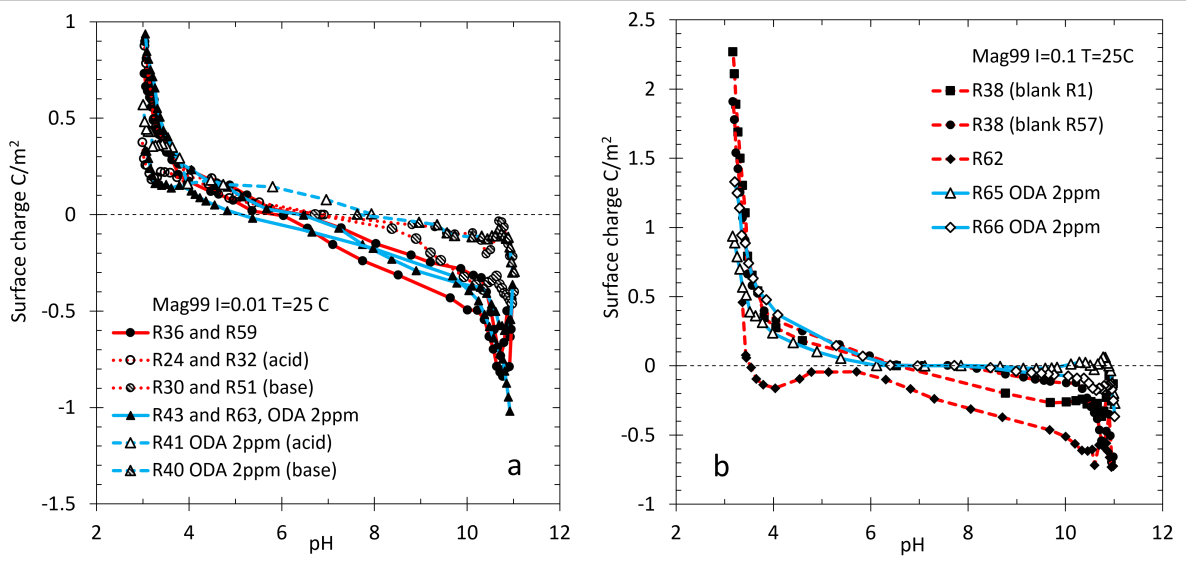

Figure 4.17: Surface charge density of magnetite in the presence and absence of 2ppm ODA, with a background electrolyte strength of a: 0.01M KNO_3, and b:0.1M KNO_3, both at 25 °C. Surface charge density curves determined via the standard method are denoted with: (acid), and (base).

For curves determined via the quick/continuous titration method, no effect of the 2ppm ODA was seen on the magnetite surface charge density curve, see Figure 4.17a. This was judged based on similarity of the experimental scatter of the two magnetite only surface charge density curves (R36 and R59), and 2 performed magnetite and ODA surface charge density curves (R43 and R63). As depicting the standard deviations was not possible due to a non-alignment, with respect to pH, of the produced data points.

For curves determined via the standard titrations method however, it was seen that at a pH between 5 and 7, the presence of ODA increased the surface charge density with approx. 0.1 C/m^2 above the magnetite surface charge scatter. An increase of surface charge density was also observed under presence of ODA at an ionic strength of 0.1M, see Figure 4.17b. As, in the region pH 6 to pH 11, the experimental scatter of the ODA and magnetite surface charge densities (R65 and R66) were well above the scatter of the magnetite surface charge

densities (R38 and R62).

Summarised, at a temperature of 25 °C, and ionic strength of 0.1M the presence of 2ppm ODA increased/neutralised the magnetite (10g/L) surface charge density in the alkaline region. Whereas, a similar temperature, and a lower ionic strength of 0.01, 2ppm ODA did not effect the magnetite (10g/L) surface charge density in the alkaline region. Possible explanations for this are discussed in subsection 4.4.1. Lastly, with 2ppm ODA present the pH_{cip} and pH_{infl} were 6.40, and 7.22 ±0.58 respectively. All pH_{pzc} of this study are related and compared to literature in Figure 4.25.

4.8. Effect OLDA on surface charge magnetite colloids

This section presents and discusses the effect of OLDA on the magnetite colloid surface charge density curves at 25 °C, see subsection 4.8.1, and at 150 °C, see subsection 4.8.2.

4.8.1. Titrations at room temperature

Potentiometric titrations were performed on a blank solution, magnetite dispersion, and magnetite OLDA dispersion, in electrolyte strengths of 0.1 and 0.01M, according to section 3.12. Standard titrations performed are denoted with, acid or base, for the respective titrations with a strong acid or base. Figure 4.18a and b, show the results of the OLDA effect on the magnetite surface charge density curves at an ionic strength of 0.01, and 0.1M, respectively.

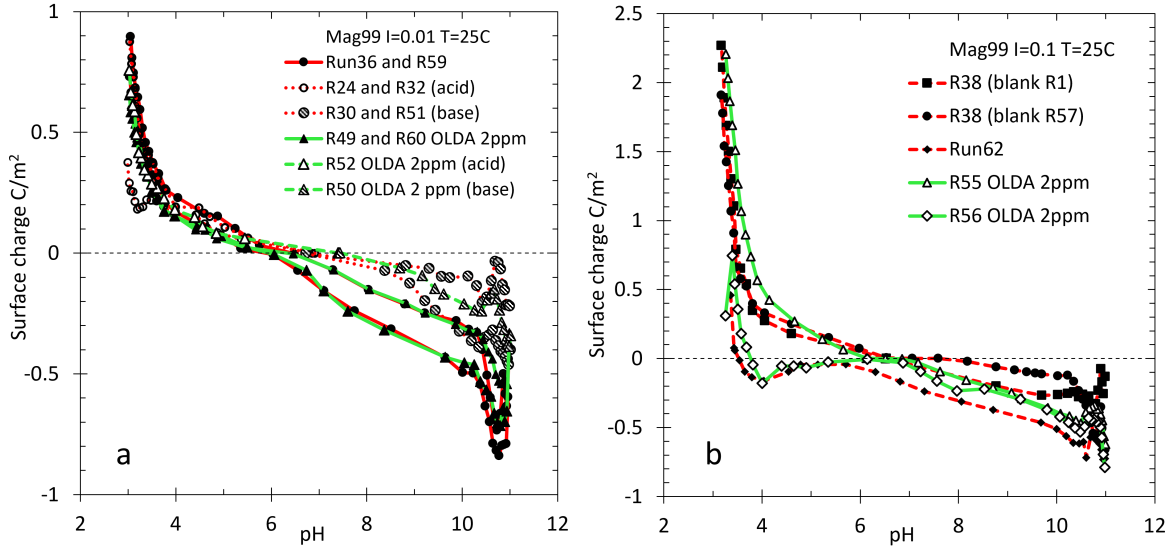

Figure 4.18: Surface charge density of magnetite in the presence and absence of 2ppm OLDA, with a background electrolyte strength of a: 0.01M KNO_3, and b:0.1M KNO_3, both at 25 °C. Surface charge density curves determined via the standard method are denoted with: (acid), and (base).

For all the curves, determined via both the quick titration- and standard method, no effect of the 2ppm OLDA was seen on the magnetite surface charge density, as seen on Figure 4.18a, and b. This was judged based on the similarity of the experimental scatter of the magnetite surface charge density curves, and magnetite and OLDA surface charge density curves. As depicting the standard deviations was not possible due to a non-alignment, with respect to pH, of the produced data points.

It can be concluded that 2 ppm OLDA does not influence the surface charge density of 10g/L magnetite, at 25 °. This accounts for both the ionic strengths of 0.01M and 0.1M. Secondly, with 2ppm OLDA present the pH_{cip} and pH_{infl} were 6.34 ±0.31, and 7.07 ±0.56 respectively. All pH_{pzc} of this study are related and compared to literature in Figure 4.25.

One reason to why no effect of ODA, and OLDA was seen on the magnetite surface charge density could be the low amount of FFA present in the test solution, against the amount of magnetite. Expressed as ppm Magnetite to ppm FFA (Mag/FFA), this ratio was 5000. Compared to the literature [6, 32] this is a very high ratio, see Table 4.2. It would therefore be recommended to apply higher FFA loadings. One should note that the high Mag/FFA ratio of this study was applied due to the low adsorption of FFA onto magnetite, see section 4.6. Too much unadsorbed FFA (a weak base) can disturb the pH measurements, hence the surface charge calculation. In future studies higher FFA concentrations can only be applied when the amount of free FFA is measured during the titration, in order to account for its effect on the pH measurement. Moreover, high FFA loadings can also effect the ionic strength. Bénézeth et al. [6] suggest to perform titrations with both a lower FFA and magnetite concentration, only more precise titrations need to be performed to distinguish any effect from the null (magnetite only) result.

A high Mag/FFA ratio, does not explain why a surface charge density change was observed with 2ppm ODA present at an ionic strength of 0.1M. This could be assigned to a kinematic effect combined with a higher concentrated solution. A higher ionic strength decreases the zeta potential, and diffuse layer thickness [42]. Both combined could have led to more, and more rapid ODA adsorption onto the magnetite, before magnetite itself could have reached a stable surface charge equilibrium. Two indications for this were the adsorption experiments, and fraction FFA left after the titration measurements. See, section 4.6 and Appendix N respectively. The first showing a rapid ODA adsorption followed by desorption, indication that ODA adsorbed before the magnetite layer reached a surface charge equilibrium. The second shows that more FFA was adsorbed at titrations performed under an electrolyte strength of 0.1M. It is therefore recommended to apply longer equilibrium times prior to the addition of an FFA. Longer equilibrium times are not uncommon for surface charge experiments, see Table 4.2.

Table 4.2: Comparison of the equilibrium time, and ppm Magnetite to ppm FFA ratio applied in this study to literature Bénézeth et al. [6], Gasnier and Lister [32], Regazzoni et al. [88], Wesolowski et al. [121], and Zebardast et al. [123].

Study	Equilibrium time	Ratio Mag/FFA
This study 25C	15-30 min	5000
This study 150C	2 hours	5000
Wesolowski et al. 2000	Overnight	-
Zebardast et al. 2014	2 hours	-
Regazzoni et al. 1983	1.5 hours	-
Gasnier and Lister 2013	20 hours	40
Bénézeth et al. 2009 (amines)	Overnight	250 - 50

4.8.2. Titrations at 150 degrees Celsius

Potentiometric titrations performed on a blank solution, magnetite dispersion, and magnetite OLDA dispersion were performed in an electrolyte with strength 0.01M, according to section 3.13. Figure 4.19a shows the OLDA effect on the magnetite surface charge density curves at a temperature of 150 °C, and ionic strength of 0.01M. Figure 4.19b shows the comparison of the magnetite surface charge density to literature [121, 123].

No effect of the 2ppm OLDA was seen on the magnetite surface charge density, as seen on Figure 4.19a. This was judged based on the similarity of the experimental scatter of the

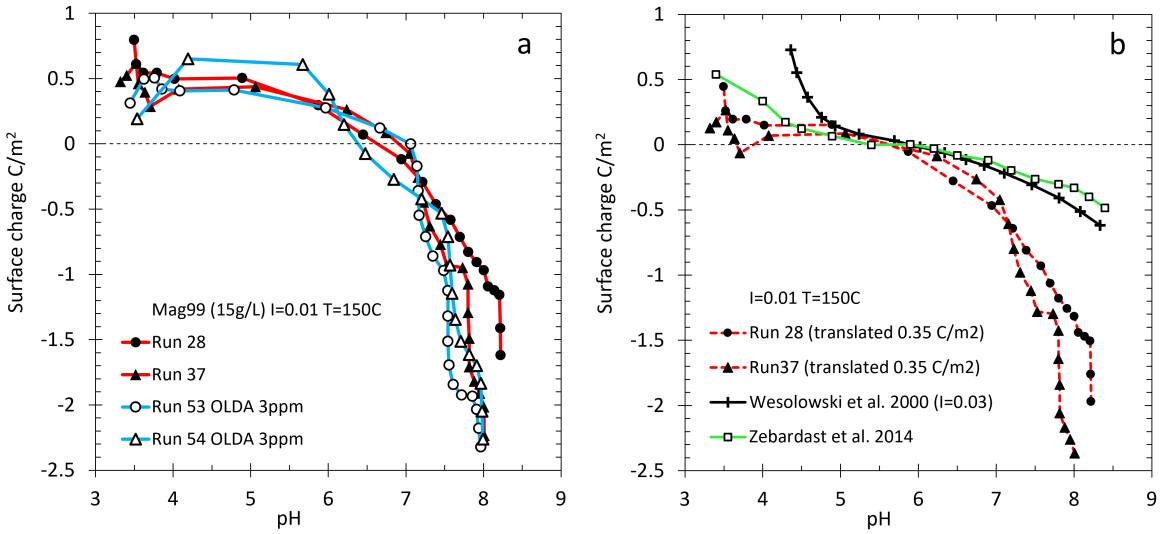

Figure 4.19: Surface charge density of magnetite in the presence and absence of 3ppm OLDA, with a background electrolyte strength of 0.01M KNO_3, at 150 °C. b: comparison of magnetite surface charge densities with literature Wesolowski et al. [121] and Zebardast et al. [123]. Experimental data shifted until pH_{infl} reached the net zero consumption line.

magnetite surface charge density curves (R28 and R37), and magnetite and OLDA surface charge density curves (R53 and R54).

It can be concluded that 3 ppm OLDA does not influence the surface charge density of 15g/L magnetite, at 150 °C, and ionic strengths of 0.01M. Secondly, with 3ppm OLDA present the pH_{infl} was 5.19 ±0.21. In comparison, the pH_{infl} with no OLDA present, was 4.94 ±0.05. All pH_{pzc} values of this study are related and compared to literature in Figure 4.25.

Again, the reason to why no effect of the OLDA was seen on the surface charge density of magnetite could be the low amount of OLDA present in the test solution, as already discussed in subsection 4.8.1. Also see Table 4.2.

The magnetite surface charge density curves determined by the high temperature potentiometric titrations should be considered with caution. As it is assumed that the pH- and reference electrode combination (ZrO_2 based pH probe and a Ag/AgCl reference probe) drifted toward more acidic pH values during the duration of the experiments. This is believed, despite calibrations of the electrodes repeatedly indicated a Nernstian trend (within the manufacturers set range of the theoretical value), see subsection 3.10.1, due to the following two reasons. The first reason are the proton concentration calibration plots of Run 10 and Run 11, see section 3.11. The 'Sb' values derived from these runs were quite low compared to what was calculated using PHREEQC. In addition, the 'Sb' value of Run 20, a standard titration of a blank solution with base starting from neutral pH, was 0.1405. This is an extremely low value. According to Szekeres and Tombácz [101] this would correspond to a malfunctioning probe. The second reason follows from the comparison of the experimental magnetite surface charge densities (Run 28 and 37) to the literature [121, 123], see Figure 4.19b. It shows a steep decline of the surface charge density curves in the alkaline region. Higher surface areas, leading to more proton adsorption could not have been the cause, according to the particle size measurements, see section 4.9. All considered, these curves should actually thus be considered as relative surface charge densities rather than absolute surface charge densities.

The probe drift could have been caused by the temperature effect on the external reference Ag/AgCl electrode. As the temperature of the Ag/AgCl section affects the potential of the

probe, e.g. when the temperature of the probe varies between 25 °C and 75 °C, the potential is affected by 25mV. Taken the measured calibration slopes, at 150 °C, of approx. 75 mv/pH this effect can lead to a 0.3 pH change. The temperature effect could be cancelled out in case the temperature of the external probe section is controlled at the same value during calibration and during measurements [43]. This was not done during this study. Moreover, a calibration time of 30 min to 1 hour was applied, opposed to an equilibrium times of 15 min, and 2 hours for blank, and magnetite titrations, respectively. Therefore it was suspected that the reference probe was probably hotter during the magnetite titrations, leading to a higher potential reading (ergo. lower pH values). For future research a cooling unit, formed with a thin copper wire tubing wrapped around the reference probe would be recommended.

4.9. Effect of various conditions on the magnetite colloid size

This section describes the effect of the various titration conditions, including ODA, and OLDA, on the magnetite colloids, in terms of particle diameter. The average particle sizes after each titration were determined via PSD, subsection 4.9.1, and digital microscopy, subsection 4.9.2.

4.9.1. Effect on size determined by PSD

The particle size distribution of magnetite particles after a titration were determined according to the procedure explained in subsection 3.14.1. The average values of the PSD measurements are presented in Figure 4.20.

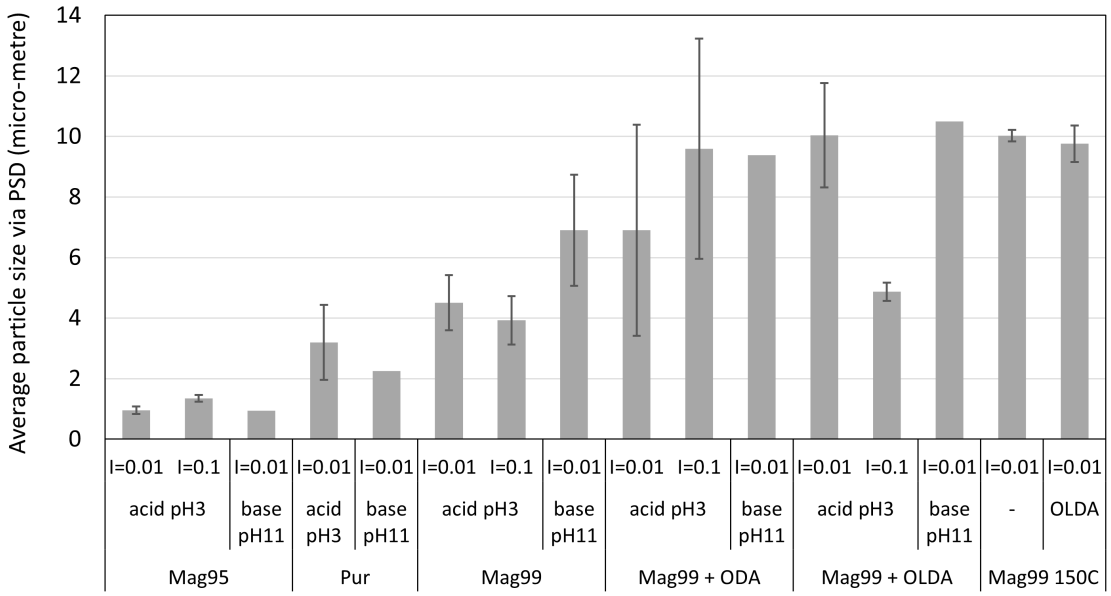

Figure 4.20: Particle size of magnetite particle after the titrations measured with PSD. Titrations categorised based on commercial magnetite (Mag95, Mag99 and Pur) used, in combination with ODA or OLDA, the final pH value of titration (pH 3 or pH 11), and the ionic strength of the electrolyte.

Figure 4.20 shows that the magnetite particles of the 95% reagent grade magnetite powder (Mag95) were the smallest, followed by the Puratronic, and 99.99% reagent grade magnetite (Mag99). This correlates to the BET determined surface areas, see Table 3.7, as bigger particles generally yield a lower surface area. Furthermore, Mag99 was smaller after titrations ending at a pH of 3 than titrations ending at a pH of 11. Possibly due to the strong dissolution of this magnetite in the low pH range.

From the data it follows that, at 25 °C, the presence of 2ppm ODA, and OLDA both resulted in bigger magnetite particles. Magnetite particles after the titrations with ODA, and OLDA were 59.64%, and 66.94% bigger compared to the magnetite only titrations, respectively. This is in line with findings of Gasnier and Lister [32]. Namely they reported the agglomeration of a 30ppm dispersed magnetite solution containing 0.9ppm FFA.

From the experimental data, observations, and literature the following hypothesis is formed, to explain why ODA and OLDA did not seem to effect the surface charge but did cause agglomeration of magnetite particles. Namely, at lower concentration ratios of FFA to magnetite, the FFA mainly acts as a flocculant. Whereas at higher concentration ratios it will mainly act as a coagulant, neutralising the charge to eventually act as a dispersant by providing a positive charge in the alkaline region combined with possible sterric effects. This is analogous to the use of polyelectrolytes, in particular cationic polyelectrolytes, within water treatment applications. These molecules react with colloidal matter by neutralising the charge, or bridging them together, and when an excess amount is adsorbed, the particles can be restabilised, either by charge reversal or by steric stabilisation [29, 102].

Literature supporting the hypothesis, made in the previous paragraph, are observations of magnetite particle agglomeration by FFA during bench-top boiling experiments, and cationically stabilised magnetite particles at a higher FFA to magnetite concentration ratio, during zeta potential measurements [32]. Moreover, Gasnier and Lister [32] reason that FFA adsorbs onto the magnetite FeOH sites and is partly protonated afterwards, see subsection 2.6.4. Indicating that at low FFA/Magnetite loading the FFA causes agglomeration, at higher FFA/Magnetite loading it causes charge reversal and stabilisation. Experimental data, of this study, supporting the hypothesis was the charge neutralisation of magnetite at 25 °C, and ionic strength of 0.1M, by 2ppm ODA, together with the effect of ODA, and OLDA on particle size. All together this indicates both coagulant and flocculant characteristics to be present. Lastly, observations made after the adsorption experiments show, for both ODA and OLDA, some stabilised magnetite particles, see section M.2. Also, some particles observed with the digital microscope indicated stabilisation (probably hydrophobic in nature), similar to what is observed for polymeric surfactant stabilisation [27], see section M.1.

Multiple titrations and subsequent PSD measurements could be performed, applying different FFA to magnetite ratios, in order to assess whether the hypothesis, discussed in the previous two paragraphs, is indeed valid.

4.9.2. Effects on size determined by digital microscopy

The particle size distribution of magnetite particles after a titration were determined according to the procedure explained in subsection 3.14.1. The average values of the PSD measurements determined via digital microscopy are presented in Figure 4.21.

Figure 4.21 shows that the magnetite particles of the 95% reagent grade magnetite powder (Mag95) was the smallest, followed by the Puratronic, and 99.99% reagent grade magnetite (Mag99). This corresponds to the BET determined surface areas, see Table 3.7. Furthermore, Mag99 measured after titrations that end at pH3, appeared to be smaller. A possible reason could be to the stronger dissolution of this magnetite. These trends were also observed for the PSD determined magnetite particle sizes. However, in contrast to the particle size results determined via the PSD, no change in magnetite particle size was observed via the digital microscope. Magnetite particles after titrations with ODA, and OLDA included were 8.53% smaller, and 5.94% bigger compared to the magnetite only titrations, respectively. In addition particle sizes determined via the digital microscope appeared to be approx. 3 times bigger

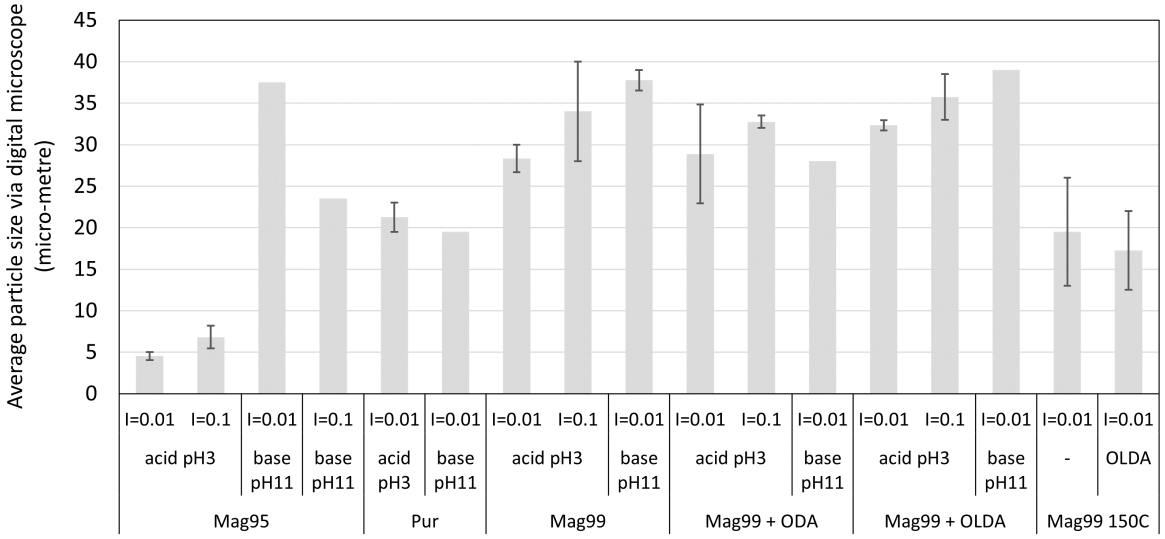

Figure 4.21: Particle size of magnetite particle after the titrations measured with Digital Microscope.

than via PSD.

The difference in results might be caused by the nature of the measurements. The PSD presumably breaks up particles. Namely, in the PSD particles are carried by a flow, passing a laser light source, the detected diffraction is used to determine its size. Whereas particles examined under a microscope lie still between two microscope slides. Secondly, magnetite particles were examined at a magnification of 100 times, a higher magnification/resolution could have helped the software to better distinguish between particles, see Figure 3.9.

4.10. PHREEQC surface charge model curves

This section presents the results obtained after the fitting exercise, performed according to section 3.15. Subsection 4.10.1 presents the SCM curves, based on the fitting to the experimental magnetite surface charge density curves. The following subsection, 4.10.2, presents the simulated effect of ODA, and OLDA on the magnetite surface charge density, using the SCM.

4.10.1. Magnetite surface charge model curves

Experimentally determined magnetite surface charge density curves have been simulated with the PHREEQC SCM. The SCM was first fitted to the experimentally obtained magnetite (Mag99) surface charge density curves. To obtain the equilibrium constants, pKa1 and pKa2, governing the protonation-, and deprotonation reactions of the surface active groups, and to obtain the amount of sites per square nanometer. This simulation is presented together with the a similar simulation, and surface charge density data of Mayant et al. [62] in Figure 4.22. Other potentiometric titrations were also used for fitting the SCM model, Table 4.3 summarises the titration runs modelled, together with the RMSE values of the fit, and the fitting parameters.

From Figure 4.22 it can be seen that, in general, the SCM curve with fitted parameters: pKa1 = 5.7, pKa2 = 7.3 and sites 30 (/nm^2) was quite similar to the experimentally determined magnetite surface charge density scatter. Moreover, the model corresponds well to the model of Mayant et al. [62], which is based on similar pKa values. The average pKa value of the SCM model was 6.5. This value corresponds to the pH_{pzc}, following the relation given in

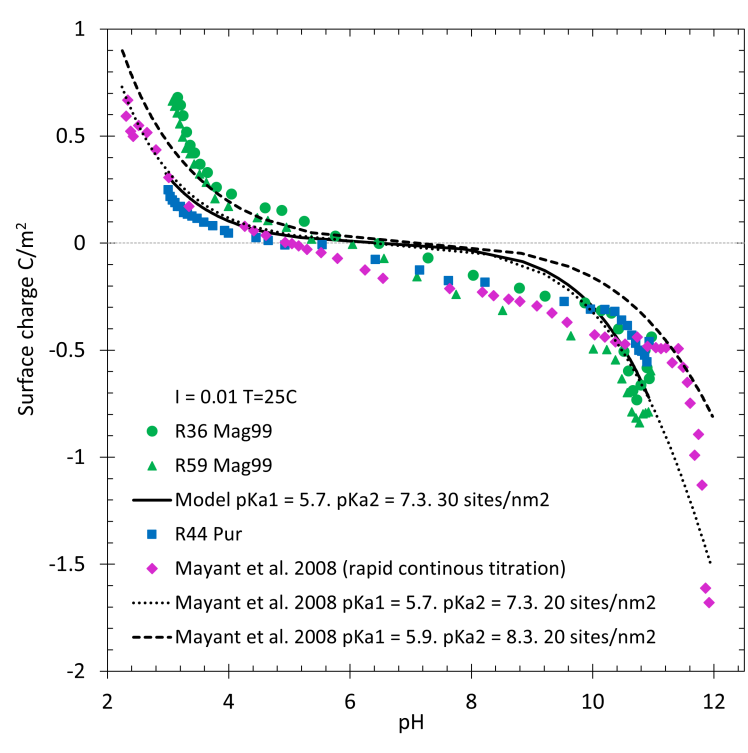

Figure 4.22: Fit of surface complexation model (solid line) on the surface charge density of magnetite, with a background electrolyte strength of 0.01M KNO_3, at 25 °C. Compared with surface complexation model (dashed lines) and experimental data of Mayant et al. [62].

Equation 2.33. All pH_{pzc} of this study are related and compared to literature in Figure 4.25. RMSE values were calculated for the model fit of Mayant et al. [62] to its own experimental data, see Table 4.5. This was to relate the fit of the SCM to literature. It is concluded that the fitted SCM was able to adequately simulate the surface charge density curve.

The SCM appeared to adequately simulate the surface charge density. However, it should be discussed whether this was a case of parameter overfitting. Furthermore, certain differences between the model simulation and the experimental data should be addressed.

To start with the differences between the model simulation and the experimental surface charge data. The model, and experimental data generally deviate from each other at two points. At a pH below 4, the experimentally determined surface charge density was approx 0.3 C/m^2 higher compared to the model, and at a pH between 6 and 9, the experimental surface charge density appeared to be linear, whereas this was curved in the simulation. The first deviation could be explained by the magnetite dissolution, as discussed in section 4.5. The second deviation could be explained by the adsorption of a specific ion, e.g. calcium. When calcium adsorbs onto an active surface site a H^+ proton is released. This proton lowers the pH and therefore impacts the surface charge calculation, resulting in a more negative charge (in the alkaline region). This effect of 2ppm calcium has been modelled, see Figure O.1a.

Concerning the overfitting. According to Blesa et al. [11] and Philippini et al. [79] the pKa1 and pKa2 values range between 3.87 and 5.1, and 8.26 and 9.10, respectively. The obtained values of pKa1 (5.7) and pKa2 (7.3) were both outside of this reported range. pKa values closer to the neutral point of water (pkw) result in higher simulated surface charges on either sides of this point. In this respect the data could be overfitted. Considering the amount of surface sites per nm^2, a value of 30 was selected. This value is higher compared to the model

value of 20 sites/nm^2 from Mayant et al. [62] and 21.8 sites/nm^2 from Wesolowski et al. [121]. However it was seen that for a site density of 20 and 30 generally similar surface charge density curves were obtained, see Figure 4.22. Still a surface charge density of 20 is quite high compared to the results of Tombácz et al. [106]. This study indicates a number of 1 to 2 surface sites per nm^2. To rule out overfitting, it would be recommended to reassess the model fit to the experimental data, using a site density of 2 sites/nm^2 and pKa values within the range reported by literature [11, 79].

Table 4.3: PHREEQC SCM fitting parameters with respective runs the SCM was fitted onto, and RMSE of the fit.

Data from experiments				Fitted parameters						
Temp	**Magnetite**	**Ionic S**	**FFA**	**Pka 1**	**Pka 2**	**Pka ave**	**Pkad FFA**	**Sites/nm^2**	**RMSE**	**Fit to runs**
25	Pura	0.01	-	5.3	-7.8	6.55	-	20	0.0842 ±0.0116	R14,15,44
	Mag99	0.01	-	5.7	-7.3	6.5	-	30	0.1471 ±0.0238	R36, 59
		0.1	-	5.7	-7.3	6.5	-	10	0.1991 ±0.0201	R38,62
		0.01	ODA	5.7	-7.3	6.5	15	29.5	0.1077 ±0.0103	R43, 63
		0.1		5.7	-7.3	6.5	15	10	0.2268 ±0.0027	R65,66
		0.01	OLDA	5.7	-7.3	6.5	15	5	0.1248 ±0.0393	R49,60
		0.1		5.7	-7.3	6.5	15	5	0.1524 ±0.0004	R55,56
150	Mag99	0.01	-	4.8	-5.5	5.15	-	30	0.5806 ±0.0526	R28,37
		0.01	OLDA	4.8	-5.5	5.15	15	29.3	0.2681 ±0.0238	R53,54

4.10.2. Magnetite and FFA surface charge model curves

The experimental data of the FFA and magnetite surface titrations did not yield any significant effect of the added FFA on the surface charge density, see section 4.7 and section 4.8. Hence, fitting the SCM to this data was not performed as described in subsection 3.15.2. Instead, the effect of 2ppm ODA, and OLDA on the magnetite (10 g/L) surface charge density has been simulated with the PHREEQC SCM, using an selected FFA pKad value of 15. The results can be seen in Figure 4.23a, and b. In addition, the effect of 2.5ppm OLDA on the surface potential of 100ppm magnetite has been modelled, after the experiment of Gasnier and Lister [32], these results are presented in Figure 4.23c, and d.

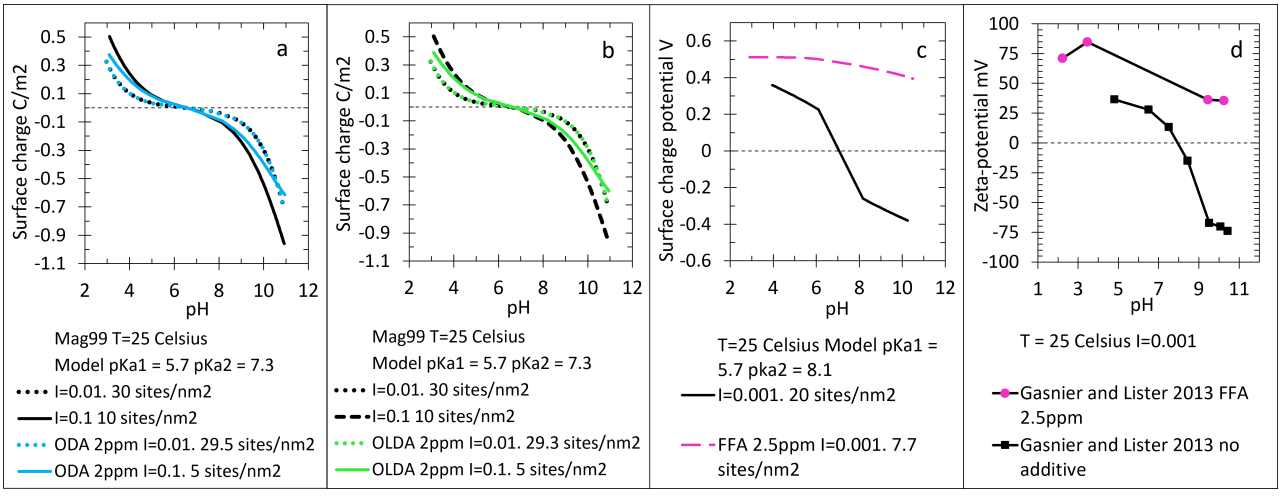

Figure 4.23: a: surface charge simulation of the magnetite titration with and without ODA present, b: surface charge simulation of the magnetite titration with and without OLDA present, c: Surface potential simulation using the experimental parameters of Gasnier and Lister [32] as input, d: Gasnier and Lister [32] experimental zeta potential measurements.

Figure 4.23a, and b, indeed indicate no change of the simulated surface charge density of magnetite, at 25 °C, and ionic strength of 0.01 when both ODA or OLDA were included into the model. The best fit was obtained for the magnetite surface charge density simulation, at 25 °C, and ionic strength of 0.1, when a surface site density of 10 sites/nm^2 was used. For similar conditions, and including 2ppm FFA to the model, the best fit was obtained with a surface site density of 5 sites/nm^2. These lower surface sites could indicate that the magnetite surface charging did not reach equilibrium during the experiment at a higher ionic strength, especially so when an film former was present. This seems to support the hypothesis formulated in subsection 4.8.1. It states that at higher ionic strengths, especially when ODA was present the magnetite needs more time to reach equilibrium.

To test the hypothesis formulated by Gasnier and Lister [32] based on observations and literature [38, 113, 114], see subsection 3.15.1. The effect of OLDA on the surface potential of magnetite was simulated using the experimental data of Gasnier and Lister [32], basically using a ppm Magnetite to ppm OLDA ratio of 40. The input parameters of the model can be seen in Table 4.4. The hypothesis of Gasnier and Lister [32] states that an OLDA molecule adsorbs onto a surface site via the free electron pair of the amine group, while the other amine group acquires a positive charge due to protonation. Figure 4.23c, and d, show the result of the PHREEQC simulation, and experimental results of Gasnier and Lister [32], respectively. It can be seen that the simulated surface potential follows a similar trend as the measured zeta potential. This makes the hypothesis plausible. Lastly, two things should be mentioned. First, an one to one comparison was not possible as this study simulated the surface potential, whereas Gasnier and Lister [32] give the effect of FFA on the zeta potential. Second, the IEP reported by Gasnier and Lister [32] is higher than the commonly accepted pH_{pzc} range of 6 to 7. Gasnier and Lister [32] believe this is due to protonated amine adsorption as result of the use of a weak base (ammonia) to adjust the pH during the experiment.

Figure 4.24a, shows the results of the SCM surface charge density simulation of magnetite, at 150 °C after the fitting exercise. The best fit was obtained when a specific surface area of 12 m^2/g was used together with an ionic strength of 0.02M. This could indicate that the specific surface area during the 150 °C titration was much higher than the expected 2.15 m^2/g, and the ionic strength too. Although this could be overfitting. A more plausible explanation is the drifting of the high temperature probes, leading to more negative surface charge density data. As discussed in subsection 4.8.2. Therefore, the PHREEQC SCM model was also fitted to magnetite surface charge density data, at elevated temperature, obtained from literature [121, 123]. This was done to still obtain pKa1 and pKa2 values over temperature.

Figure 4.24a, also shows the surface charge density data of Wesolowski et al. [121], and the results of the SCM fit to this data. The experimental data (e.g. specific surface area of 0.922 m^2/g) of Wesolowski et al. [121] was used as input for the SCM. A better fit was obtained without increasing the specific surface area by a factor of 6. Table 4.4 summarises the results of the SCM fits to the literature surface charge data, together with the RMSE values of the fits, and fitting parameters.

Wesolowski et al. [121] also fitted his model to his own experimental data, an one pKa model. The calculated RSME of the best and worst reported fits of Wesolowski et al. [121] are given in Table 4.5. The reason on why the RMSE values of Wesolowski et al. [121] are lower could be the additional parameters incorporated into his model. One of them is the additional specific cation binding constant, above 100 °C, to fit the steep asymmetrical surface charge curves above the pH_{pzc}.

Lastly, Figure 4.24b also indicates no change of the simulated surface charge density of magnetite, at 150 °C, and ionic strength of 0.01 when OLDA was included into the model. This

is in line with the low ppm FFA ratio to ppm Magnetite ratio to yield any significant effect, as discussed in subsection 4.8.1.

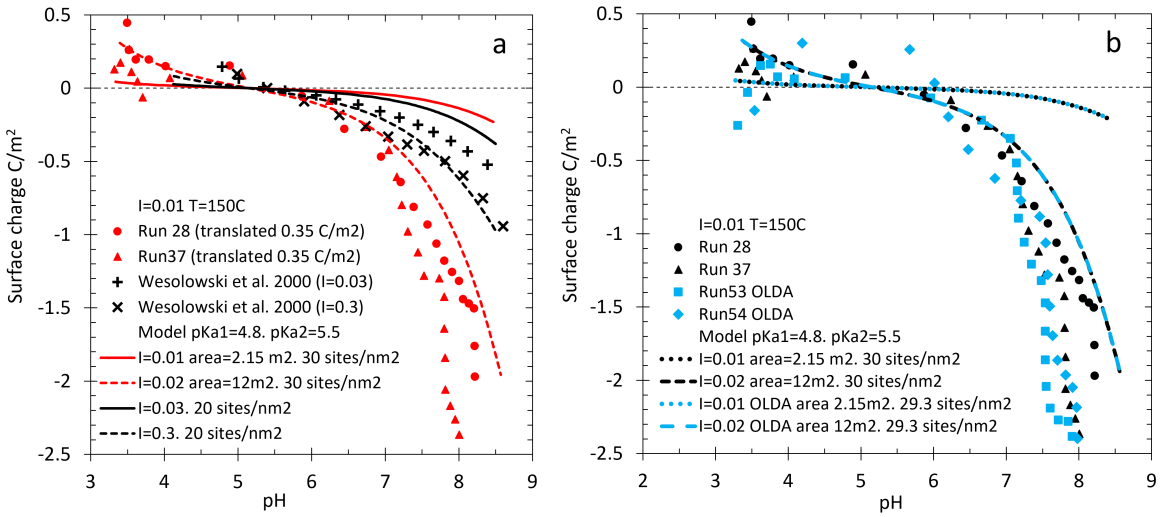

Figure 4.24: a: fit of the surface complexation model (red lines) on the experimentally determined surface charge density of magnetite (red dots), with a background electrolyte strength of 0.01M KNO_3, at 150 °C. The black lines and black dots represent the SCM fit onto the experimental data of Wesolowski et al. [121]. b: SCM simulation of the surface charge density with FFA present, at 150 °C and ionic strenght of 0.01M.

Table 4.4: PHREEQC SCM fitting parameters with respective literature data the SCM was fitted onto, and RMSE of the fit. Data from Gasnier and Lister [32] and Wesolowski et al. [121] and Zebardast et al. [123] was used.

Data from literature				Fitted parameters						
Temp	**Magnetite**	**Ionic S**	**FFA**	**Pka 1**	**Pka 2**	**Pka ave**	**Pkad FFA**	**Sites/nm2**	**RMSE**	**Fitted to**
25	Pura	0.001	OLDA	5.7	-8.1	6.9	15	7.71	N/A	Gasnier and Lister 2013
150	Synthesis	0.03	-	4.8	-5.5	5.15	-	20	0.0862	Wesolowski et al. 2000
		0.3	-	4.8	-5.5	5.15	-	20	0.0638	Wesolowski et al. 2000
150	Pura	0.01	-	4.8	-5.5	5.15	-	20	0.1431	Zebardast et al. 2008
	Pura	0.1	-	4.8	-5.5	5.15	-	20	0.2596	Zebardast et al. 2008
200	Pura	0.1	-	4.3	-4.9	4.6	-	20	0.1775	Zebardast et al. 2008
250	Synthesis	0.03	-	4	-4.6	4.3	-	30	0.1325	Wesolowski et al. 2000
		0.3	-	4	-4.6	4.3	-	30	0.1079	Wesolowski et al. 2000
290	Synthesis	0.03	-	4.2	-4.7	4.45	-	30	0.0911	Wesolowski et al. 2000
		0.3	-	4.2	-4.7	4.45	-	30	0.0793	Wesolowski et al. 2000

Table 4.5: Calculated RMSE values of SCM fits to respective experimental surface charge density curves, both obtained from literature, Mayant et al. [62] and Wesolowski et al. [121].

Models, obtained from literature, fitted to own experimental data										
Temp	**Pka values**	**Ionic S**	**FFA**	**Pka 1**	**Pka 2**	**Pka ave**	**Pka FFA**	**Sites/nm2**	**RMSE**	**Study**
22	Pura	0.01	-	5.7	-7.3	6.5	-	20	0.1948	Mayant et al. 2008
				5.9	-8.3	7.1	-	20	0.2507	Mayant et al. 2008
50	Synthesis	0.03	-	6.59*	N/A	6.59	-	21.8	0.0496	Wesolowski et al. 2000
150	Synthesis	0.03	-	5.7*	N/A	5.7	-	21.8	0.0276	Wesolowski et al. 2000

* only one pKa as Wesolowski et al. [121] is an one pKa model

4.11. Experimental and modelled PZC over temperature

Figure 4.25 shows the comparison of the results obtained in this study, being the experimentally determined pH_{pzc} (more specific pH_{cip}, and pH_{infl}), and fitted pKa average values of the SCM model, with a number of results obtained from literature [3, 91, 117, 121, 123]. The figure demonstrates that the values of this study are in good agreement with the values of Barale et al. [3], Schoonen [91], Vidojkovic et al. [117] and the pH_{cip} values of Wesolowski et al. [121].

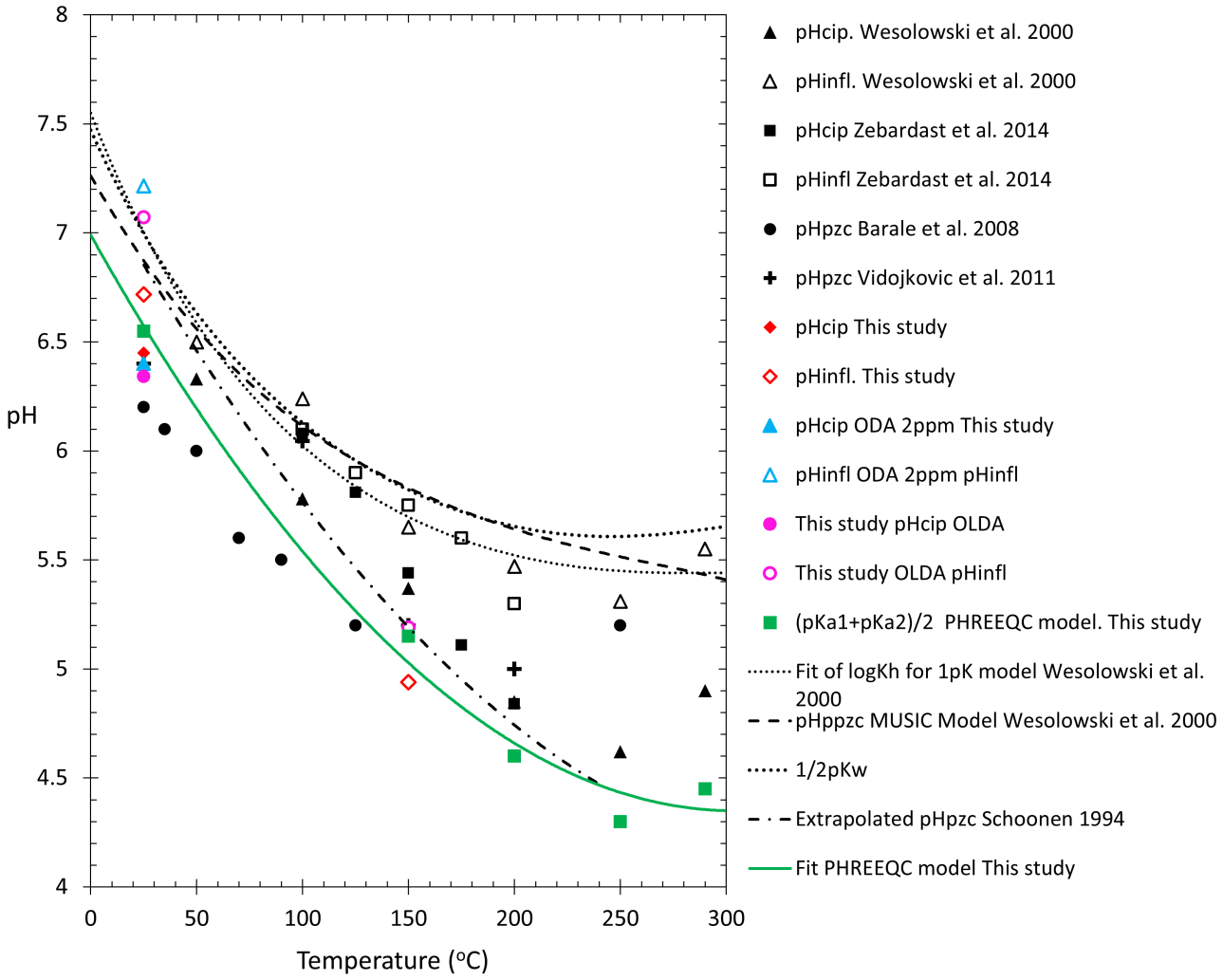

Figure 4.25: Effect of temperature and FFA on the pH_{cip}, pH_{infl} and pKa_{ave} for magnetite (Mag99) obtained from the titrations, and SCM fitting over a temperature range of 25 to 290 °C and ionic strengths of 0.1M, and 0.01M KNO_3. Compared with a number of published results for theoretical, modelled and experimental vales of the pH_{pzc} of magnetite. Results obtained from Barale et al. [3], Schoonen [91], Vidojkovic et al. [117], Wesolowski et al. [121], and Zebardast et al. [123].

Figure 4.25 shows that in the study of Wesolowski et al. [121] and Zebardast et al. [123] the pH_{infl} points are also higher than the pH_{cip} values. Furthermore it can be seen that the presence of ODA, and OLDA increased the pH_{infl} of the magnetite slightly. At 25 °C ODA, and OLDA increased the pH_{infl} from 6.718 ±0.3076, to 7.215 ±0.580, and 7.072 ±0.560, respectively. At 150 °C OLDA increased the pH_{infl} from 4.94 ±0.05 to 5.19 ±0.21. Whereas, the pH_{cip} remained unchanged. The kinematic/equilibrium effect could be a reason for this, discussed

in subsection 4.8.1. The argument is that an intersecting point of two surface charge density curves could not easily be affected by kinetics, but the shape of the curve could, especially in the extreme pH ends. In turn this can influence the polynomial fit on which the pH_{infl} is determined.

Lastly, it should be noted that the pKa average values of the model from this study, together with the 2nd degree polynomial fit through these points (green points and green line in Figure 4.25) are lower compared to the two models from Wesolowski et al. [121]. The reason is that the model from this study was fitted to its own experimental pH_{pzc} values and the pH_{cip} data of Wesolowski et al. [121]. Whereas Wesolowski et al. [121] fitted his one pKa model assuming the pKa to be equal to his pH_{infl} values.

4.12. PHREEQC surface charge prediction

The effect of various OLDA concentration ratios (ppm Magnetite/ ppm OLDA) at 290 °C in a background electrolyte of 0.01M has been simulated using the PHREEQC SCM model, using the pKa values obtained from the fitting exercise. See section 3.15 for this procedure. The results are given in Figure 4.26.

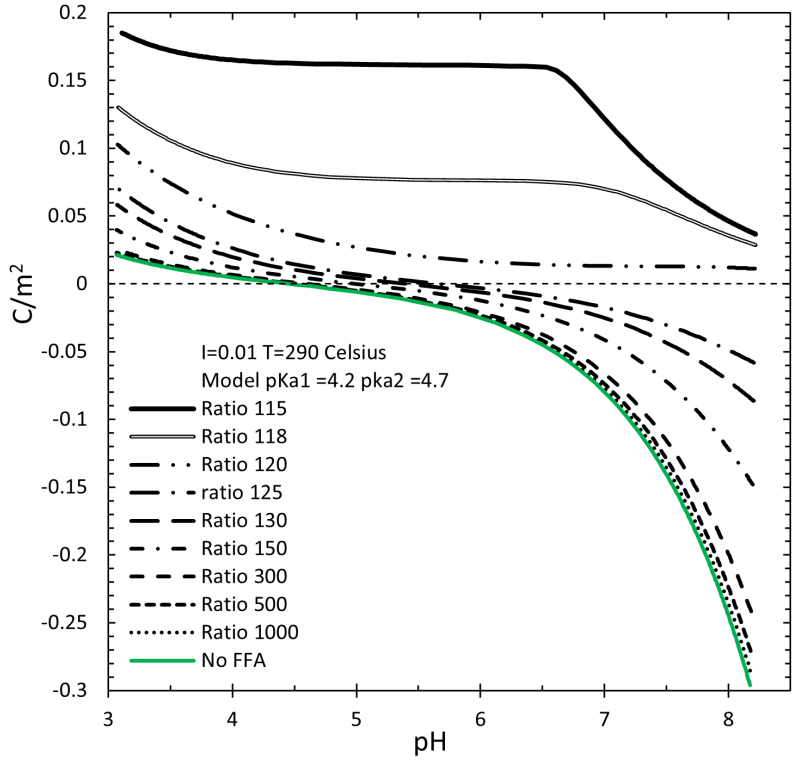

Figure 4.26: Simulated effect of various OLDA concentration ratios (ppm-magnetite/ppm-OLDA) on the surface charge density curve of magnetite at 290 °C and ionic strength of 0.01M. Modelled using a PHREEQC SCM model.

From Figure 4.26 it can be seen that the magnetite has a negative surface charge in the alkaline region (neutral point of water at 290 °C is approx 5.65). At a Mag/FFA ratio of 1000 an increase of the surface charge can be seen, less negative at pH above pzc and more positive at pH below pzc. This trend continues until the charge is positive over the whole pH range, i.e. the flipping of the charge, as reported by Gasnier and Lister [32]. Furthermore, as the ratio decreases the pzc shifts to higher pH values, such a trend is reported by Turner et al. [113]. He reports that the alkalising amines: MOR, ETA and ammonia increase the pH_{pzc} of magnetite from pH 6.7 to 7.2, 7.6, and 8.4, respectively. Eventually, as more OLDA was

present in the model, meaning even lower ppm-OLDA/ppm-Magnetite ratio values, the surface became more positive, resulting in cationic stability.

To determine the validity of this prediction, a similar prediction should be made for a (lower) temperature at which this prediction can be experimentally verified. Additionally the fitting exercise could be repeated using these novel results to improve the pKad value, which was assumed to be 15 as mentioned in subsection 4.10.2. Until this has been done, drawing any conclusions from the simulated predictions would be premature.

5

Conclusions

The main objective of this research was to determine the effect of ODA, and OLDA on the magnetite layer growth and its resistance against acidic FAC pertinent to feed and condensate water, and to determine plus model the effect of ODA, and OLDA on the surface charge density plus pzc of colloidal magnetite. The research questions raised in section 1.6 were answered by performing lab immersion and re-immersion tests, adsorption experiments, potentiometric titrations, and PHREEQC modelling.

1. *What is the effect of ODA, and OLDA, in addition to ammonia opposed to: 1) only ammonia and 2) no chemical additive, on the formation of a (protective) magnetite layer?*

   The immersion tests performed during this study proofed sufficient to grow oxide layers on C1010 metal coupons. X-Ray diffraction measurements indicated that under all chemistries, magnetite was formed as only compound. SEM+EDS cross section images showed that under all additives, thinner layers were formed than under a blank chemistry. Layers formed under ODA, and OLDA, in addition to ammonia were not thinner than those formed under an only ammonia chemistry. Combined with SEM surface images, it was observed that ODA, and OLDA, in addition to ammonia, formed smoother more uniform magnetite layers.

2. *What magnetite layer is best resistant to acidic FAC such as in locally low pH regions and condensate/condenser systems?*

   During the re-immersion tests acidic FAC was simulated with a stirred setup, and an acetic acid chemistry. Magnetite layers formed under ODA added to ammonia, and OLDA added to ammonia were better resistant against acidic FAC than layers formed under the ammonia only chemistry, and blank chemistry, with less reduction of the magnetite layer thickness. SEM surface images of the ODA and ammonia formed layer showed the magnetite crystals to be least affected by dissolution and erosion. The least resistant layer was formed under the blank chemistry.

   Layers formed under both ODA in addition to ammonia, and OLDA in addition to ammonia chemistry offered better protection against acidic FAC, in terms of weight loss based, and SEM derived corrosion rate, than the layers formed under an ammonia only or a blank chemistry.

3. *How do commercial magnetite of 95% purity and 99% purity compare with Puratronic in terms of surface charge over pH and pH_{pzc}?*

   Potentiometric titrations, performed at 25 °C, proofed useful to measure the surface charge density curves of the three commercial magnetite powders. The pH_{pzc} was represented via the pH_{cip} and pH_{infl}. It was found that magnetite 99% reagent grade powder was more similar to Puratronic magnetite in terms of surface charge density and point of zero charge than magnetite 95% reagent grade powder. Both surface charge density curves from Puratronic, and magnetite 99% purity showed to be in good agreement with literature [62, 121]. All considered, magnetite 99% reagent grade powder was considered a suitable Puratronic substitute for further surface charge titrations.

4. *What is the adsorption behaviour of ODA, and OLDA to magnetite particles?*

   24 hour adsorption experiments conducted under nitrogen atmosphere at 25 °C, and pH7, and pH11 were performed to determine the adsorption behaviour of ODA, and OLDA onto magnetite colloids. The adsorption was characterised with the Henry adsorption constant (L/m^2). At pH 11, for both ODA, and OLDA a rapid adsorption was followed by desorption. The suggested reason for this was the repulsion of FFA when magnetite obtained a negative surface charge. At equilibrium, more ODA, and OLDA adsorbed at a neutral pH of 7, 0.1395 L/m^2 for ODA, and 0.2016 L/m^2 for OLDA, than at an alkaline pH of 11, 0.0329 L/m^2 for ODA, and 0.0332 L/m^2 for OLDA. The overall ODA and OLDA adsorption to magnetite powder was relatively poor compared to a literature reported value of 45 L/m^2 for OLDA adsorption to stainless steel [39].

5. *What is the effect of ODA, and OLDA on the surface charge and pH_{pzc} of magnetite at 25 °C, and at an elevated temperature of 150 °C?*

   Potentiometric titrations were employed to measure the surface charge, and determine the pH_{pzc} of magnetite, at an ionic strength of 0.01, and 0.1 mol/kg (KNO_3) in the presence and absence of ODA, or OLDA. As a result of poor ODA, and OLDA adsorption a concentration ratio of 5000 ppm-magnetite/ppm-FFA was used for all the titrations to minimise the effect of unadsorbed ODA or OLDA on the surface charge calculations. At this applied concentration loading, of 5000, it was found that OLDA did not influence the surface charge density curve of magnetite, at 25 °C nor at 150 °C. At a temperature of 25 °C, and ionic strength of 0.1M, ODA increased/neutralised the magnetite surface charge density in the alkaline region. At a similar temperature, and a lower ionic strength of 0.01, ODA did not effect the magnetite surface charge density curve.

   The presence of ODA, and OLDA increased the pH_{infl} of the magnetite slightly. At 25 °C ODA, and OLDA increased the pH_{infl} from 6.718 ±0.3076, to 7.215 ±0.580, and 7.072 ±0.560, respectively. At 150 °C OLDA increased the pH_{infl} from 4.94 ±0.05 to 5.19 ±0.21. The pH_{cip} remained unchanged.

   It was also found that ODA, and OLDA both agglomerated magnetite particles. PSD measured average magnetite particle sizes after the titrations with ODA, and OLDA were 59.64%, and 66.94% bigger, respectively. Magnetite agglomeration in the presence of FFA is in agreement with literature [32].

6. *Can a surface complexation model adequately describe the experimental results and subsequently yield surface charge predictions at higher temperatures?*

   A PHREEQC diffuse double layer complexation model (SCM) could be adequately fitted to the experimental magnetite surface charge density curves of the titrations performed at 25 °C. The three fitting parameters were: the surface site density, and pKa values of the protonation and deprotonation reactions. This gave a pKa1 of 5.7, and pKa2 of 7.8, and a site density of 30 sites/nm^2. A similar fit is reported by Mayant et al. [62]. The model could not be fitted to the steep magnetite surface charge density curve of the titrations performed at 150 °C, without increasing the specific surface area input. The suggested reason for this was the drift of the high temperature reference probe, affecting the pH measurement, in turn affecting the surface charge calculation. Consequently, the model was adequately fitted to the magnetite surface charge curves, over a temperature range of 150 °C to 290 °C, obtained from literature [121, 123].

   The SCM was not fitted to the FFA and magnetite surface titrations, as the ODA, and OLDA did not significantly impact the magnetite surface charge density. Instead, for the prediction of various OLDA concentration loadings on the magnetite surface charge density, at 290 °C, an OLDA adsorption constant (pKad) of 15 was assumed. Furthermore, the hypothesis formulated by Gasnier and Lister [32], stating that OLDA adsorbs via one amine group while the other amine group acquires a positive charge via protonation, was used in the model. Until a non-assumed pKad value is used, obtained by fitting, and a similar prediction at lower temperature of e.g. 150 °C is validated by experiment, drawing conclusions from this prediction would be premature.

6

Recommendations

This chapter provides recommendations for follow-up research, regarding improvements of the experimental procedures, and future research. The chapter is divided into three parts: first for recommendation related to FAC research, second part is related to adsorption and surface charge research, the last part deals with recommendations regarding the surface complexation modelling.

FAC research

This part contains all recommendations regarding the (acidic) FAC immersion and re-immersion research.

Rotating cage setup This study found a deviation in magnetite layer thickness determined via the SEM cross section image, and weight loss determined thickness. See subsection 4.1.2. This could partly be explained by the location of the measurement, the SEM images taken at the part experiencing most heavy flow conditions, whereas the weight loss is averaged over the whole coupon. For future research the use of a stirred cage setup where the coupons are moved relative to the liquid, providing more uniform flow conditions along the entire coupon, is recommended. Another option would be to cover other parts of the coupon (with e.g. 3M polyester tape with silicone adhesive) which are less exposed to the hydrodynamic conditions. These measures should reduce differences between the SEM and Weight loss determined thickness.

Immersion test duration This study applied immersion and re-immersion test durations of 48 hours. This was enough to form observable magnetite oxide layers on the coupons, observed via SEM images. However, the crystals formed under ammonia, and OLDA + ammonia chemistry appeared to not be fully grown. Moreover, literature reports more compact crystal forming under a polyamine treatment compared to an ammonia treatment [46], this was not clearly visible in this study. Given the setup permits, longer immersion tests should be performed, giving crystals more time to grow, and as consequence better represent any differences in applied chemistry. In addition, longer times should be applied for the re-immersion test for similar reasons. Moreover, if a re-immersion time of >200 hours is applied the FAC speed becomes linear dependent on time [45], leaving out any effects of the initial layer formation on the corrosion rate.

Quantification FFA layer This study applied contact angle measurements to verify the presence of an FFA layer via the layers hydrophobicity. However, the roughness of the surface

could impact the contact angle reading. Additional methods to semi or fully quantify the presence of an FFA layer after the immersion-, and re-immersion tests could be the Kurita 'whipe test' or X-ray Photo-electron Spectroscopy. These could be applied to differentiate whether contact angle measurements implicate more porous/rough layers or decreased FFA films.

Future research During this research the magnetite layers were formed under zero flow conditions at 230 or 250 °C. This was done to form a magnetite layer within 50 hours. The next step could be to test the addition of ODA, and OLDA to ammonia compared to ammonia alone on the formation of a magnetite layer under flow conditions and a lower temperature. This will correspond more to conditions under which magnetite layers are formed in feed, and condensate systems.

Adsorption and surface charge research

This part contains all recommendations regarding the FFA adsorption and surface charge research via potentiometric titrations.

FFA adsorption experiments The adsorption experiments in this research, performed at a temperature of 25 °C, and pH of 11 showed ODA, and OLDA to first adsorb onto magnetite followed by desorption. The suggested reason was that as magnetite became more negative, in alkaline pH, adsorbed FFA molecules are repelled by the negative surface charge. See section 4.6. To test the hypothesis one should first determine the amount of time it takes for magnetite to reach surface charge equilibrium. Secondly, during adsorption experiments one can add the FFA after half, or all, of this equilibrium time has passed. This to see whether the adsorption and desorption effect are half to what was observed to non observable.

The next step would be to perform FFA adsorption experiments at elevated temperatures more representative to the water-steam cycle conditions.

Magnetite purification This research concluded that magnetite reagent grade 99% powder was a suitable Puratronic substitute for further surface charge titrations, based on surface charge curve and pH_{pzc} similarities. Magnetite 95% reagent grade showed to be less similar regarding these aspects. The suggested reason for this were hematite impurities. Future research could verify whether magnetite 95% pure powder is suitable for surface charge titrations after hydrothermal pretreatment. This can remove the last hematite impurities. The recommended hydrothermal pretreatment, in the presence of nickel metal powder, and water, at 500 °C for 2 weeks, can be obtained from Wesolowski et al. [121].

Drift of high temperature probes This study found steep surface charge density curves for magnetite at 150 °C. This curve indicated a very negative surface charge in the alkaline pH region. A suggested reason was the drift of the probes, causing too low pH readings. The drift could have been caused by a the temperature effect on the external Ag/AgCl reference probe. This as the temperature of the Ag/AgCl section affects the potential of the probe. According to the manufacturer the temperature effect could be cancelled out in case the temperature of the external probe section is controlled at the same value. A cooling unit, through which water flows as coolant, formed with a thin copper wire tubing wrapped around the reference probe is recommended.

Future research No significant effect of ODA, and OLDA on the magnetite surface charge curve was observed during this study at an ionic strength of 0.01M. A reason could be the low amount of ODA, and OLDA present in the test solution. It would therefore be recommended

to apply higher FFA loading's. However, the high ppm-Mag/ppm-FFA ratio of this study was applied due to the low adsorption of FFA onto magnetite. Too much unadsorbed FFA (a weak base) can affect the pH measurements, hence the surface charge calculation. In future studies higher FFA concentrations can only be applied when the amount of free FFA is measured during the titration, in order to account for its effect on the pH measurement and subsequently on the surface charge calculation. Additionally, this suggested method can also provide the FFA to magnetite adsorption over pH.

The suggested titration method, where free FFA is measured during the titration in order to account for its effect on the charge calculations, allows for titrations using different FFA loading ratios (ppm-Mag/ppm-FFA). This could be useful to test the following hypothesis. From observations during this study and literature, it is assumed that at at lower concentrations of FFA to magnetite, the FFA mainly acts as a flocculant. Whereas at higher concentrations it will mainly act as a coagulant, neutralising the charge to eventually act as a dispersant by providing a positive charge in the alkaline region. This was discussed in subsection 4.9.1. At lower temperatures, e.g. room temperature, zeta-potential measurements could also be used to (indirectly) study the effect of different FFA concentration loadings on the magnetite charge and its reversal. Calculation of the unadsorbed FFA effect would not be necessary, whereas performing multiple measurements to obtain a zeta-potential curve over pH would be a disadvantage.

The only effect seen, in this study, on the surface charge density curve was for a titration with ODA, at an ionic strength of 0.1M and temperature of 25 °C. In subsection 4.8.1 it was discussed that a 'kinematic effect' could be the reason for this. Where the magnetite surface did not reach a surface charge equilibrium with the solution, via protonation deprotonation reactions, before starting the titration. It is therefore recommended to apply longer equilibrium times prior to the addition of a FFA, and titrant, especially when a titration is started at a high pH, such as pH 11.

Surface complexation modelling.

This part contains all recommendations regarding the surface complexation modelling using PHREEQC.

Fitting SCM In this research the SCM was not fitted to the FFA and magnetite surface titrations, as the ODA, and OLDA did not significantly affect the magnetite surface charge density curves. Instead an adsorption constant (pKad) of 15 was assumed for both the ODA, and OLDA to magnetite reactions. Given future research provides significantly affected magnetite surface charge curves, new fitting exercises should be performed in order to try to obtain the pKad reaction constant.

FFA dissociation constant For temperatures besides 25 °C the dissociation constant of ammonia was used as a replacement for the dissociation constants of ODA and OLDA. For follow-up modelling it would be more accurate to use the FFA base dissociation constant over the temperature rage 25 to 300 °C given by Ramminger et al. [87].

Overfitting To rule out overfitting of the fitting parameters, it would be recommended to reassess the model fit to the experimental data, using a site density of 2 sites/nm^2 and pKa values that are within the range reported by literature, see subsection 4.10.1.

Bibliography

[1] Yolitzin Alvarado, Rosenberg Romero, Juan Carlos García, Adrian del Pozo, Roberto Zenit, and Sergio Alonso Serna. “Using CFD and PIV to investigate rotating cage-related hydrodynamics for CO2 corrosion studies analyzing 2-, 4-and 8-coupons setups”. In: *Anti-Corrosion Methods and Materials* (2019). DOI: 10.1108/ACMM-09-2017-1836.

[2] C Anthony J Appelo and Dieke Postma. *Geochemistry, groundwater and pollution*. CRC press, 2004.

[3] M Barale, C Mansour, F Carrette, EM Pavageau, H Catalette, G Lefèvre, M Fedoroff, and G Cote. “Characterization of the surface charge of oxide particles of PWR primary water circuits from 5 to 320 C”. In: *Journal of Nuclear Materials* 381.3 (2008), pp. 302–308. DOI: 10.1016/j.jnucmat.2008.09.003.

[4] R Bäßler, M Uhlemann, and K Mummert. “Inhibiting effect of octadecylamine on pitting corrosion behaviour of stainless steel type 1.4541 up to 250 C”. In: *Materials and Corrosion* 50.3 (1999), pp. 146–153. DOI: 10.1002/(SICI)1521-4176(199903)50:3<146::AID-MACO146>3.0.CO;2-G.

[5] Jordan Baux, Nicolas Caussé, Jérôme Esvan, Sophie Delaunay, Jonathan Tireau, Marion Roy, Dominique You, and Nadine Pébère. “Impedance analysis of film-forming amines for the corrosion protection of a carbon steel”. In: *Electrochimica Acta* 283 (2018), pp. 699–707. DOI: 10.1016/j.electacta.2018.06.189.

[6] Pascale Bénézeth, David J Wesolowski, Donald A Palmer, and Michael L Machesky. “Effect of amines on the surface charge properties of iron oxides”. In: *Journal of solution chemistry* 38.7 (2009), pp. 925–945. DOI: 10.1007/s10953-009-9419-y.

[7] Iva Betova, Martin Bojinov, and Timo Saario. “Film-Forming Amines in Steam/Water Cycles–structure, properties, and influence on corrosion and deposition processes”. In: *VTT, Espoo, Finland* (2014).

[8] Iva Betova, Martin Bojinov, and Timo Saario. “Predictive modelling of flow-accelerated corrosion–unresolved problems and issues”. In: *VTT research report No VTT-R-08125-10* (2010).

[9] Geoffrey Bignold. “Transport of iron in steam/water cycles. Sources and sinks”. In: *Power Plant Chemistry* 11 (2009).

[10] GJ Bignold, K Garbett, and IS Woolsey. “Mechanistic aspects of the temperature dependence of erosion-corrosion”. In: *Corrosion-Erosion of Steels in High Temperature Water and Wet Steam, eds. Ph. Berge, F. Kahn (Les Renardieres, France: Electricite de France, 1982), paper* 12 (1982).

[11] Miguel A Blesa, Nestor M Figliolia, Alberto JG Maroto, and Alberto E Regazzoni. “The influence of temperature on the interface magnetite—aqueous electrolyte solution”. In: *Journal of colloid and interface science* 101.2 (1984), pp. 410–418. DOI: 10.1016/0021-9797(84)90052-3.

[12] ASME Boiler. “American Society of Mechanical Engineers, ASME Boiler and Pressure Vessel Committee, Subcommittee on Pressure Vessels. Rules for Construction of Pressure Vessels; An international code VIII, Division 1 VIII, Division 1”. In: *American Society of Mechanical Engineers: New York, NY, USA* (2010).

[13] Duško Čakara, Motoyoshi Kobayashi, Michal Skarba, and Michal Borkovec. “Protonation of silica particles in the presence of a strong cationic polyelectrolyte”. In: *Colloids and Surfaces A: Physicochemical and Engineering Aspects* 339.1-3 (2009), pp. 20–25. DOI: 10.1016/j.colsurfa.2009.01.011.

[14] Rachel L Chamousis and Frank E Osterloh. “Use of potential determining ions to control energetics and photochemical charge transfer of a nanoscale water splitting photocatalyst”. In: *Energy & Environmental Science* 7.2 (2014), pp. 736–743. DOI: 10.1039/C3EE42993H.

[15] EV Chernyshev, EN Veprov, VA Petrov, SL Bogdanov, T Yu Levina, TI Petrova, VI Kashinskii, AA Zonov, and AE Verkhovskii. “Increasing the corrosion resistance of equipment due to the use of film-forming amines”. In: *Power Technology and Engineering* 40.1 (2006), pp. 34–37.

[16] B Chexal, J Horowitz, and B Dooley. *Flow-accelerated corrosion in power plants. Revision 1*. Tech. rep. Electric Power Research Inst., 1998.

[17] F Cuoq, J Benguigui, C Geijselaers, and F Lampert. “Linking Thermoelectric Effect and Adsorption of Film Forming Amine as a Corrosion Inhibitor for Industrial Systems”. In: *Industrial & Engineering Chemistry Research* 59.17 (2020), pp. 8492–8495. DOI: 10.1021/acs.iecr.0c00576.

[18] E. De Meyer. “The behaviour of organic matter in industrial demineralization and steam-water cycles”. PhD thesis, Ghent University, Belgium, 2020.

[19] Tim De Seranno, Ellen Lambrechts, Evelyn De Meyer, Wolfgang Hater, Nathalie De Geyter, Arne RD Verliefde, Tom Depover, and Kim Verbeken. “Effect of Film-Forming Amines on the Acidic Stress-Corrosion Cracking Resistance of Steam Turbine Steel”. In: *Metals* 10.12 (2020), p. 1628. DOI: 10.3390/met10121628.

[20] D. Disci-Zayed, J. Jasper, and W. Hater. “Adsorption of Oleyl Propylenediamine on Metal Surfaces”. In: *PowerPlant Chemistry* 21.3 (June 2019), pp. 146–154.

[21] Barry Dooley and Derek Lister. “Flow-Accelerated Corrosion in Steam Generating Plants”. In: *Power Plant Chemistry* 20.4 (2018), pp. 194–244.

[22] R Barry Dooley. “Flow-accelerated corrosion in fossil and combined cycle/HRSG plants”. In: *Power Plant Chemistry* 10 (2008).

[23] R Barry Dooley, J Denis Aspden, Andrew G Howell, and Francois du Preez. “Assessing and controlling corrosion in air-cooled condensers”. In: *PowerPlant Chemistry* 11.5 (2009), p. 264.

[24] RB Dooley and VK Chexal. “Flow-accelerated corrosion of pressure vessels in fossil plants”. In: *International Journal of Pressure Vessels and Piping* 77.2-3 (2000), pp. 85–90. DOI: 10.1016/S0308-0161(99)00087-3.

[25] Vivekanand Dubey and Vivekanand Kain. “Oxidation Behavior of Carbon Steel: Effect of Formation Temperature and pH of the Environment”. In: *Journal of Materials Engineering and Performance* 26.11 (2017), pp. 5312–5322. DOI: 10.1007/s11665-017-3027-6.

[26] David A Dzombak and Francois MM Morel. *Surface complexation modeling: hydrous ferric oxide*. John Wiley & Sons, 1990.

[27] Jordi Esquena, Francisco J Domínguez, Conxita Solans, Bart Levecke, Karl Booten, and Tharwat F Tadros. “Stabilization of latex dispersions using a graft copolymer of inulin based surfactants”. In: *Langmuir* 19.25 (2003), pp. 10463–10467. DOI: 10.1021/la035092v.

[28] C Esseboom and P Verolme. *Determination of the specific surface area of three magnetite samples, analysed with nitrogen gas adsorption. Reference: 20-DSS-0949*. Tech. rep. Delft Solid Solutions B.V., Molenweer 2B 2291 NR Wateringen (The Netherlands), 2020.

[29] Daniel Flynn. *Nalco water handbook*. McGraw-Hill Education, 2009.

[30] LGJ Fokkink, A De Keizer, and J Lyklema. “Temperature dependence of the electrical double layer on oxides: Rutile and hematite”. In: *Journal of colloid and interface science* 127.1 (1989), pp. 116–131. DOI: 10.1016/0021-9797(89)90012-X.

[31] M. G. Fontana. *Corrosion Engineering 3rd*. McGraw-Hill Book Company, 1987.

[32] C. Gasnier and DH. Lister. “The effects of chemical additives on magnetite deposition in boiling heat transfer”. In: *Proceedings International Conference on Heat Exchanger Fouling and Cleaning*. 2013, pp. 9–14.

[33] Cyprien Gasnier. “The effect of chemical additives on the deposition of magnetite onto alloy-800 under nucleate boiling heat transfer”. PhD thesis. University of New Brunswick, 2014.

[34] Paul WJ Glover and Matthew D Jackson. “Borehole electrokinetics”. In: *The Leading Edge* 29.6 (2010), pp. 724–728. DOI: 10.1190/1.3447786.

[35] Sabine Goldberg, Louise Criscenti, David Turner, James Davis, and Kirbie Cantrell. “Adsorption–Desorption Processes in Subsurface Reactive Transport Modeling”. In: *Vadose Zone Journal* 6 (Aug. 2007). DOI: 10.2136/vzj2006.0085.

[36] Jan W Gooch. *Encyclopedic dictionary of polymers*. Vol. 1. Springer Science & Business Media, 2010. ISBN: 978-1-4419-6246-1.

[37] Anton Graf. *Method for the determination of polyamines*. Jan. 1996. URL: https://patents.google.com/patent/EP0562210A1/en.

[38] A Hajdú, E Tombácz, E Illés, D Bica, and L Vékás. “Magnetite nanoparticles stabilized under physiological conditions for biomedical application”. In: *Colloids for Nano-and Biotechnology*. Springer, 2008, pp. 29–37. DOI: 10.1007/2882_2008_111.

[39] W Hater, A de Bache, and T Petrick. “Dry lay-up of steam generators with film forming amines-Studies and field experiences”. In: *Cahiers de l’Association Scientifique Européenne pour l’Eau et la Santé* 19 (2014), p. 5. DOI: 10.1051/asees/2016003.

[40] W Hater and A De Bache. “Film-forming amines in boiler feed water treatment”. In: *IPW (Int. Paper World)* (2010), pp. 10–11.

[41] Wolfgang Hater, Julia Jasper, and Patrick Kraft. “The film formation and corrosion inhibition of oleylamines on aluminium”. In: *efcweb.org* ().

[42] David Hendricks. *Fundamentals of water treatment unit processes: physical, chemical, and biological*. Crc Press, 2010.

[43] Corr Instruments. *General Specifications/Instructions UltraDeg® H-P and/or H-T Reference Probes (Additional instructions must be used for refillable probes and gas-tolerant probes).* Tech. rep. 23 Affonso Drive, NV8906, Carson City.

[44] M Jack, S Weerakul, and DH Lister. “The interaction of a film-forming amine with surfaces of a recirculating experimental water loop”. In: *The International Conference on Heat Exchanger Fouling and Cleaning XI, held June*. 2015, pp. 7–12.

[45] P. Janssen. *Literatuurstudie naar procedures voor de bestrijding van erosie-corrosie in stoomsytemen*. 1996.

[46] Peter Janssen and Jo Savelkoul. “In search of an alternative high-pressure boiler water treatment program”. In: *Power Plant Chemistry* 14 (2012).

[47] Essi Jäppinen, Tiina Ikäläinen, Sari Järvimäki, Timo Saario, Konsta Sipilä, and Martin Bojinov. “Corrosion behavior of carbon steel coated with octadecylamine in the secondary circuit of a pressurized water reactor”. In: *Journal of Materials Engineering and Performance* 26.12 (2017), pp. 6037–6046. DOI: 10.1007/s11665-017-3035-6.

[48] Adam J Johnston. *Temperature-Entropy Diagram for Water*. Aug. 2016. URL: https://demonstrations.wolfram.com/TemperatureEntropyDiagramForWater/.

[49] Rickard Jolsterå, Lars Gunneriusson, and Allan Holmgren. “Surface complexation modeling of Fe3O4–H+ and Mg (II) sorption onto maghemite and magnetite”. In: *Journal of colloid and interface science* 386.1 (2012), pp. 260–267. DOI: 10.1016/j.jcis.2012.07.031.

[50] Vivekanand Kain. “Flow accelerated corrosion: forms, mechanisms and case studies”. In: *Procedia Engineering* 86 (2014), pp. 576–588. DOI: 10.1016/j.proeng.2014.11.083.

[51] Olga N Karasyova, Ludmila I Ivanova, Leonid Z Lakshtanov, and Lars Lövgren. “Strontium sorption on hematite at elevated temperatures”. In: *Journal of colloid and interface science* 220.2 (1999), pp. 419–428. DOI: 10.1006/jcis.1999.6474.

[52] Dl Kern. “A theoretical analysis of thermal surface fouling”. In: *Br. Chem. Eng.* 4 (1959), pp. 258–262.

[53] Rajiv Kohli and KL Mittal. *Developments in Surface Contamination and Cleaning, Volumes 12*. Elsevier, 2019.

[54] JS Laskowski. “Surface chemistry fundamentals in fine coal processing”. In: *The Coal Handbook: Towards Cleaner Production*. Elsevier, 2013, pp. 347–421. DOI: 10.1533/9780857097309.2.347.

[55] M Lendi. “Continuous photometric determination of film-forming amines”. In: *Power Plant Chemistry* 17.1 (2015), pp. 1–5.

[56] D Lister, A Feicht, K Fujiwara, M Khatibi, L Liu, Taku Ohira, and Shunsuke Uchida. “The mitigation of flow-accelerated corrosion in the feedwater systems of nuclear reactors-the influence of dissolved oxygen under different operating conditions”. In: (2010).

[57] Derek Lister. “Flow-accelerated corrosion in power plants: The influence of corrosion-product oxides”. In: *Proceedings of the EUROCORR 2019 The Annual Congress of the European Federation of Corrosion, Seville, Spain*. 2019, pp. 9–13.

[58] Derek H Lister and Shunsuke Uchida. “Reflections on FAC mechanisms”. In: *Power Plant Chemistry* 12 (2010).

[59] Johannes Lützenkirchen, Tajana Preočanin, Davor Kovačević, Vladislav Tomišić, Lars Lövgren, and Nikola Kallay. “Potentiometric titrations as a tool for surface charge determination”. In: *Croatica Chemica Acta* 85.4 (2012), pp. 391–417. ISSN: 00111643. DOI: 10.5562/cca2062.

[60] Michael L Machesky, David J Wesolowski, Donald A Palmer, and Moira K Ridley. “On the temperature dependence of intrinsic surface protonation equilibrium constants: an extension of the revised MUSIC model”. In: *Journal of colloid and interface science* 239.2 (2001), pp. 314–327. DOI: 10.1006/jcis.2001.7584.

[61] C Mansour, G Lefèvre, EM Pavageau, H Catalette, M Fédoroff, and S Zanna. “Sorption of sulfate ions onto magnetite”. In: *Journal of colloid and interface science* 331.1 (2009), pp. 77–82. DOI: 10.1016/j.jcis.2008.11.009.

[62] C Mayant, Bernd Grambow, Abdesselam Abdelouas, S Ribet, and S Leclercq. “Surface site density, silicic acid retention and transport properties of compacted magnetite powder”. In: *Physics and Chemistry of the Earth, Parts A/B/C* 33.14-16 (2008), pp. 991–999. DOI: 10.1016/j.pce.2008.05.011.

[63] Edward McCafferty. *Introduction to corrosion science*. Springer Science & Business Media, 2010.

[64] S Milonjić, M Kopečni, and Z Ilić. “The point of zero charge and adsorption properties of natural magnetite”. In: *Journal of Radioanalytical and Nuclear Chemistry* 78.1 (1983), pp. 15–24. DOI: 10.1007/bf02519745.

[65] Michael J Moran, Howard N Shapiro, Daisie D Boettner, and Margaret B Bailey. *Fundamentals of engineering thermodynamics*. John Wiley & Sons, 2010.

[66] Michael James Moran, Pixie A Hamilton, and John S Zogorski. *Volatile Organic Compounds in the Nation’s Ground Water and Drinking-water Supply Wells: A Summary*. US Department of the Interior, US Geological Survey, 2006.

[67] ASTM NACE et al. “Standard guide for laboratory immersion corrosion testing of metals”. In: *ASTM International, West Conshohocken, PA* (2012).

[68] ASTM NACE et al. “Standard Practice for Evaluating and Qualifying Oil Field and Refinery Corrosion Inhibitors Using Rotating Cage1”. In: *ASTM International, West Conshohocken, PA* (2020).

[69] ASTM NACE et al. “Standard Test Method for Corrosivity of Water in the Absence of Heat Transfer (Weight Loss Method)”. In: *ASTM International, West Conshohocken, PA* (2015).

[70] Seifollah Nasrazadani and Shokrollah Hassani. “Modern analytical techniques in failure analysis of aerospace, chemical, and oil and gas industries”. In: *Handbook of Materials Failure Analysis with Case Studies from the Oil and Gas Industry* (2016), pp. 39–54. DOI: 10.1016/B978-0-08-100117-2.00010-8.

[71] S Nesic and J Postlethwaite. “Relationship between the structure of disturbed flow and erosion—corrosion”. In: *Corrosion* 46.11 (1990), pp. 874–880. DOI: 10.5006/1.3580852.

[72] Nathalie Ochoa, Francis Moran, and Nadine Pébère. “The synergistic effect between phosphonocarboxylic acid salts and fatty amines for the corrosion protection of a carbon steel”. In: *Journal of applied electrochemistry* 34.5 (2004), pp. 487–493. DOI: 10.1023/B:JACH.0000021702.49827.11.

[73] Suat Odar. “Use of film forming amines (FFA) in nuclear power plants for lay-up and power operation”. In: *Advanced Nuclear Technology International Europe AB, ANT International* (2017).

[74] T van Os. In: *Technical Bulletin Vecom*. 2. Jan. 2006.

[75] S Palchoudhury, M Baalousha, and JR Lead. *Characterization of nanomaterials in complex environmental and biological media, 8*. 2015.

[76] David L Parkhurst and CAJ Appelo. *Description of input and examples for PHREEQC version 3: a computer program for speciation, batch-reaction, one-dimensional transport, and inverse geochemical calculations*. Tech. rep. US Geological Survey, 2013.

[77] David L Parkhurst, CAJ Appelo, et al. "User's guide to PHREEQC (Version 2): A computer program for speciation, batch-reaction, one-dimensional transport, and inverse geochemical calculations". In: *Water-resources investigations report* 99.4259 (1999), p. 312.

[78] Nestor Perez. "Electrochemical corrosion". In: *Electrochemistry and Corrosion Science*. Springer, 2016, pp. 1–23. DOI: 10.1007/978-3-319-24847-9_1.

[79] Violaine Philippini, Aude Naveau, Hubert Catalette, and Stéphanie Leclercq. "Sorption of silicon on magnetite and other corrosion products of iron". In: *Journal of Nuclear materials* 348.1-2 (2006), pp. 60–69. DOI: 10.1016/j.jnucmat.2005.09.002.

[80] Sergey Pivovarov. "Acid–base properties and heavy and alkaline earth metal adsorption on the oxide–solution interface: Non-electrostatic model". In: *Journal of colloid and interface science* 206.1 (1998), pp. 122–130. DOI: 10.1006/jcis.1998.5647.

[81] Biomass Power Plants. "The International Association for the Properties of Water and Steam". In: (2016).

[82] Elisaveta Potapova, Mattias Grahn, Allan Holmgren, and Jonas Hedlund. "The effect of calcium ions and sodium silicate on the adsorption of a model anionic flotation collector on magnetite studied by ATR-FTIR spectroscopy". In: *Journal of colloid and interface science* 345.1 (2010), pp. 96–102. DOI: 10.1016/j.jcis.2010.01.056.

[83] EC Potter. "Oxidation of mild steel in high-temperature aqueous systems". In: *Proc. 1st Int. Cong. Metallic Corrosion, London, UK (1961)* (1961), pp. 417–426.

[84] Bryan Poulson, Brian Greenwell, Bindi Chexal, and Jeff Horowitz. "Modelling hydrodynamic parameters to predict flow assisted corrosion". In: *Proceedings of the fifth international symposium on environmental degradation of materials in nuclear power systems-water reactors*. 1992.

[85] *Principles of corrosion*. 2011. URL: http://www.corrscience.com/products/corrosion/intro-to-corrosion/principles-of-corrosion/.

[86] Stephen A Rackley. *Carbon capture and storage*. Butterworth-Heinemann, 2017.

[87] Ute Ramminger, Stephan Hoffmann-Wankerl, and Jörg Fandrich. "The application of film-forming amines in secondary side chemistry treatment of NPPs". In: (2012).

[88] Alberto E Regazzoni, Miguel A Blesa, and Alberto JG Maroto. "Interfacial properties of zirconium dioxide and magnetite in water". In: *Journal of Colloid and Interface Science* 91.2 (1983), pp. 560–570. DOI: 10.1016/0021-9797(83)90370-3.

[89] J Savelkoul. *Advies voor het tegengaan van erosie-corrosie in de water/stoom circulatieleidingen van V201 in UF1000 DCF*. 1993.

[90] Caroline A Schneider, Wayne S Rasband, and Kevin W Eliceiri. "NIH Image to ImageJ: 25 years of image analysis". In: *Nature methods* 9.7 (2012), pp. 671–675. DOI: 10.1038/nmeth.2089.

[91] Martin AA Schoonen. "Calculation of the point of zero charge of metal oxides between 0 and 350 C". In: *Geochimica et Cosmochimica Acta* 58.13 (1994), pp. 2845–2851. DOI: 10.1016/0016-7037(94)90118-X.

[92] Ashok K Singh. *Engineered nanoparticles: structure, properties and mechanisms of toxicity*. Academic Press, 2016. Chap. Chapter 4 - Experimental Methodologies for the Characterization of Nanoparticles. ISBN: 9780128014066. DOI: 10.1016/B978-0-12-801406-6.00004-2. URL: https://www.sciencedirect.com/science/article/pii/B9780128014066000042.

[93] Bill Smith, Paul McCann, Kazuyoshi Uchida, Shintarou Mori, Julia Jasper, and Wolfgang Hater. "Determination of Oleyl Propylenediamine, a Commonly Used Film Forming Amine, on the Surfaces of Water-Steam Cycles". In: *Abstracts Service (CAS) Number* 7173 (2017), pp. 62–8.

[94] Dennis A Snow. *Plant engineer's reference book*. Elsevier, 2001.

[95] Theodros Solomon. "The definition and unit of ionic strength". In: *Journal of Chemical Education* 78.12 (2001), p. 1691. DOI: 10.1021/ed078p1691.

[96] Geun Dong Song, Soon-Hyeok Jeon, Yeong-Ho Son, Jung Gu Kim, and Do Haeng Hur. "Galvanic effect of magnetite on the corrosion behavior of carbon steel in deaerated alkaline solutions under flowing conditions". In: *Corrosion Science* 131 (2018), pp. 71–80. DOI: 10.1016/j.corsci.2017.10.017.

[97] Garrison Sposito. "On points of zero charge". In: *Environmental science & technology* 32.19 (1998), pp. 2815–2819. DOI: 10.1021/es9802347.

[98] Katrin Stiller, Tobias Wittig, and Michael Urschey. "The analysis of film-forming amines. Methods, possibilities, limits and recommendations; Die Analytik filmbildender Amine. Methoden, Moeglichkeiten, Grenzen und Empfehlungen". In: (2010).

[99] Werner Stumm and James J Morgan. *Aquatic chemistry: chemical equilibria and rates in natural waters*. 1996.

[100] P Sturla. "Oxidation and deposition phenomena in forced circulating boilers and feedwater treatment". In: *Proc. Fifth National Feedwater Conf. Prague, Czech*. 1973.

[101] Márta Szekeres and Etelka Tombácz. "Surface charge characterization of metal oxides by potentiometric acid–base titration, revisited theory and experiment". In: *Colloids and Surfaces A: Physicochemical and Engineering Aspects* 414 (2012), pp. 302–313. DOI: 10.1016/j.colsurfa.2012.08.027.

[102] Tharwat F Tadros. *Interfacial phenomena and colloid stability: basic principles*. Vol. 1. Walter de Gruyter GmbH & Co KG, 2015.

[103] *The Geochemists Workbench the toolset for aqueous chemists*. 2011. URL: https://www.gwb.com/index.php.

[104] William Thielicke and Eize Stamhuis. "PIVlab–towards user-friendly, affordable and accurate digital particle image velocimetry in MATLAB". In: *Journal of open research software* 2.1 (2014). DOI: 10.5334/jors.bl.

[105] J Thiellier, A Van Pelt, J Savelkoul, and H Raaphorst. In: *Contact Group on Corrosion in the Dutch Process Industry* (1986).

[106] Etelka Tombácz, Erzsébet Illés, Andrea Majzik, Angéla Hajdú, Nóra Rideg, and Márta Szekeres. "Ageing in the inorganic nanoworld: example of magnetite nanoparticles in aqueous medium". In: *Croatica Chemica Acta* 80.3-4 (2007), pp. 503–515.

[107] Etelka Tombácz and Márta Szekeres. "Interfacial acid- base reactions of aluminum oxide dispersed in aqueous electrolyte solutions. 1. Potentiometric study on the effect of impurity and dissolution of solid phase". In: *Langmuir* 17.5 (2001), pp. 1411–1419. DOI: 10.1021/la001322j.

[108] Holger Topp, Wolfgang Hater, Andre de Bache, and Christian zum Kolk. “Film-forming amines in shell boilers”. In: *PowerPlant Chemistry* 14.1 (2012), pp. 38–48.

[109] Holger Topp, Dieter Steinbrecht, Wolfgang Hater, BK Giulini, Andre de Bache, et al. “The influence of film-forming amines on heat transfer during saturated pool boiling”. In: *Power Plant Chemistry* 12 (2010).

[110] Peter R Tremaine and Jacques C LeBlanc. “The solubility of magnetite and the hydrolysis and oxidation of Fe 2+ in water to 300 C”. In: *Journal of solution chemistry* 9.6 (1980), pp. 415–442. DOI: 10.1007/BF00645517.

[111] Benjamin F Turner and Jeremy B Fein. “Protofit: a program for determining surface protonation constants from titration data”. In: *Computers & geosciences* 32.9 (2006), pp. 1344–1356. DOI: 10.1016/j.cageo.2005.12.005.

[112] Carl W Turner. “Rates of particle deposition from aqueous suspensions in turbulent flow: A comparison of theory with experiment”. In: *Chemical engineering science* 48.12 (1993), pp. 2189–2195. DOI: 10.1016/0009-2509(93)80236-J.

[113] Carl William Turner, DA Guzonas, and SJ Klimas. *Surface chemistry interventions to control boiler tube fouling*. Tech. rep. Atomic Energy of Canada Limited, 2000. DOI: 10.1017/CBO9781107415324.004.

[114] CW Turner, SJ Klimas, and MG Brideau. “The effect of alternative amines on the rate of boiler tube fouling”. In: (1997).

[115] Mikko Vepsäläinen and Timo Saario. “Magnetite dissolution and deposition in NPP secondary circuit”. In: *VTT Technical Research Centre of Finland, VTT* (2010).

[116] Arnoldus WP Vermeer and Luuk K Koopal. “Charge adjustments upon adsorption of a weak polyelectrolyte to a mineral oxide: the hematite–humic acid system”. In: *Journal of colloid and interface science* 212.1 (1999), pp. 176–185. DOI: 10.1006/jcis.1998.6050.

[117] Sonja Vidojkovic, Victor Rodriguez-Santiago, Mark V Fedkin, David J Wesolowski, and Serguei N Lvov. “Electrophoretic mobility of magnetite particles in high temperature water”. In: *Chemical engineering science* 66.18 (2011), pp. 4029–4035. DOI: 10.1016/j.ces.2011.05.021.

[118] Sonja M Vidojkovic and Marko P Rakin. “Surface properties of magnetite in high temperature aqueous electrolyte solutions: A review”. In: *Advances in colloid and interface science* 245 (2017), pp. 108–129. DOI: 10.1016/j.cis.2016.08.008.

[119] *Water - Ionization Constant, pKw, of normal and heavy water*. 2017. URL: https://www.engineeringtoolbox.com/ionization-dissociation-autoprotolysis-constant-pKw-water-heavy-deuterium-oxide-d_2004.html.

[120] Sarita Weerakul, Naravit Leaukosol, Derek H Lister, Shintaro Mori, and Wolfgang Hater. “Effects on Flow-Accelerated Corrosion of Oleylpropanediamine Under Single-Phase Water Conditions Pertinent to Power Plant Feedwater”. In: *Corrosion* 76.2 (2020), pp. 217–230. DOI: 10.5006/3225.

[121] David J Wesolowski, Michael L Machesky, Donald A Palmer, and Lawrence M Anovitz. “Magnetite surface charge studies to 290 C from in situ pH titrations”. In: *Chemical Geology* 167.1-2 (2000), pp. 193–229. DOI: 10.1016/S0009-2541(99)00209-0.

[122] DJ Wesolowski, DA Palmer, and RE Mesmer. *Measurement and control of pH in hydrothermal solutions*. Tech. rep. Oak Ridge National Lab., TN (United States), 1995.

[123] HR Zebardast, M Pawlik, S Rogak, and E Asselin. “Potentiometric titration of hematite and magnetite at elevated temperatures using a ZrO2-based pH probe”. In: *Colloids and Surfaces A: Physicochemical and Engineering Aspects* 444 (2014), pp. 144–152. DOI: 10.1016/j.colsurfa.2013.12.039.

[124] Li Li Zhang and XS Zhao. “Carbon-based materials as supercapacitor electrodes”. In: *Chemical Society Reviews* 38.9 (2009), pp. 2520–2531. DOI: 10.1039/B813846J.

A

Pourbaix of iron system at various temperatures

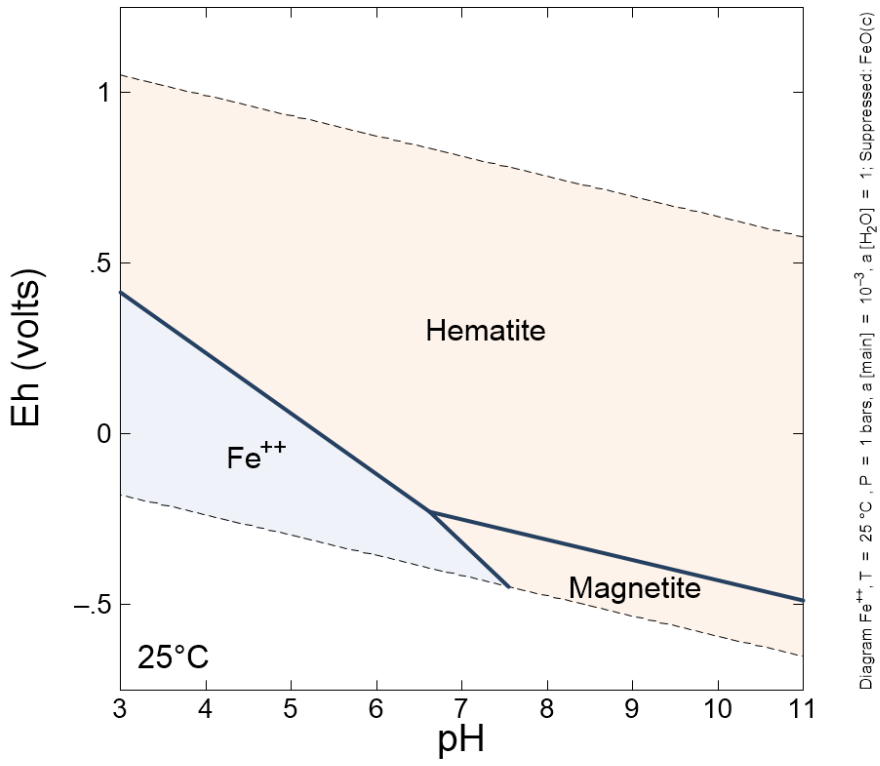

Figure A.1: Pourbaix diagram of an iron system at 25°C. Made with [103].

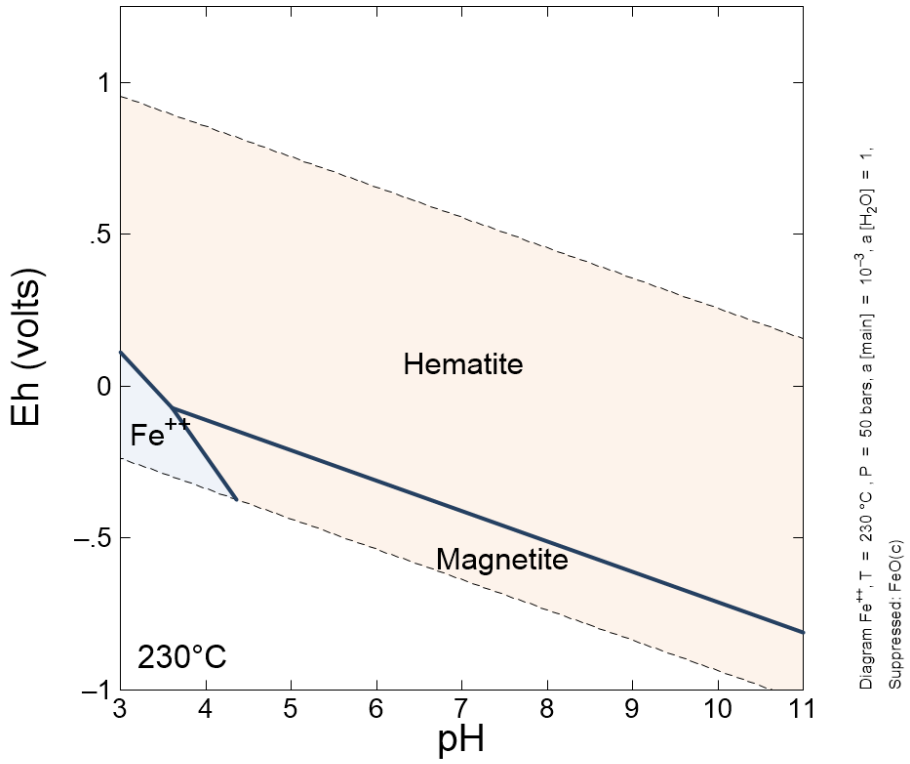

Figure A.2: Pourbaix diagram of an iron system at 230°C. Made with [103].

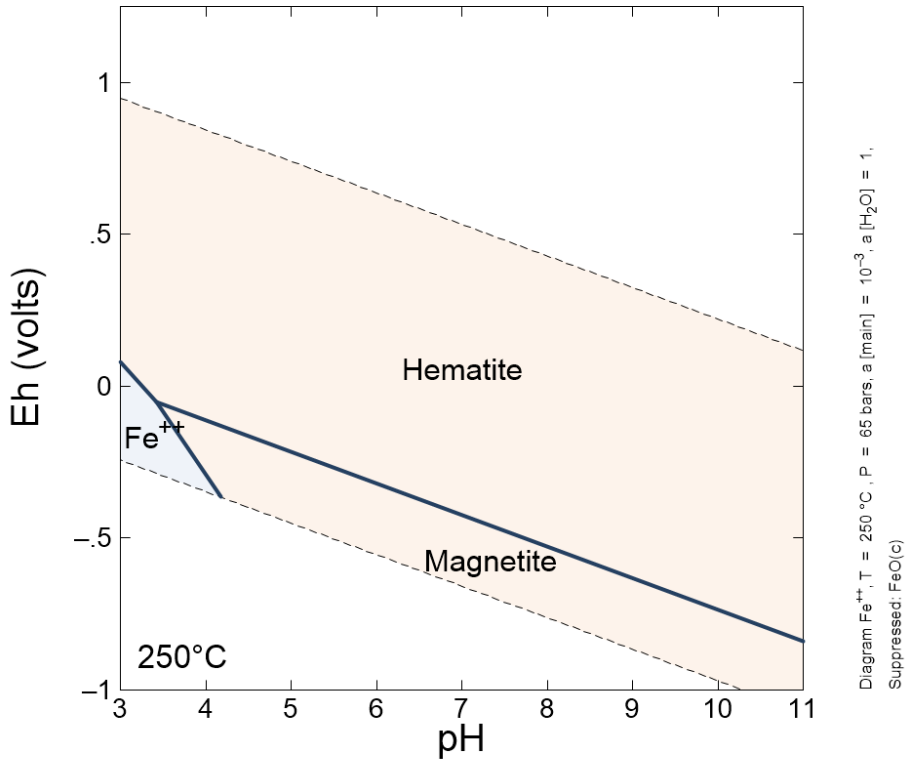

Figure A.3: Pourbaix diagram of an iron system at 250°C. Made with [103].

B

Methods of preparing the ODA solution

B.1. ODA emulsion

Slowly adding ODA powder and drops of 70◦C Milli-Q water into a bottle while manually stirring (by a stick/stirrer. Or second way First melting the ODA at 50-60◦C in an oven and adding drops of 70 ◦C Milli-Q water into the bottle while stirring. Conclusion, the first method results in a more stable emulsion. The emulsion contains 50mg of ODA in roughly 3ml of Milli-Q water.

B.2. ODA solution

Direct method, method 1
Heat 1 liter milli-Q water to 70◦C and dose ODA powder while stirring. Keep the solution at 70◦C for 30 minutes. Pour the solution in a glass flak and mix for 24hours. Materials used: magnetic stirrer and kitchen blender plus heater and warm water bath.

Direct method 2 (indirect)
Heat 1 liter milli-Q water to 70◦C and dose the ODA emulsion (see section B.1) while stirring, keep at 70 ◦C and stirring for 2 hours. Pour the solution in a pre-saturated flask and mix for 24hours. From this flak lower concentration solutions are made. Material used magnetic stirrer, heater and warm water bath.

Direct method 3 (indirect)
Heat milli-Q water to 70◦C and dose the ODA emulsion (see section B.1) keep at 70 ◦C and stirring for 2 hours. Pipette part of the solution to make a lower concentration solution (5ppm) while keeping the rest of the solution stirred at 70◦C. Pre-saturate the glassware with the 5ppm solution for 3hours, empty and refill again with a part of the original solution. Material used magnetic stirrer, heater and warm water bath.

B.3. Ultrasonic bath time

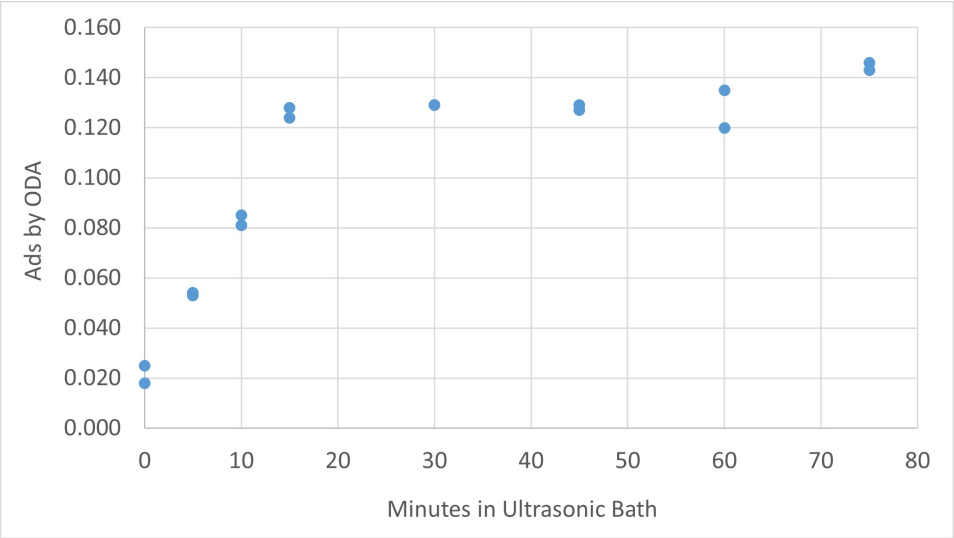

Figure B.1: Adsorption determined by spectrophotometry of a 2ppm ODA sample over time spent in the ultrasonic bath at 40 °C.

C

Pictures of setups

This section contains the pictures of the three different setups used in this study. The photo's included blue arrows indicating the different parts of the setup. section C.1 contains a photo of the setup used for the immersion and re-immersion experiments, section C.2 provides a photo of the setup used for the low temperature (25 °C) potentiometric titrations and section C.3 shows the setup used for the high temperature (150 °C) potentiometric titrations.

C.1. Setup immersion and re-immersion test

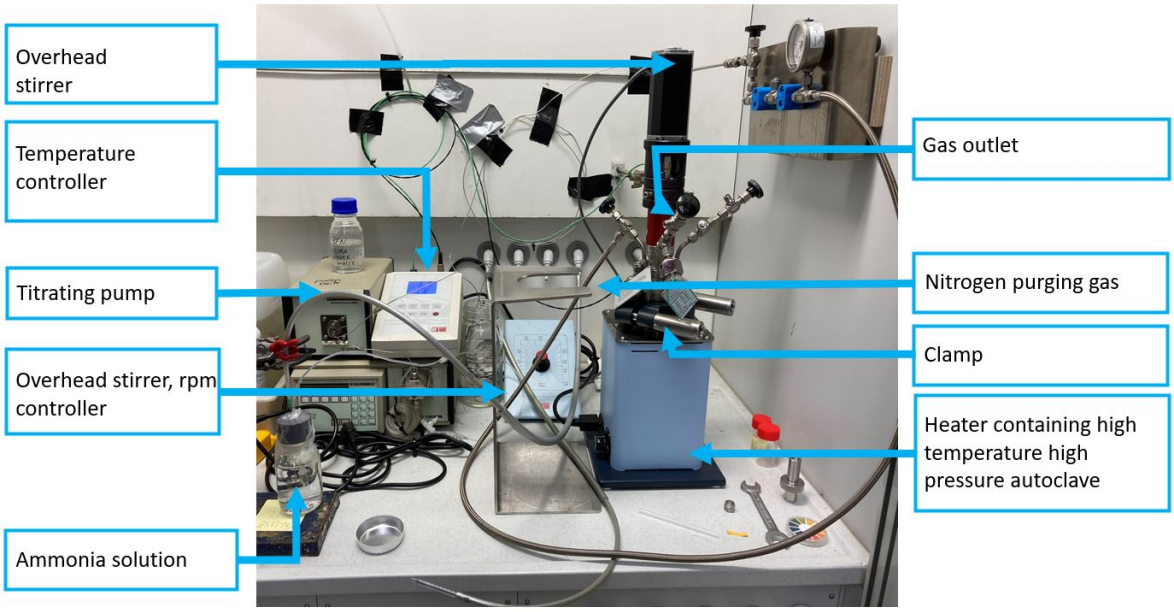

Figure C.1: Photo of the test setup for the immersion and re-immersion corrosion experiments.

C.2. Low temperature potentiometric setup

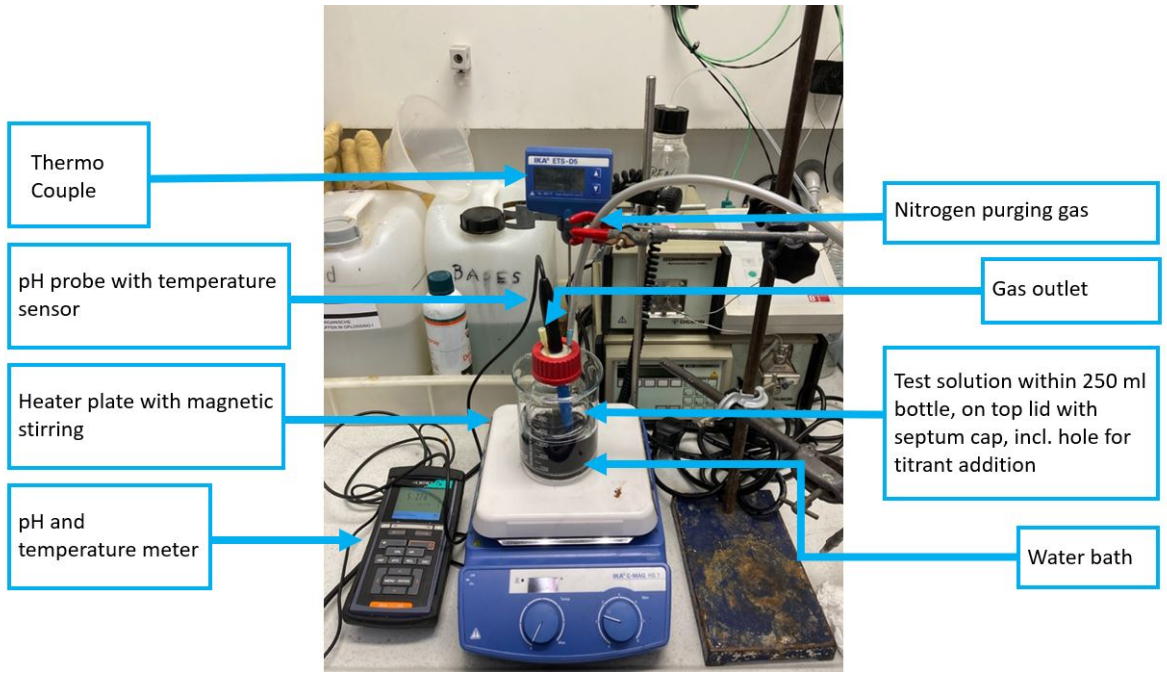

Figure C.2: Photo of the 250ml bottle setup, for the 25°C potentiometric titrations.

C.3. High temperature potentiometric setup

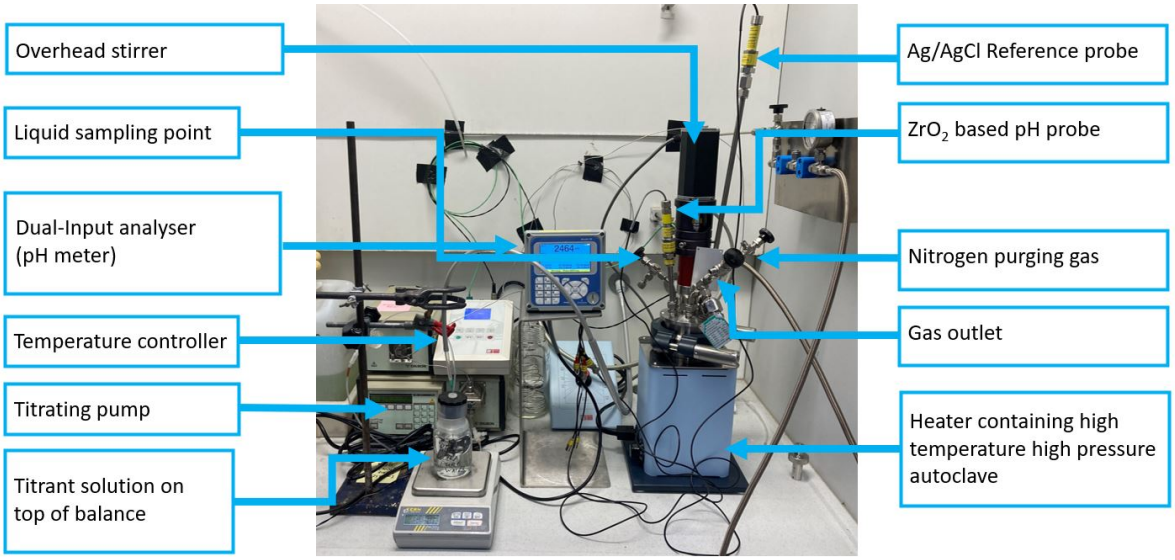

Figure C.3: Photo of the experimental setup for the high temperature potentiometric titrations.

D

Performed titration runs

Table D.1 provides an detailed overview of the performed titrations at 25°C and Table D.2 an overview for titrations performed at 150 °C. Note the column 'titrations' specifies the direction of the titration, 7 -> 11 indicates neutral to alkaline conditions (standard titration, SM, using base) and 7 -> 3 an acidic titration (standard titration, SM, using acid), 11->3 stands for a quick titration, QT. 'Mag95' stands for the 95% pure sigma-aldrich magnetite, 'Pur mag' stands for the Puratronic magnetite and 'Mag99' stands for the 99.99% pure magnetite from Sigma-Aldrich. 'b' stands for a blank titration.

Table D.1: Overview of performed magnetite potentiometric titrations at 25 °C.

Run	Date	Method	Titration	Ionic-S	Fe3O4	Mag (g/L)	FFA
1	18/08/2020	QT	7->11->3	0.1	b	-	-
2	25/08/2020	QT	7->3->11	0.1	b	-	-
3	07/09/2020	QT	11->3	0.1	Mag95	12.86	-
4	09/09/2020	QT	11->3	0.1	Mag95	5.63	-
5	10/09/2020	QT	11->3	0.1	Mag95	12.86	-
7	17/09/2020	SM	7->11	0.1	Mag95	12.86	-
9	21/09/2020	QT	7->11->3	0.01	b	-	-
12	30/09/2020	SM	7->11	0.01	b	-	-
13	30/09/2020	SM	7->3	0.01	b	-	-
14	30/09/2020	SM	7->11	0.01	PurM	10.0	-
15	30/09/2020	SM	7->3	0.01	PurM	10.0	-
16	02/10/2020	SM	7->11	0.01	Mag95	10.0	-
17	02/10/2020	SM	7->3	0.01	Mag95	10.0	-
18	07/10/2020	QT	11->3	0.01	Mag95	10.0	-
22	27/10/2020	SM	7->11	0.01	Mag99	10.0	-
23	27/10/2020	SM	7 -> 11	0.01	b	-	-
24	28/10/2020	SM	7 -> 3	0.01	Mag99	10.0	-
25,26,27	29/10/2020	SM	7 -> 11	0.001	N/A	N/A	
	30/10/2020	New low temperature probe aquired					
	30/10/2020	Start calibrating low temp probe with 5 pH stock solutions					
29	03/11/2020	SM	7 -> 11	0.001	b	-	-

Run	Date	Method	Titration	Ionic-S	Fe3O4	Mag (g/L)	FFA
30	03/11/2020	SM	7 -> 11	0.01	Mag99	10.0	-
31	03/11/2020	SM	7 -> 11	0.01	b	-	-
32	03/11/2020	SM	7 -> 3	0.01	Mag99	10.0	-
35	09/11/2020	QT	11 -> 3	0.01	b	-	-
36	09/11/2020	QT	11 -> 3	0.01	Mag99	10.0	-
38	18/11/2020	QT	11 -> 3	0.1	Mag99	10.0	-
	20/11/2020	Making of the first ODA batch					
39	27/11/2020	QT	11 -> 3	0.01	Mag99	10.0	ODA
40	01/12/2020	SM	7 -> 11	0.01	Mag99	10.0	ODA
41	01/12/2020	SM	7 -> 3	0.01	Mag99	10.0	ODA
	02/12/2020	OLDA prepatration batch one					
42	08/12/2020	QT	11 -> 3	0.01	-	-	ODA
43	11/12/2020	QT	11 -> 3	0.01	Mag99	10.0	ODA
44	15/12/2020	QT	11 -> 3	0.01	PurM	10.0	-
45	17/12/2020	QT	11 -> 3	0.01	Mag99	10.0	ODA*
46	17/12/2020	QT	11->3	0.01	Mag99	10.0	ODA
47	18/12/2020	QT	11->3	0.01	-	-	ODA
48	18/12/2020	QT	11->3	0.01	Mag99	10.0	-
49	21/12/2020	QT	11->3	0.01	Mag99	10.0	OLDA
50	22/12/2020	SM	7 -> 11	0.01	Mag99	10.0	OLDA
51	23/12/2020	SM	7 -> 11	0.01	Mag99	10.0	-
52	23/12/2020	SM	7 -> 3	0.01	Mag99	10.0	OLDA
	30/12/2020	New (3rd) low pH probe aquired					
	05/01/2021	OLDA prepatration batch 2					
55	12/01/2021	QT	11->3	0.1	Mag99	10.0	OLDA
56	12/01/2021	QT	11->3	0.1	Mag99	10.0	OLDA
57	14/01/2021	QT	11->3	0.1	b	-	-
58	15/01/2021	QT	11->3	0.01	-	-	OLDA
	22/01/2021	OLDA prepatration batch 3					
59	27/01/2021	QT	11 -> 3	0.01	Mag99	10.0	-
60	27/01/2021	QT	11->3	0.01	Mag99	10.0	OLDA
61	02/02/2021	QT	11->3	0.01	Mag99	10.0	OLDA
62	26/02/2021	QT	11-> 3	0.1	Mag99	10.0	-
	05/03/2021	ODA preparation batch 2					
63	09/03/2021	QT	11->3	0.01	Mag99	10.0	ODA
	Washed the low temp probe quite well with pH4 stock sol in addition to 2-prop						
64	10/03/2021	QT	11->3	0.01	-	-	OLDA
65	12/03/2021	QT	11->3	0.1	Mag99	10.0	ODA
66	18/03/2021	QT	11->3	0.1	Mag99	10.0	ODA

Table D.2: Overview of performed magnetite potentiometric titrations at 150 °C.

Run	Date	Method	Titration	Ionic-S	Fe3O4	Mag (g/L)	FFA
	28/07/2020	Calibration with NaOH, 1*10-4 M					
	30/07/2020	Calibration with H2SO4, 5*10-4 M					
	04/08/2020	Calibration with H2SO4, 5*10-5 M					
	05/08/2020	Calibration with NaOH, 1*10-3 M					
	13/08/2020	Calibration with NaOH, 1*10-3 M					
	27/08/2020	Calibration with HCl, 0.01 M					
	01/09/2020	Calibration with disodium tetraborate 0.01M					
6	16/09/2020	QT	11 -> 3	0.1	b	-	-
8	18/09/2020	QT	11 -> 3	0.1	b	-	-
10	23/09/2020	QT	11 -> 3	0.01	b	-	-
11	28/09/2020	QT	11 -> 3	0.01	b	-	-
19	12/10/2020	SM	7 -> 3	0.01	b	-	-
20	14/10/2020	SM	7 -> 11	0.01	b	-	-
	15/10/2020	Calibration with disodium tetraborate 0.01M					
	16/10/2020	Calibration with HCl, 0.01 M					
21	26/10/2020	QT	11 -> 3	0.001	b	-	-
	28/10/2020	Calibration again with disodium tetrborate 0.01M					
28	30/10/2020	QT	11->3	0.01	Mag99	15.0	-
33	04/11/2020	QT	11->3	0.001	b	-	-
34	06/11/2020	QT	11-> 3	0.01	b	-	-
	07/11/2020	Calibration with HCl, 0.01 M					
	08/11/2020	Calibration with disodium tetraborate 0.01M					
37	12/11/2020	QT	11->3	0.01	Mag99	15.0	-
	02/12/2020	OLDA prepatration batch one					
53	30/12/2020	QT	11->3	0.01	Mag99	15.0	OLDA
	05/01/2020	OLDA preparation batch two					
54	06/01/2020	QT	11->3	0.01	Mag99	15.0	OLDA

E

XRD results of commercial magnetite

This section contains the XRD pattern results of the iron oxide powders used during the potentiometric titrations. Figure E.1 displays the results for the 99.997% reagent grade iron oxide, Puratronic or in this study called: Pur. Figure E.2 shows the results for the 95% reagent grade iron oxide, short: Mag95 and Figure E.3 shows the results for the 99.99% reagent grade iron oxide, short: Mag99.

The instrument applied: Bruker D8 Advance diffractometer Bragg-Brentano geometry and Lynxeye position sensitive detector. Cu Kα radiation. Divergence slit V12, scatter screen height 5 mm, 45 kV 40 mA. Sample spinning. Detector settings: LL 0.19, W 0.06. The measurement performed: Coupled θ -2θ scan 8°- 110°, step size 0.020°2θ, counting time per step 1 s. Data evaluation was performed using: Bruker software DiffracSuite.EVA vs 5.2, Rietveld: Profex-BGMN

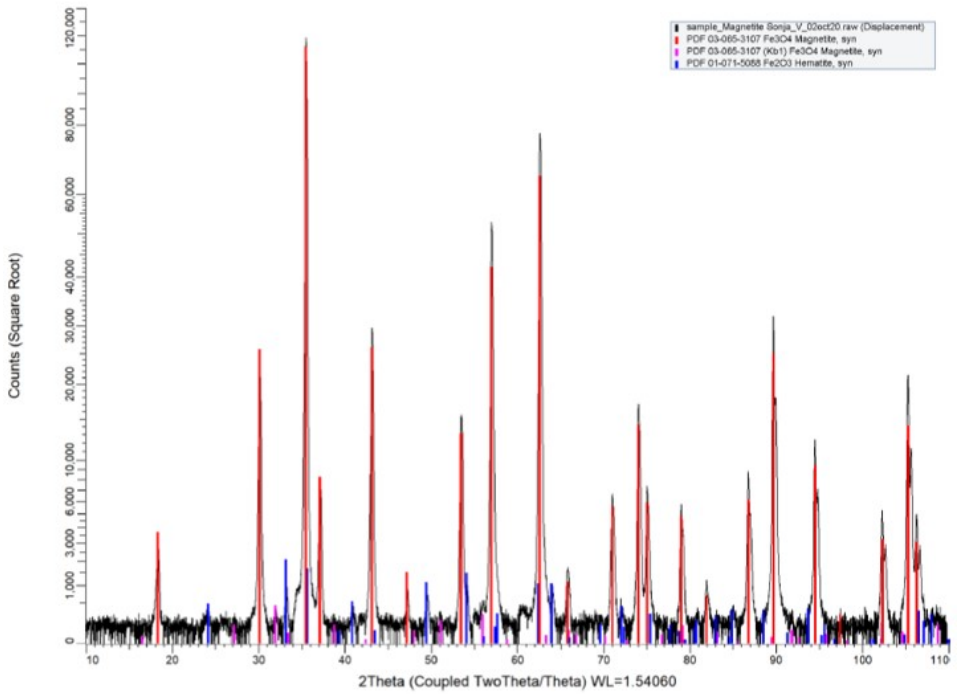

Figure E.1: XRD pattern Puratronic (Pur) sample after 2 to 3 months of storage, intensity scale square root. Measurement performed by R. Hendrikx.

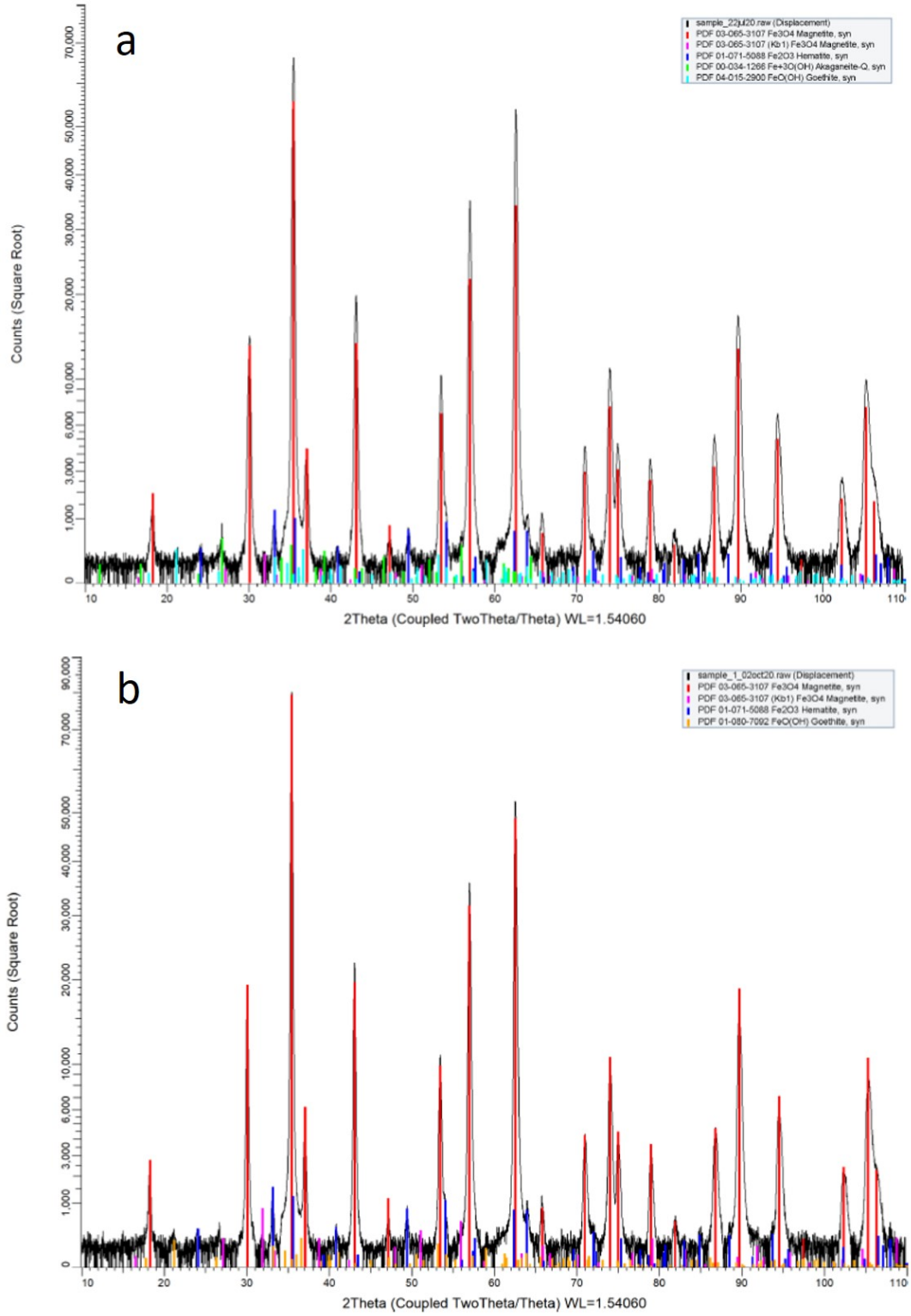

Figure E.2: XRD pattern a:Mag95 sample after purchase and b: Mag95 sample after 2 to 3 months of storage, intensity scale square root. Measurement performed by R. Hendrikx.

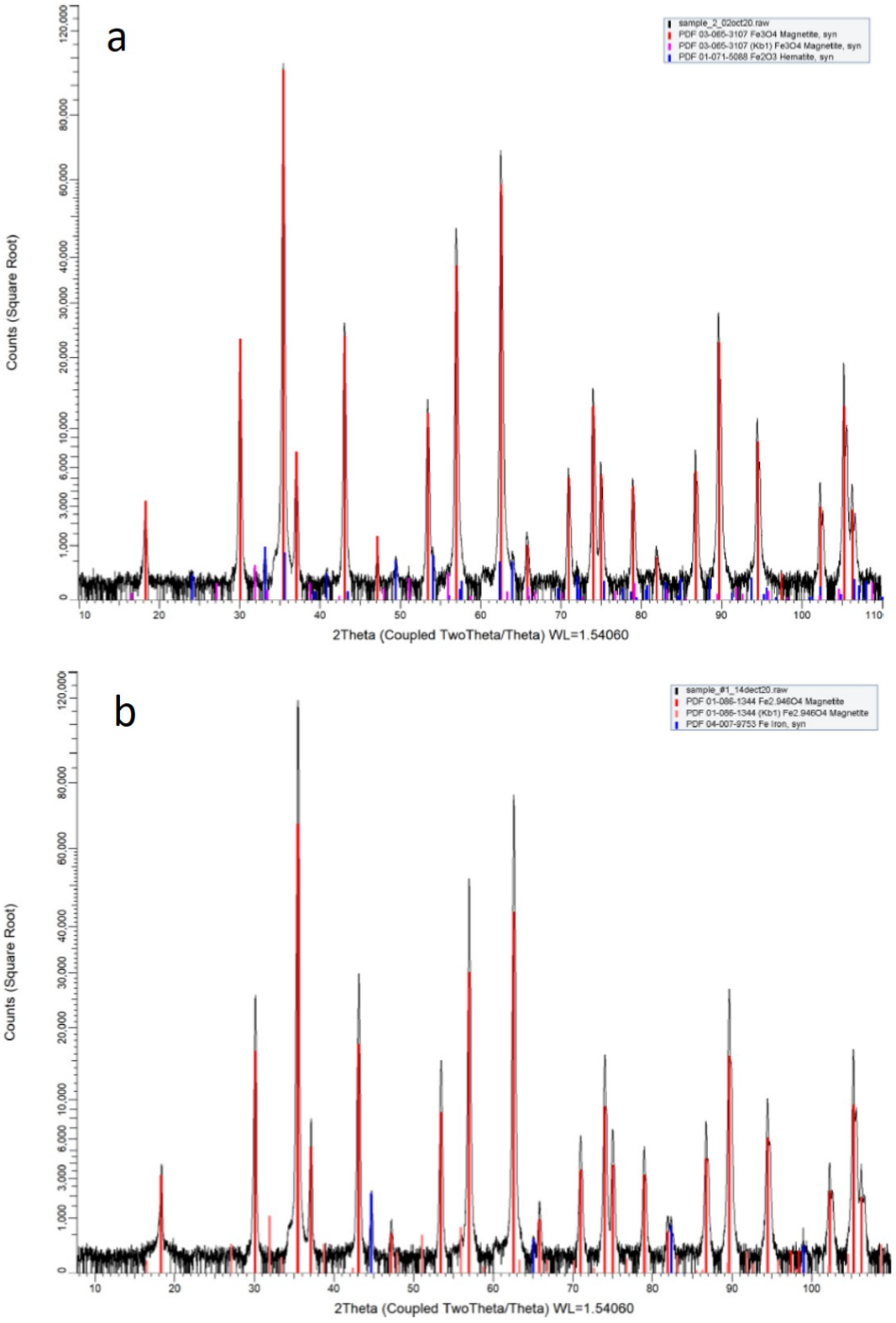

Figure E.3: XRD pattern a:Mag99 sample after purchase and b: Mag99 sample after 2 to 3 months of storage, intensity scale square root. Measurement performed by R. Hendrikx.

F

Oxygen concentrations during potentiometric titration

Oxygen levels measured during low temperature potentiometric titration, run 4. Measured with an SC-FDO 925 oxygen sensor. Figure F.1 depicts the result of the dissolved oxygen measurement, Figure F.2 depicts the same results of the dissolved oxygen measurement only focused to the region of 0 to 1 mg/L.

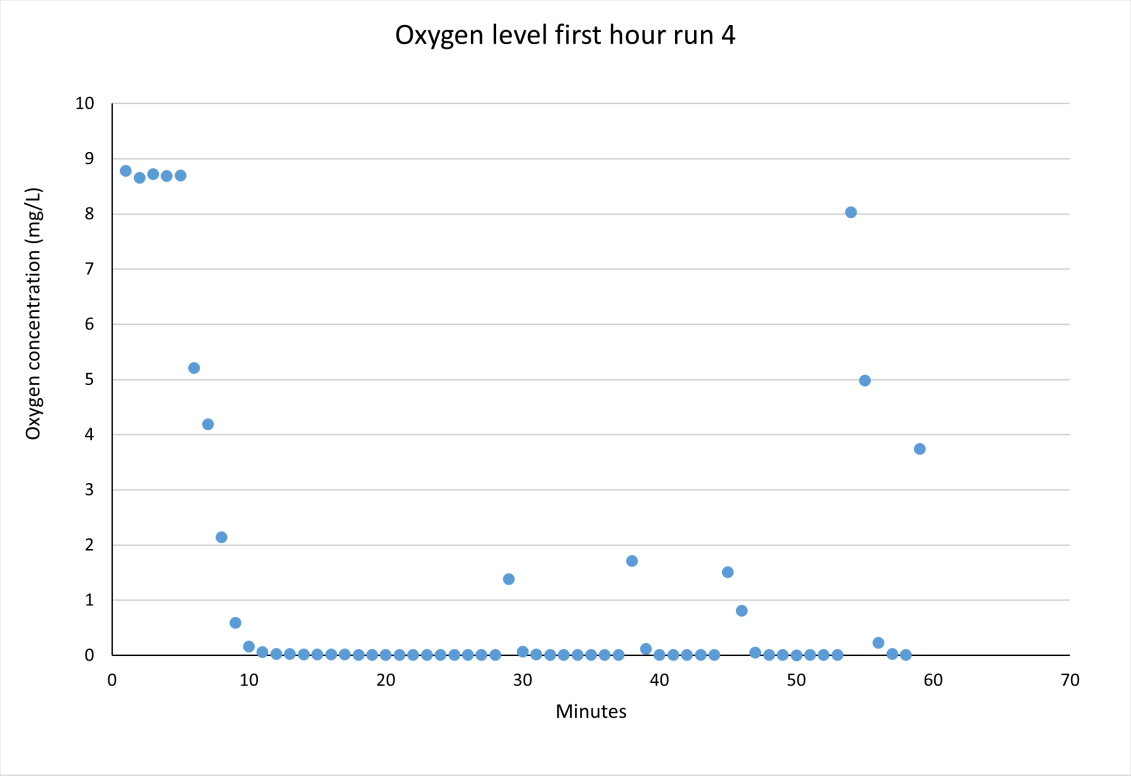

Figure F.1: Dissolved oxygen level during the first 60 minutes of potentiometric titration run 4.

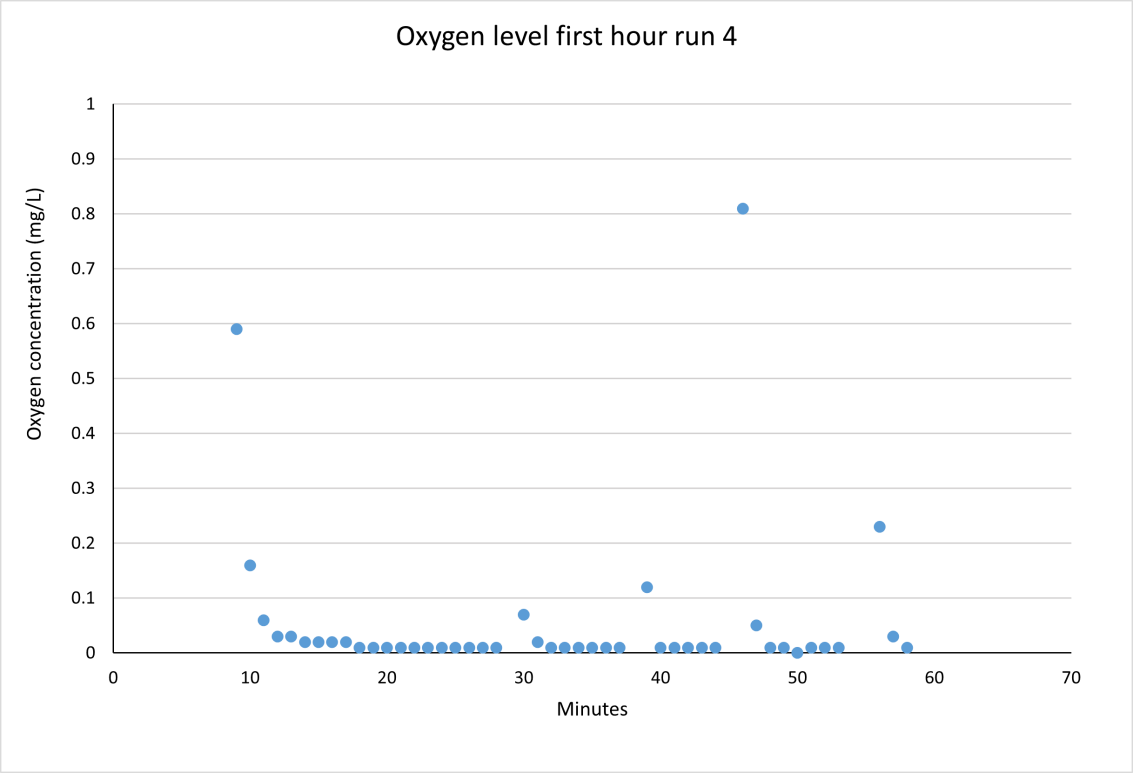

Figure F.2: Dissolved oxygen level during the first 60 minutes of potentiometric titration run 4, focusing on 0 to 1.0 mg/L region.

G

PHREEQC and Python code

G.1. PHREEQC code

Below a representative PHREEQC code is given. This code was used for the simulation of Runs 49 and 60.

```
        DATABASE PHREEQC.dat #The database used

# Hypothesis formulated by Gasnier and Lister
# ”Turner et al [17] showed that the use of amines, which are weak bases, lead to an
# increase of the IEP. This is explained by the incomplete dissociation of amines
# in water that enhance adsorption of protonated amines on surfaces, thus increasing
# the particle’s zeta potential.”

PHASES
SOLUTION_SPECIES

# Amm chosen as substitute for ODA, and OLDA
AmmH+ = AmmH+
-gamma 2.5 0
-dw 1.98e-9  312  0.95  4.53
-Vm  4.837  2.345  5.522  -2.88 1.096  3  -1.456  75.0  7.17e-3  1 # ref. 1

AmmH+ = Amm + H+
-log_k -10.65
#Dissociation constant of ODA used for both ODA and OLDA

#Note in PHREEQC: -pKa = log_k, whereas normally in chemistry  pKa = - log_k

SURFACE_MASTER_SPECIES
    Hfo_w  Hfo_wOH
# The surface active hydroxyl species (weak sites) of an oxide, magnetite
SURFACE_SPECIES
# change the log_K values to obtain the best fit
Hfo_wOH  + H+ = Hfo_wOH2+
        log_k  5.7 # = pKa1

        Hfo_wOH = Hfo_wO- + H+
        log_k  -7.3 # = -pKa2

# After the hypothesis of Gasnier and Lister 2013
Hfo_wOH + AmmH+ = Hfo_wOHAmmH+
log_k 15 #pKad, log_k 15 arbitratly selected

SURFACE_MASTER_SPECIES
Hfo_s  Hfo_sOH
# The surface active hydroxyl species (strong sites) of an oxide, magnetite
```

```
SURFACE_SPECIES
Hfo_sOH  + H+ = Hfo_sOH2+
        log_k  5.7 # = pKa1,int

        Hfo_sOH = Hfo_sO- + H+
        log_k  -7.3 # = -pKa2,int
END

#The commercial magnetite (Fe3O4) is the Puratronic powder provided by Alfar Aesar.
#The specific surface area has been determined by the Brunauer-Emmet-Teller (BET)
#method with N2 adsorption: 1.9 (±0.1) m2 g-1

SOLUTION 1 #to simulate the test solution
-units mmol/kgw
 pH 11.000  #To set the starting pH of the titration
 K 10 #To set the ionic strengt
 N(+5) 10 as NO3 #To set the ionic strengt
 #Ca 0.02  #To simulate accumulation of impurities (hardness)
 Amm 0.0061614  #2 ppm OLDA = 2mg/L = 0.0000061614mmol/kgw (MW = 324.6 g/mol)

SURFACE 1
#Definition of the magnetite particle surface
 -sites_units density
 Hfo_w 29.3 2.15 10.0
 Hfo_s 0.000
#mol sites per nm2, specific surface area (m2/g), and   concentration (g/L)

REACTION_TEMPERATURE 1 #To set the temperature of the titration
25.0
REACTION 1 #To simulate the titrant addition
H 1
NO3- 1
0.0024 moles in 120 steps
EQUILIBRIUM_PHASES 1 #As solution is sparged
O2(g) 0.0 0.001


USER_GRAPH 1 #To plot the results
-connect_simulations true
-headings x withFe3O4I0.1 Mag-total-H+
-chart_title "Run49 pH over titrant added"
-axis_titles "Amount Acid added"  "pH"
-axis_scale x_axis 0 0.0025 0.0002 0.0001
-axis_scale y_axis 1 12 1
-axis_scale sy_axis auto
-initial_solutions false
-start
05 N0 = 0.01
10 graph_x  ((tot("N"))- N0) #-LA("H+")#TC (for pH vs. Temperature)
20 graph_y  -la("H+") #-LA("e-") #-LA("e-")


SELECTED_OUTPUT #To export the results to Phyton
-file fit_run60_phreeqc_OLDA.csv
-totals Amm
-molalities Hfo_sO- Hfo_sOH2+ Hfo_wO- Hfo_wOH2+ Hfo_wOHAmmH+
```

G.2. Python code

Below a representative python code plotting the experimental and simulated data of Runs 49 and 60, followed by the 3rd order polynomial fit and its derivative. Lastly, the RMSE between the experimental data and PHREEQC simulation was calculated to determine the fit.

```
import numpy as np
%matplotlib inline
import matplotlib.pyplot as plt
import xlrd
import sys
from pandas import read_csv
from scipy.interpolate import make_interp_spline, BSpline
from sklearn.metrics import r2_score
import numpy
import scipy as sp
from scipy import optimize
from scipy.interpolate import make_interp_spline, BSpline

loc = (r'C:\Users\benbi\Documenten\TU-Afstuderen\Run60_tit_mag99+OLDA_I=0.01_B2A\Run-60.xlsx')

wb = xlrd.open_workbook(loc)
sheetres = wb.sheet_by_index(0)
sheetlutzF = wb.sheet_by_index(2)

x_pH =  np.zeros(35)
y_SC = np.zeros(35)
for i in range(len(x_pH)):
    a = sheetlutzF.cell_value(1+i, 0)
    b = sheetlutzF.cell_value(1+i, 1)
    x_pH[i]  += a
    y_SC[i] += b

ex_pH = x_pH[::-1]
ex_s0 = y_SC[::-1]

phreeqccsv3 = read_csv(r'C:\Users\benbi\Documenten\TU-Afstuderen\fit_run60_phreeqc_OLDA.csv',
delim_whitespace=True, skipinitialspace=True, index_col=0)

Hfo_sO =  np.zeros(120)
Hfo_sOH2 = np.zeros(120)
Hfo_wO = np.zeros(120)
Hfo_wOH2 = np.zeros(120)
Hfo_wOHAmmH = np.zeros(120)
Amm = np.zeros(120)
pH = np.zeros(120)
for i in range(len(Hfo_sO)):
    a = phreeqccsv3.iloc[2+i, 8]
    b = phreeqccsv3.iloc[2+i, 9]
    c = phreeqccsv3.iloc[2+i, 10]
    d = phreeqccsv3.iloc[2+i, 11]
    e = phreeqccsv3.iloc[2+i, 5]
    f = phreeqccsv3.iloc[2+i, 12]
    g = phreeqccsv3.iloc[2+i, 7]
    Hfo_sO[i] += a
    Hfo_sOH2[i] += b
    Hfo_wO[i] += c
    Hfo_wOH2[i] += d
    pH[i] += e
    Hfo_wOHAmmH[i] += f
    Amm[i] = g

Dosed_amm = phreeqccsv3.iloc[0, 7]
Abs_amm = 1.0 - (Amm / Dosed_amm)
```

```
Abs_ammr = Abs_amm[::-1]

eq_L2 = [-Hfo_sO[i] + Hfo_sOH2[i] -Hfo_wO[i] + Hfo_wOH2[i] + Hfo_wOHAmmH[i] for i in range(len(Hfo_sO))]
eq_L = - Hfo_sO + Hfo_sOH2 - Hfo_wO + Hfo_wOH2 + Hfo_wOHAmmH

area = 21.5 #(m2/L)  (2.15 m2/g times 1 gram per 0.1L)(for Mag99)
F = 96485.3329 #Faraday's concstant C/mol

Sigma_03 = (eq_L * F)/area
Sigma_0r3 = Sigma_03[::-1]
pHr3 = pH[::-1]

#Plot Experimental data and Phreeqc Simulation
plt.figure(1)
plt.plot(pHr3, Sigma_0r3, 'ro-', label='run49/60 Model PHREEQC')
plt.plot(ex_pH, ex_s0, 'o', label='exp. data run49')
plt.title('Surface charge from Phreeqc')
plt.grid(True)
plt.legend(loc='best');

#Fit of polynomial curve trough experimental data points
a2, b2, c2, d2 = np.polyfit(ex_pH, ex_s0, 3)
x_pH = np.linspace(3,11,35)
yfit2 = (a2 * x_pH ** 3) + (b2 * x_pH **2) + (c2 * x_pH) + d2

#Plot exp. data, the fit of the polynomial curve, and deriviative of fit
xd2 = np.linspace(3,11,1000)
yd2 = (3 * a2 * xd2**2) + (2*b2 * xd2**1) + (c2)
plt.figure()
plt.plot(ex_pH, ex_s0, 'bo', label='model')
plt.plot(x_pH, yfit2, 'r', label='fit')
plt.plot(xd2, yd2, label='derivative of fit')
plt.legend(loc='best')
plt.title('Fit of a 3rd degree polynomial function to the surface charge')
plt.xlabel('pH')
plt.ylabel('Surface charge (C/m^2)')
plt.show;

###Calculate the max value, or pH of max value, of the deriviative:
x = np.linspace(3,11,1000)
def f(x, a2, b2, c2):
    fx = (3 * a2 * x**2) + (2*b2 * x**1) + (c2)
    return fx

max_x = sp.optimize.fmin(lambda x: -f(x,a2,b2,c2), 0)
print('max_x aka pH of max derivitave is:', max_x)
max_y = (3 * a2 * max_x**2) + (2*b2 * max_x**1) + (c2)

#Plot derivative seperately plus max value
plt.figure()
plt.title('Derivative of the fit')
plt.plot(xd2, yd2)
plt.plot(max_x, max_y, 'go')
plt.show();

# Polynomial Regression calculation
def polyfit(x, y, degree):
    results = {}
    coeffs = numpy.polyfit(x, y, degree)
```

```
    correlation = numpy.corrcoef(x, y)[0,1]
    results['determination R2!, best apporximation'] = correlation**2
    return results
polyfit(ex_pH, ex_s0, 3)

# Smooth out data (both the model and experimental data)
pHr_smooth = np.linspace(pHr3.min(), pHr3.max(), 500)
spl = make_interp_spline(pHr3, Sigma_0r3, k=3)
Sigma0r_smooth = spl(pHr_smooth)
ex_smooth = np.linspace(ex_pH.min(), ex_pH.max(), 500)
spl = make_interp_spline(ex_pH, ex_s0, k=3)
ey_smooth = spl(ex_smooth)

#Calculate RSME
rmse = np.sqrt(np.sum((ey_smooth - Sigma0r_smooth) ** 2) / len(Sigma0r_smooth))
print('RSME', rmse)

plt.plot(pHr_smooth, Sigma0r_smooth, 'o-', label='model smooth')
plt.plot(ex_smooth, ey_smooth, 'o-', label='experimental results smooth')
plt.title('RMSE: '+str(rmse))
y_zero =  np.zeros(len(pHr_smooth))
idx = np.argwhere(np.diff(np.sign(y_zero - ey_smooth))).flatten()
plt.plot(pHr_smooth[idx], y_zero[idx], marker="*", markersize=12)
print('insterection point of exp data R36 of 0-axis is', pHr_smooth[idx])
plt.legend(loc='best')
plt.xlabel('pH')
plt.ylabel('Surface charge (C/m^2)')
plt.show();
```

H

SEM magnetite layer cross sections images

This section contains the cross section images of the magnetite layers after the four performed immersion, indicated with an a, and re-immersion, indicated with a b, runs.

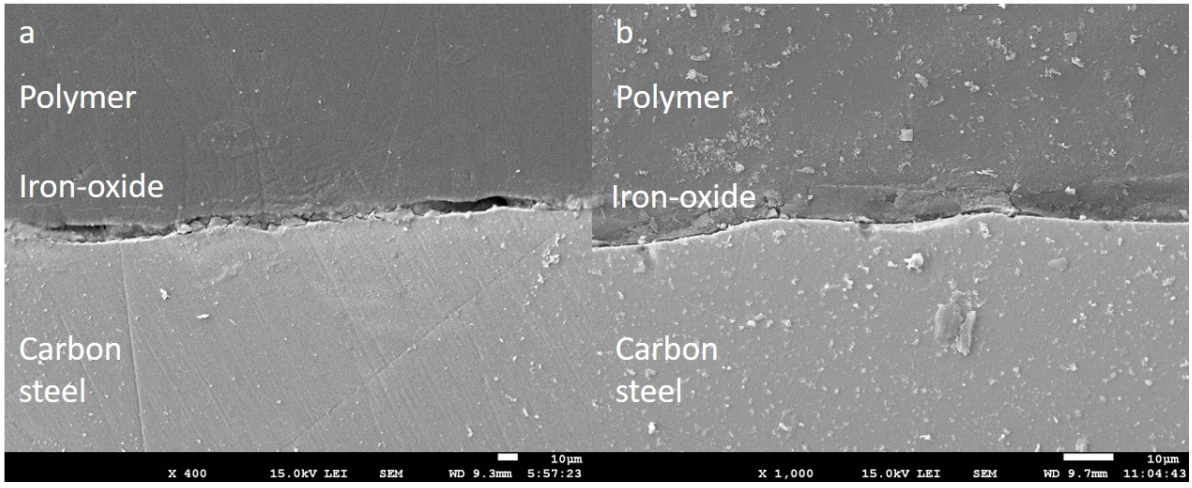

Figure H.1: SEM image of the magnetite layer cross section after a: the immersion test under a blank chemistry and b: subsequent re-immersion test under acidic FAC conditions. Pictures taken by Durga Mainali.

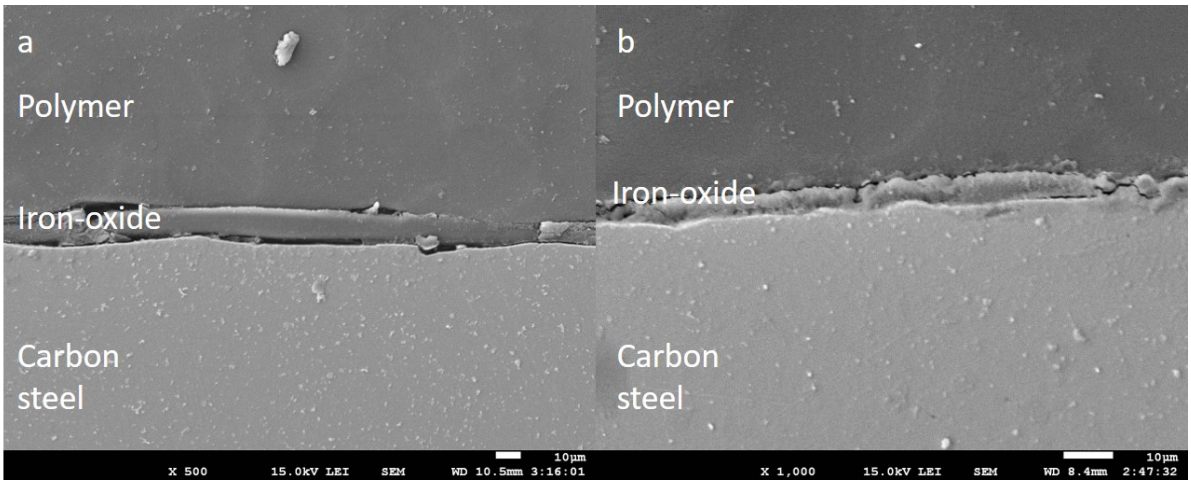

Figure H.2: SEM image of the magnetite layer cross section after a: the immersion test under the presence of 2ppm ammonia and ODA, and b: subsequent re-immersion test under acidic FAC conditions. Pictures taken by Durga Mainali.

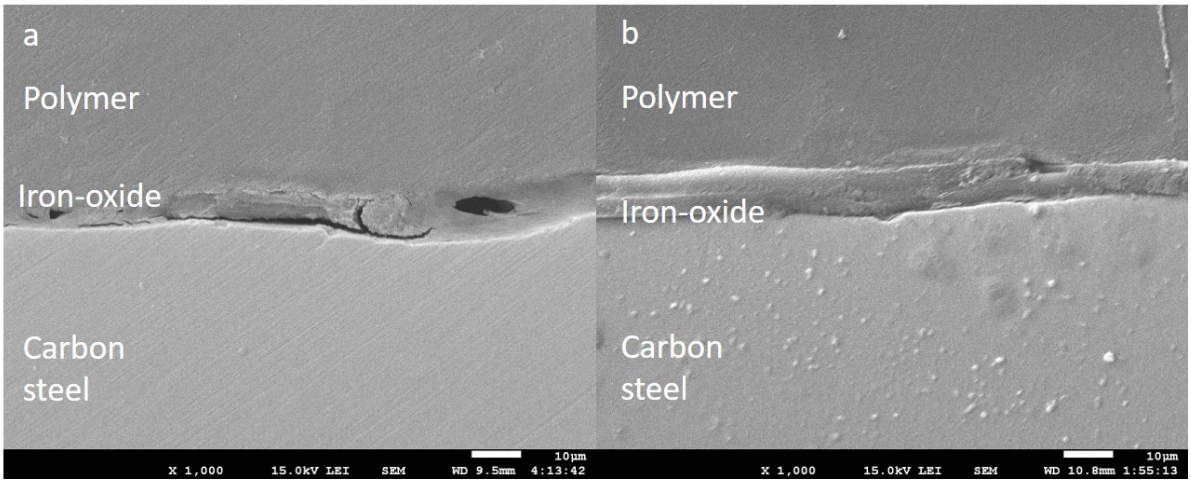

Figure H.3: SEM image of the magnetite layer cross section after a: the immersion test under the presence of 2ppm ammonia and OLDA, and b: subsequent re-immersion test under acidic FAC conditions. Pictures taken by Durga Mainali.

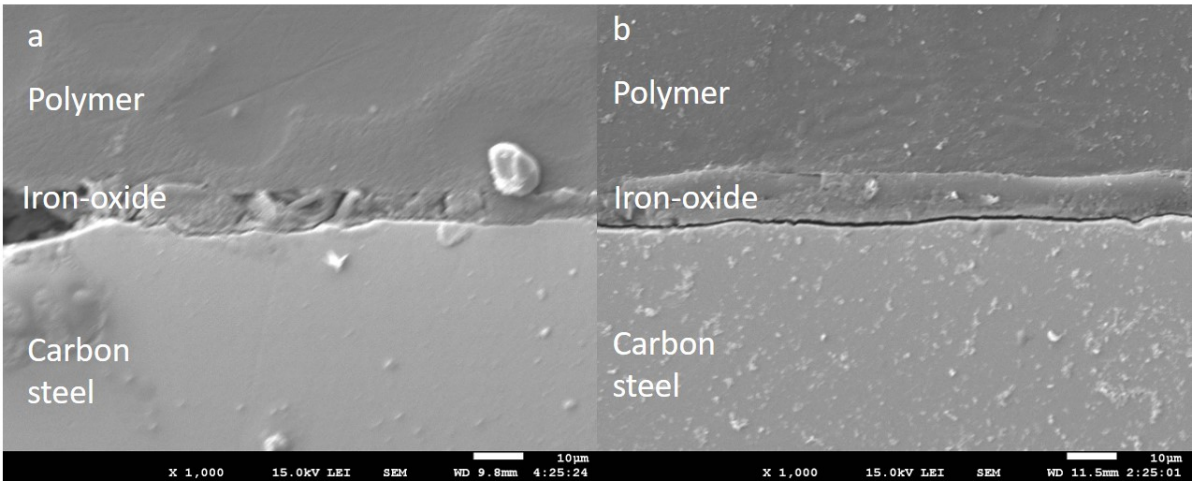

Figure H.4: SEM image of the magnetite layer cross section after a: the immersion test under the presence of 2ppm ammonia and b: subsequent re-immersion test under acidic FAC conditions. Pictures taken by Durga Mainali.

Overview immersion re-immersion tests results

Table 3.2 in section 3.3 contains the test environments of the immersion and re-immersion tests. This section will provide an overview of the immersion and re-immersion test results.

Table I.1: Overview of the test duration and results from the immersion and re-immersion tests.

Experiment		Chemistry condition			Duration (h)	FFA after run (ppm)	Henry Ads Con (L/m^2) + %ads
		Chemical (ppm)	pH25C prior	pH25C aft.			
Run 1	R1.1	Neutral	6.5	7.4	46.3	0.03	-
	R1.2	Acetic acid: 0.08	6.0	5.9	48.1	0.00	-
Run 2	R2.1	NH3: 2.00 ODA: 2.11	9.12 ±0.02	7.9	48.0	0.15	543 92.89%
	R2.2	Acitic acid: 0.08	5.8	4.9	48.0	0.20	-
Run 3	R3.1	NH3: 2.00 OLDA: 2.44	9.12 ±0.02	8.2	47.2	0.03	3300 98.77%
	R3.2	Acitic acid: 0.08	6.1	5.6	48.0	0.00	-
Run 4	R4.1	NH3: 2.00	9.12 ±0.02	8.1	47.8	0.00	-
	R4.2	Acetic acid: 0.08	6.2	6.5	47.9	0.00	-

Table I.2: Overview of the results from the immersion and re-immersion tests. Dissolved iron* is determined by measuring the difference in weight of the coupon therefore including both losses due to bare metal and/or oxide layer.

Experiment		FAC Rate (mm/y)		Thickness Fe3O4 layer (um)			Dissolved iron*	Iron in solution (mg/coupon)	
		(SEM)	(Weight loss)	SEM	EDS	Weight loss	(mg/coupon)	Total iron	Dissolved iron
Run 1	R1.1	0.175 ±0.028	0.100	1.31 ±0.29	3.68 ±1.30	0.76	1.3 ±0.2	0.11	0.09
	R1.2	0.090 ±0.021	0.070	1.06 ±0.44	1.94 ±0.14	0.64	3.1 ±1.4	0.06	0.06
Run 2	R2.1	0.137 ±0.018	0.152	0.79 ±0.11	2.20 ±0.58	0.80	3.6 ±1.4	0.38	0.34
	R2.2	0.060 ±0.011	0.057	0.69 ±0.05	1.70 ±0.37	0.83	0.05 ±0.05	0.01	0.00
Run 3	R3.1	0.158 ±0.016	0.121	0.93 ±0.17	2.37 ±0.20	0.63	3.7 ±0.3	0.89	0.81
	R3.2	0.073 ±0.003	0.060	0.85 ± 0.06	2.08 ±0.49	0.65	0.03 ±0.55	0.16	0.15
Run 4	R4.1	0.159 ±0.015	0.149	0.90 ±0.05	3.24 ±0.68	0.74	4.15 ±1.2	0.42	0.37
	R4.2	0.078 ±0.004	0.073	0.73 ±0.08	2.11 ±0.77	0.72	0.45 +_ 0.45	0.01	0.01

J

XRD results of coupons after corrosion tests

Table J.1 presents the overview of the XRD pattern results. Performed on the coupons after each immersion and re-immersion test.

Table J.1: XRD results of coupons after the immersion and re-immersion test, performed by Ruud Hendrikx X-Ray Facilities Group, Delft University of Technology, Faculty of 3mE.

After run	Additive	Coupon	Location	Compound	
1.1	Blank	Exp 1.1 C3	Middle part	Iron	Fe
				Magnetite	Fe+2Fe2+3O4
1.2	-	Exp 1.1 C1	Middle part	Iron	Fe
				Magnetite	Fe+2Fe2+3O4
2.1	ODA + NH3	Exp 2.1 C3	Middle part	Iron	Fe
				Magnetite	Fe+2Fe2+3O4
2.2	-	Exp 2.2 C4	Middle part	Iron	Fe
				Magnetite	Fe+2Fe2+3O4
3.1	OLDA + NH3	Exp 3.2 C4	Middle part	Iron	Fe
				Magnetite	Fe+2Fe2+3O4
			Top part	Iron	Fe
				Magnetite	Fe+2Fe2+3O4
3.2	-	Exp 3.2 C1	Middle part	Iron	Fe
				Magnetite	Fe+2Fe2+3O4
			Top part	Iron	Fe
				Magnetite	Fe+2Fe2+3O4
4.1	NH3	Exp 4.1 C3	Middle part	Iron	Fe
				Magnetite	Fe+2Fe2+3O4
4.2	-	Exp 4.2 C1	Middle part	Iron	Fe
				Magnetite	Fe+2Fe2+3O4

K

Digital microscope images of oxide layer

Figure K.1 showing signs of spalling on the coupon/oxide surface via the digital microscope. The lighter colour indicates the bare metal underneath the oxide layer. No signs of spalling were observed for the oxide layer formed under ODA and ammonia chemistry after being re-immersed under acidic FAC conditions.

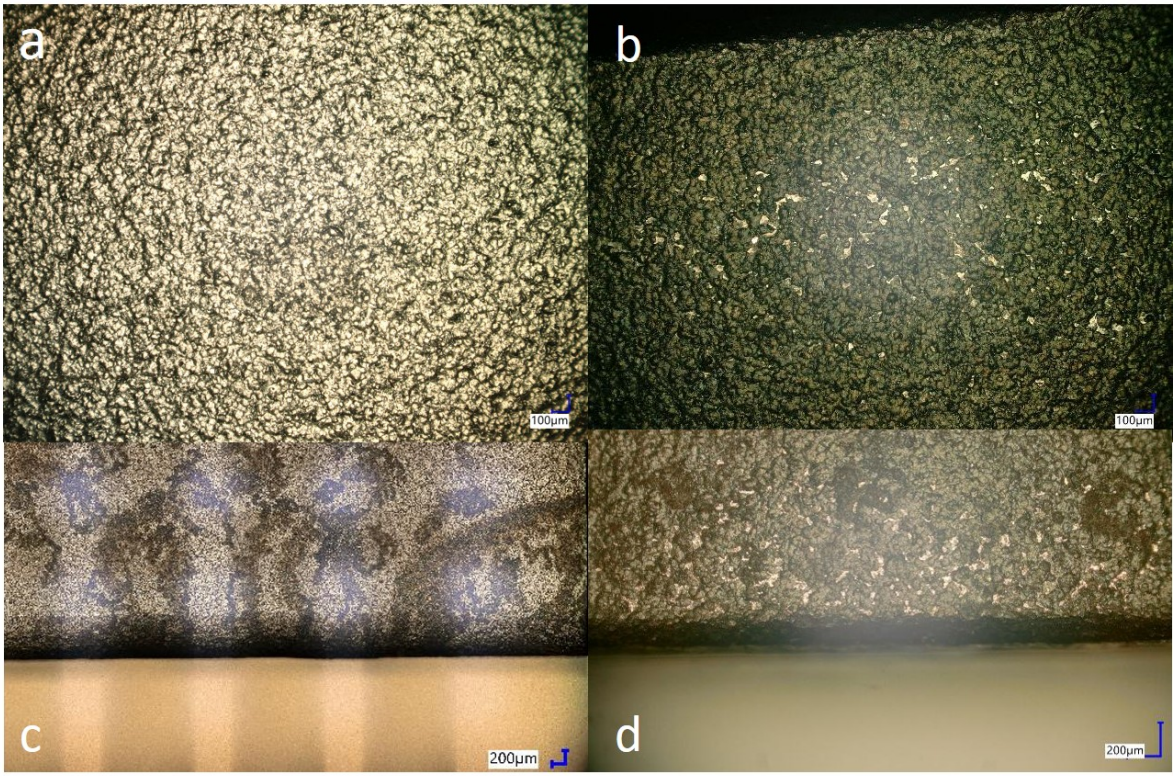

Figure K.1: Digital microscope images of the coupon/oxide surface after the re-immersion test of a: a fresh reference coupon (not been immersed), b: oxide surface formed in a blank chemistry, c: oxide surface formed under ODA and ammonia chemistry, and d: an oxide layer formed under an ammonia chemistry.

EDS of coupon cross section

A representative EDS result of the cross section is depicted in Figure L.1. The EDS results are projected on to the SEM cross section image. The figure clearly shows more elemental oxygen (green dots) being present at the light grey layer between the polymer, dark grey on top, and steel, below.

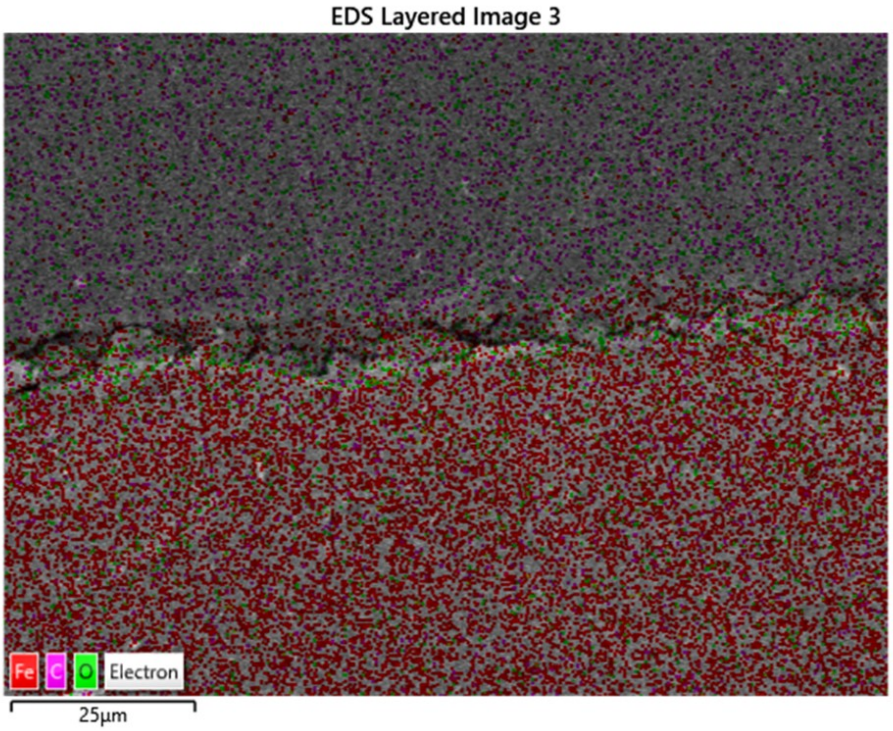

Figure L.1: EDS results overlapped on SEM image of the cross section after the immersion experiment, run 1.1. Detected elemental iron as red dots, purple for carbon and green for elemental oxygen.

M

Recorded observations

This appendix contains some notable recorded observations performed after the potentiometric titrations at 25 °C, section M.1, and the FFA to magnetite adsorption experiments, section M.2.

M.1. Observations made after titrations

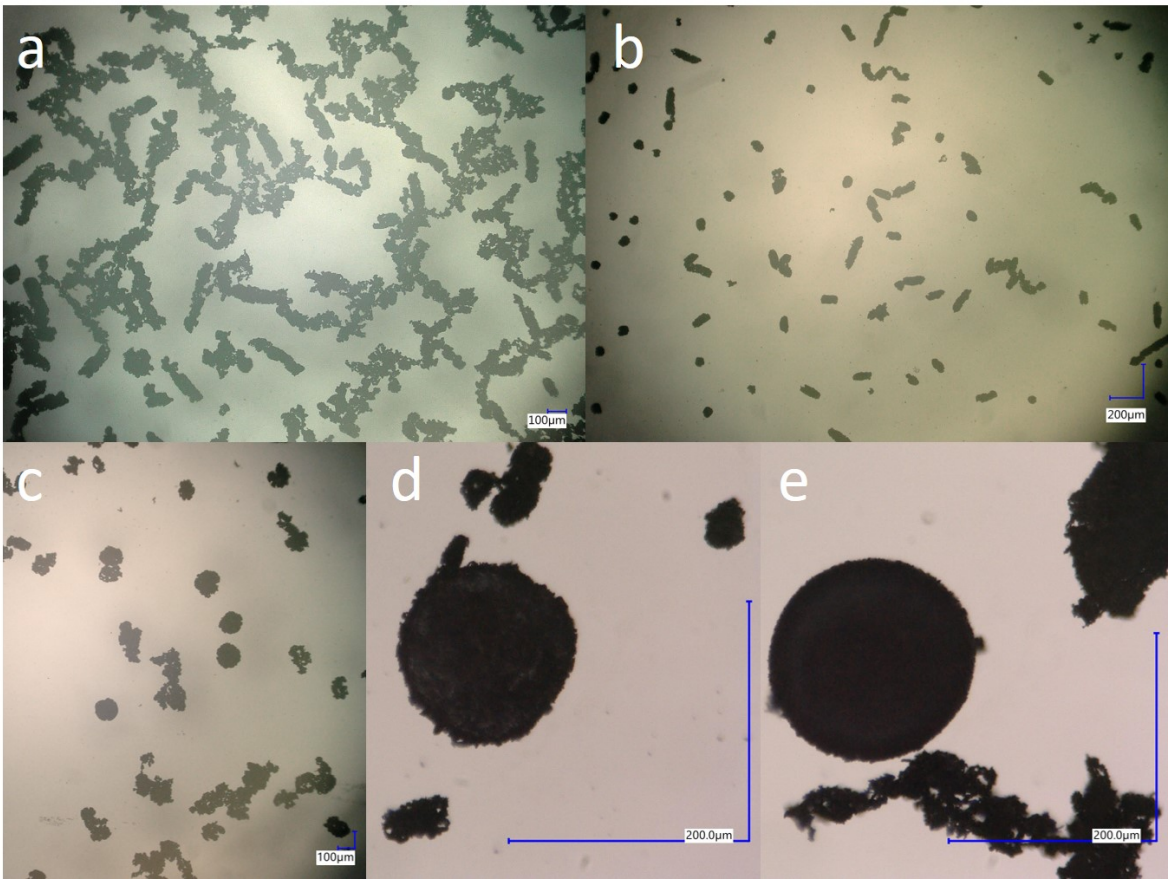

Figure M.1: Digital-microscope images of magnetite colloids after a: run 36, magnetite-only titration I=0.01 M, b: run 43, magnetite and 2ppm ODA solution I=0.01 M, c: run 55, magnetite and 2ppm OLDA I=0.1 M, d and e: run 63, magnetite and 2ppm ODA I=0.01 M. All magnetite was 99.99% reagent grade, i.e. Mag99.

Figure M.2: Picture taken after titration run 18, showing the magnetite 95% reagent grade purity, i.e. Mag95.

M.2. Observations made after adsorption experiments

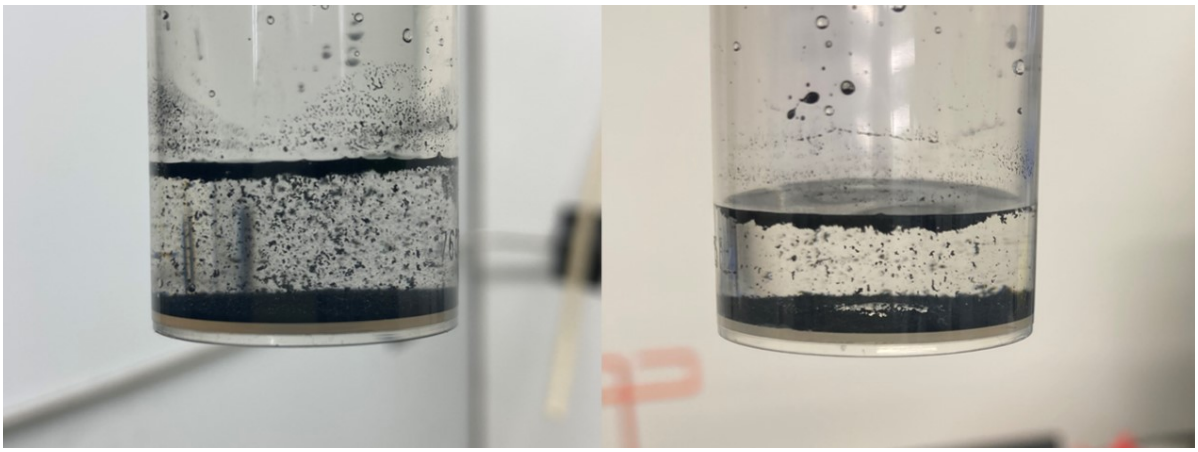

Figure M.3: Left: sample taken after OLDA to magnetite powder adsorption experiment. Right: sample taken after ODA to magnetite powder adsorption experiment. Both performed at neutral pH, at room temperature, and both samples taken after 24 hours.

N

ODA and OLDA adsorption during titrations

This appendix presents the fraction of ODA or OLDA left after a titration. Determined by measuring the FFA concentration after the titration with the Bengal Rosa dye method. This was also done for titrations were only an FFA (ODA or OLDA) was titrated, this to obtain an reference value. As FFA is known to adsorb to other available surfaces, such as the glass wall of the titration cell.

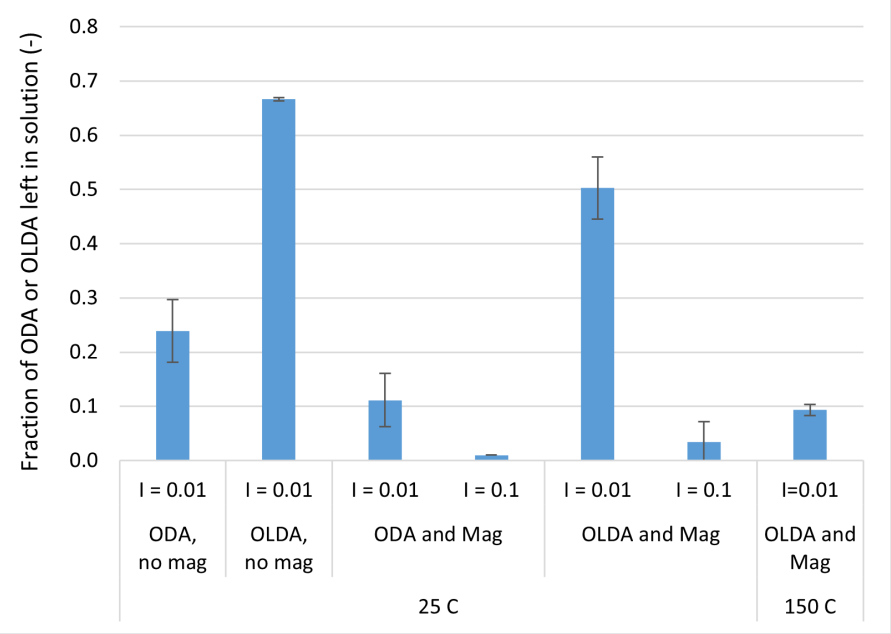

Figure N.1: Fraction of ODA and OLDA left in the test solution after a potentiometric titration. Potentiometric titrations were classified based on electrolyte strength and temperature. Magnetite (Mag) used was 99.99% reagent grade. Weight (ppm) ratio between Mag and FFA (Mag/FFA) was 5000.

Surface complexation model curves

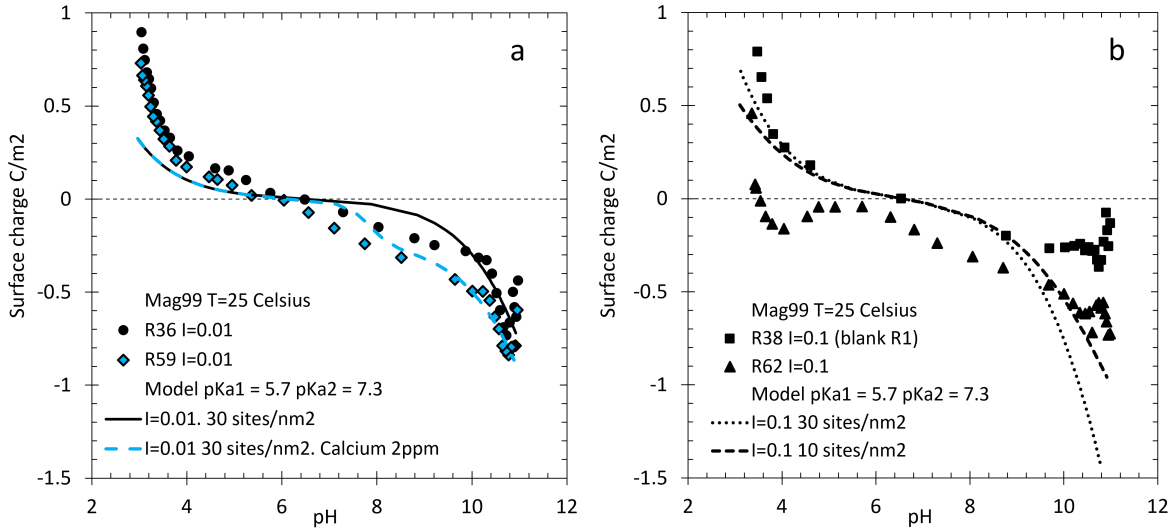

Figure O.1: Fitted model on mag99 titration data at a: 0.01 ionic strength and b: 0.1 ionic strength.